



GA - 4659

INTEGRAL NEUTRON THERMALIZATION

Annual Summary Report

October 1, 1962, Through September 30, 1963

By

J. R. Beyster	J. L. Russell, Jr.
J. R. Brown	G. D. Trimble
J. U. Koppel	J. A. Young
J. M. Neill	J. C. Young

January 24, 1964

General Atomic Division
General Dynamics Corporation
San Diego, California

metadc304063

LEGAL NOTICE

This report was prepared as an account of Government sponsored work. Neither the United States, nor the Commission, nor any person acting on behalf of the Commission:

A. Makes any warranty or representation, expressed or implied, with respect to the accuracy, completeness, or usefulness of the information contained in this report, or that the use of any information, apparatus, method, or process disclosed in this report may not infringe privately owned rights; or

B. Assumes any liabilities with respect to the use of, or for damages resulting from the use of any information, apparatus, method, or process disclosed in this report.

As used in the above, "person acting on behalf of the Commission" includes any employee or contractor of the Commission, or employee of such contractor, to the extent that such employee or contractor of the Commission, or employee of such contractor prepares, disseminates, or provides access to, any information pursuant to his employment or contract with the Commission, or his employment with such contractor.

This report has been reproduced directly from the best available copy.

Printed in USA. Price \$3.00. Available from the Office of Technical Services, Department of Commerce, Washington, D. C. 20230

GENERAL ATOMIC
DIVISION OF
GENERAL DYNAMICS

JOHN JAY HOPKINS LABORATORY FOR PURE AND APPLIED SCIENCE

P.O. BOX 608. SAN DIEGO 12. CALIFORNIA

GA-4659
PHYSICS
(TID-4500, 29th. Ed.)

INTEGRAL NEUTRON THERMALIZATION

ANNUAL SUMMARY REPORT

OCTOBER 1, 1962, THROUGH SEPTEMBER 30, 1963

Contract AT(04-3)-167
Project Agreement No. 2
U. S. Atomic Energy Commission

Work done by:

J. R. Beyster	Y. D. Naliboff
J. R. Brown	M. S. Nelkin
H. C. Honeck	D. E. Parks
G. K. Houghton	J. L. Russell, Jr.
D. H. Houston	G. D. Trimble
G. D. Joanou	F. Wikner
J. Kirkbride	J. A. Young
J. U. Koppel	J. C. Young

Report written by:

J. R. Beyster
J. R. Brown
J. U. Koppel
J. M. Neill
J. L. Russell, Jr.
G. D. Trimble
J. A. Young
J. C. Young

January 24, 1964

PREVIOUS REPORTS IN THIS SERIES

GA-2544—Annual Report for October, 1960, through September, 1961

GA-3542—Annual Report for October, 1961, through September, 1962

GA-3853—Quarterly Report for October, November, and December, 1962

GA-4176—Quarterly Report for January, February, and March, 1963

GA-4426—Quarterly Report for April, May, and June, 1963

CONTENTS

I.	INTRODUCTION	1
II.	NEUTRON THERMALIZATION IN WATER (H ₂ O)	4
	2. 1. Introduction	4
	2. 2. Temperature-dependent Infinite-medium Neutron Spectra	5
	2. 3. Spatially Dependent Angular-flux Measurements	9
	2. 3. 1. Nonmultiplying Systems	9
	2. 3. 2. Spectral Measurements in Multiplying Assembly	21
	2. 4. Total Cross Section for H ₂ O	25
	2. 5. Angular Distribution Measurements	30
	2. 6. Scattering Model for H ₂ O	50
	2. 7. Modifications of the Code GAKER	67
III.	NEUTRON THERMALIZATION IN D ₂ O	69
IV.	NEUTRON THERMALIZATION IN POLYETHYLENE	79
V.	NEUTRON THERMALIZATION IN BENZENE	85
VI.	NEUTRON THERMALIZATION IN ZIRCONIUM HYDRIDE	90
	6. 1. Temperature-dependent Infinite-medium Neutron Spectra	90
	6. 2. Scattering Models for Zirconium Hydride	95
VII.	NEUTRON THERMALIZATION IN BeO	100
	7. 1. Status of the Problem	100
	7. 2. Normal-mode Production	100
	7. 3. Calculations	101
VIII.	SCATTERING MODEL FOR BERYLLIUM	107
	8. 1. Lattice Dynamics of Beryllium	107
	8. 2. Frequency Spectrum of Beryllium	111
	8. 3. Scattering Kernel for Beryllium	115
	8. 4. Specific Heat	118
	8. 5. Elastic Scattering	118
IX.	PULSED CRITICAL ASSEMBLY	123
	9. 1. Introduction	123
	9. 2. Pulsed Neutron Measurements	123
	9. 2. 1. General	123
	9. 2. 2. Determination of α	127
	9. 2. 3. Application of Method of Garelis and Russell	130
	9. 2. 4. Results	130

9.2.5.	Error Assignments	138
9.2.6.	Conclusions	139
9.3.	Subcritical Multiplication and Critical Buckling	139
9.4.	Summary of Equations Used in Analysis Method of Garelis and Russell	141
X.	FAST-NEUTRON SHIELDING STUDIES	144
XI.	EXPERIMENTAL TECHNIQUES	152
11.1.	Sensitivity Function of the 16-m Detector Bank	152
11.2.	Collimation Studies	157
XII.	UNIVERSAL SCATTERING-KERNEL CODE	160
12.1.	Calculation of $S_{0m}(\kappa, \epsilon)$	162
12.2.	Information for the Programmer	165
12.3.	Example Showing a Possible Flow of the Program	168
XIII.	CADMIUM-CURTAIN EXPERIMENT	172
XIV.	ASYMPTOTIC (DIFFUSION-COOLED) NEUTRON SPECTRA	174
XV.	RESEARCH EQUIPMENT	177
15.1.	Linac Facility	177
15.2.	Pressure Vessel	178
15.3.	Pulsed Critical Assembly	180
15.4.	New Flight Path and Low-room-return Neutron Cave	181
Appendixes		
I.	FORMAT FOR NEUTRON-SPECTRA DATA BOOK	183
II.	MEAN-EMISSION-TIME CORRECTION FOR THE MEASURE- MENT OF STATIONARY SPECTRA BY THE PULSED- NEUTRON-SOURCE TECHNIQUE	187
REFERENCES	192

I. INTRODUCTION

This report describes the Integral Neutron Thermalization activities at General Atomic from October 1, 1962, through September 30, 1963, under Contract AT(04-3)-167, Project Agreement No. 2, with the U. S. Atomic Energy Commission. For general reviews of experimental, analytical, and theoretical investigations previously performed under this program, the reader is referred to the two previous annual reports.⁽¹⁾⁽²⁾

It will be recalled that the research program for the present contract year was to include the following areas of work:

1. Temperature-dependent neutron spectra (Sections II and VI).
2. Spectra in finite media (Section II).
3. Neutron spectra in zirconium hydride assemblies (Section VI).
4. Angular distribution measurements (Section II).
5. Spectra in poisoned D₂O (Section III).
6. BeO feasibility studies (Section VII).
7. Fast-neutron shielding studies (Section X).
8. Theoretical studies of integral neutron thermalization (these investigations are discussed in the sections devoted to the appropriate moderators of interest).
9. Alpha measurements made in conjunction with Oak Ridge National Laboratory (these measurements will be reported by the ORNL group).

To supplement the above studies, work was also performed in the following areas:

1. Total cross section of H₂O (Section II).
2. Neutron thermalization in beryllium (Section VIII).
3. Pulsed critical assembly (Section IX).
4. Experimental techniques (Section XI).
5. Universal scattering-kernel code (Section XII).
6. Neutron spectra in organic systems (Sections IV and V).

In addition, improvements were made in the research equipment available for experimental neutron thermalization studies (the current status of this equipment is discussed in Section XV). Finally, a format was designed for the summary compilation of experimentally obtained neutron spectral data and results of theoretical calculations in a concise and legible form (Appendix I). The example given here is for a typical spectral experiment. It is anticipated that in the forthcoming year spectra will be compiled for all of the best data as they become available and will be presented as a document for laboratory use.

The results of the activities undertaken in the Integral Neutron Thermalization program can be summarized as follows: It is now possible in many reactor calculations for all common moderators to utilize scattering kernels well supported by experimental spectra. The descriptions of these scattering kernels are in general still based on miscellaneous bits of experimental and theoretical knowledge for each moderator. Surprisingly, however, these simple, physically realistic descriptions are quite useful and reliable in predicting scalar and infinite-medium neutron spectra. Angular-flux spectra constitute a more severe test of the molecular models, but under the present program new experimental results have been obtained which permit testing of the properties of the scattering kernels relevant to the angular-flux problem.

During the present contract year, several papers originating from this project were presented at the American Nuclear Society Meetings or submitted to Nuclear Science and Engineering for publication:

Nuclear Science and Engineering

1. "Neutron Spectrum Measurements in H₂O, CH₂ and C₆H₆," by J. C. Young, G. D. Trimble, Y. D. Naliboff, D. H. Houston, and J. R. Beyster.
2. "Neutron Thermalization in Zirconium Hydride," by J. C. Young, J. A. Young, G. K. Houghton, G. D. Trimble, and J. R. Beyster.

ANS Meeting, Washington, D. C., November, 1962

1. "Neutron Spectra in Multiplying and Nonmultiplying Media," by J. C. Young, G. D. Trimble, J. R. Brown, D. H. Houston, Y. D. Naliboff, and J. R. Beyster.
2. "Sensitivity of Transient Neutron Spectra to Different Scattering Kernels," by J. U. Koppel and Y. D. Naliboff.
3. "Neutron Thermalization in Graphite. Part I: The Scattering Law for Graphite," by G. D. Joanou, D. E. Parks, and N. F. Wikner.
4. "Neutron Thermalization in Graphite. Part II: The Effect of the Gaussian Approximation and Various Scattering Laws on Thermal Neutron

Spectra in Homogeneous Poisoned Graphite," by G. D. Joanou, D. E. Parks, and N. F. Wikner.

5. "Neutron Thermalization in Graphite. Part III: Thermal Neutron Spectra in Heterogeneous Media," by G. D. Joanou, D. E. Parks, and N. F. Wikner.

ANS Meeting, Salt Lake City, Utah, June, 1963

1. "Neutron Thermalization in Zirconium Hydride," by G. K. Houghton, J. R. Beyster, J. C. Young, and G. D. Trimble.

2. "Spatial Dependence of Thermal Neutron Spectra Across a Temperature and Absorption Discontinuity," by N. F. Wikner, J. R. Beyster, D. E. Parks, and R. B. Walton.

II. NEUTRON THERMALIZATION IN WATER (H₂O)

2.1. INTRODUCTION

A year ago our knowledge of neutron thermalization in water-moderated systems could be summarized as follows. The molecular model proposed by Nelkin⁽³⁾ in 1958, with no further embellishments, was being used with moderate success by many workers in the field both for reactor calculations and for comparisons with experimental results. Other workers, however, believed that the free-hydrogen gas or Radkowski models⁽⁴⁾ were adequate for calculational purposes. Experimentally, the spectral work at General Atomic had shown that an adequate understanding of infinite-medium neutron spectra (at room temperature) required the use of a more realistic model than the free-gas model, for example, the Nelkin model. However, finite-medium, spatially dependent angular-flux spectra, measured both at General Atomic and in lattices by Campbell⁽⁵⁾ and Mostovoi,⁽⁶⁾ were in marked disagreement with transport theory even with hydrogen binding effects included. Many mechanisms were proposed to explain these discrepancies in angular-flux spectra. Several of these had been explored and included in the transport analyses performed at General Atomic, but residual discrepancies still persisted.

Therefore, during the past year we have endeavored further to subject proposed molecular models for H₂O to experimental test and have tried to remove some of the discrepancies, theoretical and experimental, that exist in our understanding of neutron thermalization in light water. First, a series of infinite-medium spectrum experiments was performed at temperatures up to 316°C (Section 2.2). It had been conjectured that the reasonable agreements obtained with the Nelkin water model might be fortuitous at room temperature and that model parameters would certainly have to be changed drastically as water is heated past 150°C. The spectral experiments performed this year showed fairly conclusively that neutron spectra encountered in pressurized water systems were reasonably predictable using a simple molecular model.

Second, a study of neutron spectra in one-dimensional geometrical configurations (Section 2.3.) was performed in an attempt to remove the still serious discrepancies between theory and experiment referred to above. Much of the problem was found to be associated with the geometrical arrangement of source and assembly in the experiment.

Third, a precision measurement was made of the water total cross section (Section 2. 4). Previous measurements by Melkonian⁽⁷⁾ differed significantly around 1 ev from the predictions of the Nelkin water model. In particular, \bar{T} , the average kinetic energy of the water molecule inferred from the work of Melkonian, was 20% greater than that predicted by the Nelkin water model. Based on this fact, it had been suggested that all problems with neutron spectra in water could be solved by adjusting Nelkin-model parameters to give the Melkonian \bar{T} . However, the newly measured water total cross section disagreed with the older work, and \bar{T} inferred from these data agrees with the Nelkin value within experimental error.

Fourth, a study was conducted on the scattering angular distribution $[\sigma(E, \mu)]$ for water (Section 2. 5). This experiment was undertaken because the available experimental data on double differential scattering were not precise enough and were not centered in the proper neutron energy region to test adequately the properties of the molecular model for water relevant to the spectrum problem. An experiment was desired that would serve as an adequate test from the standpoint of applicability to the accurate solution of reactor physics problems. The experimental technique involving use of the Linac was proven, and preliminary data were taken on water. The experiments were quite sensitive to the relevant portions of the scattering description, and disagreements between theory and experiment were observed above 0. 1-ev neutron energy.

Finally, a concerted effort was made this year to understand the parameters used in the bound-hydrogen water model and to improve the molecular description of water, including realistic anisotropic vibrators for the higher-energy degrees of freedom (Section 2. 6). Improved agreement with experiment has been obtained.

2. 2. TEMPERATURE-DEPENDENT INFINITE-MEDIUM NEUTRON SPECTRA

Thermal-neutron spectra have been measured under infinite-medium conditions in water poisoned with a $1/v$ absorber (boron absorption of 5. 15 barns/hydrogen atom) as a function of moderator temperature. Ten liters of boric acid solution were contained in a stainless steel pressure vessel measuring 10 in. in inside diameter. The vessel was heated electrically by an internal immersion heater located near its bottom. Both a pressure indicator and thermocouples were used to monitor the temperature of the borated water within the vessel. A cylindrical tube, or "glory hole," for neutron-beam extraction extended through the center of the vessel, perpendicular to the cylindrical axis. The pressure vessel is described in detail in Section 15. 2.

The energy-dependent, scalar neutron spectra were measured by placing a zirconium scatterer at the center of the thin-walled glory hole and measuring the neutrons scattered in the direction of the detector by a bank of $B^{10}F_3$ counters. Pulsed-beam time-of-flight techniques were used to determine the neutron energies. Mean-emission-time corrections to the data were made with the usual time moment calculations. A neutron-spectrum measurement was made at room temperature in a 10-in. -diameter, thin-walled, aluminum cylinder which had a re-entrant tube with a 5/8-in. internal diameter. This was done as a check on the over-all pressure-vessel system and in order to determine the effect on the spectrum of the stainless steel walls (0.030 in. thick) of the glory hole in the pressure vessel, since aluminum walls (0.010 in. thick) were normally used. The spectrum obtained in this manner was compared with the room-temperature spectrum obtained in the pressure vessel using the same poison concentration. These spectra, which are shown in Fig. 2.1, are in excellent agreement down to an energy of 0.02 ev. Below this energy the coherent scattering properties of the zirconium tended to make the measurements of spectra in the pressure vessel subject to error. However, above this energy the scatterer and the stainless steel walls of the pressure vessel did not necessitate any corrections to the measured neutron flux. Infinite-medium neutron spectra were measured at 30° , 150° , 232° , and 316° C.

These measurements were performed to determine the importance of molecular binding in establishing the neutron spectrum in a high-temperature, water-moderated reactor. Since it is known that molecular binding produces significant spectral shifts at room temperature, these spectral measurements serve to establish the magnitude and importance of the binding effects at elevated temperatures. A composite curve showing the infinite-medium neutron spectra at these temperatures for a homogeneously poisoned boric acid solution (5.15 barns/hydrogen atom) is shown in Fig. 2.2. The measured spectrum at each temperature is compared with predictions based on the bound-hydrogen scattering model and the free-hydrogen model. The measured neutron spectrum at 30° C is also compared with the theoretical predictions of the bound-hydrogen scattering model, which has been modified to include anisotropic vibrations of the water molecule.

Some of the salient features for these spectra are listed in Table 2.1. Column 1 gives the temperature, T , of the moderator in degrees centigrade, column 2 the temperature, E_M , of the moderator in electron volts, column 3 the neutron temperature, E_N , in electron volts, and column 4 the ratio of E_N to E_M . The neutron temperature referred to here was obtained by fitting graphically a Maxwellian shape to the observed spectrum. Column 5 gives the ratio of the spectrum calculated for bound hydrogen, ϕ_{BH} , to the measured spectrum at E_M , ϕ_{Exp} , and column 6 the ratio of the spectrum calculated for free hydrogen, ϕ_{FH} , to the measured spectrum, ϕ_{Exp} . Column 7 gives the ratio of the calculated free-hydrogen flux to the calculated bound-hydrogen flux. The

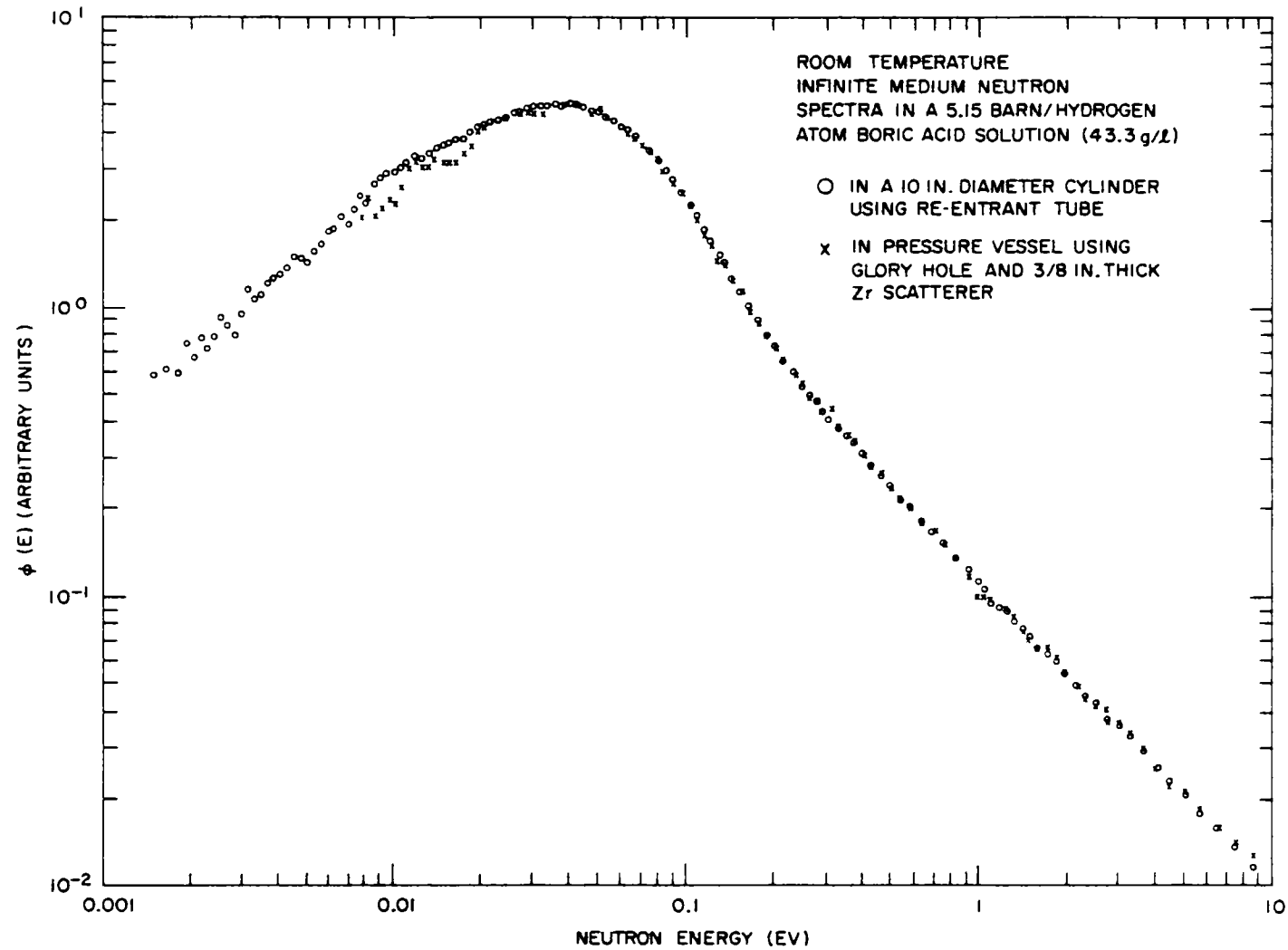


Fig. 2.1 -- Infinite-medium neutron spectra in borated water measured with different containment configurations

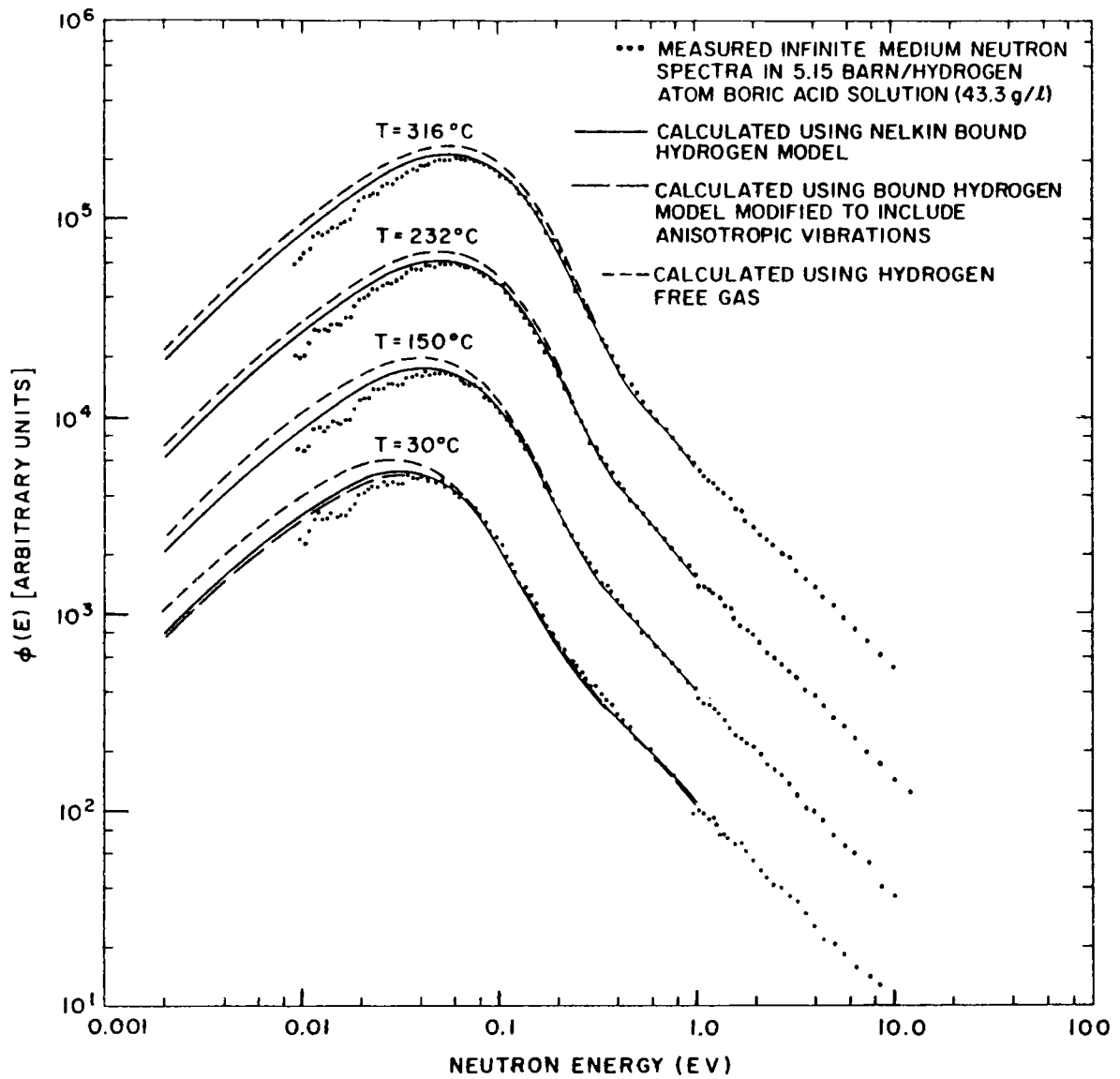


Fig. 2.2- -Infinite-medium neutron spectra in borated water as a function of moderator temperature

theoretical and experimental spectra were normalized at 1 ev for comparison and the ratio of the fluxes was compared at E_M .

Table 2. 1
COMPARISON OF THEORETICAL AND EXPERIMENTAL
SPECTRA IN BORATED WATER

Temp. (°C)	E_M (ev)	E_N (ev)	E_N/E_M	ϕ_{BH}/ϕ_{Exp}	ϕ_{FH}/ϕ_{Exp}	ϕ_{FH}/ϕ_{BH}
30	0.0261	0.036	1.38	1.10	1.27	1.15
150	0.0364	0.043	1.29	1.09	1.24	1.14
232	0.0435	0.056	1.24	1.04	1.16	1.12
316	0.0507	0.060	1.18	1.06	1.17	1.10

It can be seen from Table 2. 1 and Fig. 2. 2 that the bound-hydrogen description is adequate for describing the neutron-scattering processes in water at temperatures up to 316°C, and that the free-hydrogen calculation does not give as accurate a description of the observed spectrum in water. It can also be seen from Fig. 2. 2 that a bound-hydrogen molecular model which includes anisotropic vibrations improves the agreement with the measured neutron spectrum at 30°C. These comparisons illustrate that molecular binding is still important at operating temperatures for water-moderated reactors and that the free-hydrogen model is not appropriate for reactor calculations even at these temperatures.

Another qualitative feature of these temperature-dependent spectra is the lack of a marked change in the spectral shape as the temperature of the moderator is increased through 150°C. Results given in Table 2. 1 and Fig. 2. 2 do not appear to be consistent with Egelstaff's suggestion⁽⁸⁾ that model parameters need to be adjusted in going from 23° to 300°C. Further experiments are needed at elevated temperatures to investigate resonance-absorption effects on neutron spectra.

2. 3. SPATIALLY DEPENDENT ANGULAR-FLUX MEASUREMENTS

2. 3. 1. Nonmultiplying Systems

For some time an intensive effort has been made in the thermalization program to understand thermal-neutron spectra in the presence of a strong, one-dimensional flux gradient such as those encountered near a control rod or core interface. The measurements chosen for our clean experiments were of three general types: water poisoned with a 1/v absorber, pure water, and multiplying assemblies (water-U²³⁵). The status of this effort

at the end of the last contract year was reported in Ref. 2. The disagreements between theory and experiment for both angular and scalar fluxes were significant (25% to 30%), but have since been improved considerably.

The approach to the solution of this problem has been difficult. Every conjectured potential source of error has contributed an effect of some magnitude in one direction or the other. In this report we will not endeavor to describe in detail the entire history of the investigation conducted this year, but rather to report the more obvious developments and the present status of the agreement between theory and experiment.

Let us begin with a review of the status of the experimental analysis at the end of the last contract year. Spectra had been measured in the geometry shown in Fig. 2.3, with the fast source essentially simulating a plane wave of neutrons incident on the water tank. Two standard tank sizes were used having thicknesses of 4 in. and 2 in. for the one-dimensional flux studies. Calculations of spectra were made for both of these slab configurations. The poison concentration in both cases was about 5 barns/hydrogen atom (43.7 g/liter of boric acid). In the 4-in.-thick slab, the transport-theory (GAPLSN)⁽⁹⁾ calculation was performed with 23 energy groups, P_0 and P_1 scattering kernels, P_0 and P_1 source terms, and 82 spatial regions (10 regions within one mean free path of the slab surface). In addition, all experimental data were reanalyzed using our latest, most precise detector energy sensitivity function. Comparisons of data for both scalar and angular fluxes in the 4-in. slab are shown in Figs. 2.4, 2.5, and 2.6. The over-all agreement between theory and experiment was improved by the above procedures, but discrepancies of 15% to 20% remained. Earlier versions of the same data are reported in Ref. 2.

A more extensive GAPLSN calculation, in which the angular flux was determined at 16 angles, S-16, has been performed on the 2-in., poisoned slab for comparison with measurements. In this case, higher-order terms in the P_n expansion of the scattering matrix were used (up to P_3) to test their performance. A source term with P_0 and P_1 components was also used together with 23 energy groups and 47 spatial regions. The 2-in. tank was investigated rather than the 4-in. tank because the computing problem for 82 regions (necessary for a 4-in. tank) in the P_3 approximation would more than fill the computer memory. A more anisotropic source than P_1 was not used, since no procedure for generating it was available. The effect on the calculated spectrum was as follows: inclusion of up to P_3 scattering softens the 0° angular flux calculated at the surface by about 4% (toward better agreement) and leaves all other scalar and angular fluxes as they were with P_1 scattering only. Since the effect was small, no figure is given.

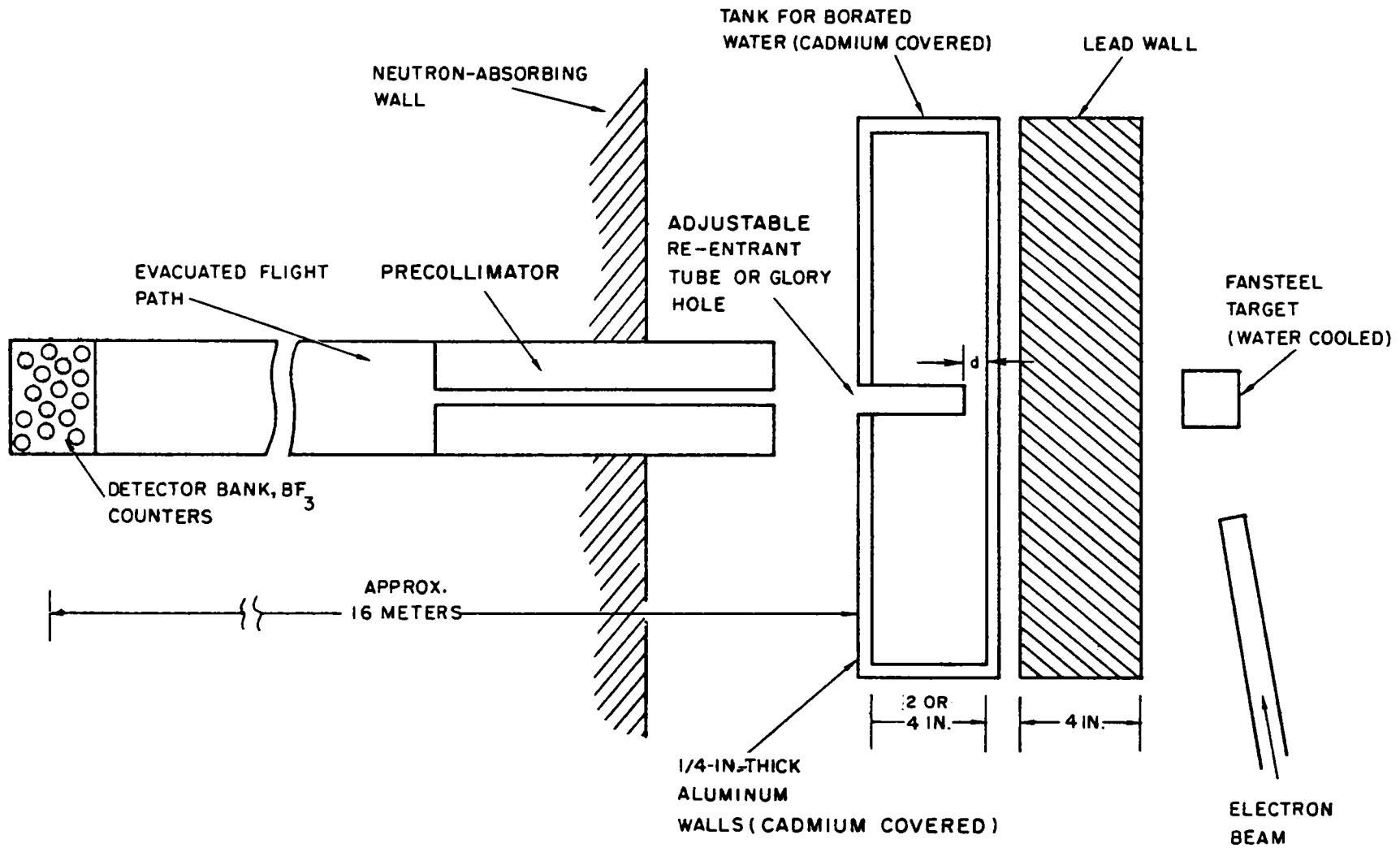


Fig. 2. 3 -- Typical experimental arrangement for measuring spatially dependent neutron spectra

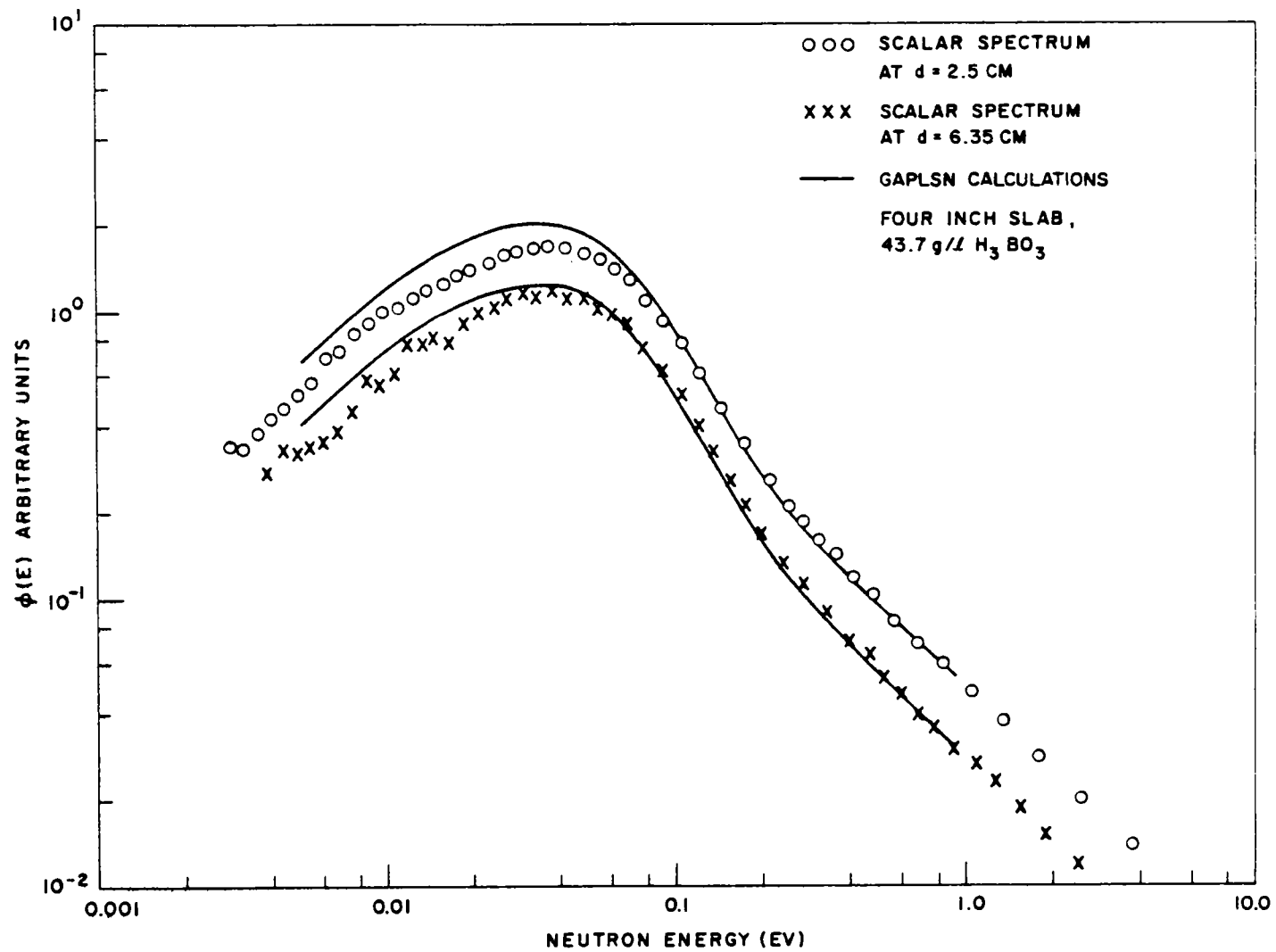


Fig. 2.4--Scalar spectra in borated water

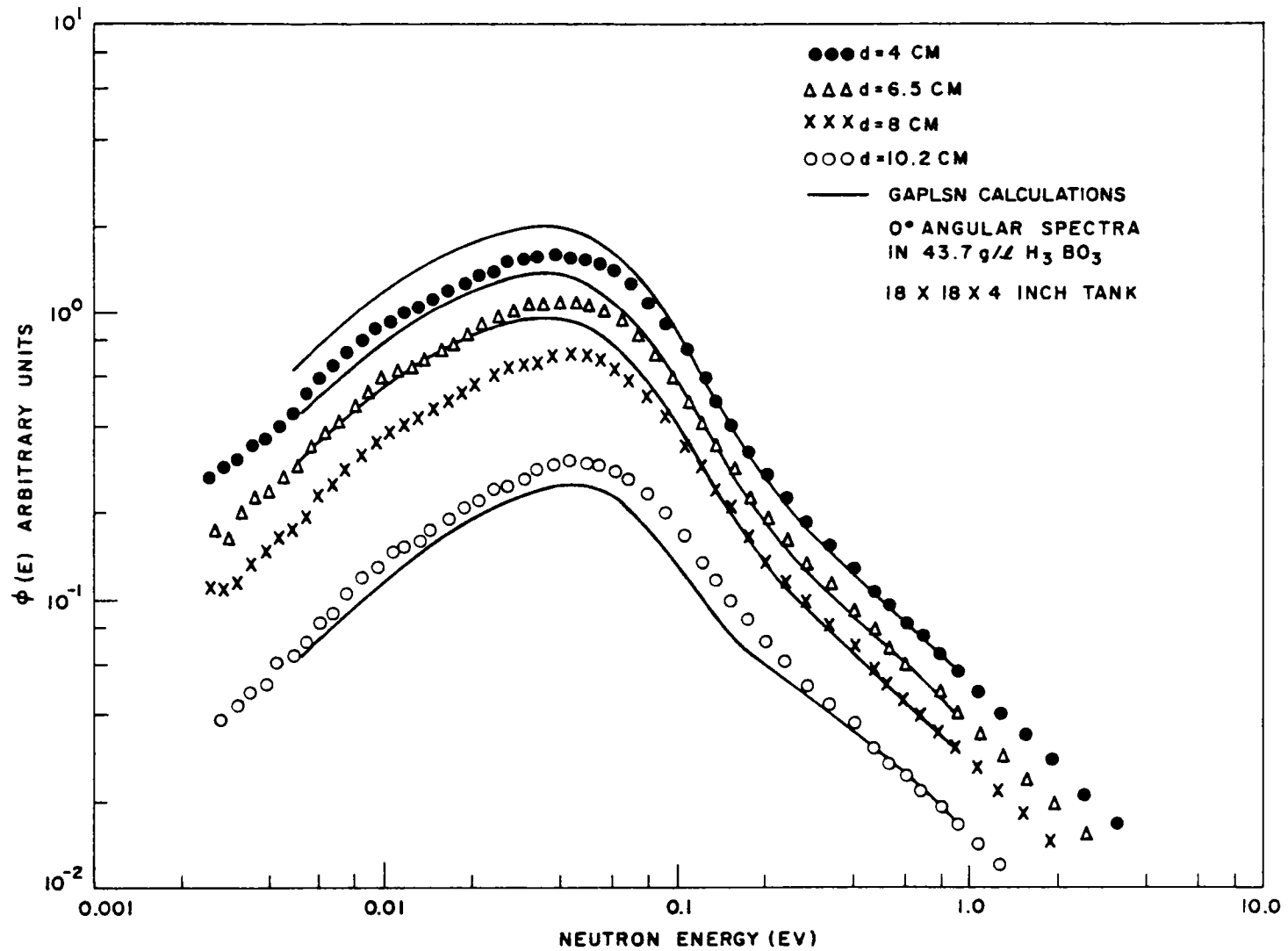


Fig. 2.5 -- Angular spectra in borated water

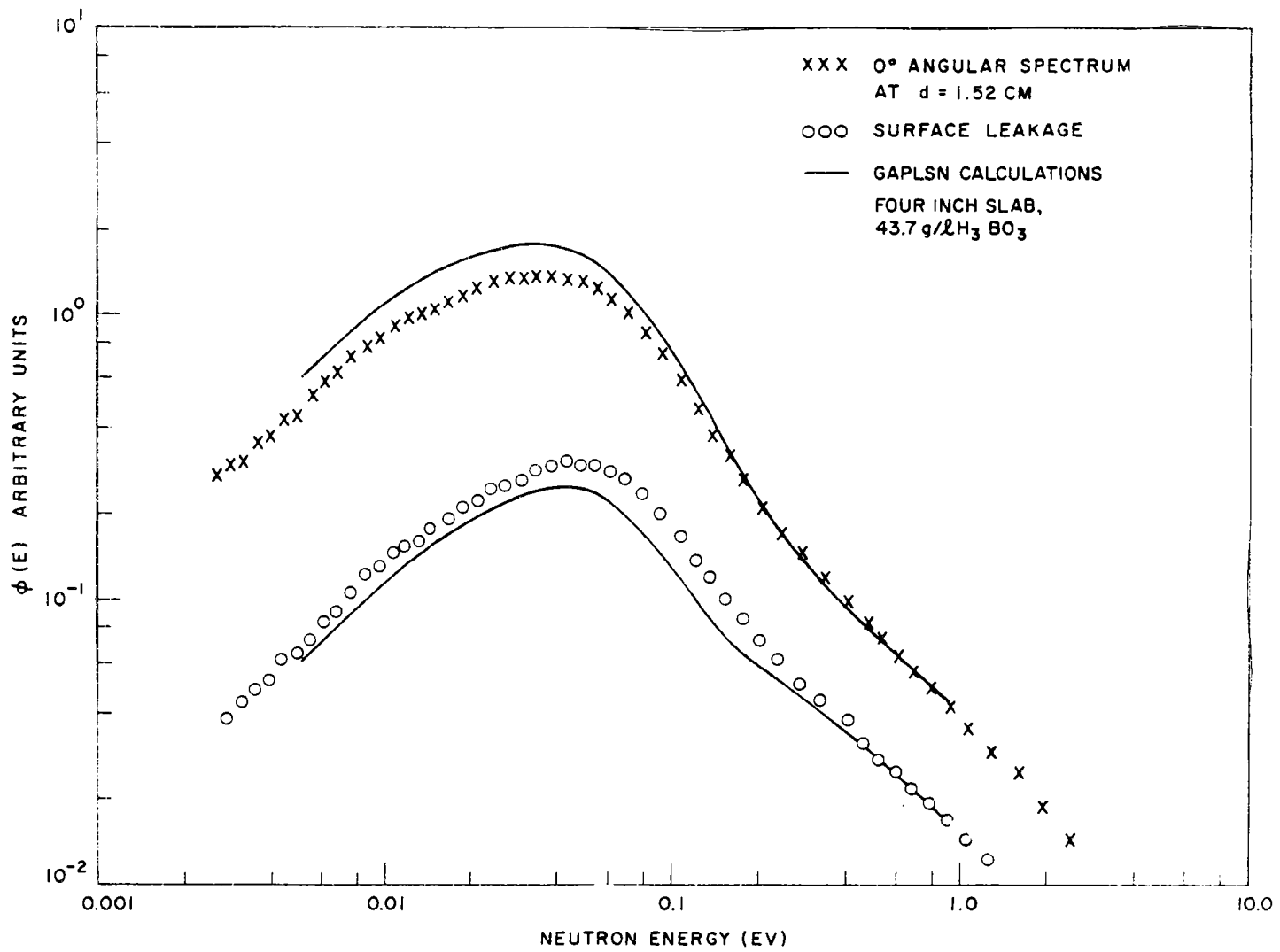


Fig. 2.6 -- Angular spectra from borated water

In addition, distortion of the leakage spectrum caused by varying the spatial source distribution was investigated in two GAPLSN calculations. This was done because the slope of the epithermal flux plot at the far edge of the 4-in. tank was much less than that for the 2-in. tank. Room return of neutrons was suspected. The calculations were performed for the 2-in. geometry with a poisoning of 5 barns/hydrogen atom (43.7 g/liter of boric acid). The calculations were set up to use the full P_3 scattering matrix, P_1 source, and S-16. The upper curve, A, in Fig. 2.7 is the surface leakage calculated for an epithermal-source flux plot having the same slope as that observed near the boundary in the 4-in. tank. The lower curve, B, was calculated with the measured 2-in. -tank flux plot, with an extrapolation to zero at $0.71\lambda_{tr} = 0.93$ cm from the boundary, joining the original curve at $\lambda_{tr}/2 = 0.66$ cm inside the surface. This extrapolation boundary condition gave a calculated surface-leakage spectrum which differed little from that resulting from using the measured flux plot for the 2-in. tank without the extrapolation to zero flux (because the flux plot for the 2-in. tank was quite steep even without the extrapolation condition). If the curves in Fig. 2.7 are normalized at 1 ev, a hardening of $\sim 13\%$ is observed, corresponding to a change in slope of normalized flux from -0.14 (4-in. tank) to -0.42 (2-in. tank). The significance of this result is as follows: If the measured flux plots are incorrect, the correct shapes must be expected to be steeper; thus, the spectra calculated using these steeper flux plots will be harder and will disagree more with experiment. In other words, removal of room-return effects in our flux plots could tend to produce a larger disagreement at the surface between theory and experiment.

A previous series of measurements which were subjected to analysis this year involved experiments on angular flux performed in pure water. A study of both the scalar and angular flux was conducted for pure water in a 4-in. one-dimensional geometry. The GAPLSN calculation for this case in a P_1 approximation has been completed and is compared with experiment in Figs. 2.8 and 2.9. The discrepancies between theory and experiment are similar in magnitude to those mentioned in Section 2.3 for boric acid--perhaps a little larger for pure water. However, the trends are the same, i. e., calculated internal leakage and scalar flux are softer than experiment and calculated surface leakage is in relatively closer agreement with experiment than in the other cases. On the basis of these as well as other data, it seems unlikely that neutron room return to the assemblies is the major cause of the disagreement.

A suggested analytical investigation was carried out on angular-flux spectra measured in the geometry of Fig. 2.3. It had occurred to us that the epithermal source retained a memory of the incident source direction and that this effect was not adequately taken into account in the description of the epithermal source by diffusion theory. Therefore, the complete transport problem was solved from fission energies to thermal energies in two

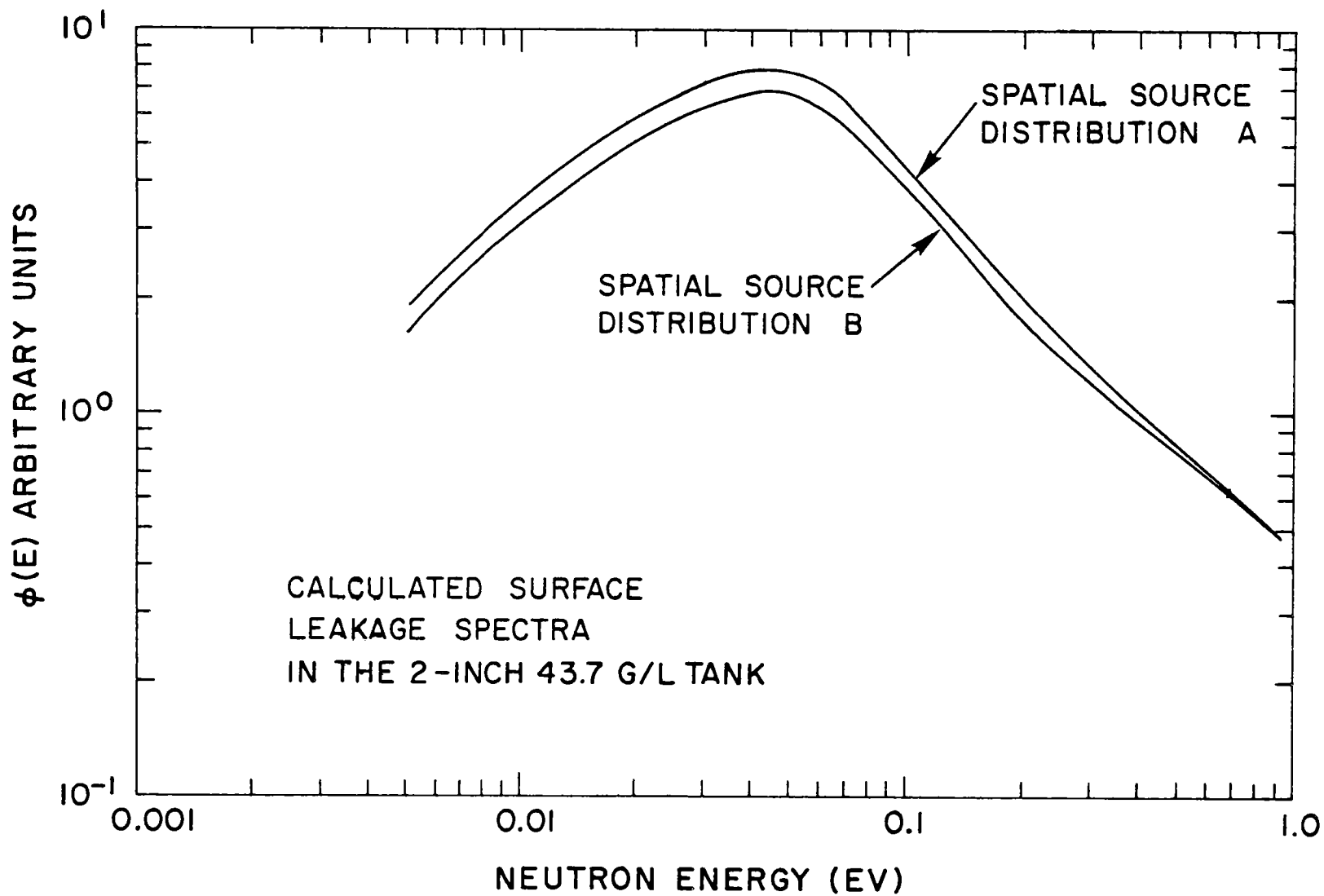


Fig. 2.7--Calculated surface-leakage spectra in borated water from two different spatial source distributions

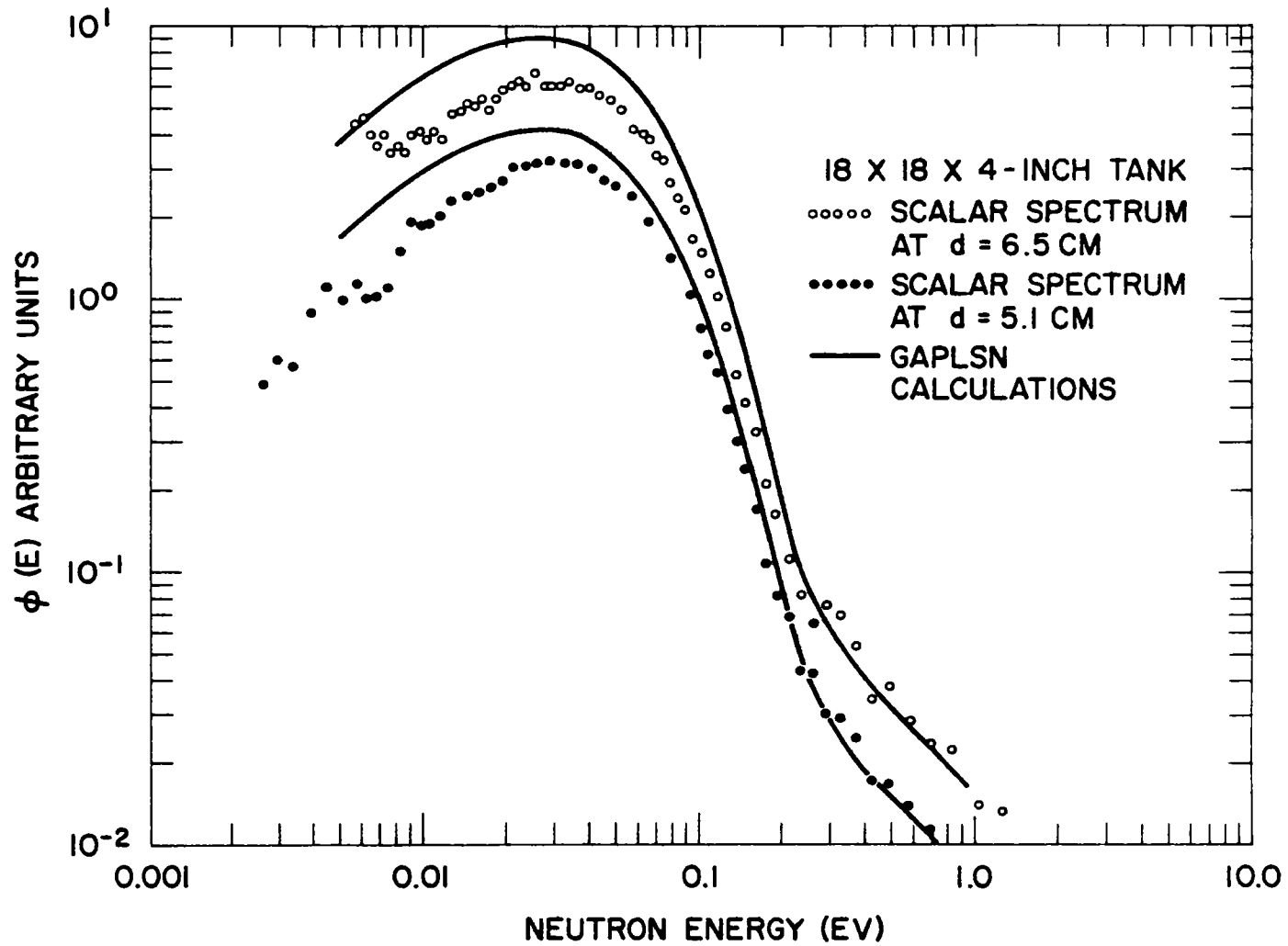


Fig. 2. 8 --Scalar spectra in a 4-in. slab of pure water

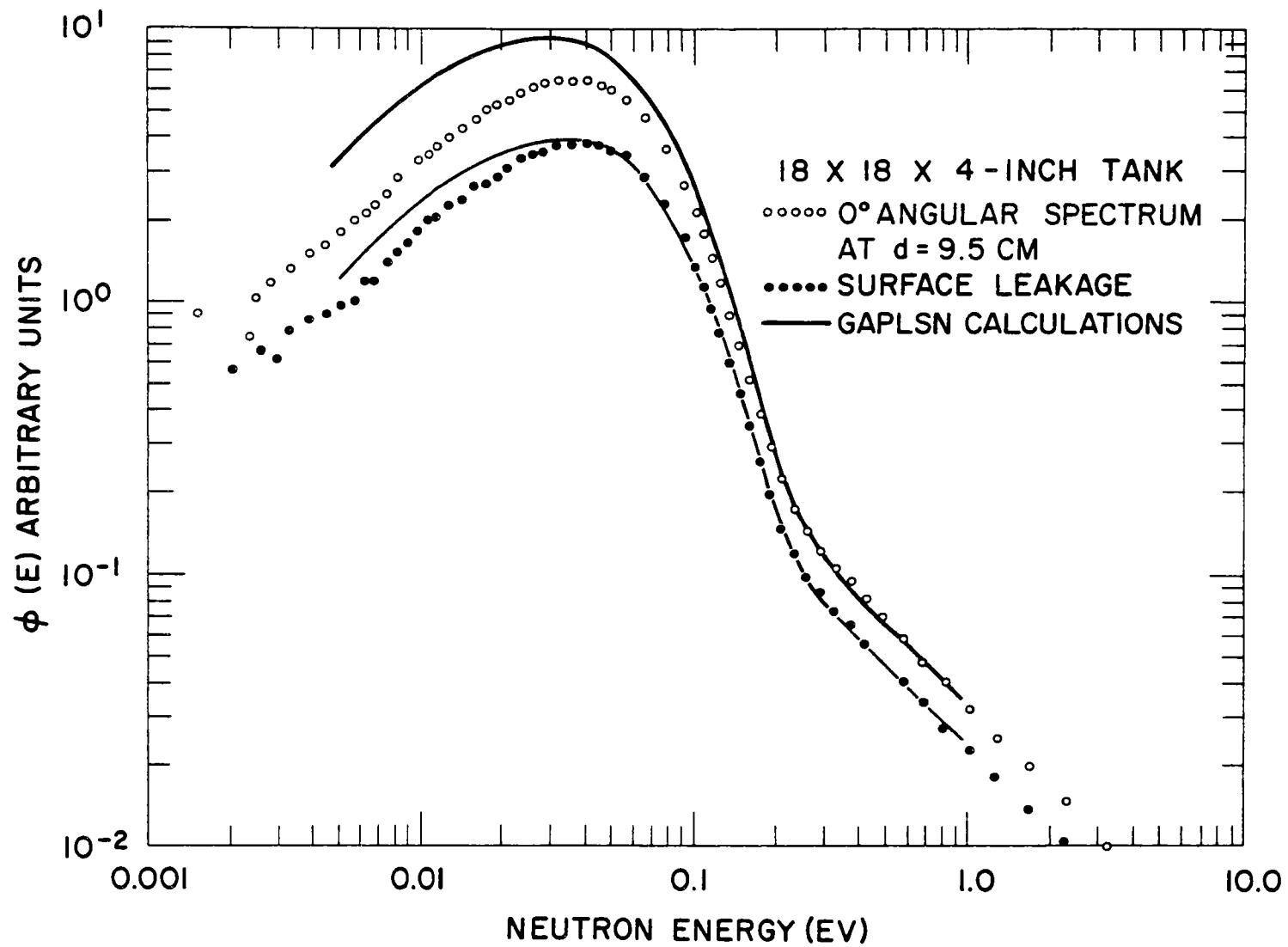


Fig. 2.9-- Angular spectra in a 4-in. slab of pure water

parts for the 4-in. tank. A fission-spectrum neutron source, incident normally on the lead wall, was assumed and the epithermal-source angular shape was calculated throughout the water geometry. The angle of incidence of the source on the lead was investigated and was found to first approximation to have little effect on the final epithermal angular distribution. This angular distribution was resolved into P_0 and P_1 parts, and the energy dependences obtained by the procedures described in Ref. 2 were used. Thus, the following thermal problem was solved by GAPLSN:

$$\mu \frac{df}{dx}(E, x, \mu) + \sum_t (E) f(E, x, \mu) = \int_0^\infty dE' \int_{-1}^1 d\mu f(E', x, \mu) \sum_s (E' \rightarrow E, \mu) + S(E, x, \mu) .$$

The scattering kernel is expanded in Legendre polynomials:

$$\sum_s (E' \rightarrow E, \mu) = \sum_{\ell=0}^n \frac{2\ell+1}{2} \sum_{s\ell} (E' \rightarrow E) P_\ell(\mu) .$$

The source is assumed to contain spherical harmonics through $\ell = 1$. Thus, the epithermal source term used explicitly was

$$S(E, x, \mu) = S_0(E)Q(x)A - 3S_1(E)\mu Q(x)B ,$$

where $Q(x)$ is the measured spatial shape of the epicadmium source, A and B are the relative amplitudes of the P_0 and P_1 source contributions as determined by the fast DSN problem, and

$$S_0(E) = \sum_s \phi(E^*) \operatorname{erf}(x) ,$$

$$S_1(E) = \sum_s \phi(E^*) \frac{2D}{3} \sqrt{\frac{E}{E^*}} \left[\left(1 - \frac{1}{x}\right) \operatorname{erf}(x) + \frac{2}{\sqrt{\pi}} \frac{1}{x} e^{-x^2} \right] ,$$

where E^* is the thermal cutoff energy; $\operatorname{erf}(x)$ is the error function $x = \sqrt{E/\bar{E}}$, where \bar{E} is the effective proton temperature; and \sum_s and D have their usual meanings. The DSN treatment handles the problem through $\ell = 1$, while the GAPLSN treatment is used when the P_2 and P_3 scattering kernels are included.

The improved agreement between theory and experiment is shown in Fig. 2.10. These results indicated that an exact evaluation of the experimental arrangement shown in Fig. 2.3 is a very hard problem, dependent probably on the detailed energy distribution of the fast source. Since we are not interested in considering fast-source (essentially shielding) problems at this time in the program, it was decided to test

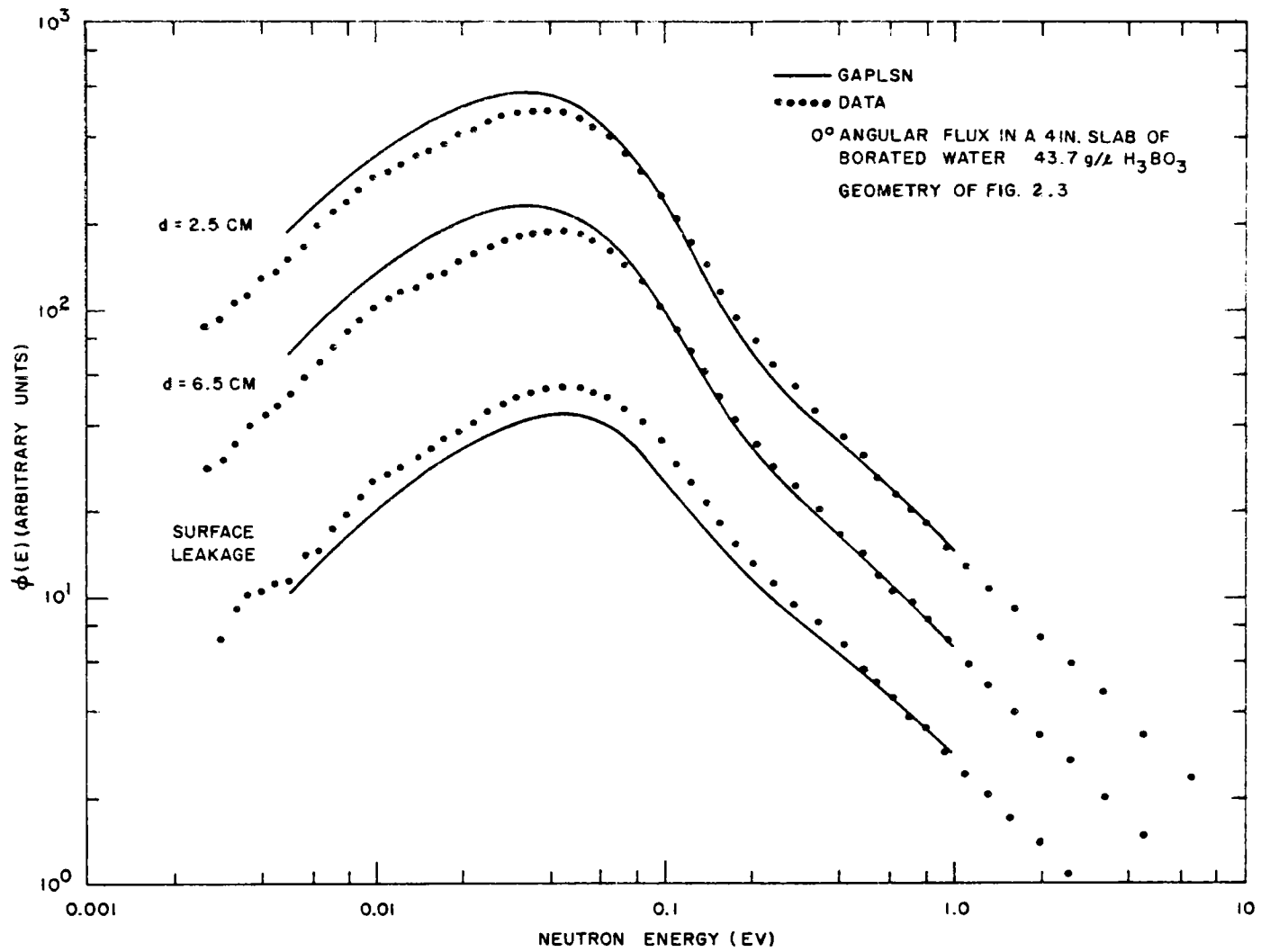


Fig. 2.10--0° angular flux in a 4-in. slab of borated water

a new geometrical arrangement which might eliminate the fast-source directional sensitivity. The measurements were made with the pulsed neutron source at 90° to the precollimator assembly centerline. This geometrical arrangement produced a cosine distribution of the spatial flux in the thin dimension of the slab and a flattened flux distribution in the long dimension. The thin-dimension distribution was measured using cadmium-covered indium foils and was used as the epithermal-source distribution in the transport-theory code DSN. Measurements were made at the center, at 0.5 in. in, and at the surface of a 2-in. -thick slab. Results are shown in Fig. 2.11. The water was poisoned to about 5 barns/hydrogen atom.

The angular fluxes measured in a 4-in. -thick slab are shown in Fig. 2.12. The angular fluxes calculated with DSN in P_1 approximation (both source and bound-hydrogen kernel) are shown in the figures. It can be seen that the experimental data agree better, in general, with the calculations of transport theory made with the Nelkin scattering kernel than those obtained previously for the 2-in. case. The spectra calculated with the P_1 Radkowski kernel are also shown in Fig. 2.11. The residual disagreements between the Nelkin theory and experiment are still greater than those encountered for the infinite-medium spectra which suggests that further refinements may have to be made at least in part by improving the molecular scattering model for water.

2.3.2. Spectral Measurements in Multiplying Assembly

In nonmultiplying media the neutron spectral distortions in the presence of strong flux gradients are very large, and are hard to calculate, as is seen in Fig. 2.5. The primary purpose of the multiplying-assembly study was to measure spectra under distributed source conditions to determine if the problems encountered in the nonmultiplying assemblies would persist. The spectra reported here were measured early in 1962 and are reported in Ref. 2. However, the method of analysis for these transport spectra has been greatly improved this year and the comparison of theory with experiment is therefore shown.

The multiplying assembly developed for this work was made by accurately spacing thin plates of uranium-aluminum alloy 1/8 in. apart in a water tank. The assembly was designed initially to study bare, homogeneously poisoned systems. An axial hole, the glory hole, traversing the assembly was lined up with the precollimator to permit extraction of the beam of neutrons for neutron-spectrum measurements. At the final loading, the assembly had a time decay constant or die-away of 400 μ sec. Figure 2.13 shows a top view of the geometrical arrangement with the electron beam entering from the left. The core was surrounded by a 6-in. -thick lead wall to permit access to the work and loading areas after running the assembly at high power levels. It was also terminated on all sides by borated polyethylene and cadmium.

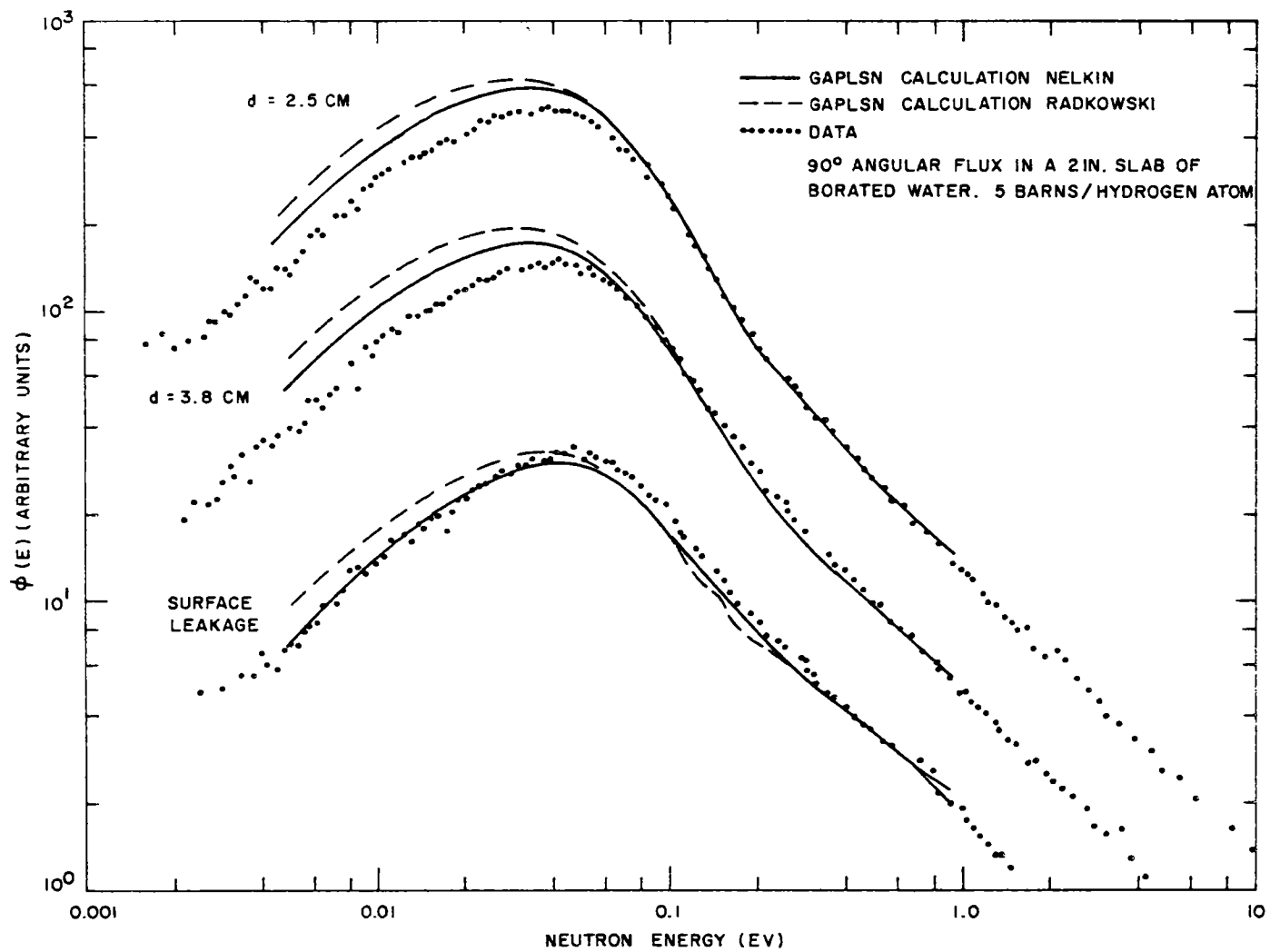


Fig. 2.11--90° angular flux in a 2-in. slab of borated water

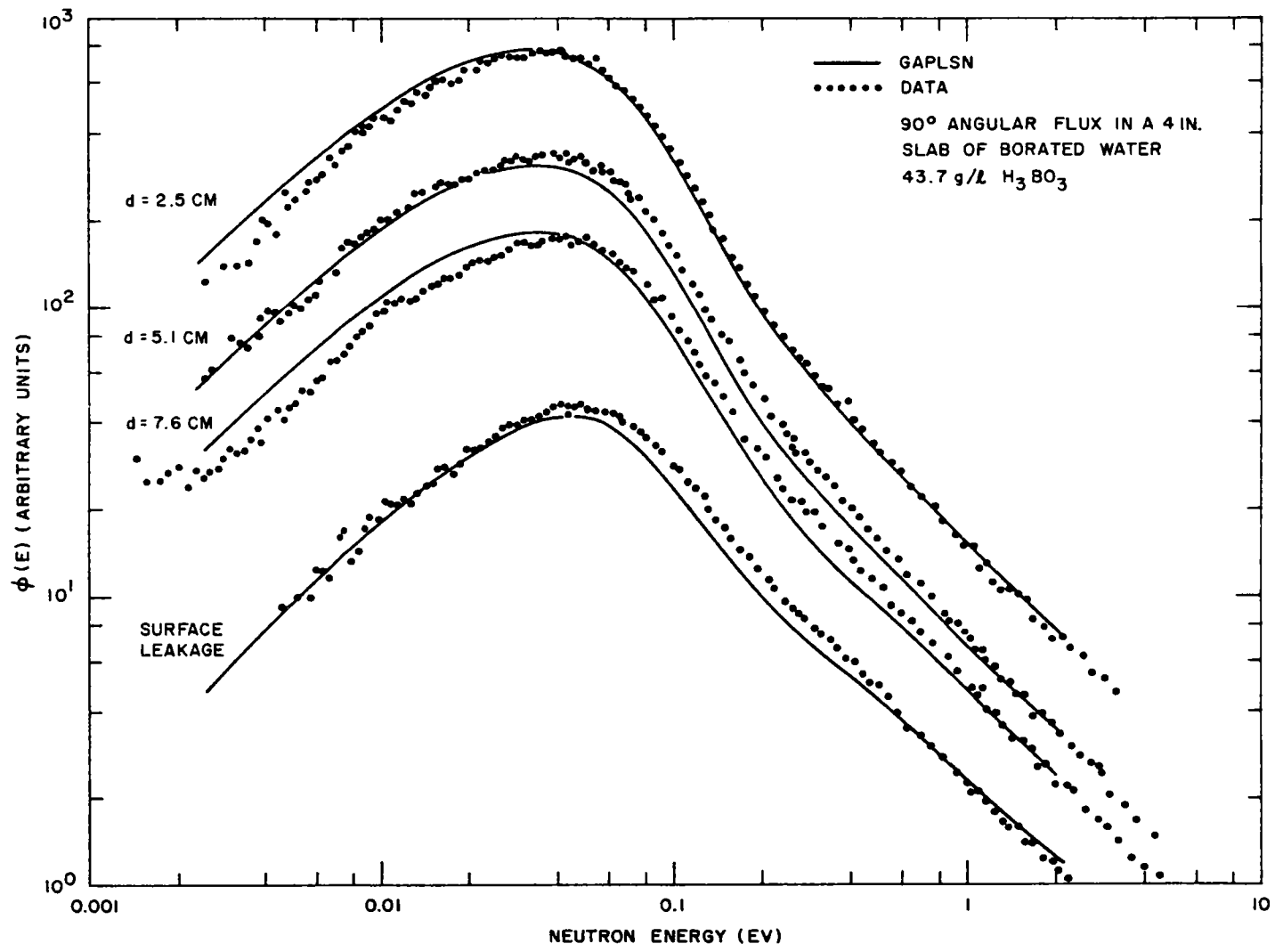


Fig. 2.12--90° angular flux in a 4-in. slab of borated water

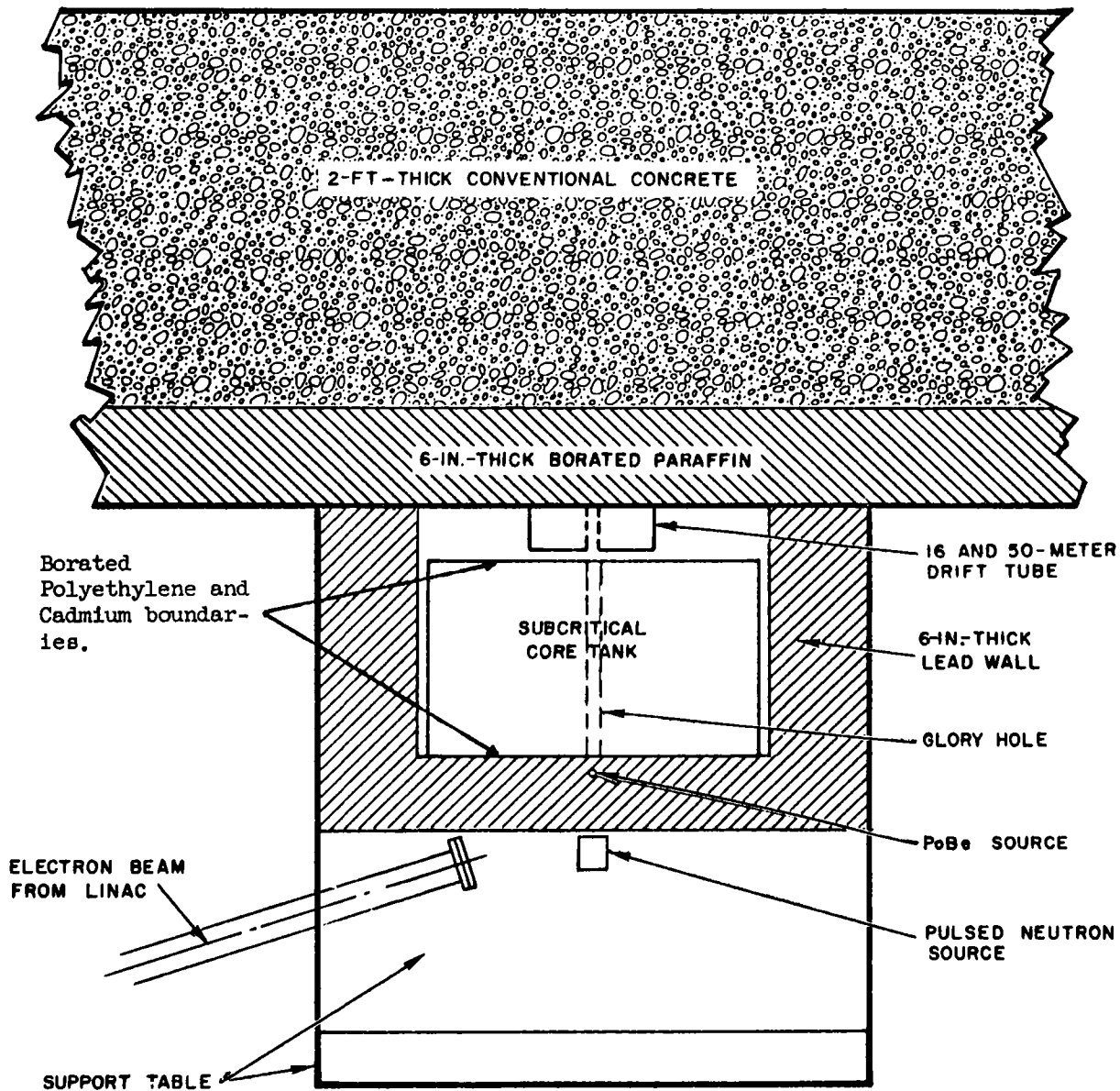


Fig. 2.13--Plan view of geometrical arrangement for multiplying-assembly measurements

Epithermal spatial neutron distributions were taken in the subcritical assembly to provide the input source distribution necessary for calculating the thermal spatial spectra by transport theory. Flux distributions were also measured using bare indium foils and sulphur foils. These distributions were similar to the normal-mode distribution; hence, the multiplying assembly adequately accomplished the desired result, namely, that of redistributing both the thermal and epithermal neutrons spatially in approximately the normal-mode distribution.

Scalar neutron spectra were measured in the assembly for comparison with theoretical predictions. The transport code GAPLSN (S-32) was used for the calculations, and the source term and the scattering kernel included P_1 contributions. A very fine spatial mesh was used in the calculations. The results of the previous measurements are shown in Fig. 2.14 and are compared with calculations of spectra performed with the bound-hydrogen kernel. The atom densities ($\times 10^{-24}$) were:

$$\begin{aligned} &5.76 \times 10^{-2} \text{ hydrogen, } 2.88 \times 10^{-2} \text{ oxygen,} \\ &1.68 \times 10^{-4} \text{ uranium (235), } 8.07 \times 10^{-3} \text{ aluminum.} \end{aligned}$$

Agreement with previous infinite-medium nonmultiplying studies⁽¹⁰⁾ was good. One of the scalar spectra was taken where there was no flux gradient and one was taken in the presence of a strong gradient. The spectrum measured in the presence of the gradient is about 20% harder. Two internal 0° angular spectra were also measured in the core (Fig. 2.15). The comparisons for the internal, angularly dependent spectra indicated good agreement with these recent DSN calculations. A surface-leakage measurement disagreed seriously with predictions, but it is believed that this measurement was in error.

In conclusion, the subcritical assembly has been shown to be a very workable facility for experimental spectral investigations. It does not appear to be necessary to utilize this type of facility for infinite-medium spectral studies, but it will prove highly useful for many investigations of spatially dependent spectra, such as spectra near control rods. Predictability of spatially dependent spectra in the subcritical assembly seems to be considerably improved, especially for angular spectra, over predictions in nonmultiplying geometries (Section 2.3.1). Since the epithermal source in the multiplying assembly is more nearly isotropic, a probable explanation is that many of the previous calculations for the nonmultiplying systems have not included sufficient source anisotropy.

2.4. TOTAL CROSS SECTION FOR H₂O

The total cross section of H₂O was measured between 0.005 and 10 ev by a transmission experiment with time-of-flight energy analysis. The

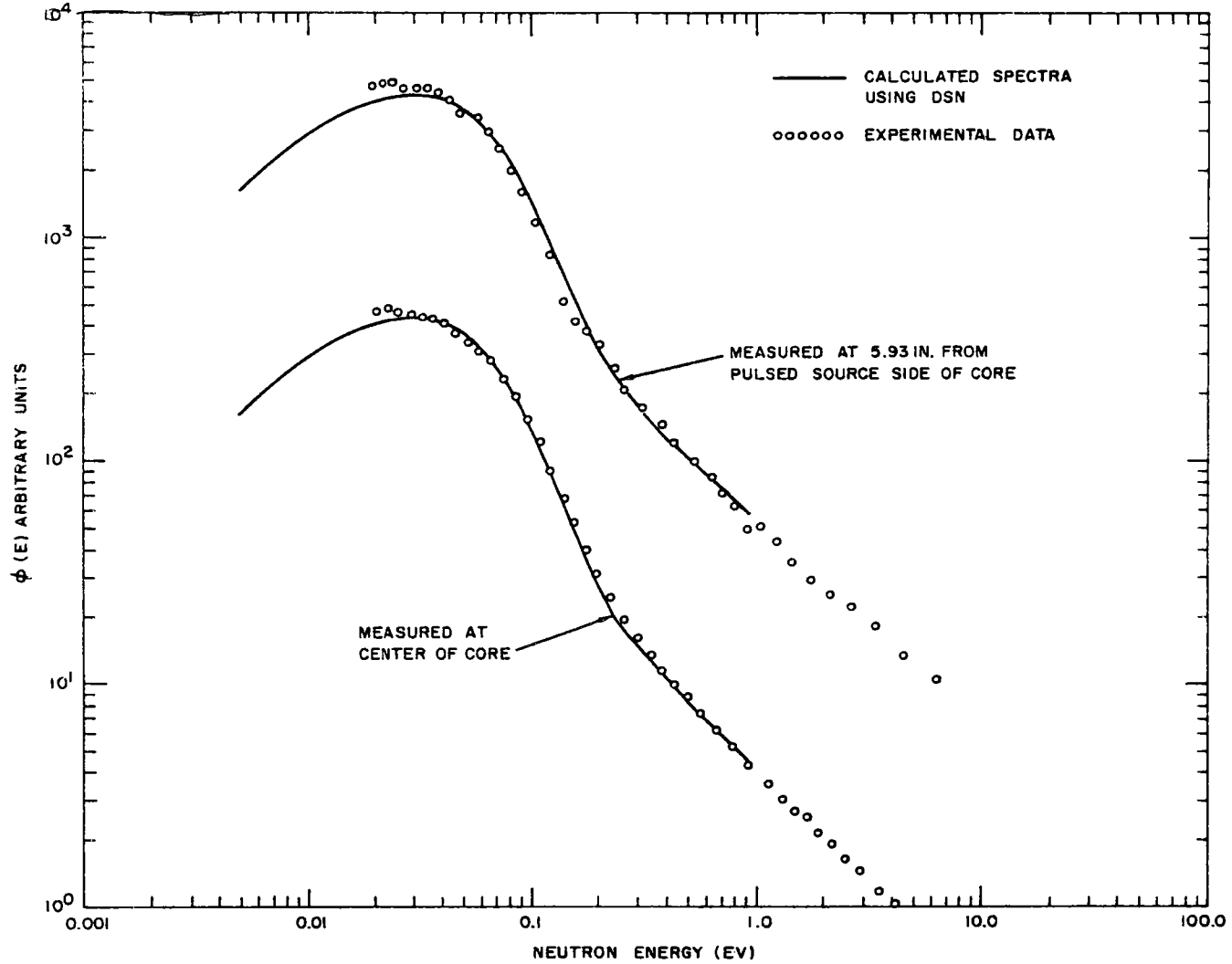


Fig. 2.14--Scalar neutron spectra in subcritical assembly

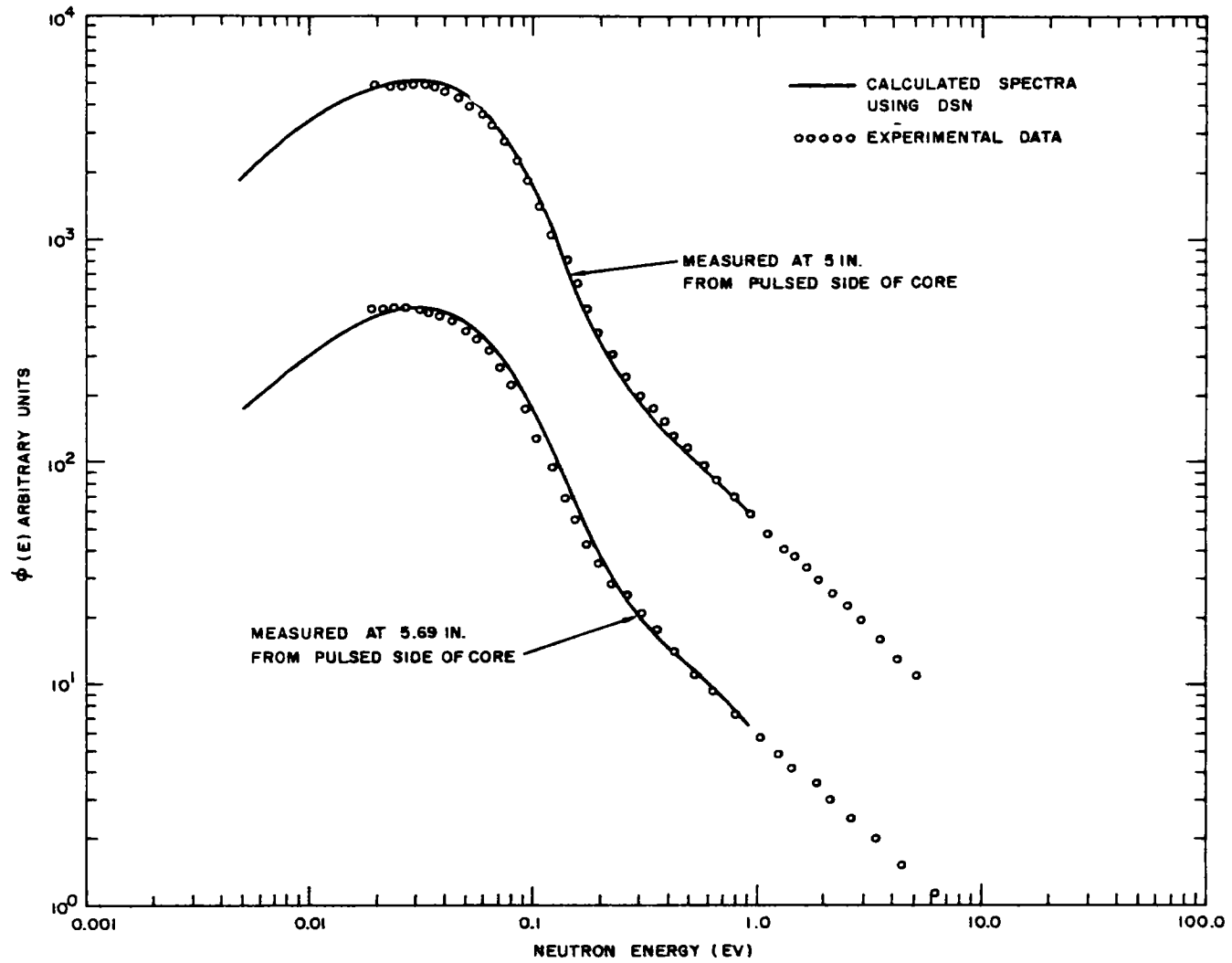


Fig. 2.15--0⁰ angular flux in subcritical assembly

purpose of the experiment was to reduce the error in the determination of \bar{T} (the average kinetic energy of a proton bound in the water molecule). The water cross section at high energy, above 1 ev, can be written⁽¹¹⁾ as

$$\sigma_w = \sigma_a + \sigma_0 + 2 \sigma_H \left[1 + \frac{\bar{T}}{2ME} - \frac{1}{32} \left(\frac{M+1}{M} \right)^2 \frac{\bar{C}}{ME^3} + \dots \right], \quad (1)$$

where σ_w = total water cross section (barns),

σ_0 = total oxygen cross section (3.8 barns),

σ_H = free-hydrogen cross section (20.4 barns),

σ_a = $1/v$ absorption cross section (barns),

E = neutron energy (electron volts),

M = mass ratio of hydrogen to neutron,

$\bar{T} = 1/2 \sum_i \lambda_i \omega_i \coth(\omega_i/2T + (T/18))$,

T = temperature (ev),

$\bar{C} = 1/2 \sum_i \lambda_i \omega_i^3 \coth(\omega_i/2T)$,

$\lambda_i = 1/2.32, 1/5.84, 1/2.92$ (weightings based on effective masses),

$\omega_i = 0.06, 0.205, 0.48$ ev (molecular excitation energies).

Because Eq. (1) is an asymptotic expansion, its validity below ~ 1 ev is doubtful. Melkonian⁽⁷⁾ measured the water cross section, with high precision, above 1 ev and fitted the data with Eq. (1) to obtain \bar{T} . However, the effect of the chemical binding above 1 ev was too small to yield a \bar{T} of useful precision. Even with the developments of the decade since that work was published, it would be a formidable task to improve significantly on the precision of the experiment.

The present experiment was undertaken with the view of establishing the validity of a Nelkin model⁽³⁾ for water over the energy range 0.1 to 10 ev. Because those model parameters which determine \bar{T} also dominate the cross section in this range, \bar{T} calculated by the model would be essentially an experimental number, with the GAKER⁽¹²⁾ computer code replacing Eq. (1) in the experimental analysis.

Figure 2.16 is a comparison of the experimental data, plotted versus $1/E$, with the Nelkin model. Above 1 ev the asymptotic expansion is used; below 1 ev the results of a GAKER calculation are used. The numerical approximations in GAKER limit the accuracy of the calculated cross section to about 1% except in the most interesting regions (at the resonances and the model change at 0.32 ev), where it can be in error by 2%.

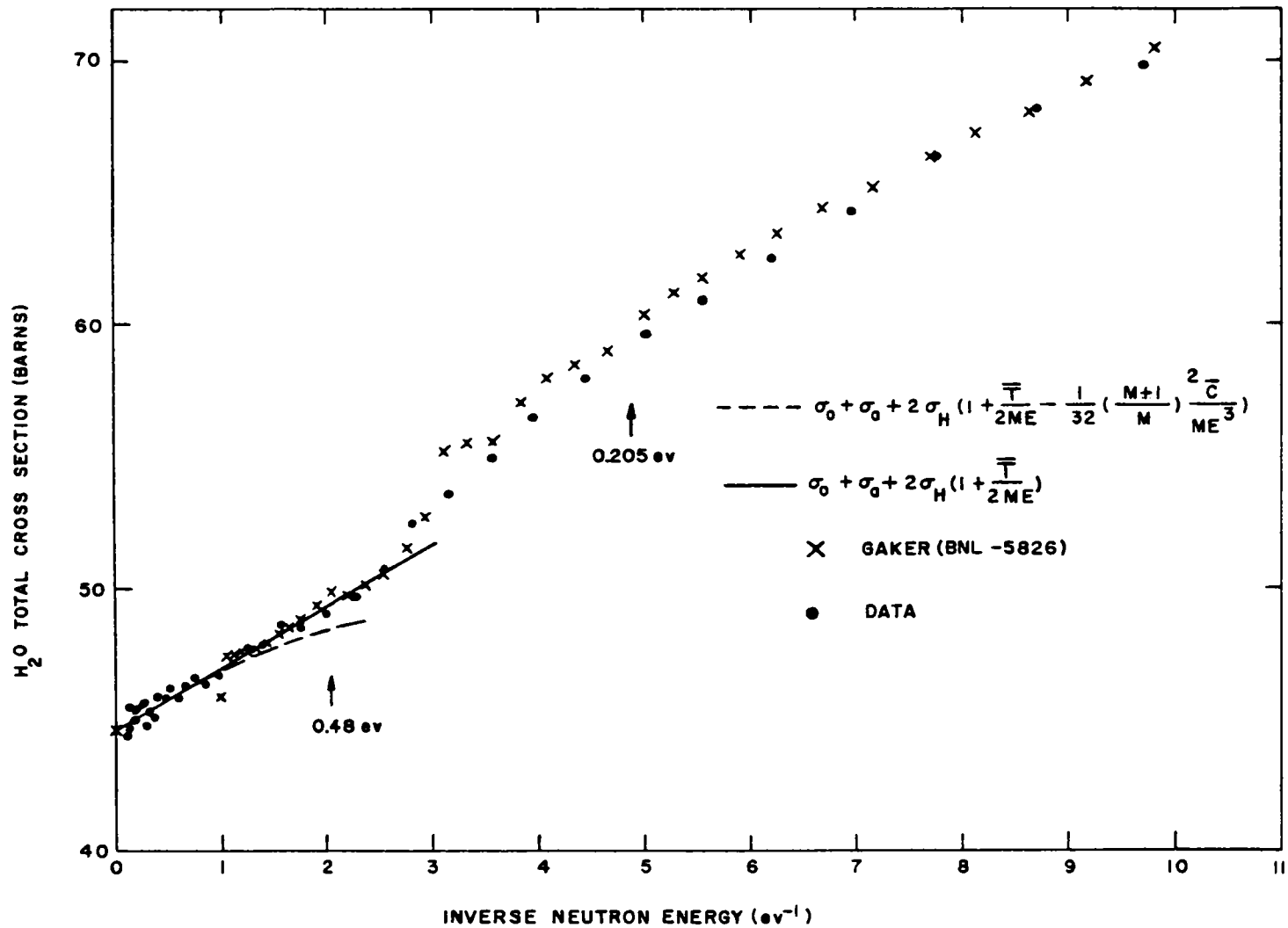


Fig. 2.16--Variation of H₂O total cross section with inverse neutron energy

It is not possible to rigorously determine the accuracy of \bar{T} by this method without an assessment of the foundations of the Nelkin model and the integration routine in GAKER.

The discrepancy between theory and experiment at 4 ev^{-1} is 0.7 barn. Theory and experiment can be brought together here if the model parameters are changed to reduce \bar{T} by $\sim 6\%$. This would, of course, introduce small discrepancies at other energies, depending on how the parameters are altered. The GAKER calculations imply that the cross section is a straight line on this plot down to much lower energies than would be expected from consideration of either the E^{-3} term in the expansion or the proximity of the 0.48-ev level. A least-squares fit of a straight line to all data above 0.5 ev leads to a \bar{T} of 0.113 ± 0.006 , as compared with the Nelkin value of 0.116. \bar{T} probably lies inside the range 0.116 ± 0.007 .

2.5. ANGULAR DISTRIBUTION MEASUREMENTS

There are a number of possible methods which have been investigated for obtaining scattering kernels for reactor spectral calculations. The scattering kernel $\sigma_n(E, E')$ is usually defined by the following relationship:

$$\sigma(E, E', \mu) = \sum_n \sigma_n(E, E') P_n(\mu) \frac{2n+1}{2} \quad (1)$$

For most thermal and near-thermal neutron spectral problems, this kernel must be known in the desired energy mesh for $n = 0$ and $n = 1$. One could proceed by measuring directly $\sigma(E, E', \mu)$; however, the procedure would be impractical because this function of three variables varies rapidly with all of the variables. A second procedure⁽¹³⁾ is to reduce $\sigma(E, E', \mu)$ to a function of two variables, for example, energy and momentum transfer. This so-called scattering-law representation thus permits the experimenter to make far fewer measurements than in the first procedure. A third method is to try to construct a molecular model from general information available about the moderator. This information includes calculated or measured molecular frequency spectra, measured dispersion relationships, total-cross-section data, specific-heat data, and studies of the molecular dynamics. From the model, $\sigma_n(E, E')$ is calculated and the whole procedure is checked by comparing measured spectra (which it is, of course, desired to be able to predict) with the calculations based on the theoretical $\sigma_n(E, E')$. The last procedure is the one utilized at General Atomic in the thermalization study of the common moderators. The second procedure is that used by Egelstaff,⁽¹³⁾ and no one has yet taken seriously the first approach.

It is necessary, of course, to attempt to evaluate which procedure will satisfy the thermalization requirements of the reactor physicist and

engineer. One generalization which can certainly be stated at the present time is that it has been possible to construct scattering kernels by the third method which are at least as reliable as those constructed by the second method. However, as noted above for water, we have not been able to construct completely adequate scattering kernels for all classes of spatially dependent spectral problems likely to be encountered in reactor design. Although the P_0 scattering matrix produced by the bound-hydrogen scattering model for water appears to be relatively reliable, the P_1 matrix, which strongly affects neutron transport, does not appear to be as good. This becomes apparent in attempts to predict cell spectra and spectra near control rods. It has been our objective this year to investigate an experimental procedure which appeared to be simpler and more appropriate to the reactor problem than the double differential experiment, and which should allow improvements to be made in our present scattering kernels. The experiment is designed to measure the scattering cross section integrated over E' , the outgoing energy channel, namely,

$$\sigma(E, \mu) = \int \sigma(E, E', \mu) dE' .$$

There are at least two choices in the interpretation of these experimental measurements: (1) performing the measurement of $\sigma(E, \mu)$ over a fine energy and angle mesh and trying by inversion to find $\sigma(E, E', \mu)$, and (2) just comparing the experimental results directly with $\sigma(E, \mu)$ calculated by a given molecular model and using the experiment to guide the analytical improvements being made in the models. For example, the following integrals can be performed on the experimental $\sigma(E, \mu)$ and the results compared with the theoretical calculations in order to investigate in a gross fashion the reliability of the various orders of the theoretical scattering matrices:

$$\sigma_n(E) = \int_{-1}^{+1} P_n(\mu) \sigma(E, \mu) d\mu .$$

In this way it is possible to obtain $\sigma_{\text{transport}}(E) = \sigma_0 - \sigma_1$, a quantity directly needed for reactor analysis. With the experimental data obtained for water during this contract year, both analytical procedures referred to above are being tried with encouraging success.

The question of sensitivity of the measured result, $\sigma(E, \mu)$ to the scattering model is a valid one to consider. It might be supposed that since the data have been integrated once over energy, much of the important physics is removed. This is, however, not generally the case. A typical illustration of this point is shown in Fig. 2.17, where the calculated $\sigma(\mu)$ for $E = 0.2$ ev is plotted versus the cosine of the scattering angle in the laboratory coordinate system. The bound-hydrogen water model is used

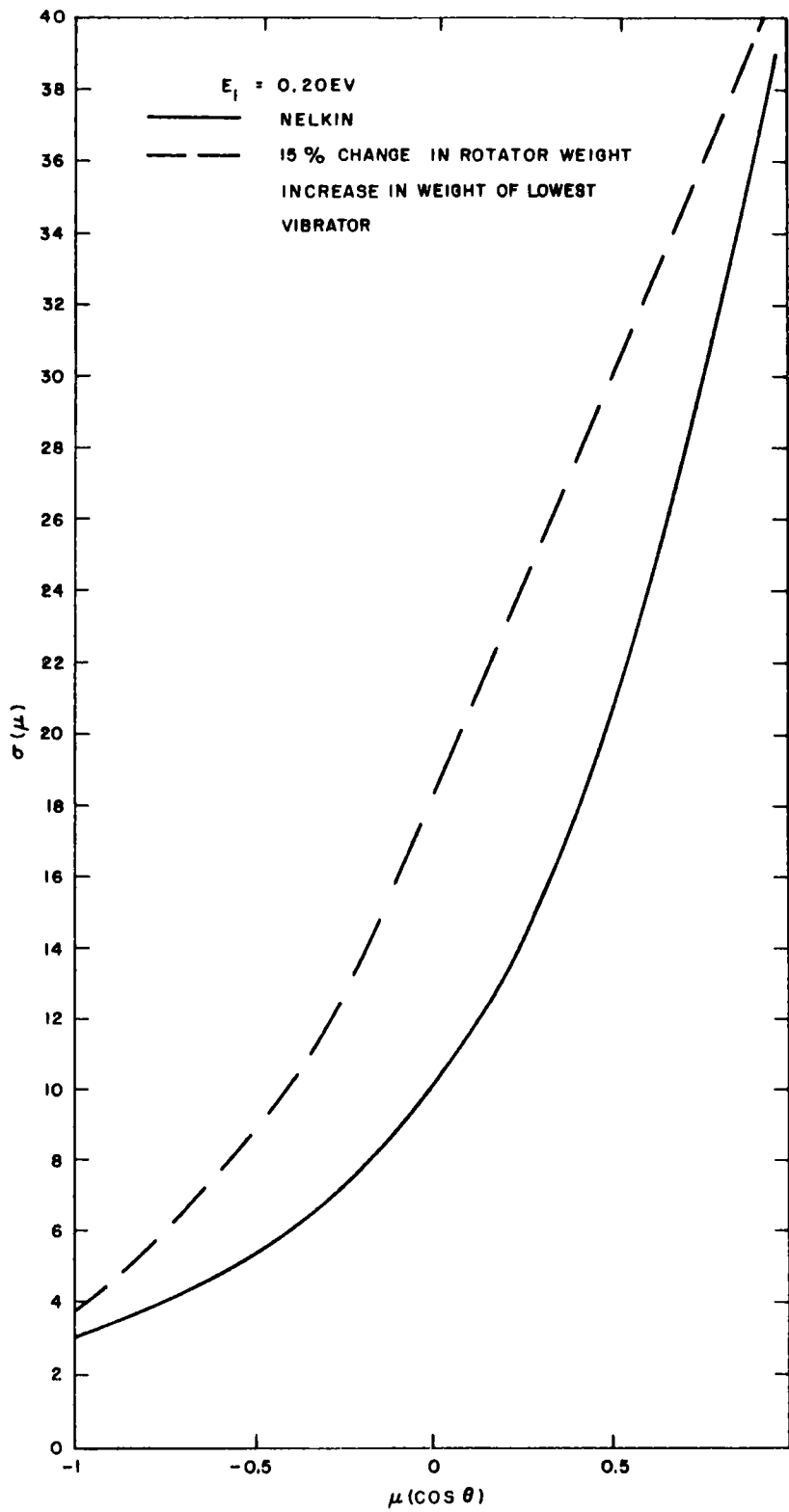


Fig. 2.17--Effect on $\sigma(\mu)$ for a 15% change in the rotator weight and an increase in the lowest vibrator weight

for the calculation, and, as indicated, a rather minor redistribution of the oscillator weights produces a pronounced, easily measured change in the angular-distribution function.

Before discussing these new results and their significance, let us first consider how to establish a good measurement of $\sigma(E, \mu)$, and then present briefly a sampling of some previous measurements.

There are certain general considerations in setting up any scattering experiment to study energy transfer at low neutron energies. These considerations apply to both double differential scattering experiments and the experiments to be discussed here. With the exception of investigations by a very few workers in the field, some of these considerations have largely been overlooked or neglected in previous work. The first general point to make is that multiple-scattering effects on the neutron scattering can be very large if one is not careful of sample design. For water, a sample with a thickness of 0.010 in. or less, properly oriented with respect to the incoming and outgoing neutron directions, is necessary, and even here multiple scattering can contribute significantly for large scattering angles. Sample containers must be thin-walled, hopefully a few mils of aluminum thick, or they contribute in the complex multiple-scattering analysis. Sample orientation cannot be arbitrary, or long exit path lengths for the neutrons at various scattering angles will be obtained. Even after these precautions, a well-established procedure to correct for residual second-order scattering effects must be utilized before these data are presented for theoretical analysis. To date, and to our knowledge, none of the experimental differential scattering data have been corrected properly for multiple scattering in the sample.

A second general consideration for scattering work is that absolute differential cross sections, not plots of counting rate versus time of flight, are needed. Clues regarding the types of refinements required for the existing molecular models are not likely to be found in normalized uncorrected data. This means, for example, that precautions must be taken in thin-sample design so the sample thickness can be precisely determined since the cross section is obviously as uncertain as the sample thickness or atom density.

A third general point is that angular distributions based on work at two or three angles are not sufficiently comprehensive to be useful. An ability to select interesting and significant angles for study must be built into the experimental apparatus, since much structure in the angular distributions is observed in characteristic energy regions. Further data simply should not be taken with fixed arbitrary, angular setups. In view of the many difficulties encountered with the double differential scattering experimental arrangements, the feasibility of the $\sigma(E, \mu)$ experiment has

been studied this year at General Atomic. The experimental arrangement is shown schematically in Fig. 2.18. A "black" detector is rotated around a very thin scattering sample located 12 in. away. The angular resolution is about 6 degrees. This assembly is located 1000 in. from a high-intensity, thermalized, pulsed neutron source. Since a neutron scattered in the sample can assume a large range of energies after the collision, the flight path to the detector must be a small fraction of that from the neutron source to the scatterer in order to preserve the energy resolution. The energy resolution of the system can be estimated from the simple relation

$$\frac{\delta E}{E} = 2 \frac{l_2 v_1}{l_1 v_2} .$$

For our system, an energy change on collision of a factor of 25 gives an experimental energy resolution of 12%, which is adequate. Such large energy changes are quite improbable, however, so the actual experimental resolution for the incident energy is generally much better.

The black detector is, of course, necessary to ensure that all exit energies are counted with the same probability. The detector was a 2-in.-diameter, 1/2-in.-thick Li^6 glass mounted on a photomultiplier tube. The crystal energy sensitivity falls off by 5% only from very low energies to 1-ev neutron energy. The detector is, however, gamma-sensitive, which necessitates a rather comprehensive shield construction to eliminate undesirable backgrounds. The facility constructed for this purpose is shown in Fig. 2.19. The thin sample holders and the boron carbide shield for the Li^6 glass detector are also shown in this figure.

In the above discussion, some general criteria for scattering experiments were enumerated. There are a few more specific criteria which must be observed in the scattering angular distribution experiment. Obviously, when using time-of-flight methods, the relative distance from source to sample must far exceed that from sample to detector. Further, this experiment always requires a short, black detector. Long BF_3 tubes, although they may be black over the total length, present a different solid angle to each neutron energy. Thus, $\sigma(E, \mu)$ is not measured. Finally, Fig. 2.19 shows the experimental setup in a rather confined shield. Guarantees that internal scattering and reflection do not perturb the results are necessary under these circumstances.

There have been some previous attempts to measure $\sigma(E, \mu)$ during the last few years. These experiments demonstrated feasibility but were not utilized seriously to attempt to improve our knowledge of low-energy neutron scattering. Data were reported at the Vienna conference in 1960⁽¹⁴⁾ on an angular distribution measurement performed with an analyzed neutron beam from a reactor source. Some of these data are reproduced in

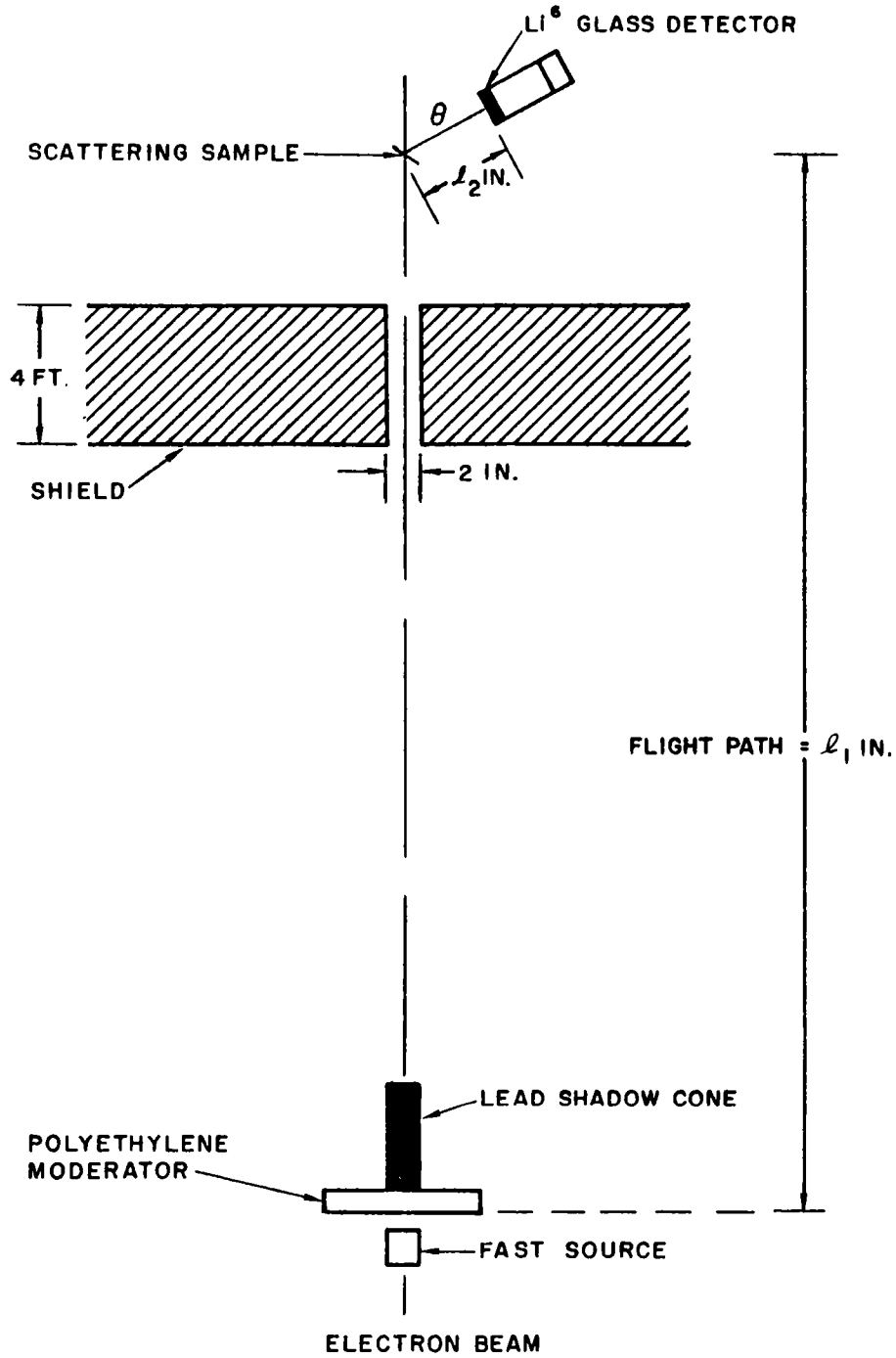


Fig. 2.18--Experimental arrangement for measurement of the differential scattering cross section of water

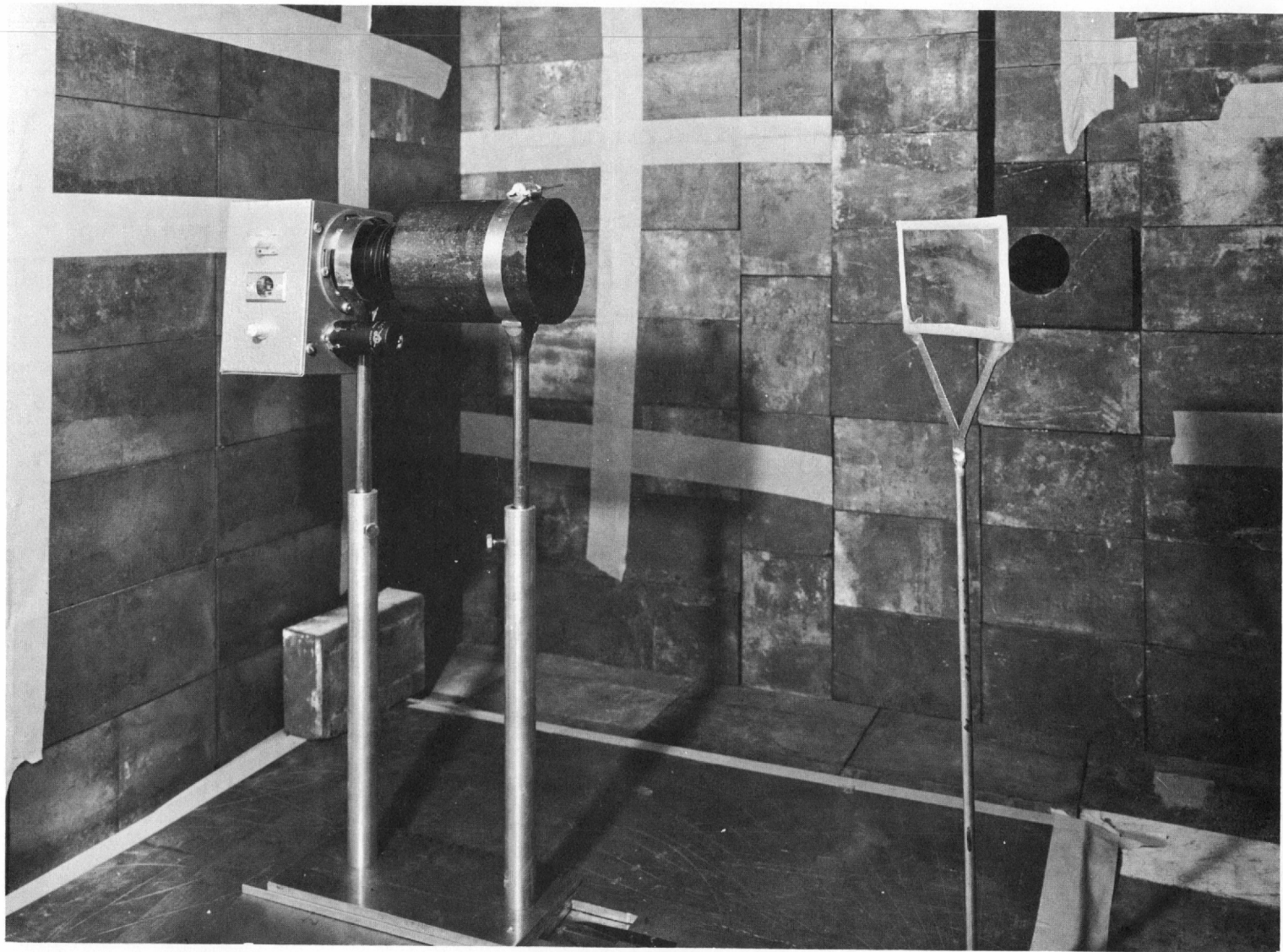


Fig. 2.19--Apparatus for measurement of the differential scattering cross section of water

Figs. 2.20, 2.21, and 2.22, where they are compared with the predictions of the Nelkin water model. Absolute cross-section comparisons are not possible, and theory and experiment are normalized at the first experimental angle, 30° . The discrepancies between theory and experiment would appear to be quite large and deserve considerable attention in view of the transport difficulties in spectral calculations. These experimental data were not corrected for multiple scattering or the unknown sensitivity of the long BF_3 counter used. A second series of experiments based on approximately the same technique was performed by Reinsch⁽¹⁵⁾ with the Munich research reactor. These data are compared with the water-model theoretical predictions in Figs. 2.23 and 2.24. In general, at the higher energies, smaller variations than those given in Ref. 14 can be seen, but at 0.04 eV all appears to go well with the water model from these experiments. The systematic variation of the cross section with angle at 0.078 eV should be predicted by the molecular model. Obviously, a disagreement exists between the two previous sets of measurements on water and possibly between measurement and theory.

During the last year, exploratory angular distributions were run at 50 incident energies, using the setup shown in Fig. 2.18, from 0.006 eV to 1 eV, and 5 scattering angles for a thin water sample. These data have been corrected approximately for multiple scattering in the sample by the Vinyard technique⁽¹⁶⁾ and are shown in Figs. 2.25 through 2.31. The general agreement with the Nelkin model is good in contrast to some of the earlier data shown, although it is far from perfect. The calculations of the angular distribution functions were performed with the computer code GAD, written by H. C. Honeck of Brookhaven National Laboratory. This computational technique utilizes basically the procedures of the GAKER scattering formalism. Differences seem to be most pronounced above 0.1-eV neutron energy. This effect is probably consistent with the spectral discrepancies observed previously at and near sharp flux discontinuities. The large multiple-scattering corrections shown here are not sufficiently exact to be taken very seriously. More accurate techniques for correcting the data are under development, and of course very thin samples must be used in the future for these studies.

These experiments, however, have established the efficacy of this new technique for studies of the angular properties of the scattering kernels. Backgrounds are low, counting rates are reasonable, sensitivity to model is high, and the present setup can be put on a production basis with a rather modest expenditure for multiple Li^6 glass instrumentation. This we will attempt to accomplish during the next contract year.

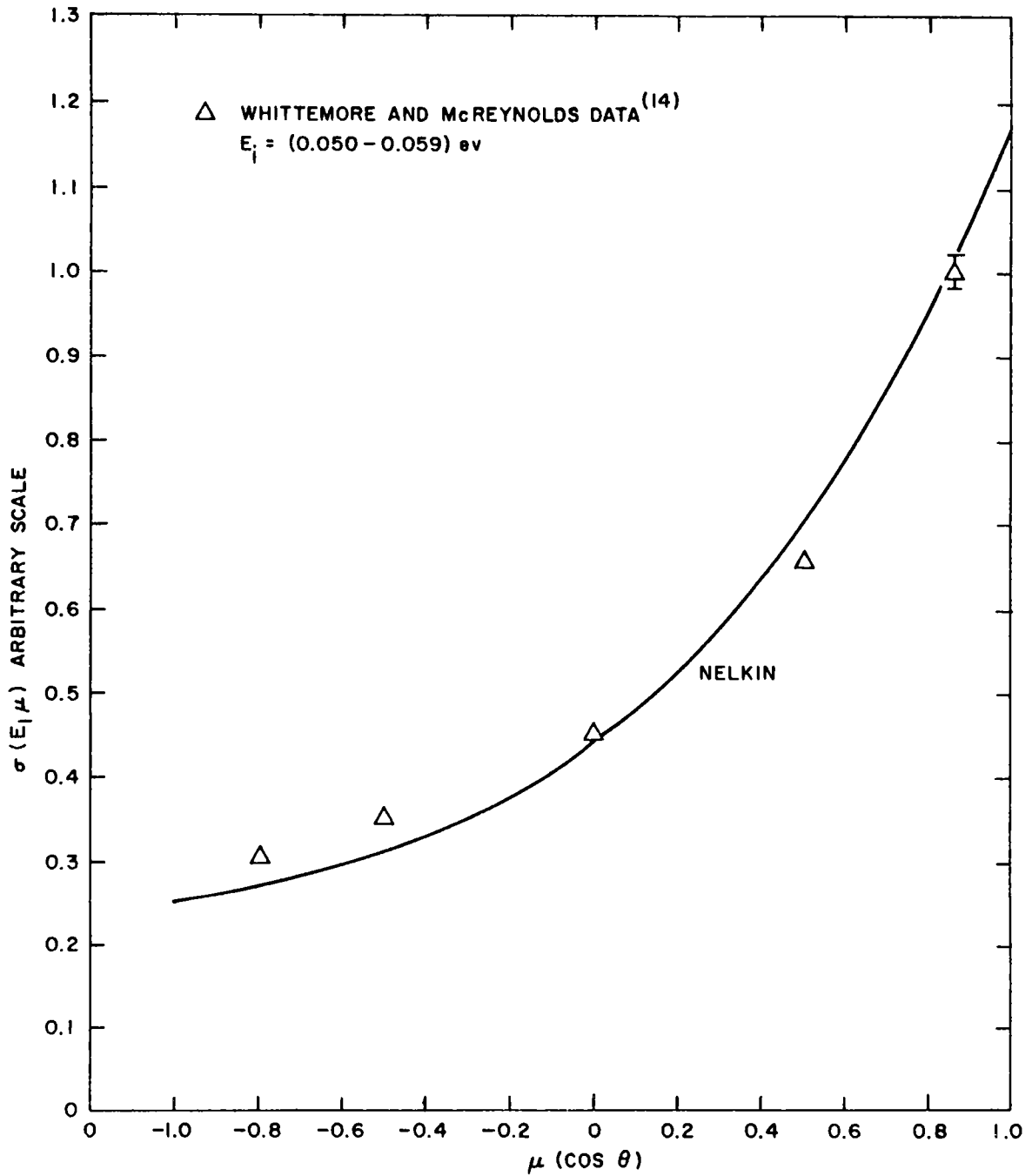


Fig. 2.20--Comparison of Whittemore and McReynolds' data with Nelkin's theory for an angular distribution measurement at an incident neutron energy of 0.050 to 0.059 eV

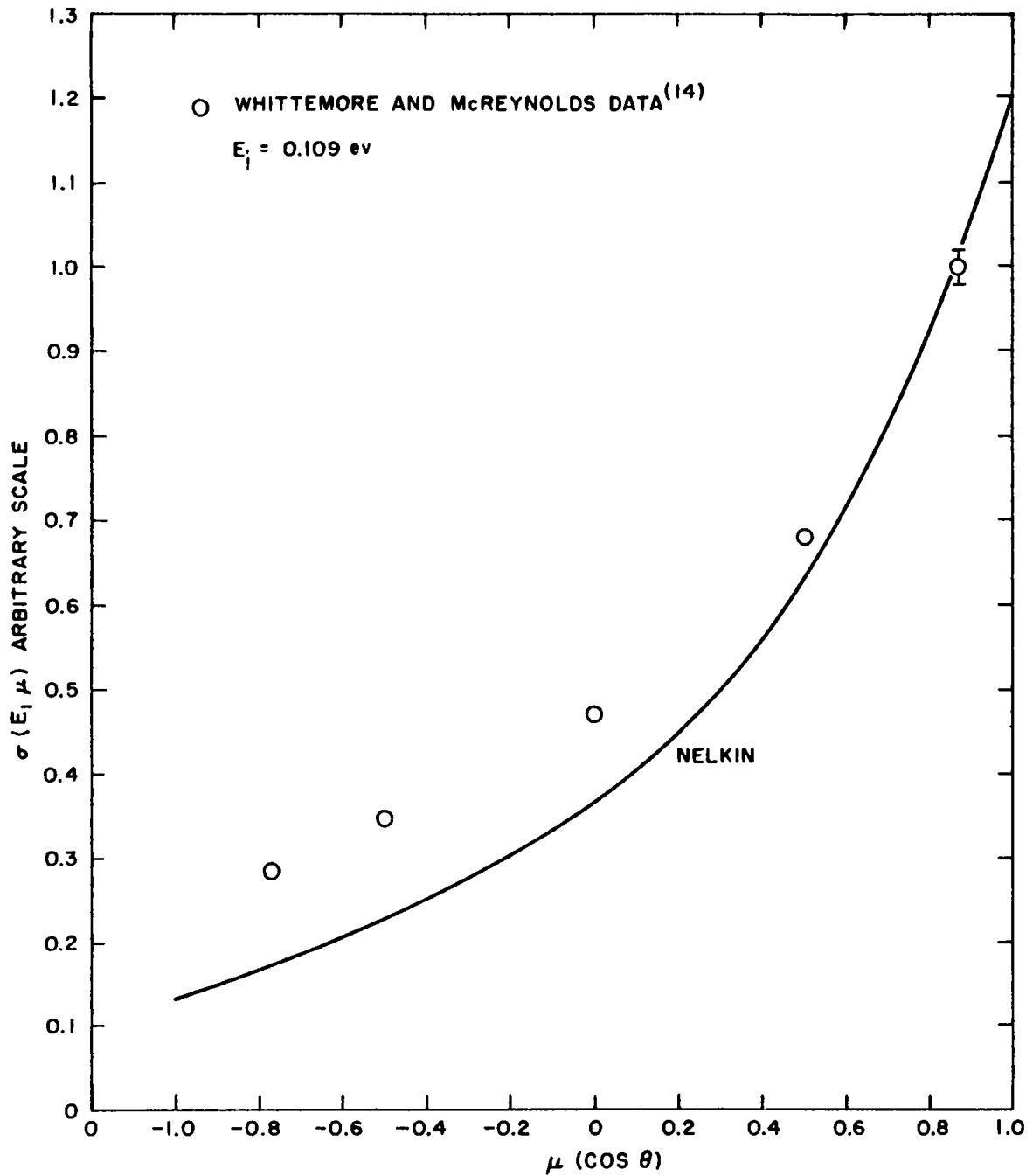


Fig. 2.21--Comparison of Whittemore and McReynolds' data with Nelkin's theory for an angular distribution measurement at an incident neutron energy of 0.109 eV

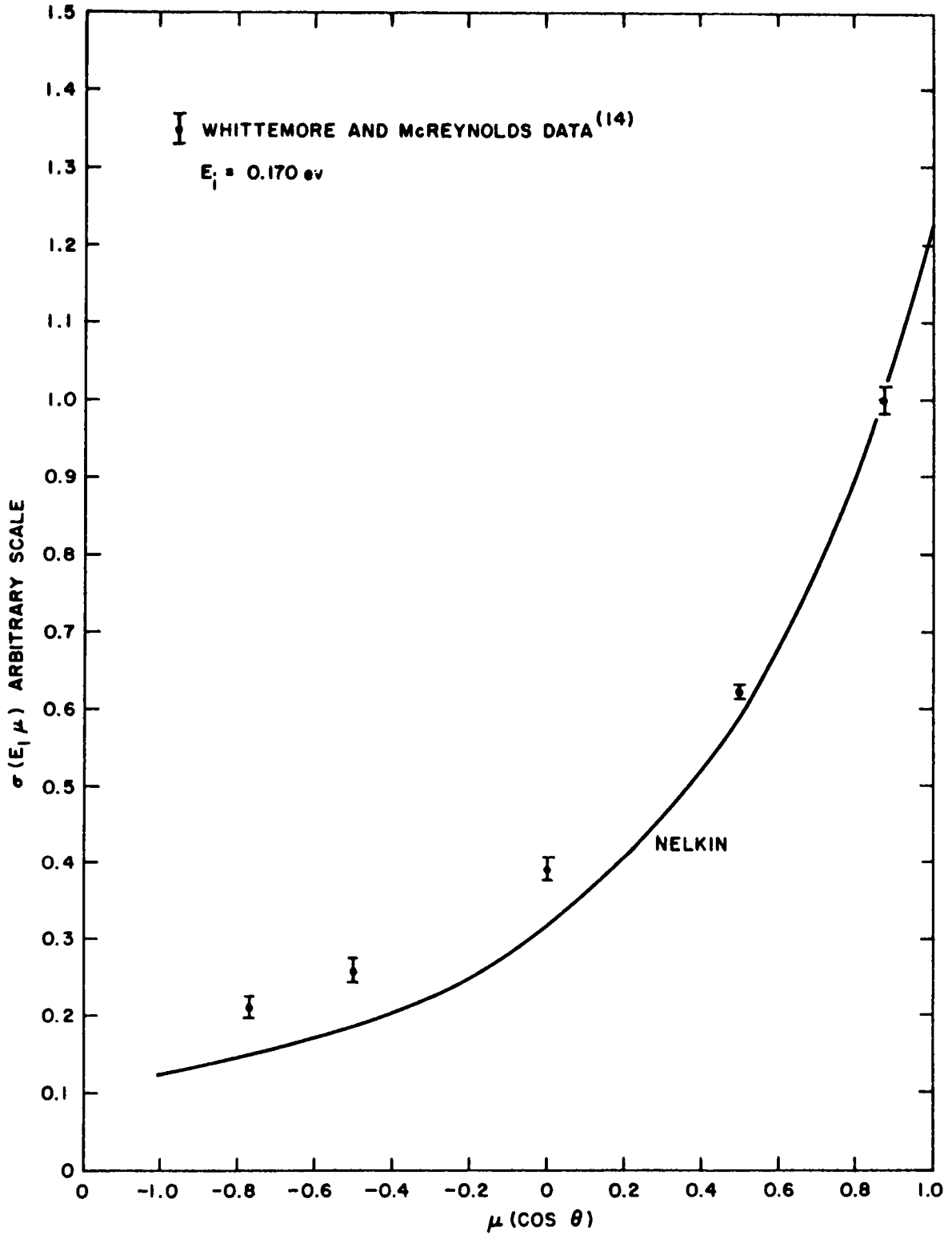


Fig. 2.22--Comparison of Whittemore and McReynolds' data with Nelkin's theory for an angular distribution measurement at an incident neutron energy of 0.170 eV

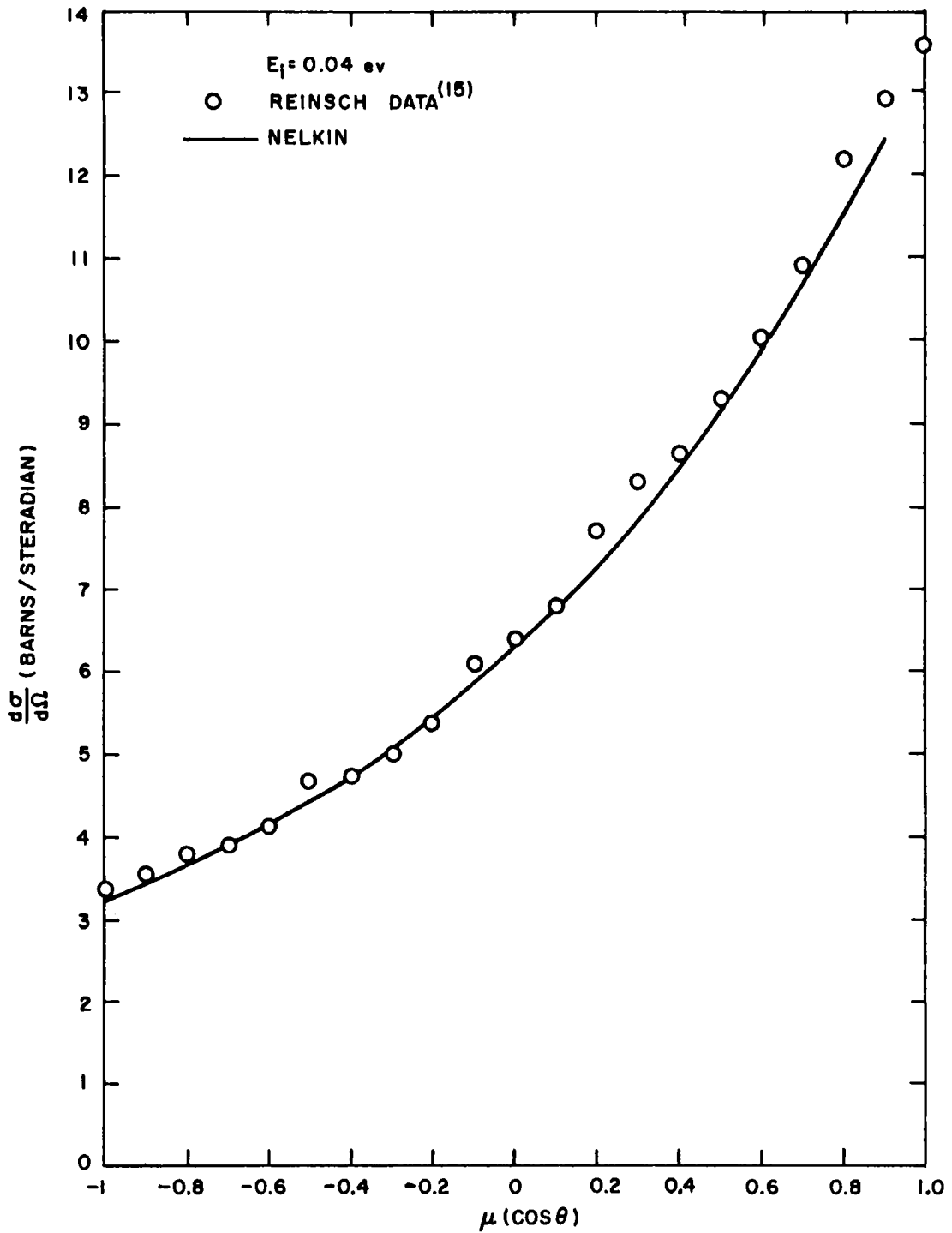


Fig. 2. 23--Comparison of Reinsch's data and Nelkin's theory for the differential cross section of water at an incident neutron energy of 0. 04 eV

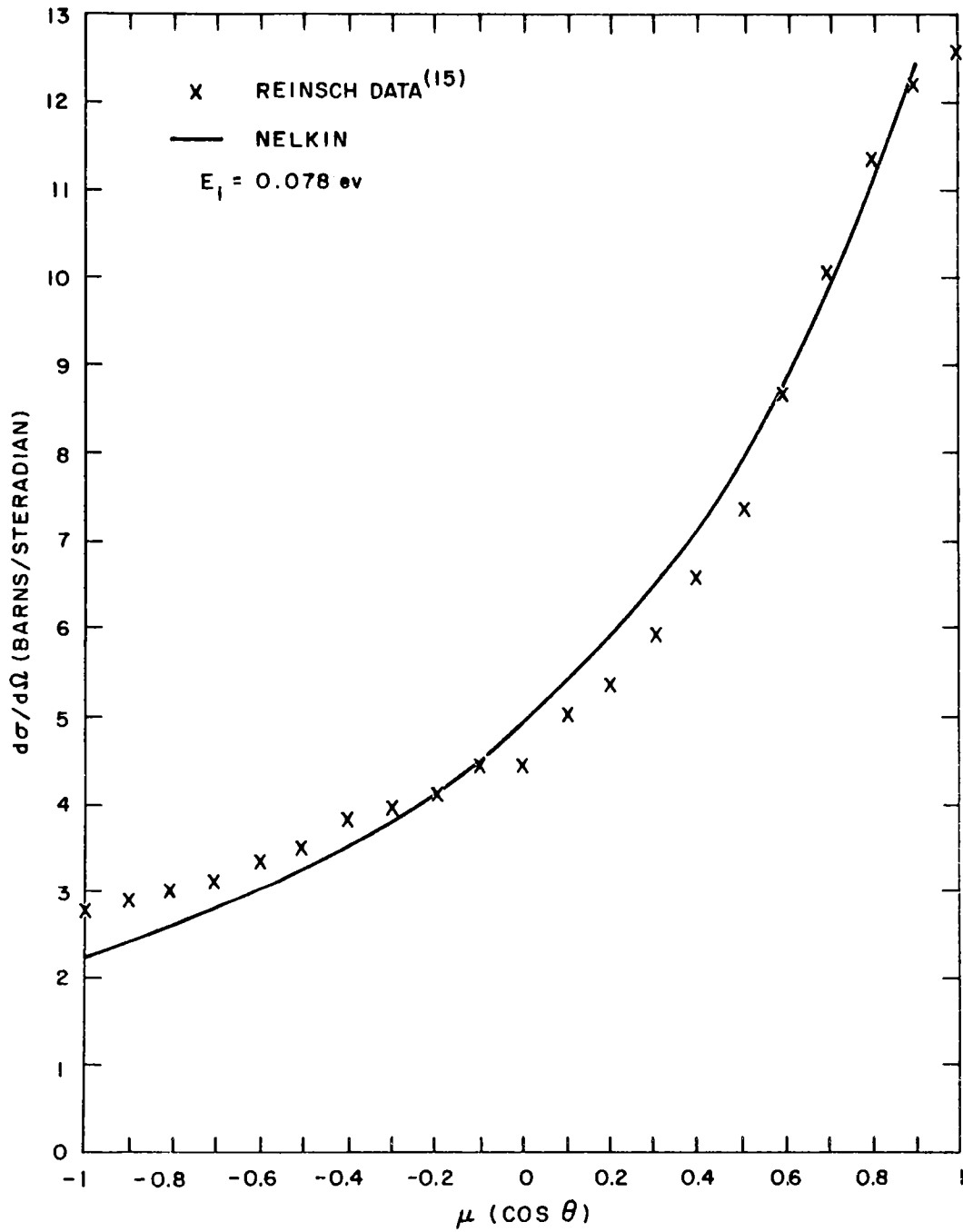


Fig. 2.24--Comparison of Reinsch's data and Nelkin's theory for the differential cross section of water at an incident neutron energy of 0.078 eV

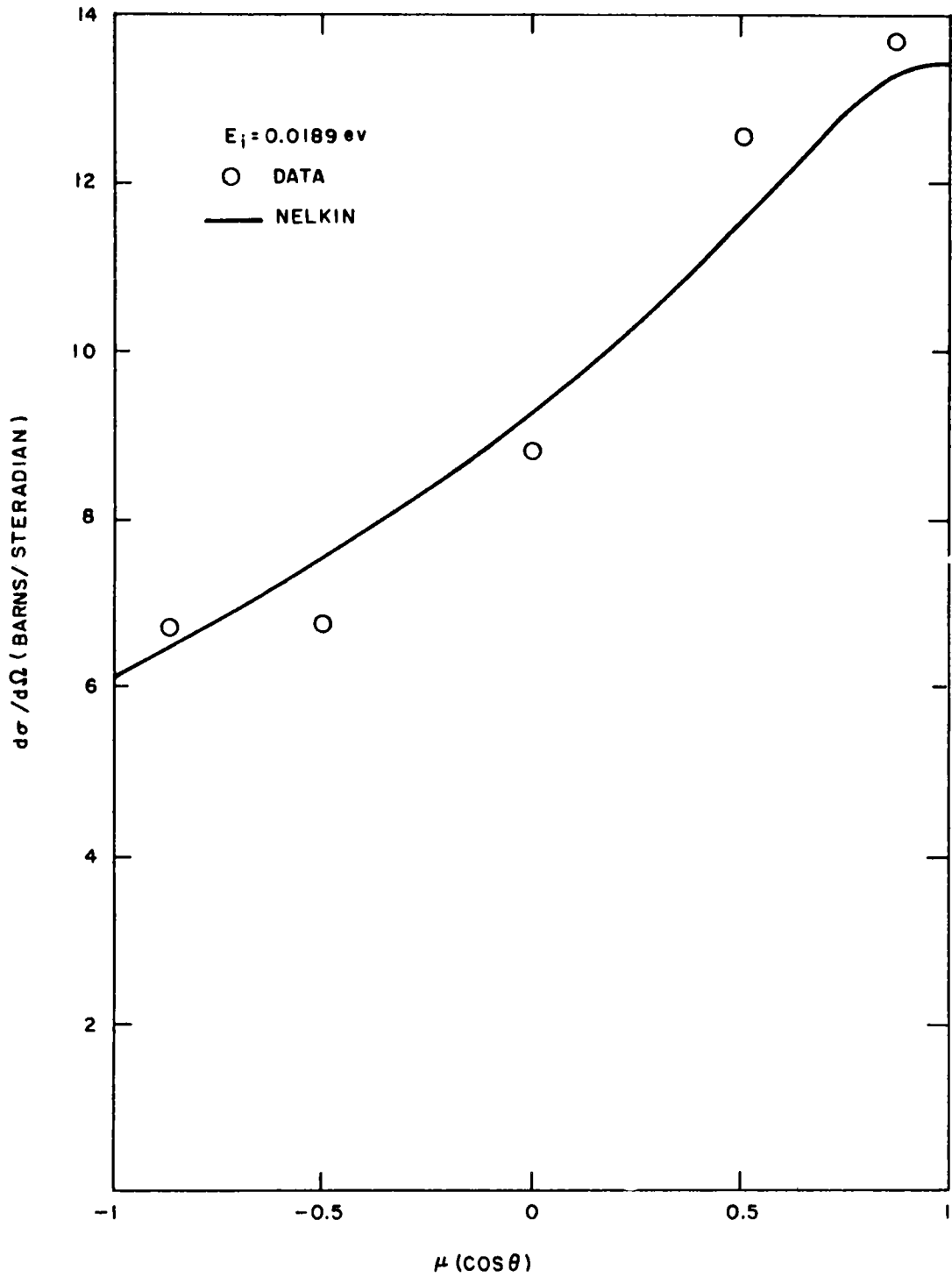


Fig. 2.25--Comparison of measurement and theory for the differential cross section of water at an incident neutron energy of 0.0189 eV

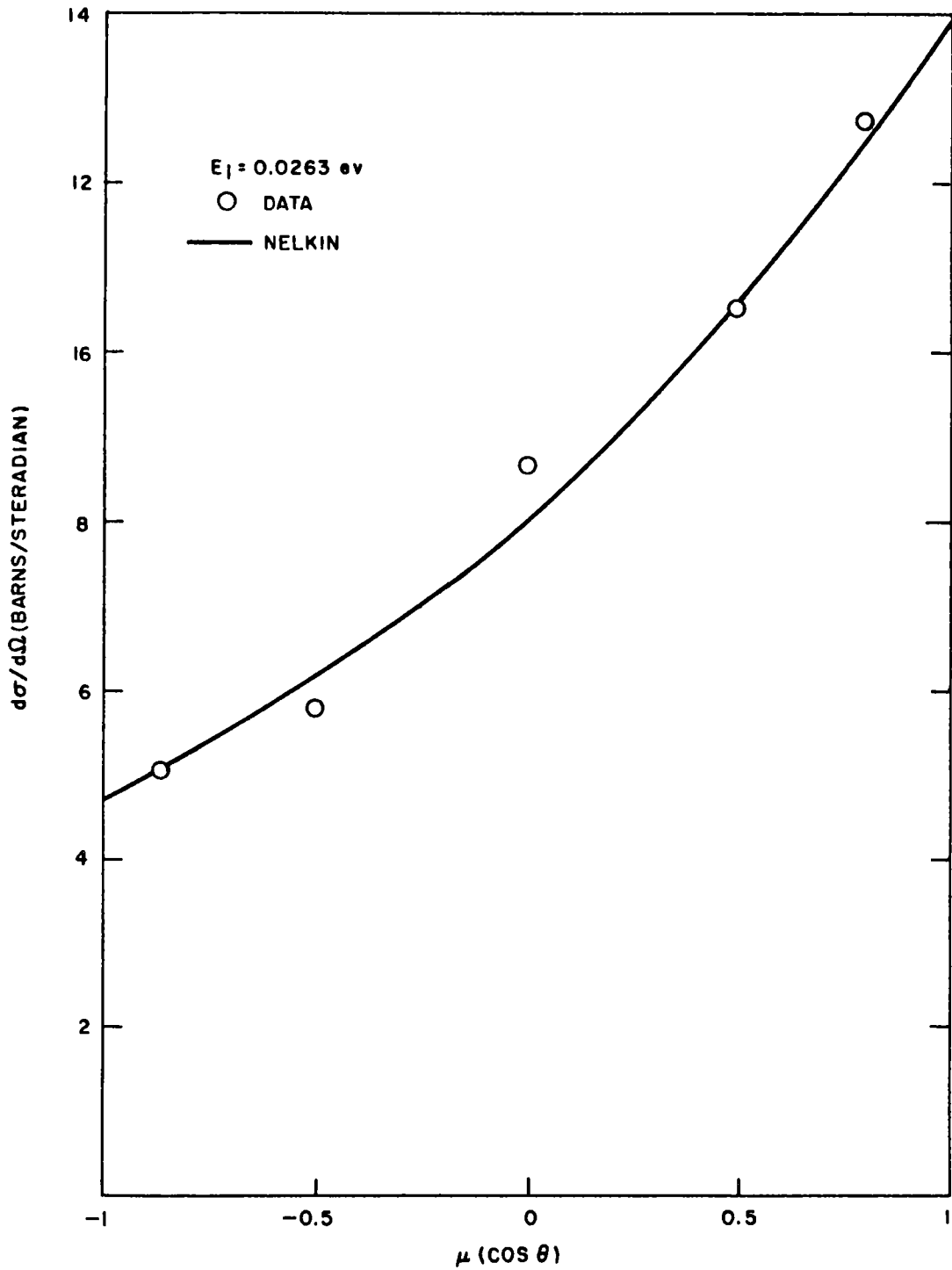


Fig. 2.26--Comparison of measurement and theory for the differential cross section of water at an incident neutron energy of 0.0263

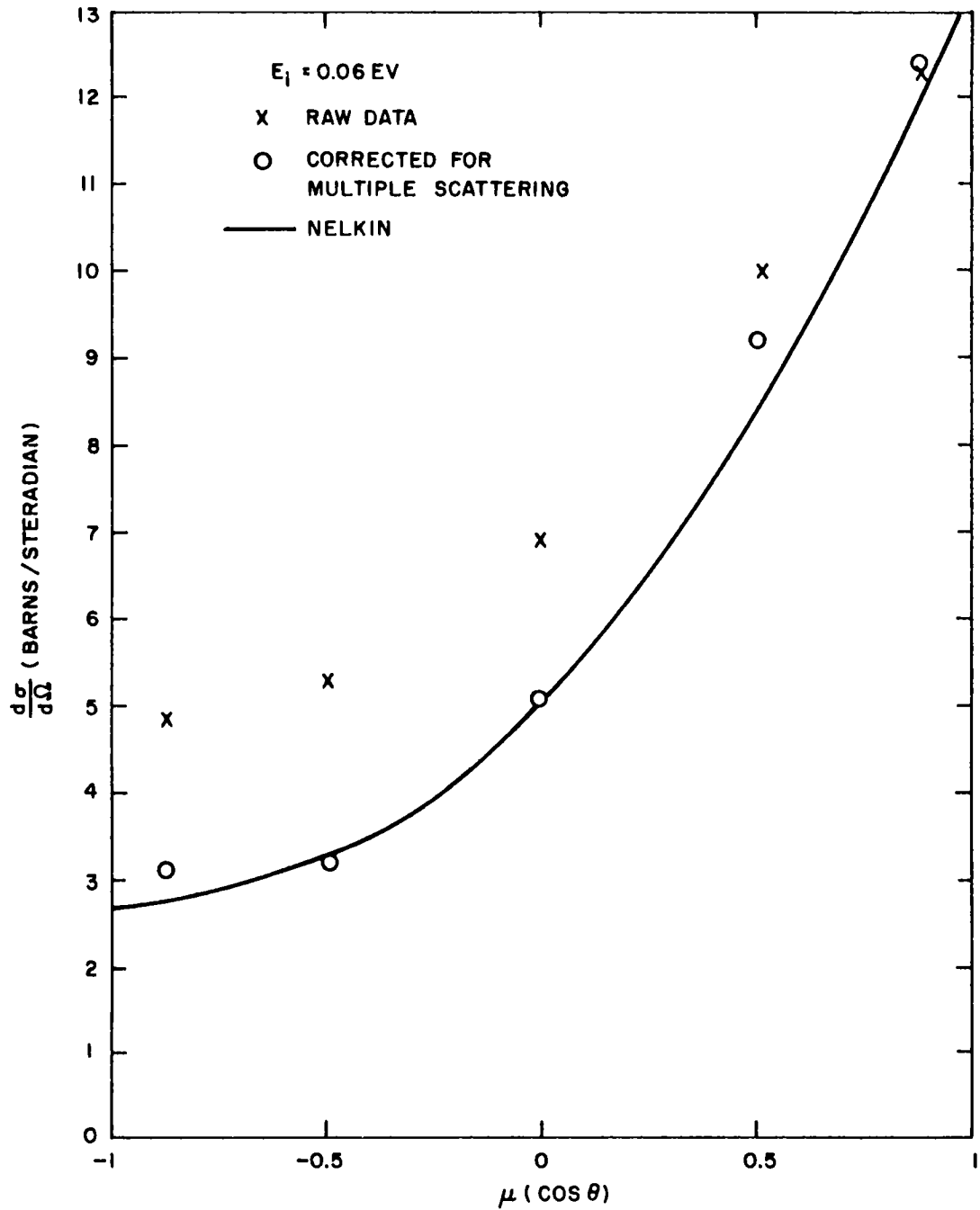


Fig. 2.27--Comparison of measurement and theory for the differential cross section of water at an incident neutron energy of 0.06 eV

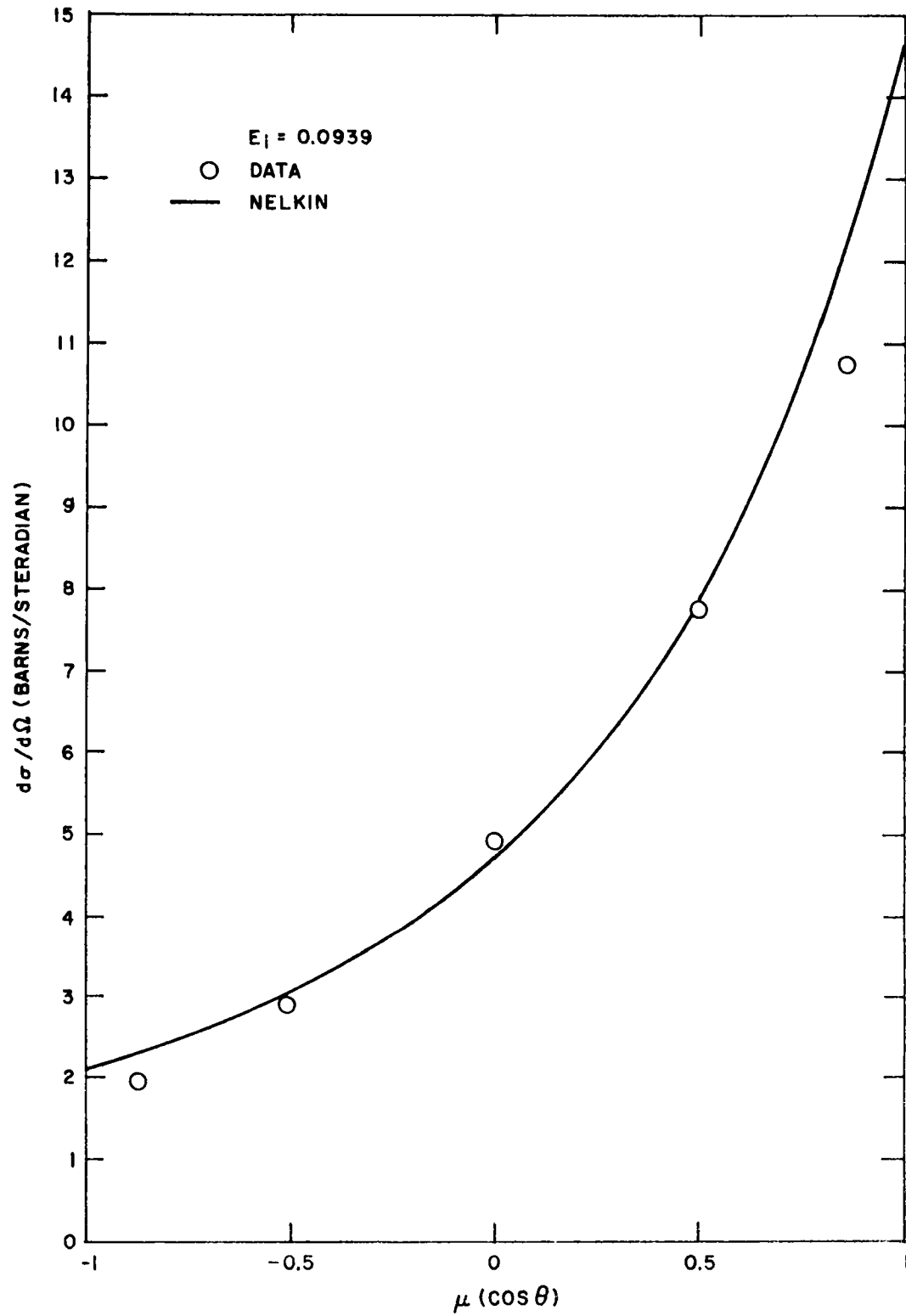


Fig. 2.28--Comparison of measurement and theory for the differential cross section of water at an incident neutron energy of 0.0939 eV

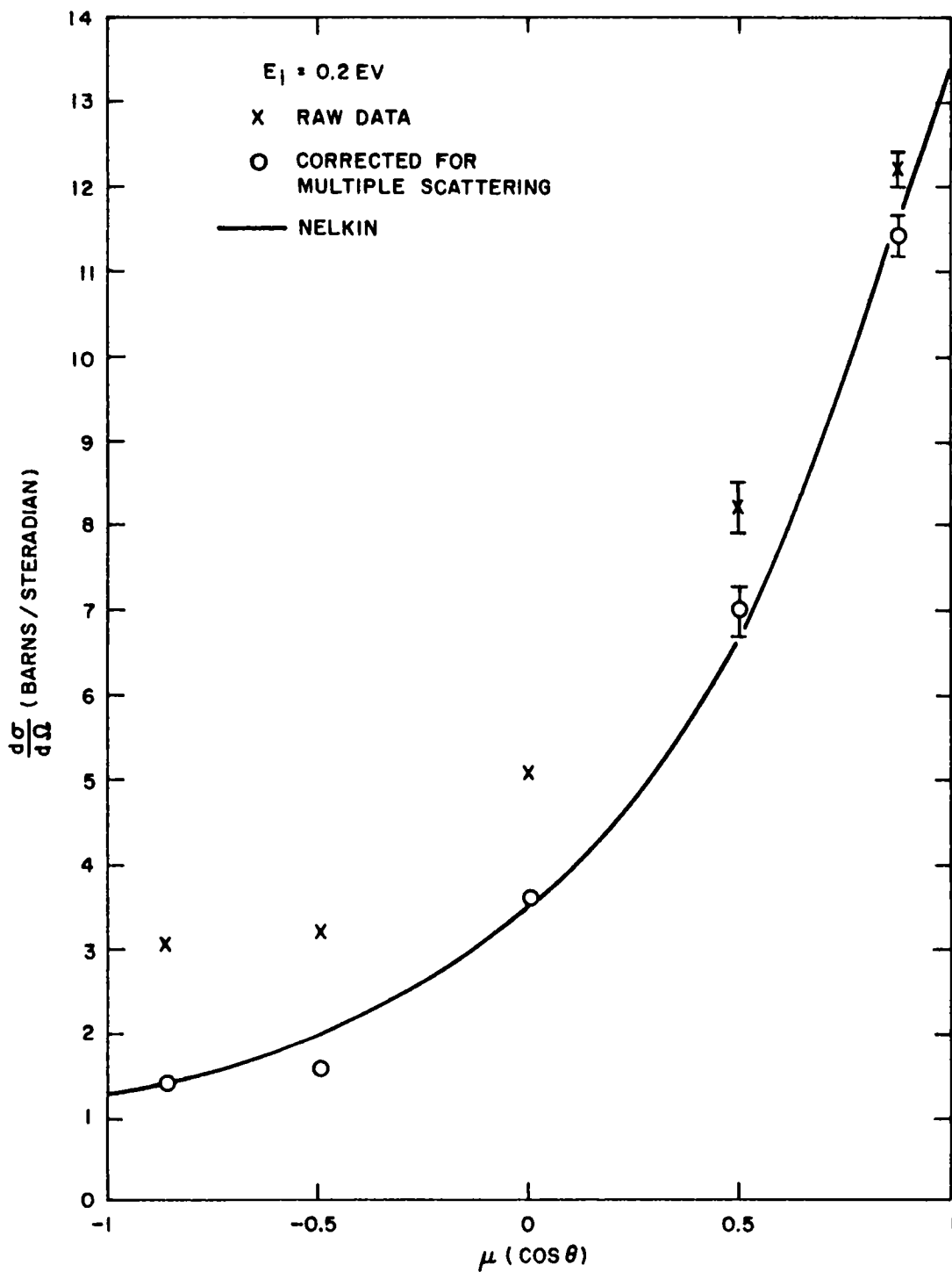


Fig. 2.29--Comparison of measurement and theory for the differential cross section of water at an incident neutron energy of 0.2 eV

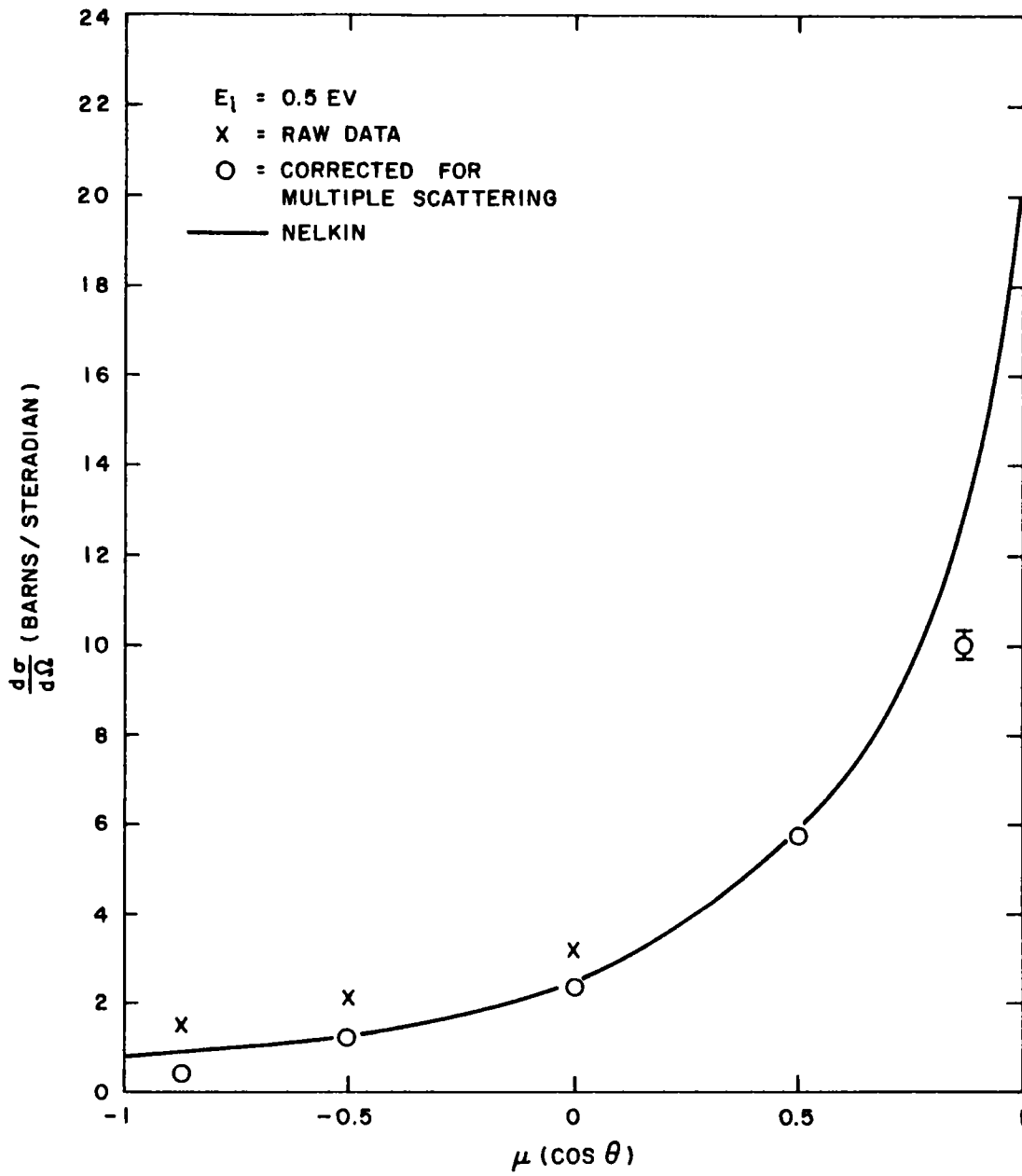


Fig. 2.30--Comparison of measurement and theory for the differential cross section of water at an incident neutron energy of 0.5 eV

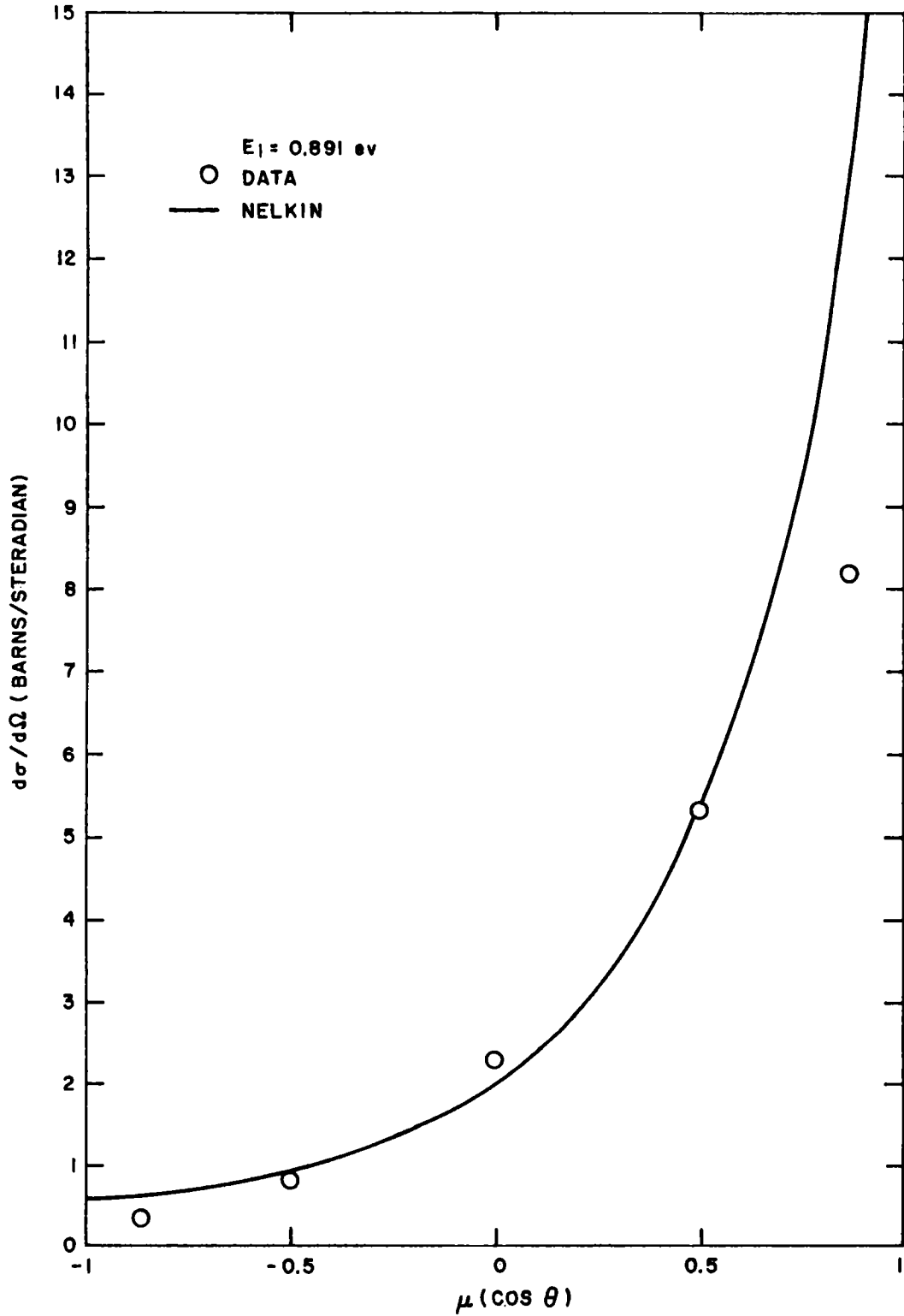


Fig. 2.31--Comparison of measurement and theory for the differential cross section of water at an incident neutron energy of 0.891 eV

2. 6. SCATTERING MODEL FOR H₂O

As has been stated elsewhere in this report, infinite-medium spectra calculated with Nelkin's bound proton kernel have been found to be systematically softer than measured spectra. For instance, in the case of heavily $1/v$ poisoned media (5 barns/H of boric acid) the discrepancy is of the order of 10%. In seeking possible causes for this discrepancy, at least three features not considered rigorously in Nelkin's kernel immediately come to mind:

1. Diffusion of the H₂O molecules (or complexes of molecules), instead of the free translations assumed by Nelkin.
2. The rotational modes of motion cover a broad band of frequencies instead of a single frequency.
3. The vibrational modes of motion are far from being isotropic in space as is assumed implicitly in Nelkin's model.

The first of these refinements is of no consequence for infinite-medium spectra because it only affects the small energy exchange (quasi-elastic) scattering, which essentially drops out of the balance equation for an infinite medium.

Consideration of the second improvement requires a code which can handle a distributed frequency spectrum, such as the one measured by Egelstaff with his method of extrapolating $(1/\alpha) S(\alpha, \beta)$ to zero α (momentum exchange). An attempt was made at General Atomic to obtain a scattering kernel from this spectrum (in addition to the higher frequencies corresponding to the internal vibration of the H₂O) using the code SUMMIT.⁽¹⁷⁾ The results were not satisfactory since the total cross section obtained was in error. This is believed to be due to the fact that the measured frequency spectrum is too complicated to be handled accurately by SUMMIT. These calculations will be continued with the new universal code now being prepared (referred to in Section XII).

Finally, the third feature not considered in Nelkin's model, namely, the spatial anisotropy of the oscillatory motion of the H₂O molecule, has been analyzed within certain approximations. In Nelkin's model of the dynamics of the H₂O molecule, all oscillations are assumed to be isotropic in space. In order to get some idea of the influence of the actual anisotropic motion of the protons on the neutron scattering law, it is useful to consider a very simple model which maintains the essential features of the scattering system. This model consists of two protons bound harmonically to the much heavier oxygen nucleus, whose relative mass is assumed to be infinite. The restoring forces produced when the protons are moved away from their equilibrium position are (1) a force in the direction of the O-H

bond proportional to the change of length of the bond, and (2) a force perpendicular to each of the O-H bonds proportional to the change of angle between them. Besides these internal restoring forces, it is assumed that the rotations of the whole molecule about its principal axis of inertia are completely hindered by a harmonic torsional potential. In other words, for small displacements with the coordinates of Fig. 2.32, the potential energy will be given by

$$V = k_a(x_1^2 + x_2^2) + k_b(y_1 + y_2)^2 + k_c(y_1 - y_2)^2 + k_d(z_1^2 + z_2^2) + k_e(z_1 - z_2)^2, \quad (1)$$

or else

$$V = k_1(q_1^2 + q_2^2) + k_2(q_3^2 + q_4^2) + 2k_3q_3q_4 + k_4(q_5^2 + q_6^2) + 2k_5q_5q_6 = \sum_i \sum_j V_{ij}q_iq_j, \quad (2)$$

where

$$k_1 = k_a; \quad k_2 = k_b + k_c; \quad k_3 = k_b - k_c; \quad k_4 = k_d + k_e; \quad k_5 = k_d - k_e;$$

and

$$q_{1,2} = x_{1,2}; \quad q_{3,4} = y_{1,2}; \quad q_{5,6} = z_{1,2}.$$

The kinetic energy is obviously

$$T = \frac{m}{2} \sum_{i=1}^6 \dot{q}_i^2. \quad (3)$$

This very simple picture of the H₂O molecule dynamics yields six normal modes of motion. In the three rotational modes and in the H-O-H bending modes, each H atom moves in a plane which is perpendicular to the O-H bond, whereas in the two O-H stretching modes, which have the same frequency because of the infinite mass assumed for the oxygen, the motion is in the direction of the O-H bond. In order to find the frequencies and amplitudes of the normal modes of oscillation corresponding to this model, one has to diagonalize the matrix $[(V_{ij})]$. This is equivalent to solving the eigenvalue problem:

$$\sum_j V_{ij} A_{jk} = A_{ik} \lambda_k, \quad (4)$$

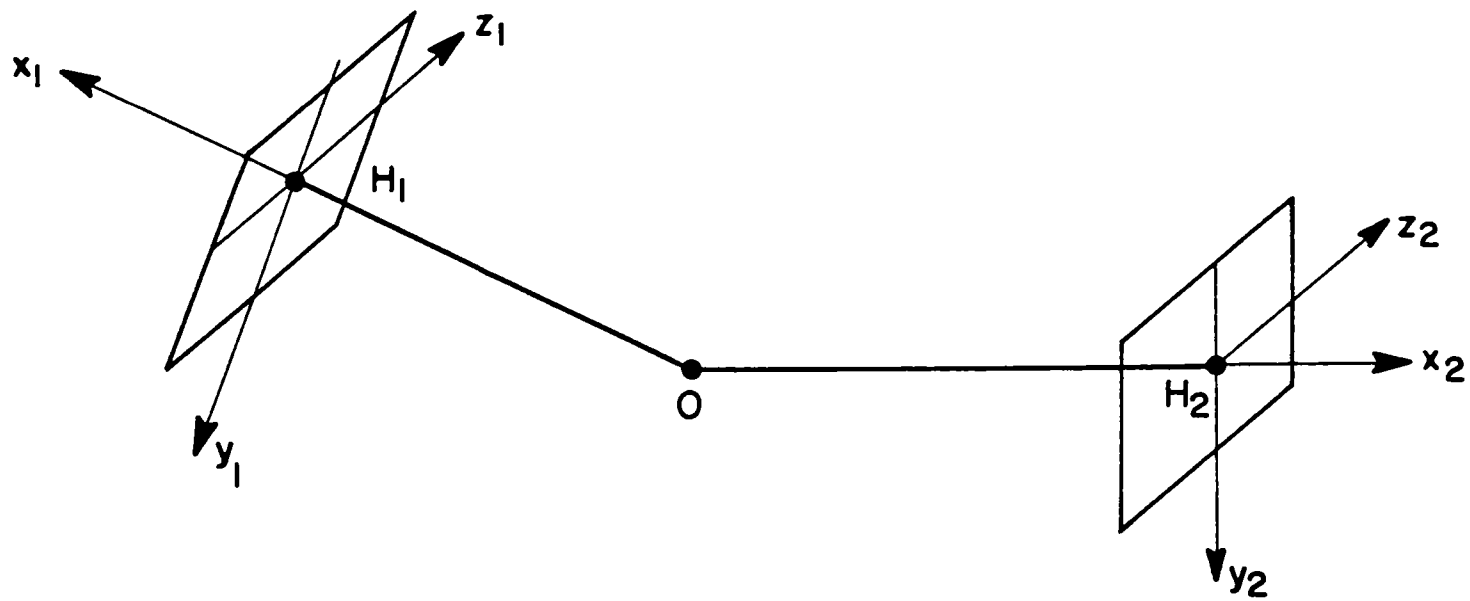


Fig. 2.32-- H_2O molecule

where A_{ik} are the amplitudes corresponding to the coordinate q_i in the normal mode of eigenvalue λ_k . They satisfy the two orthogonality conditions

$$\sum_{i=1}^6 A_{ik} A_{il} = \delta_{kl} \quad k, l = 1, 2, \dots, 6 \text{ (sum over coordinates)}, \quad (5a)$$

$$\sum_{k=1}^6 A_{ik} A_{jk} = \delta_{ij} \quad i, j = 1, 2, \dots, 6 \text{ (sum over modes)}. \quad (5b)$$

The secular determinant of the homogeneous system, Eq. (4), can be factored as follows:

$$\Delta(\lambda) = (k - \lambda)^2 \begin{vmatrix} k_2 - \lambda & k_3 \\ k_3 & k_2 - \lambda \end{vmatrix} \cdot \begin{vmatrix} k_4 - \lambda & k_5 \\ k_5 & k_4 - \lambda \end{vmatrix},$$

and its roots are obviously

$$\begin{aligned} \lambda_1 &= \lambda_2 = k_1 = k_a \text{ (degenerate mode)}, \\ \lambda_3 &= k_2 + k_3 = 2k_b, \\ \lambda_4 &= k_2 - k_3 = 2k_c, \\ \lambda_5 &= k_4 + k_5 = 2k_d, \\ \lambda_6 &= k_4 - k_5 = 2k_c. \end{aligned} \quad (7)$$

For the amplitudes it is found that

$$\begin{aligned} A_{11} &= A_{22} = 1, \\ A_{33} &= A_{43} = A_{34} = -A_{44} = A_{55} = A_{65} = \sqrt{1/2}. \end{aligned} \quad (8)$$

All the remaining A_{ij} are 0.

Considering only the incoherent scattering by hydrogen, the differential cross section is given by

$$\frac{d\sigma}{d\Omega d\epsilon} = \frac{a_{\text{inc}}^2}{2\pi} \int e^{-i\epsilon t} [x_1(\vec{\kappa}, t) + x_2(\vec{\kappa}, t)] dt, \quad (9)$$

where $\epsilon = E_0 - E$ (energy exchange) and $\vec{\kappa} = \vec{k}_0 - \vec{k}$ (momentum exchange),

and

$$x_1(\vec{\kappa}, t) = \exp \left[\frac{1}{2m} \sum_{k=1}^6 (\kappa_{x1} A_{1k} + \kappa_{y1} A_{3k} + \kappa_{z1} A_{5k})^2 f_k \right], \quad (10)$$

$$x_2(\vec{\kappa}, t) = \exp \left[\frac{1}{2m} \sum_{k=1}^6 (\kappa_{x2} A_{2k} + \kappa_{y2} A_{4k} + \kappa_{z2} A_{6k})^2 f_k \right]. \quad (11)$$

Here, κ_{xi} , κ_{yi} , and κ_{zi} are the components of $\vec{\kappa}$ along the coordinate axis of Fig. 2.31,

$$f_k = \frac{1}{w_k} [(n_k + 1) (e^{i w_k t} - 1) + n_k (e^{-i w_k t} - 1)], \quad (12)$$

with

$$n_k = \left(\exp \frac{w_k}{T} - 1 \right)^{-1},$$

$$w_k^2 = \frac{2}{m} \lambda_k.$$

Introducing the values found for A_{ik} ,

$$x_i(\vec{\kappa}, t) = \exp \left\{ \frac{1}{2m} \left[\kappa_{xi}^2 f_1 + \frac{1}{2} \kappa_{yi}^2 (f_3 + f_4) + \frac{1}{2} \kappa_{zi}^2 (f_5 + f_6) \right] \right\}. \quad (13)$$

This expression must now be averaged over all orientations of κ . This can obviously be done independently for x_1 and x_2 and the average is the same for both terms. Hence, in the following it is unnecessary to distinguish between them. For small values of κ^2 it is sufficient to average in the exponent. Hence,

$$x(\kappa^2, t) = \exp \left\{ \frac{\kappa^2}{2m} \left[\frac{1}{3} f_1 + \frac{1}{6} (f_3 + f_4) + \frac{1}{6} (f_5 + f_6) \right] \right\} \quad (14)$$

for

$$\frac{\kappa^2}{2m w_k} \ll 1.$$

This corresponds to five isotropic oscillators with mass $3m$ for w_1 and $6m$ for the other frequencies. For the real water molecule, the square of the amplitudes A_{ik} must be slightly smaller in order to take care of the motion of the oxygen atom and still satisfy the first normalization condition implied by Eq. (5a):

$$\sum_i A_{ik}^2 = 1 \quad k = 1, 2, \dots, 6 . \quad (15)$$

Of course, now there are three additional modes to be considered, which make up for the difference in the second normalization condition,

$$\sum_k A_{ik}^2 = 1 . \quad (16)$$

For instance, if we consider the extreme case of free translations of the whole molecule, the χ -function should be multiplied by a factor

$$x_{tr} = \exp \left[\frac{\kappa^2}{36m} (it - Tt^2) \right] . \quad (17)$$

Now the masses of the equivalent isotropic oscillators would have to satisfy the condition

$$\frac{1}{18} + \sum_{i=1}^6 \frac{1}{M_i} = 1 , \quad (18)$$

and since these masses should not be smaller than those for the infinitely heavy molecule (because otherwise the square amplitudes would have to be greater), it is found that

$$6 \leq M_i \leq 9 . \quad (19)$$

Furthermore, assuming that only the torsional modes have non-zero oxygen amplitudes leads to the following mass distribution:

Translation	18
3 torsional modes ($\lambda_4, \lambda_5, \lambda_6$)	2.25
Lower vibrational mode (λ_3)	6
2 higher vibrational modes (λ_1, λ_2)	3

It is clear from Eq. (19) that 6 is an absolute minimum of the mass which can be associated with a single frequency. This is important since models with masses smaller than 6 have been proposed.

Now, coming back to our simplified model, if κ^2 is not small the correct average must be obtained by

$$x_{av}(\kappa^2, t) = \left\langle \exp \left\{ \frac{\kappa^2}{2m} \left[f_1 \cos^2 \theta + \frac{f_3 + f_4}{2} \cos^2 \theta + \frac{f_5 + f_6}{2} \cos^2 \Psi \right] \right\} \right\rangle , \quad (20)$$

with

$$\cos \theta = \frac{\kappa_x}{\kappa}, \quad \cos \phi = \frac{\kappa_y}{\kappa}, \quad \cos \Psi = \frac{\kappa_z}{\kappa} .$$

Using Eq. (20), the full anisotropy of the normal modes would be retained but the numerical calculations become too cumbersome. A reasonable approximation for taking into account the anisotropy in Eq. (20) is to replace $\cos^2 \phi$ and $\cos^2 \Psi$ by $(1 - \cos^2 \theta)/2$.

This is equivalent to assuming that the two-dimensional oscillation of the proton in the bending and torsional modes is isotropic in the plane perpendicular to the O-H bond, which would be exact if the corresponding frequencies were all the same. The one-dimensional vibrations of the stretching modes are treated exactly. Making now the assumptions that the translations of the whole molecule are free, that the torsional frequencies are all the same, and that the small change of the amplitudes A_{ij} , due to the finite mass of the oxygen, only affects the rotational modes, the χ function becomes

$$\chi(\kappa^2, t) = \frac{1}{2} \exp\left[\frac{\kappa^2}{36m}(it + Tt^2)\right] \int_{-1}^1 d\mu \exp\left\{\frac{\kappa^2}{2m}\left[f_s \mu^2 + \left(\frac{f_b}{4} + \frac{f_r}{1.5}\right)(1 - \mu^2)\right]\right\}, \quad (21)$$

where the subscripts s, b, and r stand for stretching, bending, and rotating modes, respectively. For small values of κ^2 , this result reduces essentially to the expression given by Nelkin.

The double differential cross section obtained with Eq. (21) shows important deviation from the isotropic calculations, especially for energy exchanges above the 0.48-ev threshold of the stretching vibration. As an example, in Fig. 2.33 the two models are compared for an initial energy of 1 ev and a scattering angle of 32° . The influence of anisotropy is not averaged out by summing over angles, as becomes apparent from Figs. 2.34 and 2.35, in which the two P_0 and P_1 energy transfer kernels are compared for an initial energy of 0.65 ev. But the difference in total cross section never exceeds a couple of percent, and in this context the agreement of both models with experiment is satisfactory. This can be seen in Fig. 2.36, where the points above 0.1 ev were measured by Russell (Section 2.4) and the lower-energy points were taken from BNL-325.⁽¹⁸⁾ All cross sections are referred to 1 hydrogen atom and only include scattering by

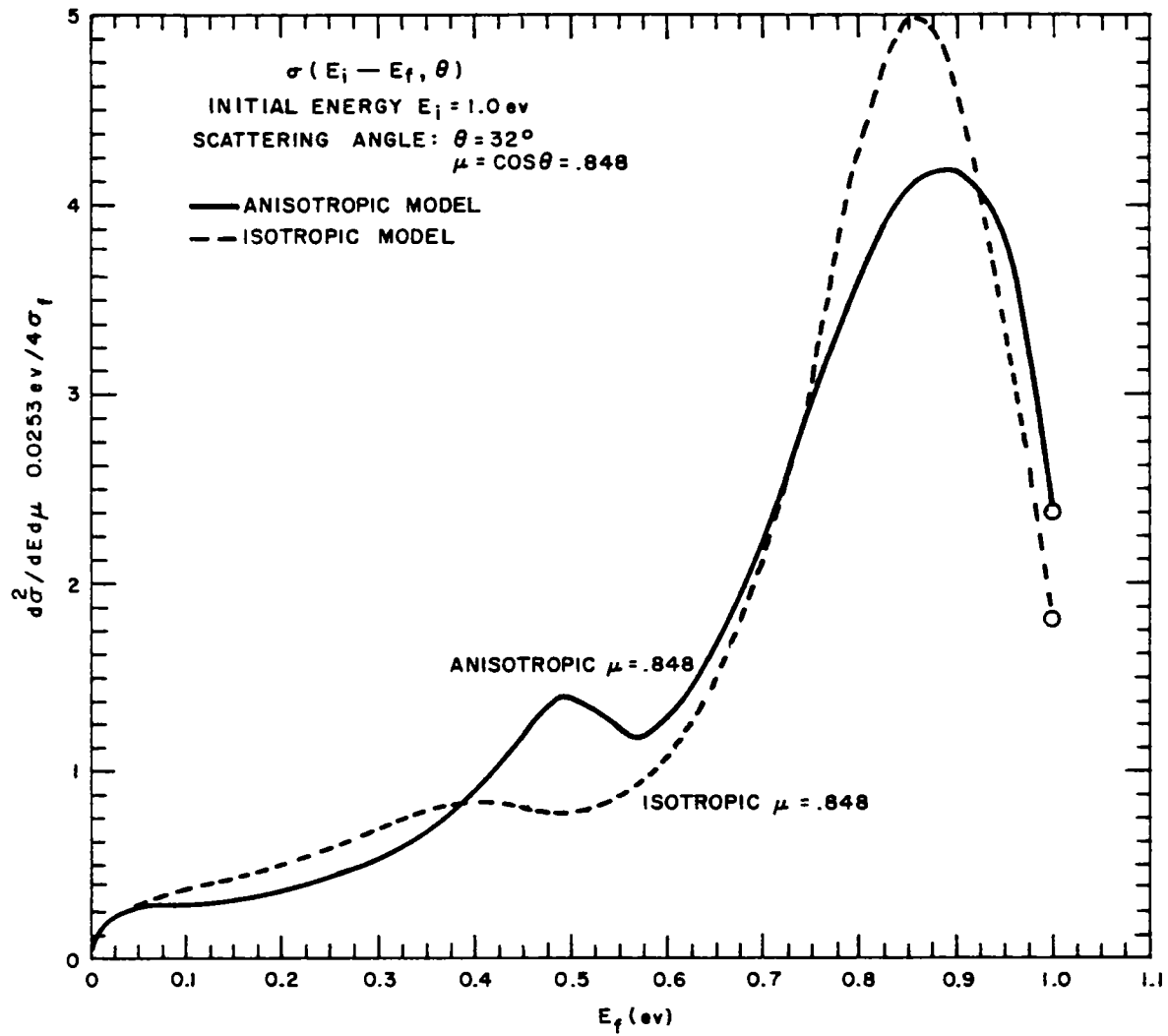


Fig. 2.33--Theoretical differential cross section of water as a function of scattered neutron energy

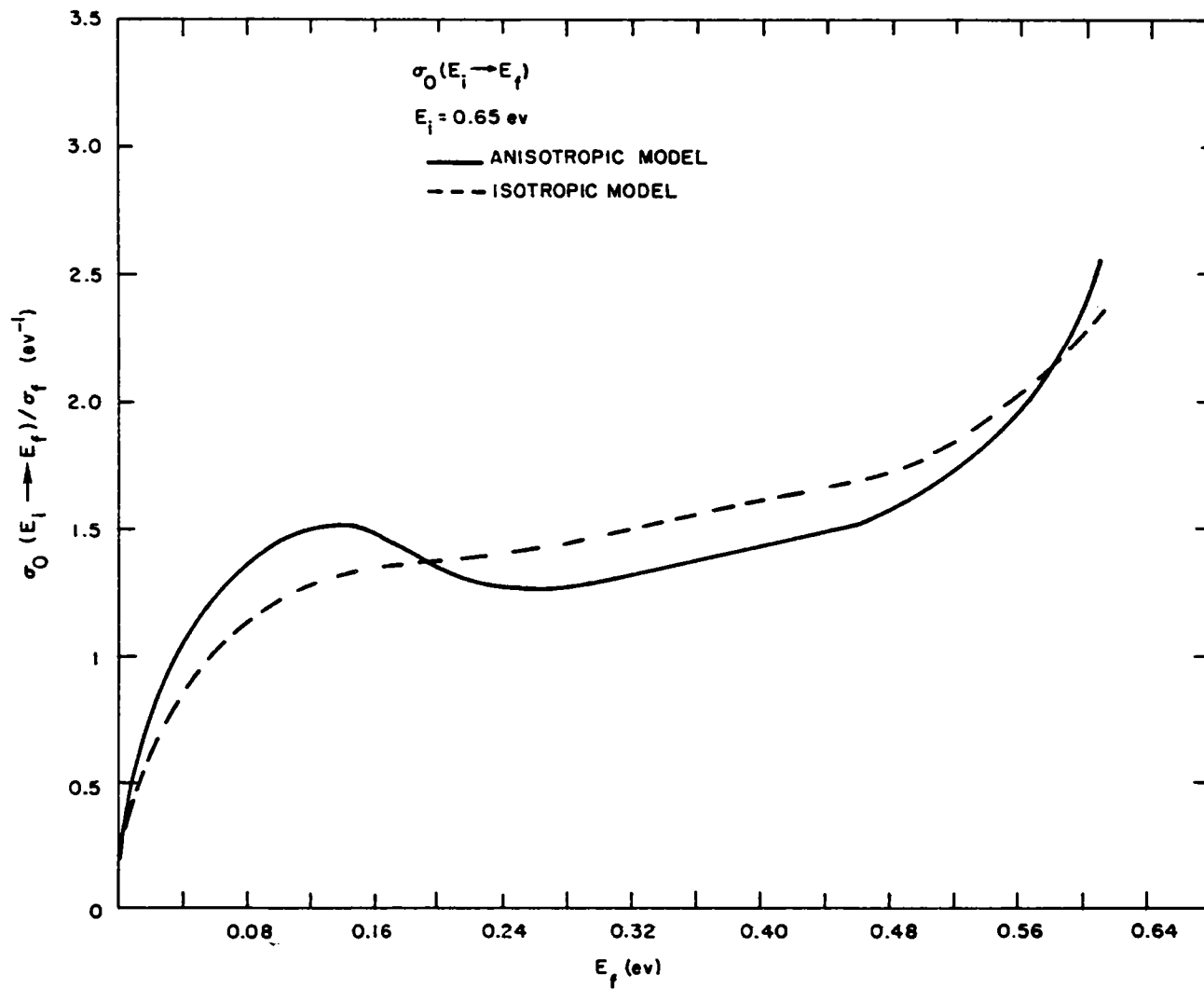


Fig. 2.34--Theoretical variation of the normalized P_0 differential scattering cross section of water with scattered neutron energy

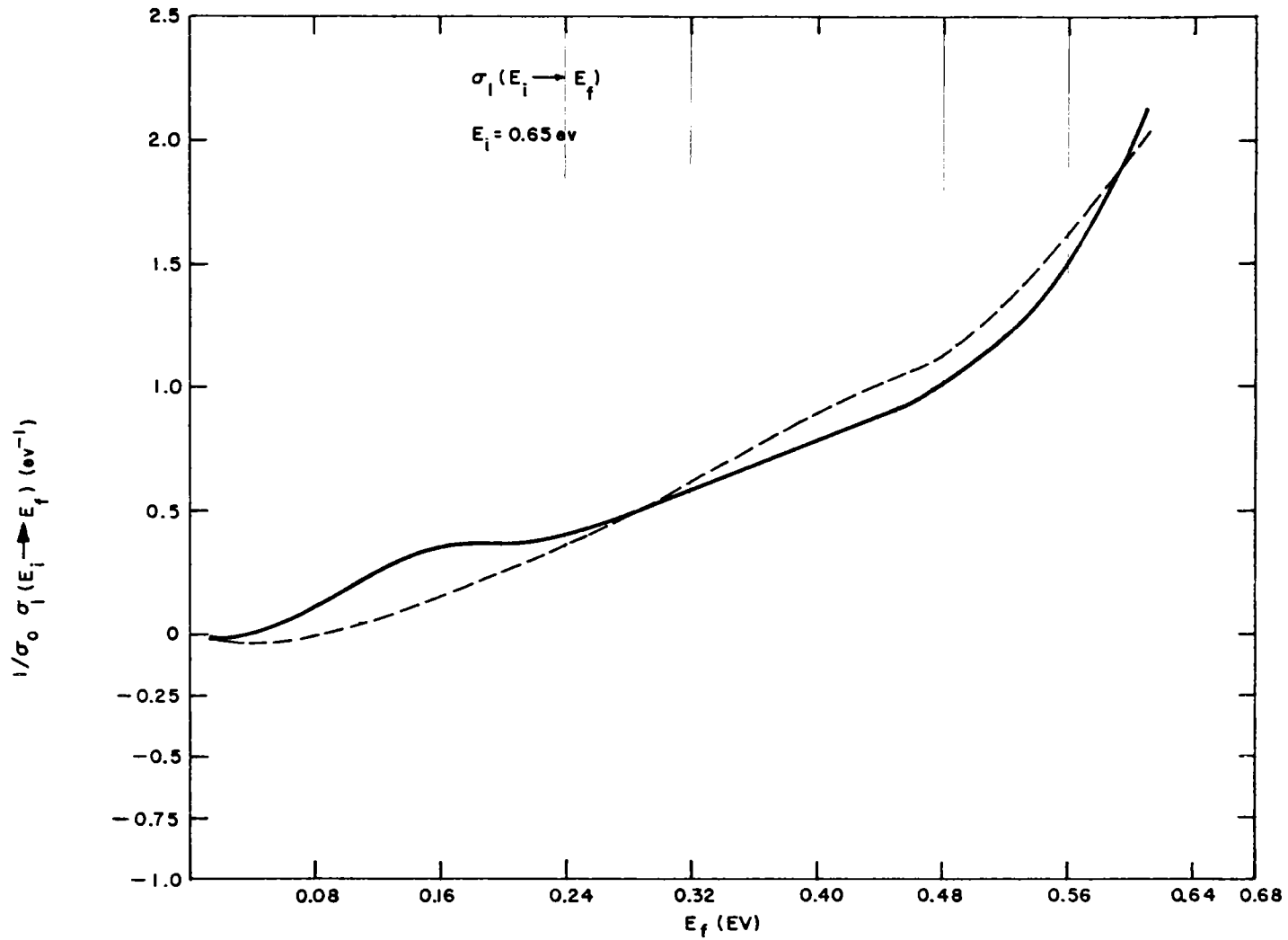


Fig. 2.35--Theoretical variation of the normalized P_1 differential scattering cross section of water with scattered neutron energy

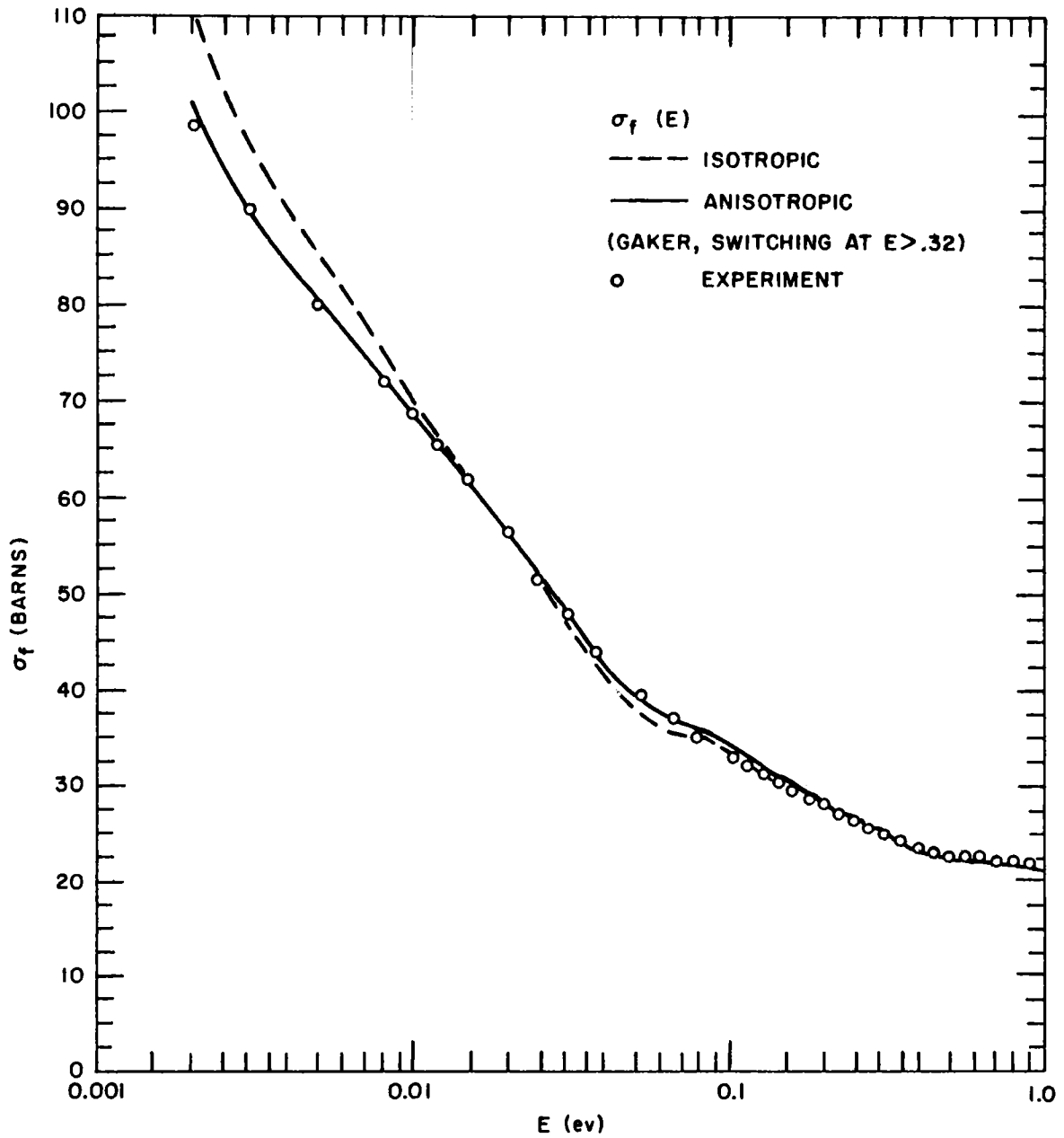


Fig. 2.36--Variation of the free-atom scattering cross section of water with incident neutron energy

hydrogen.* The transport cross sections are compared in Fig. 2.37. It is also interesting to compare magnitudes averaged over a Maxwellian neutron spectrum. These magnitudes are relevant for the die-away experiments and the approach to thermal equilibrium between neutrons and moderator. Table 2.2 is a comparison of the average total scattering cross section, $\bar{\sigma}_{s0}$, the average diffusion coefficient, \bar{Dv} , and the quantity usually denoted by M_2 ,

$$M_2 = \frac{1}{\sigma_b T^4} \iint dE dE' (E - E')^2 e^{-E/kT} E \sigma(E \rightarrow E') .$$

Table 2.2

COMPARISON OF PARAMETERS FROM THEORETICAL SPECTRA
PERTAINING TO THE ISOTROPIC AND ANISOTROPIC MODELS
FOR THE WATER MOLECULE

Model	$\bar{\sigma}_{s0}$ (barns)	\bar{Dv} ($\text{cm}^2 \text{sec}^{-1}$)	M_2
Isotropic	46.00	37,906	1.105
Anisotropic	46.05	36,532	1.040

Again, it is seen that the scattering cross section is very insensitive to the anisotropy, whereas the diffusion coefficient is changed by nearly 4%, coming closer to the Brookhaven⁽¹⁹⁾ experimental value of $\bar{Dv} = 35,850 \text{ cm}^2 \text{sec}^{-1}$. The 6% decrease in M_2 shows that the mean square energy exchange between moderator and thermal spectrum is overestimated in the isotropic model. This result is confirmed by the comparisons in Figs. 2.38 and 2.39 of infinite-medium spectra (with high-energy source leading to a $1/E$ asymptotic spectrum) in highly concentrated solutions of boric acid. The anisotropic kernel gives a somewhat harder spectrum, reducing the roughly 10% discrepancy between experiment and isotropic calculations. Similar comparisons are made in Figs. 2.40 and 2.41 for spectra in highly concentrated solutions of cadmium sulfate.

In summary, the refinement of introducing the anisotropy of the molecular vibration into Nelkin's model changes the calculated thermal

*The extremely good agreement between the anisotropic model and the experimental scattering cross section below 0.01 eV is not believed to be too meaningful, since the physical assumptions of the model break down at low energy. Also, the accuracy of the numerical integration is in doubt in this energy region.

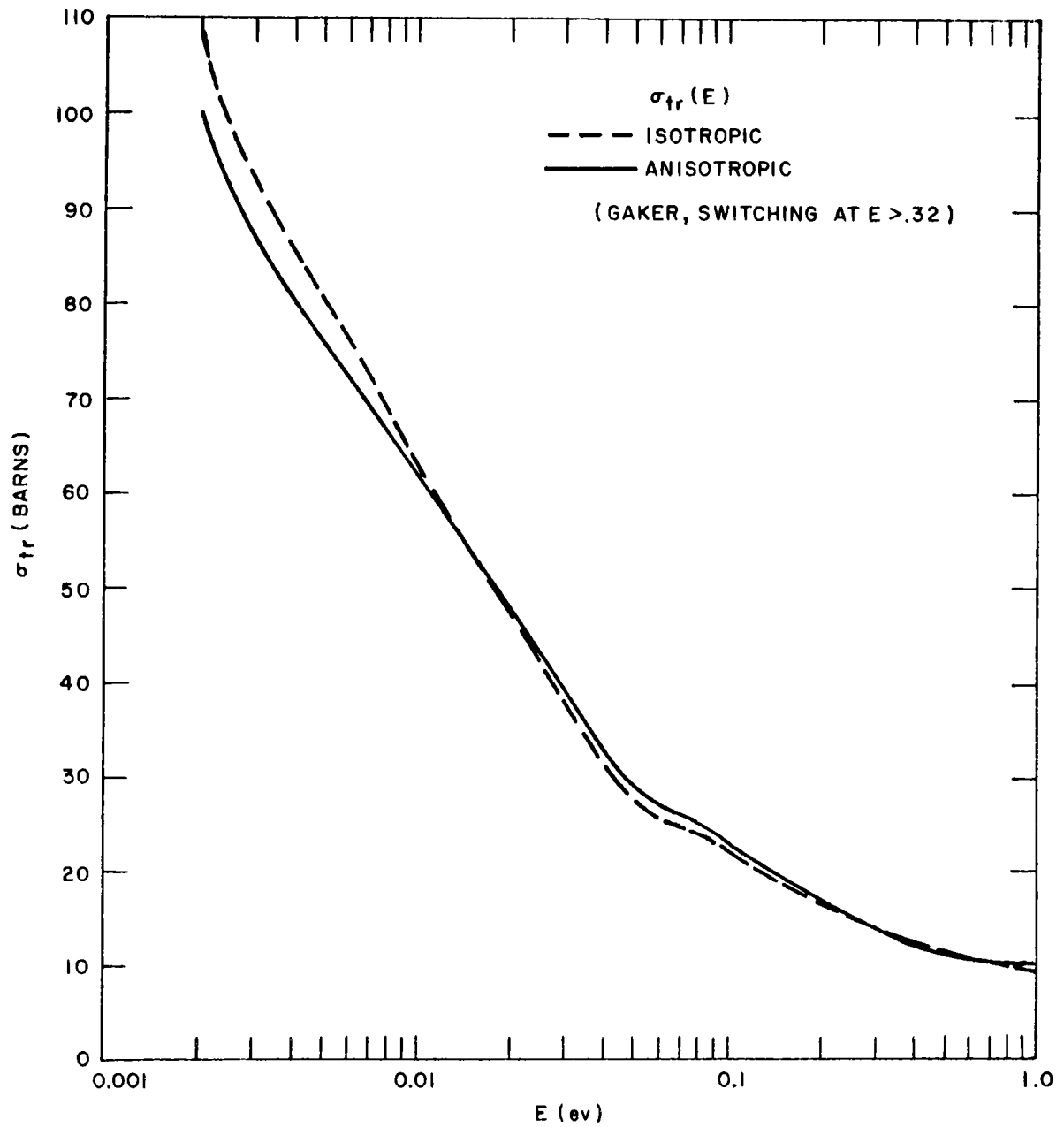


Fig. 2.37--Theoretical variation of σ_{tr} with incident neutron energy

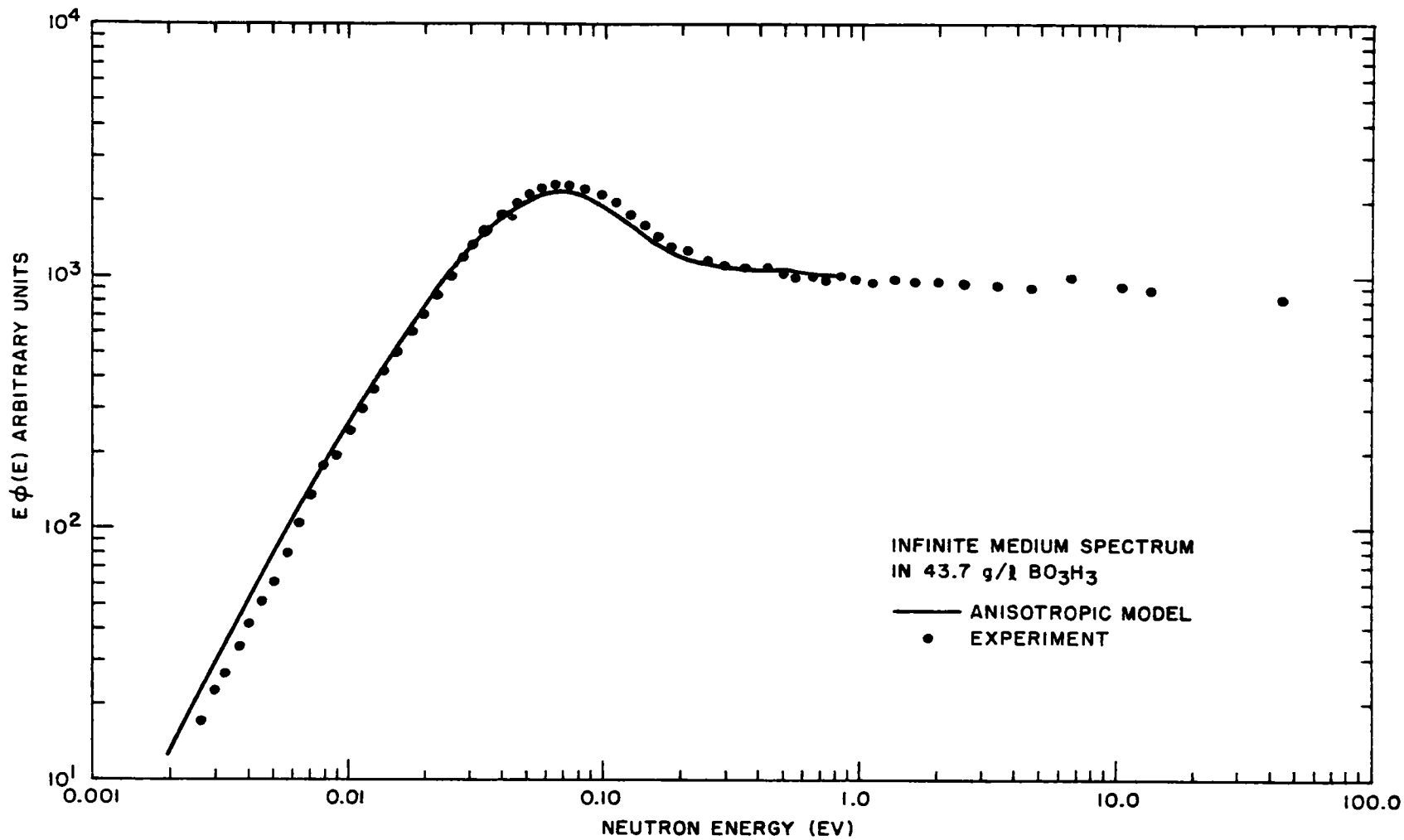


Fig. 2.38--Comparison of experimental and theoretical spectra (anisotropic model) in borated water

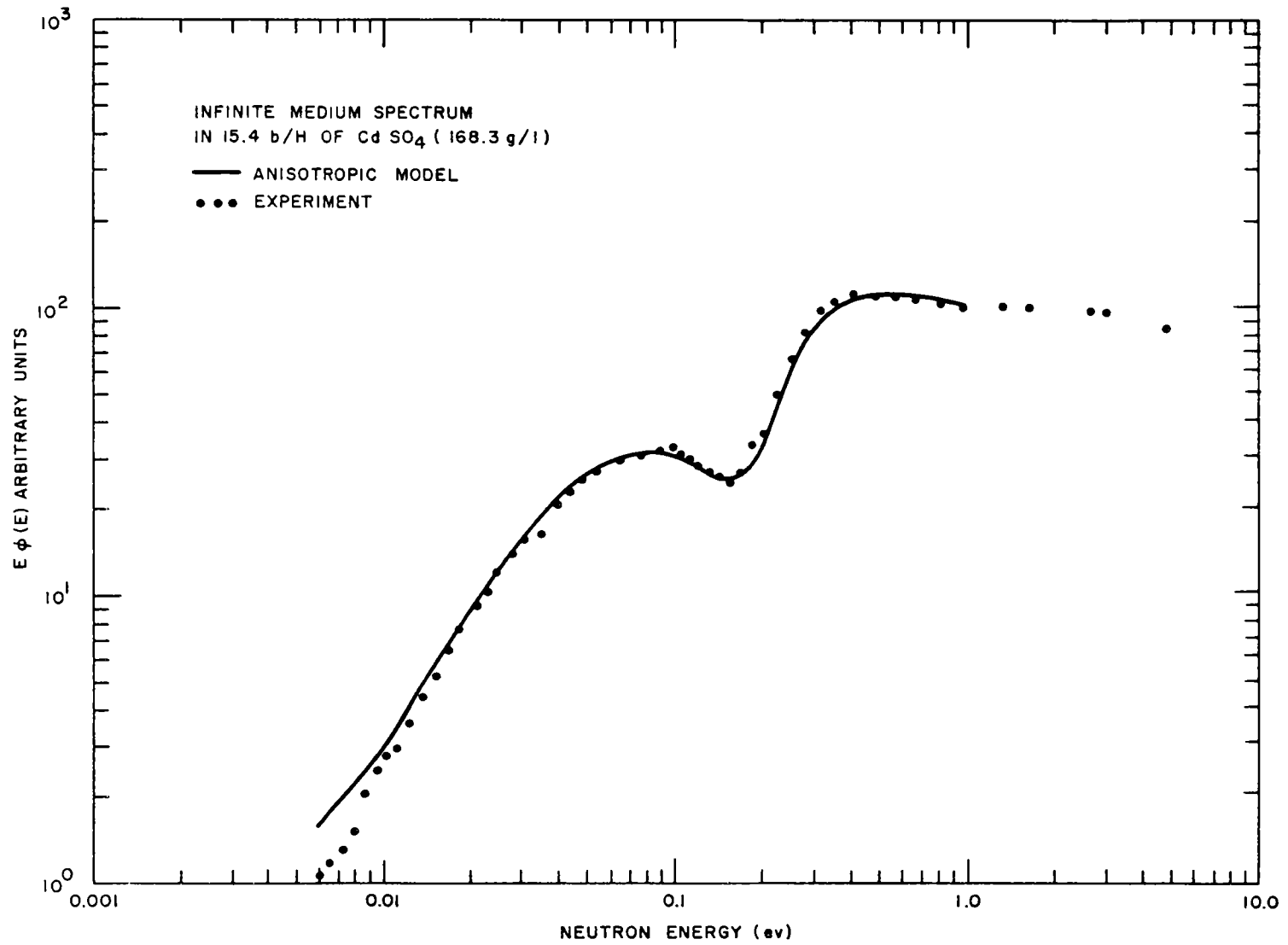


Fig. 2. 40--Comparison of experimental and theoretical spectra (anisotropic model) in cadmium sulphate solution

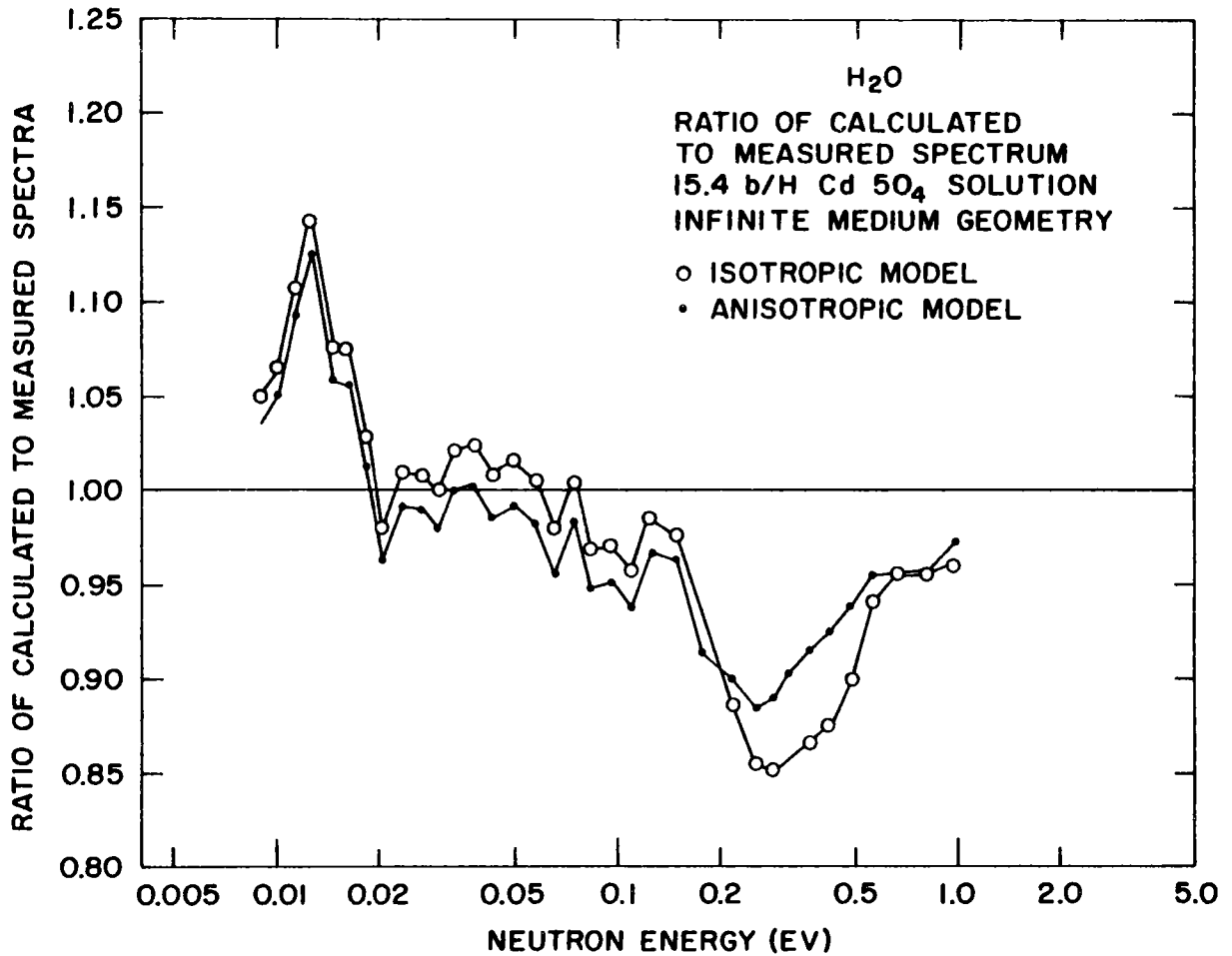


Fig. 2.41--Comparison of fluxes calculated for the isotropic and anisotropic models for water with cadmium sulphate poisoning

infinite-medium spectra in heavily poisoned water by roughly 5% to 7%, and it seems that this correction is always in the right direction to bring theory in better agreement with experiment.

2. 7. MODIFICATIONS OF THE CODE GAKER

In order to calculate the refined scattering kernel for H₂O referred to in the previous section, an extra loop was built into the code GAKER, (12) which performs the average over molecular orientations.

Another modification of GAKER under study is a more accurate integration over angles for the calculation of the P_n(E → E') matrices. In fact, the 0 phonon term of the Nelkin-model double differential cross section for H₂O has a singularity at $\left\{ \frac{\mu}{E} = \frac{1}{E'} \right\}$, which might impair the accuracy of numerical integration over angles. This term has the form

$$F(\alpha) = C \sqrt{\frac{\epsilon'}{\epsilon}} \frac{1}{\sqrt{\alpha}} e^{-a\alpha} I_0(b\alpha) \exp \left[-\frac{1}{4\alpha} (\epsilon' - \epsilon + \alpha)^2 \right], \quad (1)$$

with

$$\alpha = (\epsilon + \epsilon' - 2\mu \sqrt{\epsilon\epsilon'}) \frac{m}{M}; \quad \epsilon = \frac{E}{kT}; \quad \epsilon' = \frac{E'}{kT}.$$

The singularity at $\alpha \rightarrow 0$ (i. e., at $\mu \rightarrow 1$, $\epsilon' \rightarrow \epsilon$) is thus described by

$$f(\alpha) = \frac{1}{\sqrt{\alpha}} \exp \left[-\frac{1}{4\alpha} (\epsilon' - \epsilon + \alpha)^2 - a\alpha \right], \quad (2)$$

which can be integrated analytically to give

$$\int_{-1}^1 f[\alpha(\mu)] d\mu = 4 \frac{M}{m} \frac{1}{\sqrt{\epsilon\epsilon'}} \int_{-y_{\min}}^{y_{\max}} dy \exp \left[-\frac{1}{4} \left(y + \frac{\gamma}{y} \right)^2 - ay^2 \right], \quad (3)$$

with $y = \sqrt{\alpha}$ and $\gamma = \epsilon' - \epsilon$. It is found that

$$\begin{aligned} \int_{-1}^1 f(\alpha) d\mu &= \frac{C'}{\sqrt{\eta\epsilon\epsilon'}} \exp \left[\gamma \left(\sqrt{\eta} - \frac{1}{2} \right) \right] \frac{\sqrt{\pi}}{2} [\operatorname{erf}(z_{\max}) - \operatorname{erf}(z_{\min})] \\ &+ \frac{C'}{\sqrt{\eta\epsilon\epsilon'}} \exp \left[-\gamma \left(\sqrt{\eta} + \frac{1}{2} \right) \right] \frac{\sqrt{\pi}}{2} [\operatorname{erf}(x_{\max}) - \operatorname{erf}(x_{\min})], \quad (4) \end{aligned}$$

where

$$\eta = a + \frac{1}{4}; \quad C' = 2 \frac{M}{m}; \quad y_{\min}^{\max} = |\sqrt{\epsilon'} \pm \sqrt{\epsilon}|$$

and

$$z = y \sqrt{\eta} + \frac{\gamma}{2y},$$

$$x = y \sqrt{\eta} - \frac{\gamma}{2y}.$$

Hence, in order to integrate numerically over the singularity, we write

$$F(\alpha) = C \sqrt{\frac{\epsilon'}{\epsilon}} \left\{ \frac{e^{-a\alpha}}{\sqrt{\alpha}} [I_0(b\alpha) - 1] \exp - \left[\frac{1}{4\alpha} (\epsilon' - \epsilon + \alpha)^2 \right] + f(\alpha) \right\}. \quad (5)$$

The first term in the bracket will be regular at $\alpha \rightarrow 0$, and the integral over the second is given by the preceding formulae.

III. NEUTRON THERMALIZATION IN D₂O

Early in 1962, an experiment to measure the thermalized neutron spectrum in D₂O was begun at General Atomic, with measurements being performed with the D₂O poisoned by a uniformly distributed 1/v absorber (boron). The geometry of that experiment is shown in Fig. 3.1. However, our attempts to understand this spectrum using realistic molecular models for D₂O (Honeck⁽²⁰⁾ and Brown and St. John⁽²¹⁾) did not meet with success. Instead, the measured spectra were consistently softer (more thermal) than the calculated spectra and in fact were in reasonably good agreement with the free-gas predictions for D₂O. It was decided that possibly these experimental D₂O spectra were perturbed by source placement, as we had observed for light water. Namely, in the case of water the angular distribution of the distributed epithermal source was severely perturbed by the external source location. In fact, as was pointed out in Section II, this perturbation was so large that it was difficult to make an approximate correction for it, and the best plan was to rearrange the experiment to minimize the memory of the fast source.

Obviously, then, our next step was to reorient the source in the cleaner geometry shown in Fig. 3.2. The poisoning of the medium was again accomplished with boron-aluminum shim plates spaced either 1/8 in. or 1/4 in. apart. Spectra were measured at two distances, 6 and 12 in. from the distributed neutron source. The new series of measurements was conducted in the routine manner, using the 16-meter flight path and standard time-of-flight procedures.

In comparing the spectra measured in poisoned D₂O with theory, it is extremely important, owing to the small slowing-down power of D₂O ($\xi\Sigma_s$), to include in the analysis absolutely all materials present in the vessel. The atom densities of materials present are given in Table 3.1 for the three separate experiments. The old spectral experiment of 1962 performed in the geometry of Fig. 3.1 is also included for completeness.

For the calculation of the spectra in deuterium systems, one must undertake the solution of the space-energy problem. Diffusion of neutrons plays a role in establishing the spectrum, so if the external source does not induce a normal-mode distribution, appropriate corrections are necessary. The special flux plots associated with the epithermal source description for the old spectral data are given in Ref. 2, and source flux distributions for the geometry of Fig. 3.2 are given in Figs. 3.3, 3.4,

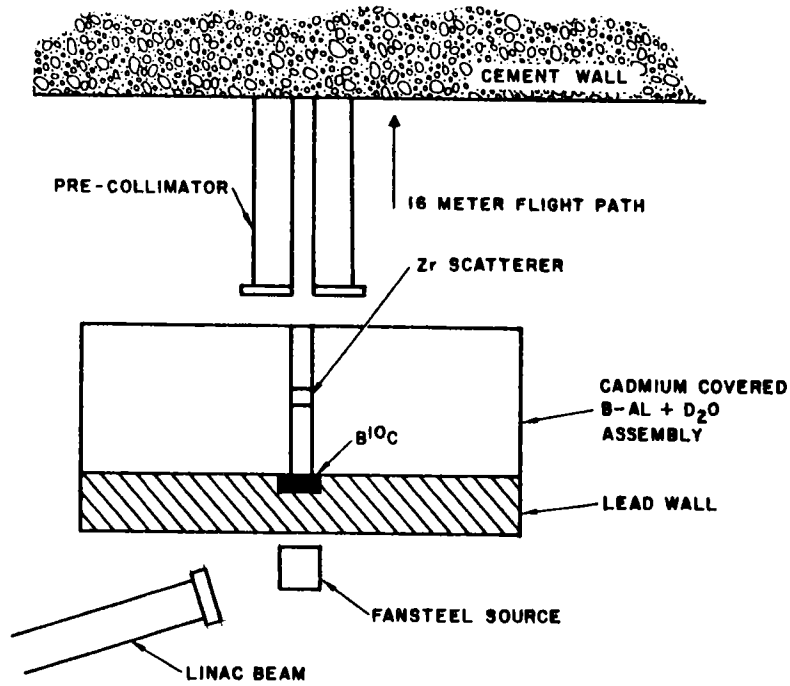


Fig. 3.1--First geometry for the poisoned D_2O spectral studies

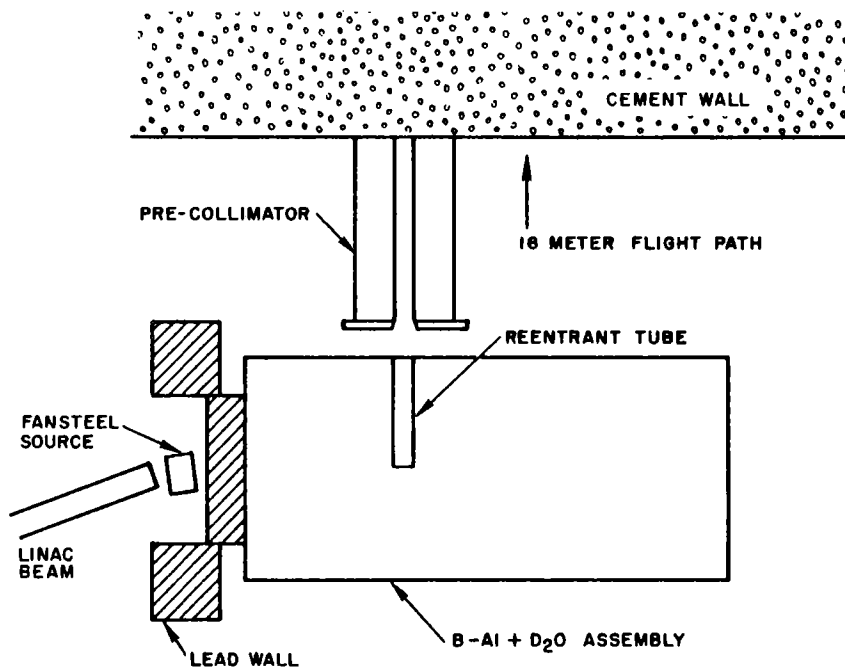


Fig. 3.2--Second geometry for the poisoned D_2O spectral studies

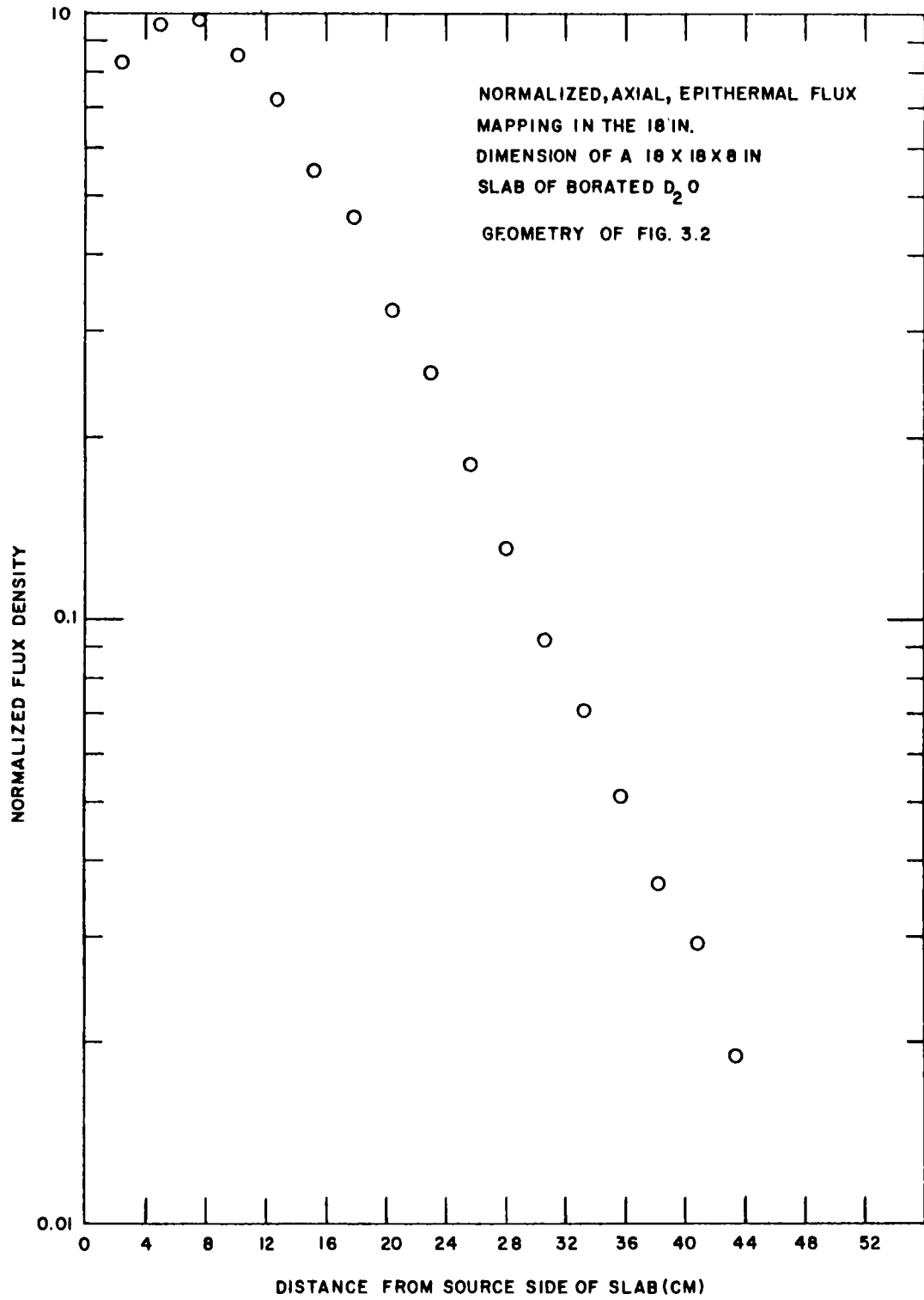


Fig. 3.3--Axial epithermal flux mapping in borated D_2O

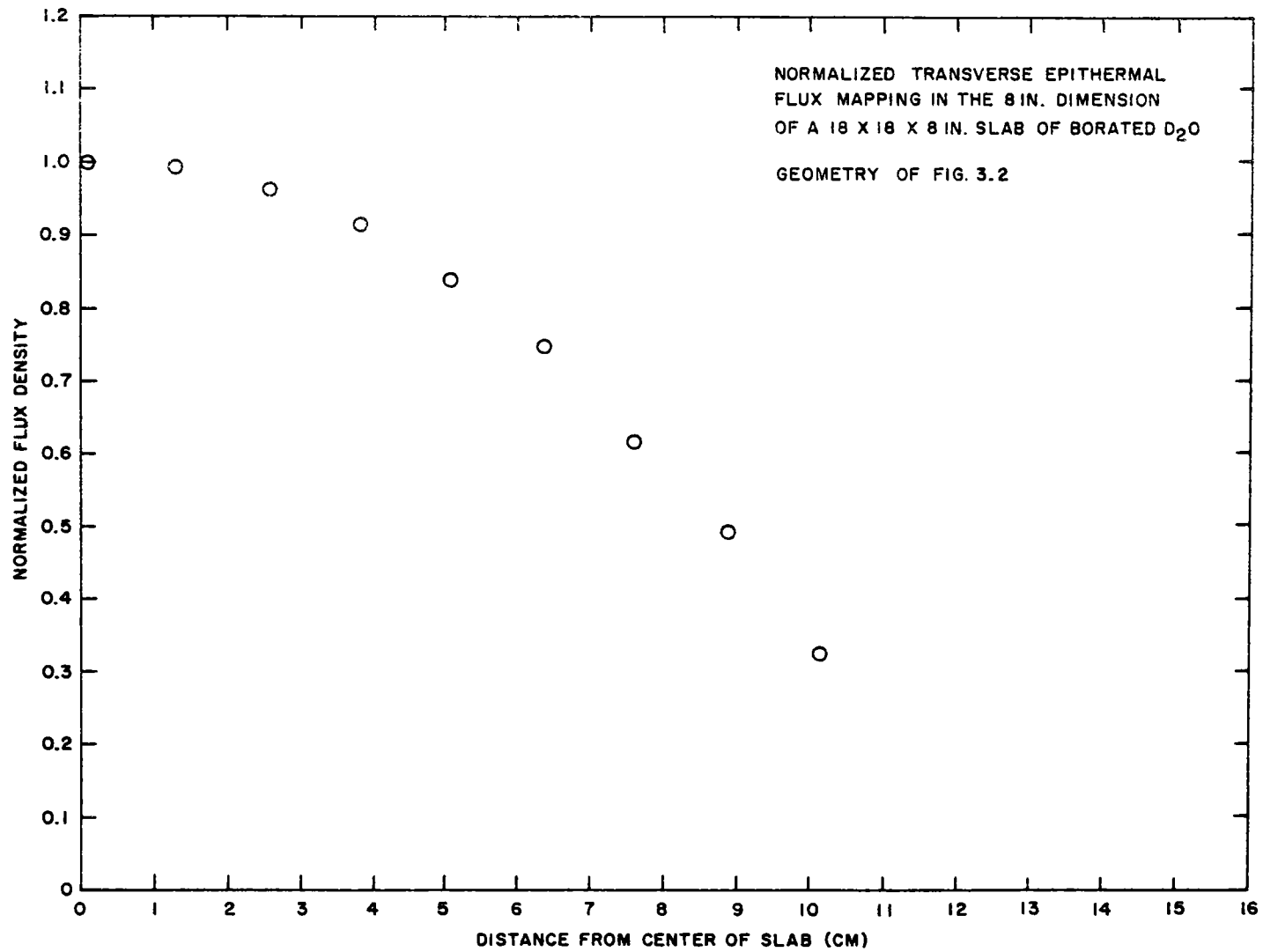


Fig. 3.4--Transverse (8-in.-dimension) epithermal flux mapping in borated D_2O

and 3.5. From the spatial flux studies, we have attained nearly a normal-mode distribution in two dimensions and an age-type distribution in the other dimension. Endeavoring to understand the measured spectra on a simple diffusion-theory basis, by introducing for example a DB^2 correction into the diffusion equation, does not result in success. For example, at 12 in. from the source the net buckling present is nearly zero, so one might naively expect the spectrum to be of the infinite-medium variety. However, the spectrum is softer by some 30% at low energies than an infinite-medium spectrum. These spectra are then of the class discussed extensively by Parks, (22) where the key quantity L^2/τ is not small, L^2 being the diffusion length and τ the age. One finds here that this quantity is about 0.20.

Table 3.1
 ATOM DENSITIES FOR D₂O MEASUREMENTS
 (In 10^{-24} atoms/cm³)

	Previous Measurement, 1/8-in. Spacing	New Measurements	
		1/8-in. Spacing	1/4-in. Spacing
N _{deuterium}	0.05348	0.05348	0.05775
N _{oxygen}	0.02764	0.02731	0.02948
N _{aluminum}	0.00832	0.00832	0.00415
N _{boron}	0.0001556	0.0001556	0.00007779
N _{hydrogen}	0.004561	0.002427	0.002427
N _{carbon}	0.001517	0.001517	0.001517

Rather than utilizing the analytical procedures introduced by Parks to solve this space-dependent problem, the spectra were all calculated numerically using the transport-theory code GAPLSN (a P_n speeded-up version of DSN). A P_1 (diffusion-theory) epithermal source was used in the calculations, and source contributions for all the constituents present were included. The one-dimensional axis for the transport problem was oriented along the line from the target through the end of the re-entrant tube for both geometries. The effect of the transverse dimensions was included by means of DB^2 corrections, since the fluxes in these dimensions corresponded closely to the normal mode. A spatial mesh of 50 regions and a 23-region energy mesh were used.

In the calculations performed so far, which are compared with the experimental data in Figs. 3.6, 3.7, and 3.8, the spectra are based only

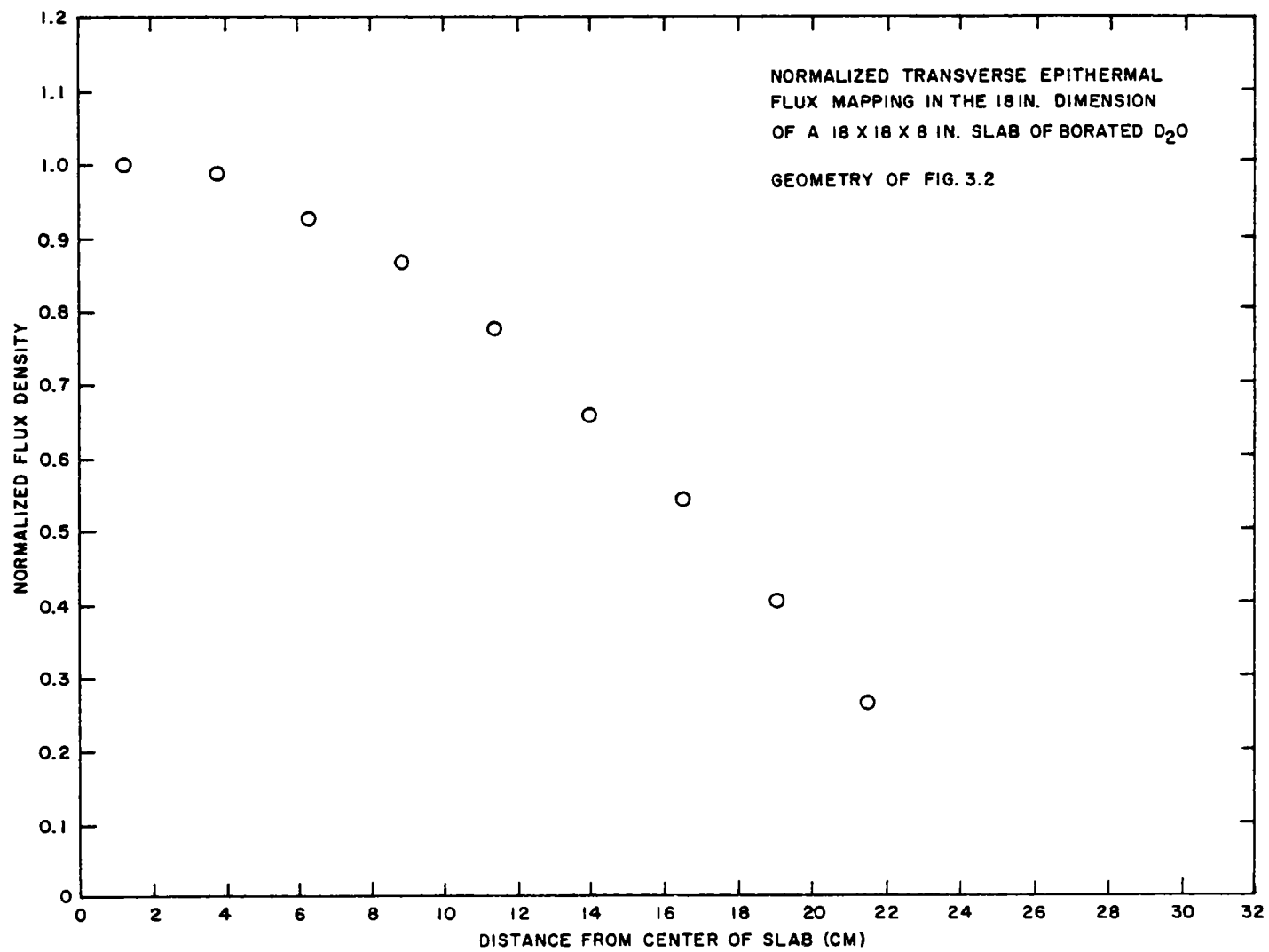


Fig. 3.5--Transverse (18-in.-dimension) epithermal flux mapping in borated D₂O

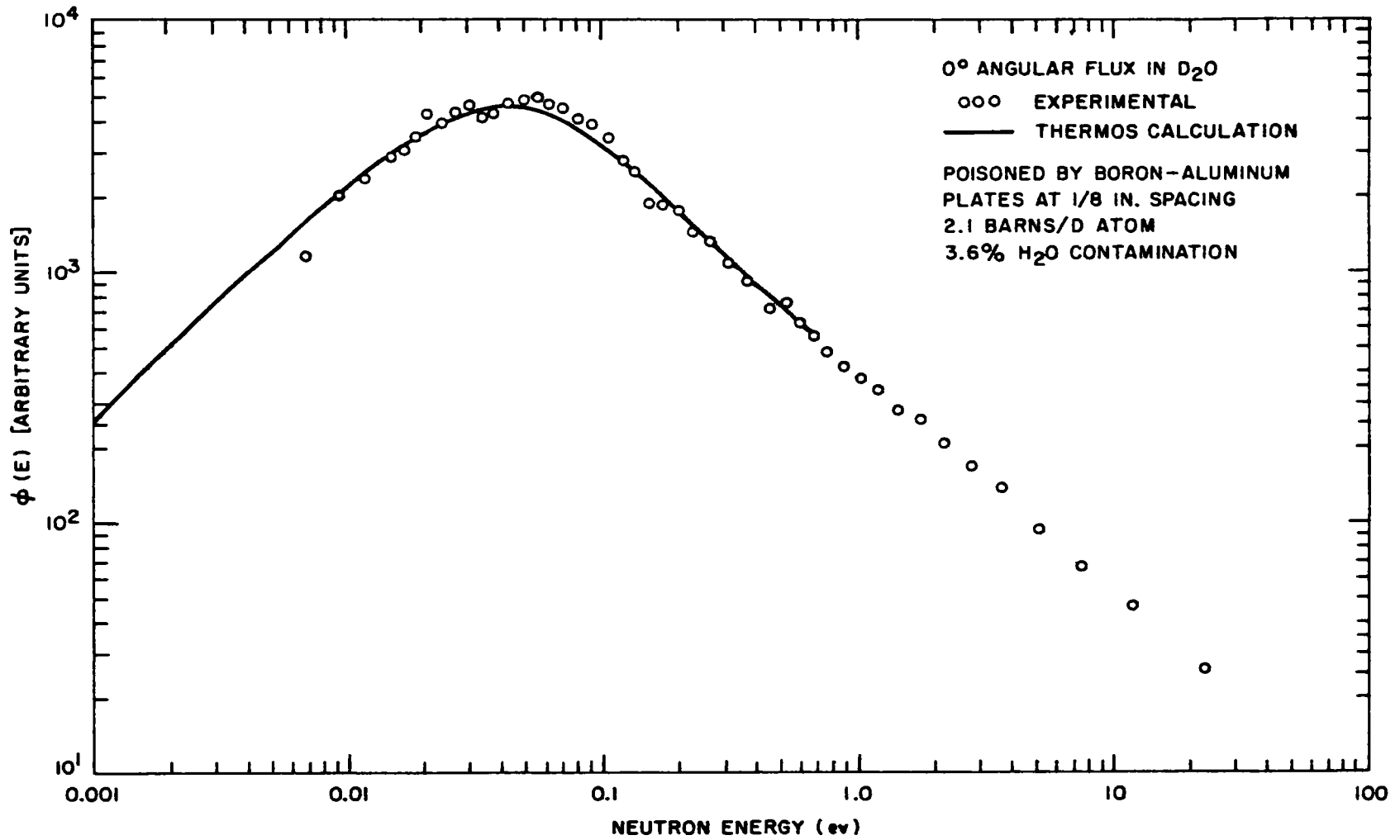


Fig. 3.6-- 0° angular flux in D_2O poisoned to 2.1 barns/D atom

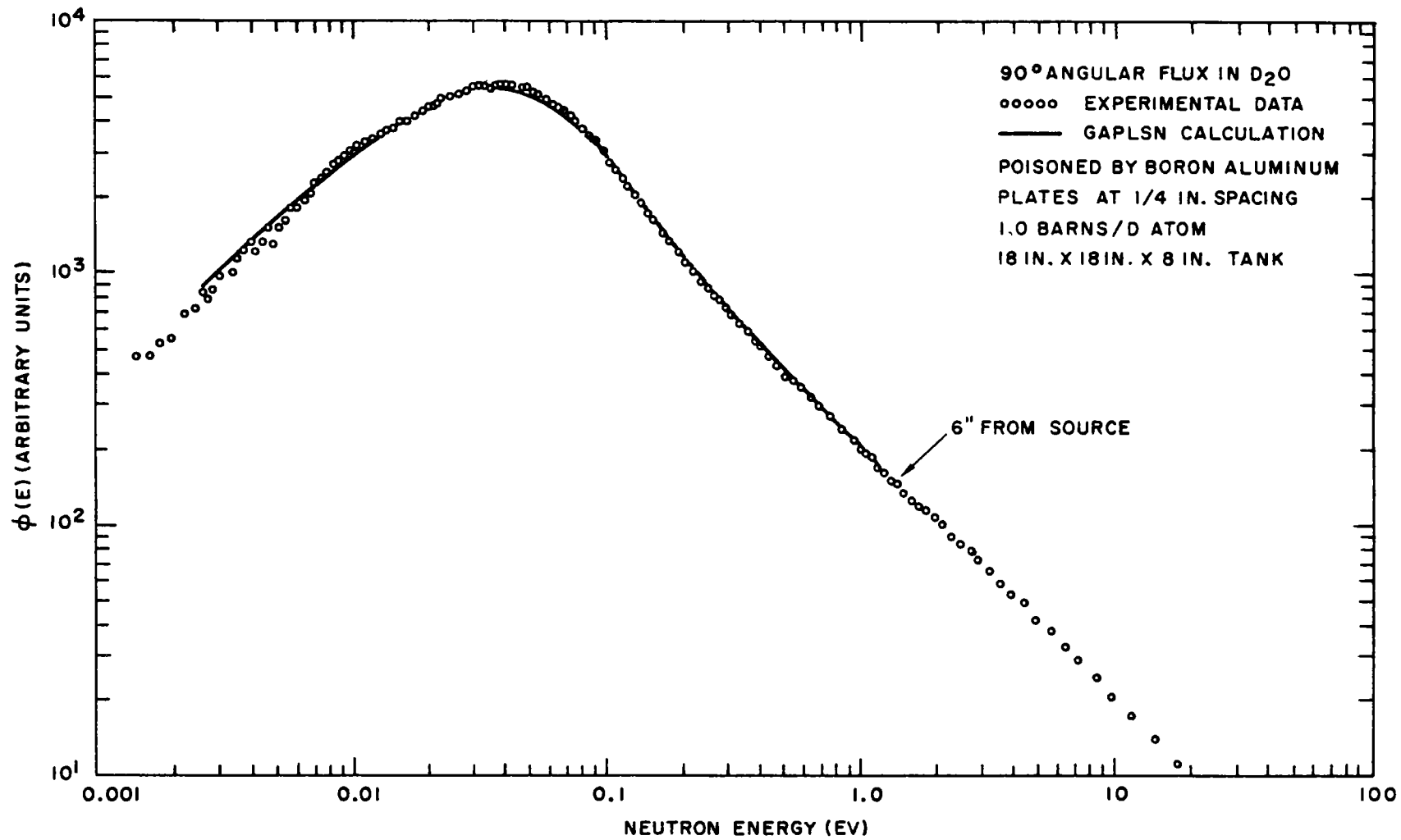


Fig. 3.7--90° angular flux in D₂O poisoned to 2.1 barns/D atom

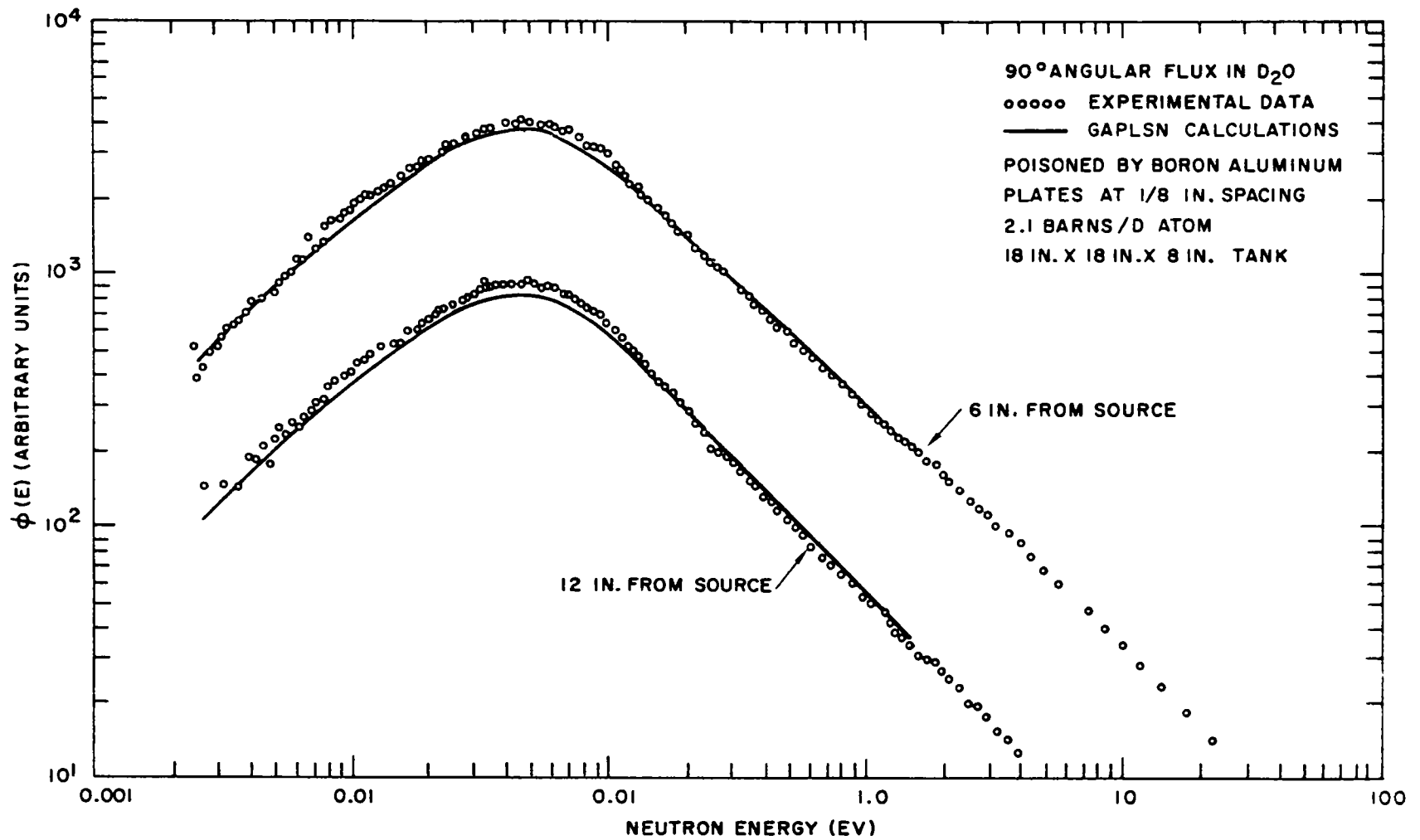


Fig. 3.8--90° angular flux in D₂O poisoned to 2.1 barns/D atom

on the Honeck scattering model. The Brown-St. John and free-gas models will also be included in future comparisons. The scattering model constructed by Honeck includes only the incoherent inelastic-scattering cross section for D₂O. The general formulation is similar to that introduced by Nelkin for light water. The molecular frequency spectrum is described by various vibrational, rotational, and translational degrees of freedom. The vibrational oscillators are chosen at energies of $\omega_{v_1} = 0.15$, $\omega_{v_2} = \omega_{v_3} = 0.35$ eV; a hindered rotation of effective mass $m_r = 4.11$ is assumed at $\omega_r = 0.05$ eV; and free translation is treated exactly.

The calculated results for all three configurations have improved agreement with experiment, which would indicate that the incoherent, discrete-oscillator kernel is giving reasonable results. There is, however, in all the above cases, one non-negligible correction which has been necessary. This is for the light water or plastic present in each geometry. In future experimental checks of D₂O spectra, all light hydrogen will be removed, resonance absorption will be studied, and angular-flux spectra will be extensively investigated to examine the importance of coherent scattering. The plans for the coming year also include the study of $\sigma(E, \mu)$ for D₂O, which should afford an excellent check on the P₁ scattering kernel.

IV. NEUTRON THERMALIZATION IN POLYETHYLENE

Neutron spectral measurements have been performed previously in room-temperature poisoned polyethylene and also liquid-nitrogen-cooled polyethylene. These measurements and some preliminary calculations of spectra have been reported in the two previous annual reports.⁽¹⁾⁽²⁾ In addition, Goldman and Federighi⁽²³⁾ have published this year a complete treatment of the polyethylene thermalization problem, including infinite-medium spectra, total-cross-section determinations, and flux distribution by foil measurements. Our efforts this year have been devoted to the development of a more physically exact scattering kernel than that previously in use. It was hoped that the residual discrepancies between the nuclear data and theory could be resolved with this more exact representation of the molecule.

First, let us review the status of polyethylene. Up to the present time the most appropriate model to use for spectral calculations in polyethylene has been that proposed by Goldman. The molecular frequency spectrum for polyethylene was inferred from the data of Nielsen and Woollett⁽²⁴⁾ on infrared absorption spectra in solid polyethylene. The frequency spectrum used is given in Table 4.1.

The general similarity of this discrete frequency spectrum to that of water suggested that a modified Nelkin model would be adequate for polyethylene. Basically, Goldman considers the dynamical unit of polyethylene to be a freely translating CH_2 molecule with internal stretching and bending vibrations. The rotational degree of freedom is strongly hindered. It has been clear for some time that this model permits reproduction of neutron spectra with a fair degree of precision. In addition, the total cross section may be calculated quite accurately up to about 0.08 eV and above 0.2 eV. However, between these two energies 10% to 15% discrepancies exist. The temperature dependence of the diffusion constant (D) as calculated by this model⁽²⁵⁾ is also not in agreement with the experiments of Esch,⁽²⁶⁾ being somewhat smaller than experiment. It is quite evident, however, that not much can be done within the framework of this simple model to resolve one discrepancy without introducing a new one. This, it will be recalled, is very nearly the same problem we encountered with water, where spectra could not be brought into agreement with theory by adjusting Nelkin-model parameters without upsetting seriously the total-cross-section agreement. We therefore decided to introduce to this problem a new model in which more of the detailed frequency spectrum could be described.

Table 4.1

MOLECULAR FREQUENCY SPECTRUM OF POLYETHYLENE

Vibrational Mode	Frequency (ev)	Neutron Mass/ Effective Mass
Translation	0	0.0714
CH ₂ rocking and wagg and twist	0.089	0.2322
CH ₂ bend	0.187	0.2322
CH symmetric stretch	0.354	0.2322
CH antisymmetric stretch	0.533	0.2322

A detailed theoretical study of the scattering of neutrons by polyethylene has also been undertaken at General Atomic. The calculational basis of the theoretical study of neutron scattering by polyethylene is embodied in the IBM-7090 code SUMMIT. The theoretical work of Wunderlich⁽²⁷⁾ on the specific heat and vibration spectrum in polyethylene provides an understanding of a large part of the atomic dynamics which is relevant to calculating neutron scattering. After complementing the work of Wunderlich with the results of other experiments, it is believed that the scattering law for polyethylene can be accurately calculated over all ranges of momentum and energy transfers. From the paper by Wunderlich, the vibrational frequencies and their abundance in polyethylene given in Table 4.2 are obtained.

Table 4.2

VIBRATIONS IN POLYETHYLENE

Type of Vibrational Mode	Frequency Limits (ev)	Fraction of All Modes
Acoustic	0 -0.064	2/9
CH ₂ , rocking	0.089 -0.145	1/9
C-C, stretch	0.108 -0.142	1/9
tCH ₂ , twist	0.130 -0.160	1/9
wCH ₂ , wagg	0.145 -0.175	1/9
SCH ₂ , bend	0.181	1/9
vCH symmetric stretch	0.353	1/9
uCH antisymmetric stretch	0.366	1/9

The acoustical vibrations are related to the C-C-C-deformation and torsional modes. The optical-vibration frequency assignments are made on the basis of infrared and Raman spectra studies. The range of acoustical

frequencies is determined on the basis of theoretical attempts to fit the specific heat in polyethylene in the temperature range 0° to 300° K.

In addition to the frequencies, Wunderlich gives the fractions of vibrations which are associated with each type of vibration. He has made a crude guess of the shape of the acoustical branch on the basis of specific-heat data and theoretical considerations.

For monatomic polycrystals, knowledge of the vibration spectrum would be sufficient to determine the neutron scattering completely in the Gaussian approximation. But in view of the fact that polyethylene is diatomic, it is required that further considerations concerning the molecular dynamics of polyethylene be made. The simplest consideration that can be made is a qualitative one which proceeds as follows: Imagine that in the acoustical branch of the vibration spectrum and in the C-C stretch mode, the H and C atoms are almost rigidly connected. Therefore, when the mass of the vibrating unit in these modes is 14, the effective mass associated with the remaining optical modes must be 14/13.

Let us denote by $\rho_{ac}(\omega)$, $\rho_{cc}(\omega)$, and $\rho_{op}(\omega)$ the densities of modes associated with the acoustical, the C-C stretch, and the optical modes, respectively. The density functions are normalized so that

$$\int [\rho_{ac}(\omega) + \rho_{cc}(\omega)] d\omega + \int \rho_{op}(\omega) d\omega = 1. \quad (1)$$

We can now construct the frequency distribution $f(\omega)$, which is to be used to compute the scattering in the Gaussian approximation:

$$f(\omega) = \frac{\alpha[\rho_{ac}(\omega) + \rho_{cc}(\omega)] + (1 - \alpha)\rho_{op}(\omega)}{\alpha \int [\rho_{ac}(\omega) + \rho_{cc}(\omega)] d\omega + (1 - \alpha) \int \rho_{op} d\omega}, \quad (2)$$

where α is chosen so that

$$\frac{\alpha \int [\rho_{ac}(\omega) + \rho_{cc}(\omega)] d\omega}{\alpha \int [\rho_{ac}(\omega) + \rho_{cc}(\omega)] d\omega + (1 - \alpha) \int \rho_{op}(\omega) d\omega} = \frac{1}{14}. \quad (3)$$

Using the information in Table 4.2, we find that $\alpha = 2/15$.

The assumption to which this result is tied, namely, that the CH_2 unit can be treated as rigid, is probably a good one for the acoustical modes, but not for the C-C stretching modes. A better assignment of the weights (effective masses) to the various branches of the vibration spectrum would require a more detailed investigation of the dynamics of solid

polyethylene. In view of the limited scope of the objectives and of the preliminary nature of the results, such an investigation is not yet warranted. Another factor of some consequence is that the shape of the acoustical vibration spectrum changes markedly over an ensemble of samples which range from amorphous to 100% crystalline. It is believed, however, that the polyethylene used in reactor technology is more than 80% crystalline, so that conclusions derived from theoretical studies of the fully crystalline substance have meaning.

At this point it is possible to make some comparisons of theoretical spectra (calculated on the basis of the new polyethylene model) with experimental results. In Fig. 4.1, room-temperature spectra for two poison concentrations are compared. It is apparent that the Goldman kernel and the Parks SUMMIT kernel both accurately reproduce the experimental results. Some extraneous structure appears to be introduced by the SUMMIT kernel, but it is questionable that this could have been observed experimentally. At liquid-nitrogen temperatures, again the two models permit spectra to be reasonably well calculated above 0.001 eV, as is seen in Fig. 4.2. Both representations have idiosyncrasies in that some structure seems to be predicted in the spectrum that is not observed. The free-hydrogen gas model is seen to be quite unsuitable for predicting the low-temperature spectra.

It has not been possible with our new model to predict reliably the total cross section of polyethylene using the code SUMMIT. This is due to an eccentricity in the code which we will endeavor to eliminate in the next rewrite. To date, the new model for describing neutron thermalization in polyethylene has not been tested completely by experiment. The model, however, is completely consistent with the molecular frequency spectrum of Wunderlich, while the Goldman model introduces a vibrational frequency of 0.533 eV, which is not observed by Wunderlich. Thus, the status of our knowledge of polyethylene is that we can predict infinite-medium and scalar-flux neutron spectra quite well using either molecular model. Predicting transport properties of the moderator is still difficult. P_1 scattering kernels for both models are completely untested to date. New data, for example $\sigma(E, \mu)$, will permit accomplishment of this test with the least expenditure of experimental effort.

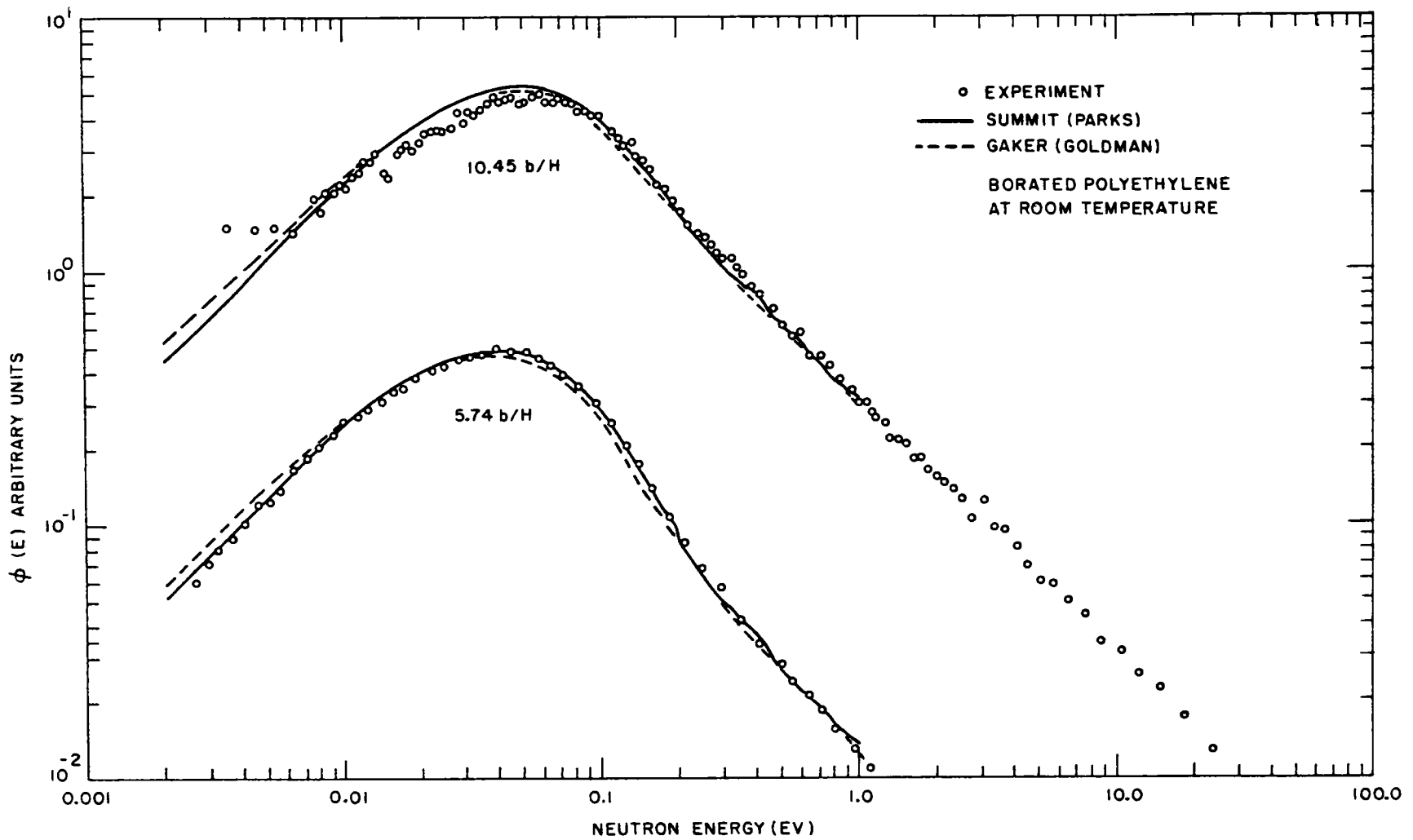


Fig. 4. 1--Infinite-medium borated polyethylene spectra at room temperature

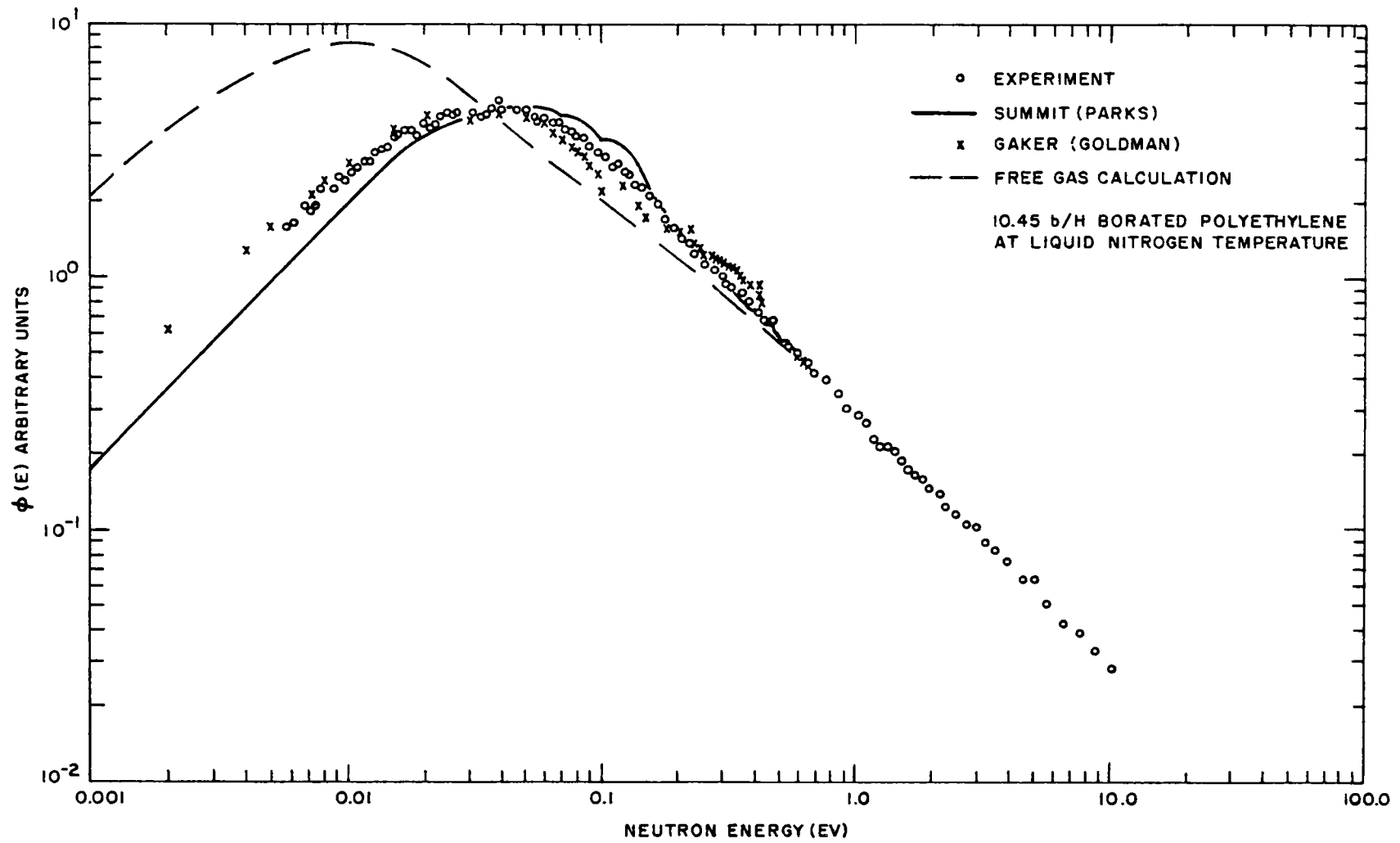


Fig. 4.2--Infinite-medium neutron spectra in borated polyethylene at liquid-nitrogen temperature

V. NEUTRON THERMALIZATION IN BENZENE

The neutron-moderating properties of organics have been studied both analytically and experimentally at many laboratories. The organic moderator most extensively investigated has been benzene and its associated multiple-ring molecules diphenyl and terphenyl. Dowtherm A, a combination of diphenyl and diphenyloxide, has also been studied. Low-energy inelastic-scattering studies, using a rotating crystal time-of-flight spectrometer, have been performed by Glaser⁽²⁸⁾ at a few neutron energies below 0.1 eV. A typical Egelstaff⁽¹³⁾ scattering-law analysis was performed based on these data and indicated that the frequency distributions for Dowtherm A and diphenyl are not significantly different. Other measurements of scattering law for the organics have been performed by Brugger.⁽²⁹⁾ Scattering laws are reported for O-terphenyl, M-terphenyl, P-terphenyl, and Santowax R. Differences between the scattering laws for these organics exist particularly for low values of α (the momentum transferred), indicating some differences between the molecular vibrational spectra. However, it is expected that neutron thermalization would be relatively insensitive to these differences.

On the basis of the existing scattering-law experimental data it is not possible to determine the complete frequency spectrum for the polyphenyls. Therefore, a theoretical model has been developed during the last few years to assist in the evaluation of neutron thermalization for the polyphenyls.⁽³⁰⁾ The approximate scattering kernel has been specified for the simplest of the polyphenyls, benzene.

This calculation was performed neglecting the neutron scattering from carbon, since $\xi\Sigma_s$ (the neutron slowing-down power) for carbon is so much smaller than that for hydrogen. The calculations were performed in the incoherent approximation, assuming harmonic oscillations. Molecular interactions were neglected as was excitation of the translational and rotational degrees of freedom of the molecule. The vibrational frequency distribution of Crawford and Miller⁽³¹⁾ shown in Fig. 5.1 was used in the calculations. A cluster of frequencies exists around 0.38 eV and another grouping occurs around 0.1 eV. Below 0.1 eV, vibrational frequencies are closely spaced, about 0.0073 eV apart. In total, the frequency spectrum consists of approximately 36 internal molecular vibrations, some of which are degenerate. The Parks-Boffi scattering kernel was generated using the computer code SUMMIT.

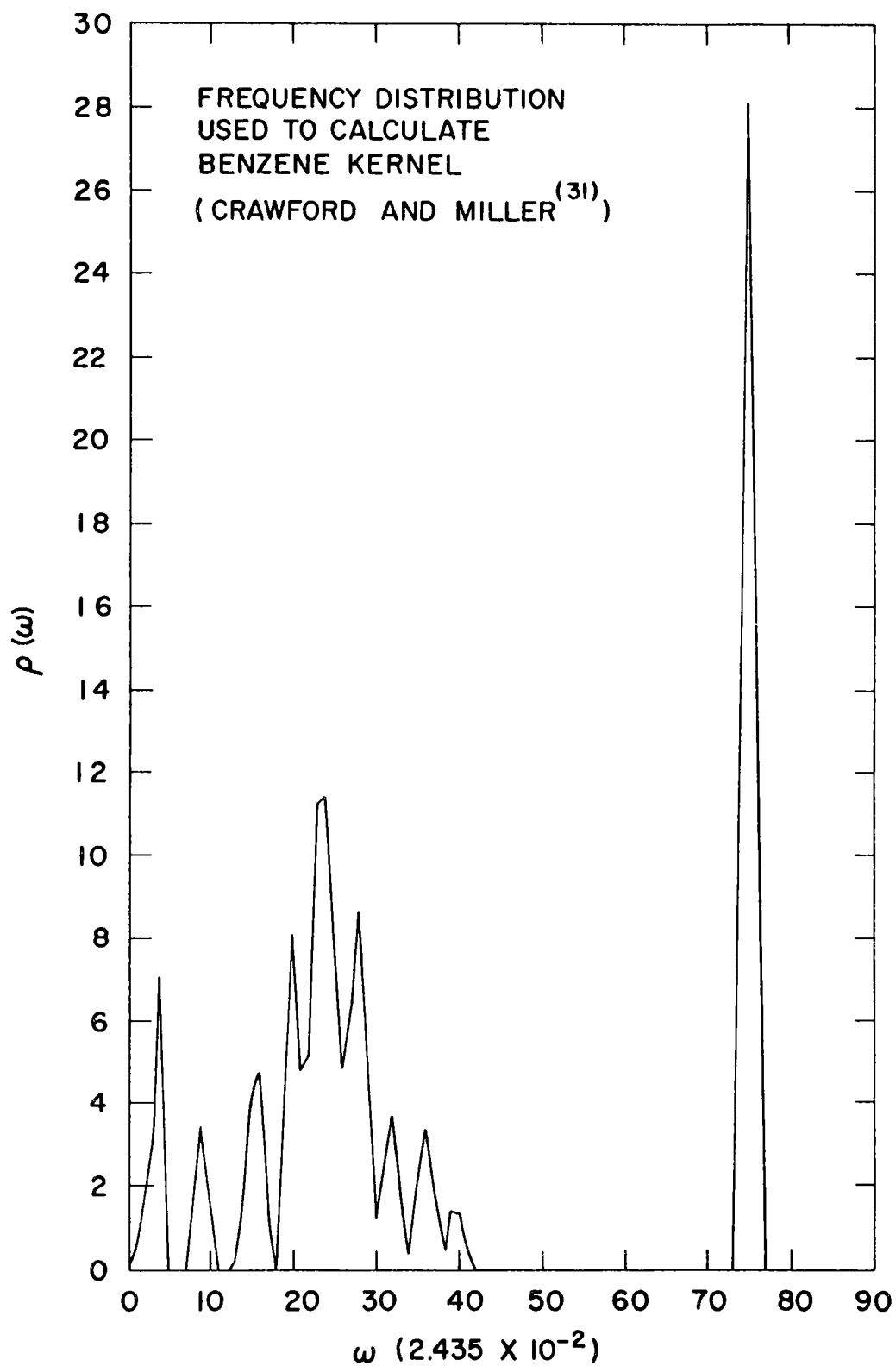


Fig. 5. 1--Frequency distribution of molecular vibrations in benzene from measurements by Crawford and Miller

Total cross sections for benzene have been calculated versus temperature using the benzene scattering model. A numerical study⁽³²⁾ to investigate the importance of including the translational and rotational degrees of freedom indicates that the omission produces noticeable differences in the calculated total cross sections. Neutron spectra under infinite-medium conditions and with $1/v$ absorption also have been calculated. It was desired, therefore, to make an over-all check of the validity of these analytical procedures by measuring the steady-state spectrum set up in benzene under the same conditions.

The experimental geometry of Fig. 5.2 was used in the measurement program. The standard 10-in. cubical assembly was used, and the benzene solution was poisoned with methyl borate to about 6 barns of absorption per hydrogen atom. The experiment was run at a temperature of 25°C. Atom densities were $N_h = 4 \times 10^{22}$ and $N_b = 3 \times 10^{20}$. No appreciable correction for buckling is necessary when the spectra are measured in the above configuration. The spectral results are shown in Fig. 5.3. The neutron-conservation criteria for the benzene spectrum were satisfied to within 5%. Also shown in Fig. 5.3 are three calculated spectra: (1) the spectrum assuming scattering from free protons, (2) predictions using Nelkin's water model, and (3) predictions using the Parks-Boffi benzene scattering kernel. Obviously, the hydrogen is rather tightly bound in benzene, more so than in water, but the Parks kernel very accurately reproduces the characteristics of the measured spectrum.

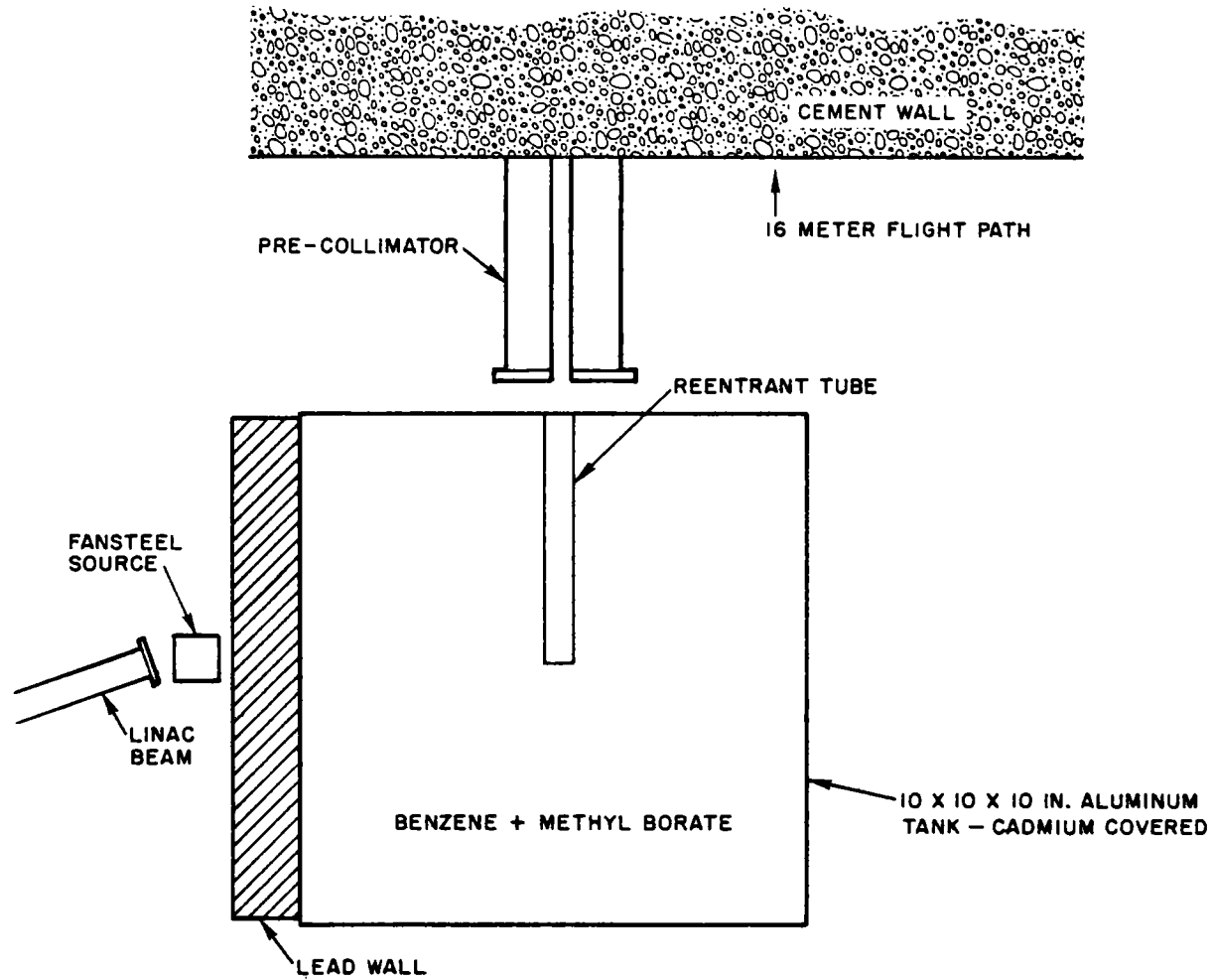


Fig. 5.2--Geometrical arrangement for infinite-medium experiments in benzene

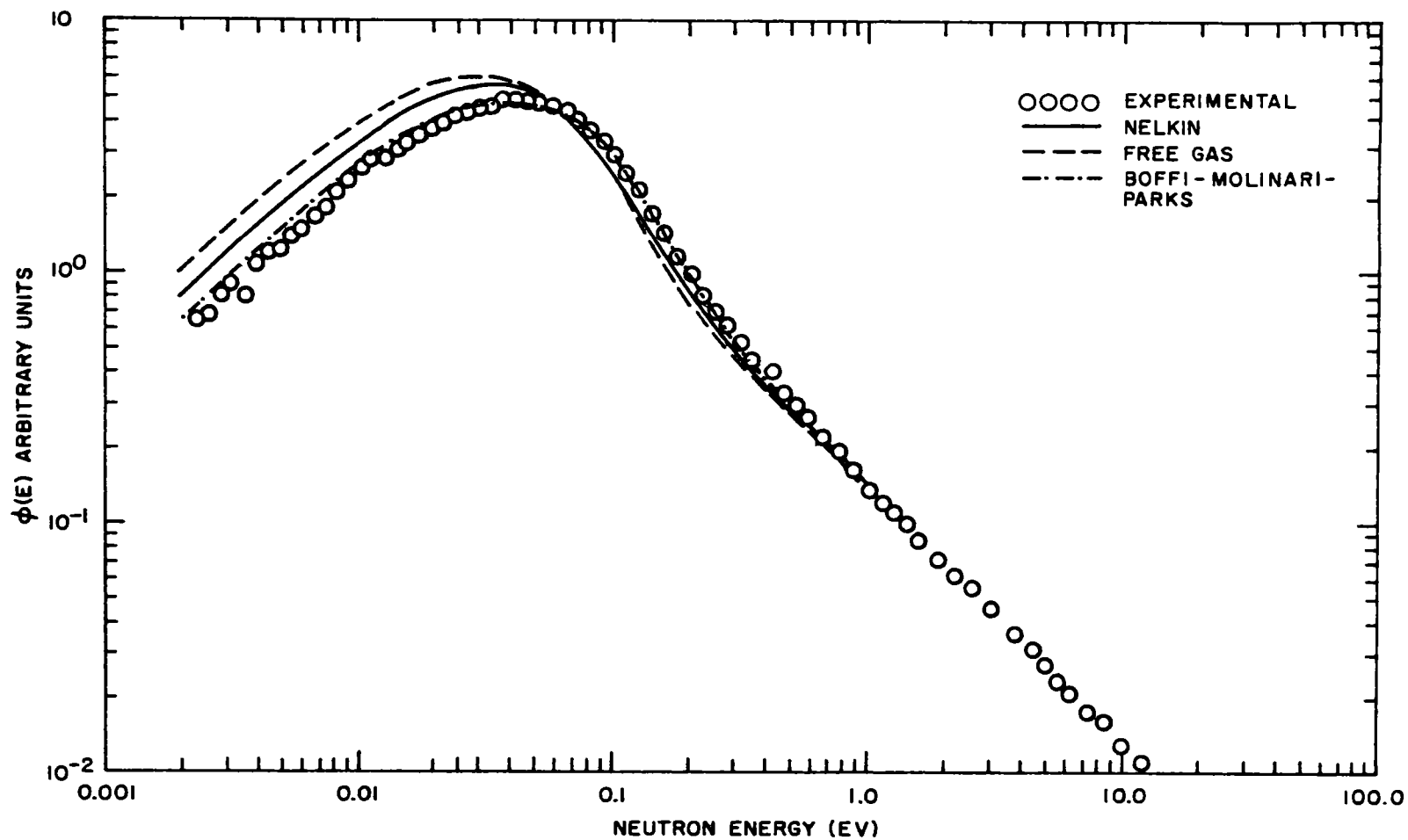


Fig. 5.3--Measured and calculated infinite-medium spectra in borated benzene

VI. NEUTRON THERMALIZATION IN ZIRCONIUM HYDRIDE

6.1. TEMPERATURE-DEPENDENT INFINITE-MEDIUM NEUTRON SPECTRA

Various solid, homogeneously fueled reactor systems have been investigated during the last few years, because they have potentially high-temperature operating capability and high power density, and also because the possibility exists of building systems with large prompt, negative-temperature coefficients of reactivity. For hydrogen-moderated reactors the first consideration, that of a relatively high-temperature fuel, limits the number of possible reactor construction materials to metal hydrides, such as those of titanium, zirconium, and uranium. Considerations of metallurgical properties and neutron economy have narrowed developmental efforts during the last few years to a promising family of zirconium hydrides. To avoid phase changes and associated changes in crystalline form during reactor startup, operation, and shutdown, hydrides of zirconium with atom ratios of H:Zr > 1.5 have been utilized.

The experimental procedures necessary for this investigation follow very closely those used in other high-temperature studies of spectra in water⁽³³⁾ and graphite assemblies. The spectral measurements were made in the usual manner. In Fig. 6.1, a cutaway view of the hot box constructed for the zirconium hydride is shown. The hot box was electrically heated with strip heaters to 1000°F. Variations of temperature over the assembly at 1000°F were about 10°F. The boundaries of the experimental assembly were established with boron carbide. The thermal-neutron spectrum was measured through a small probe tube inserted into the assembly. To obtain a homogeneous system, the zirconium hydride was purchased as ZrH_{1.75} powder (0 to 6-micron particle size) and was mixed with very fine-mesh boron carbide. Two mesh sizes of boron carbide were studied, one with particles less than 6 microns in diameter and one with particles less than 30 microns in diameter. Results were not markedly different. This information, together with simple estimates of the self-absorption for the smaller-mesh carbide particles, indicates that the experimental data do not have to be corrected for self-absorption. Mixing of the powders was accomplished by ultra-careful batch-mixing techniques to guarantee uniformity. The resulting poisoned ZrH_{1.75} was tamped into the hot box to a density of about 3.47 g/cm³. Subsequent density comparisons of samples prepared by the same technique indicate 10% uniformity. Fortunately, however, the infinite-medium spectrum is

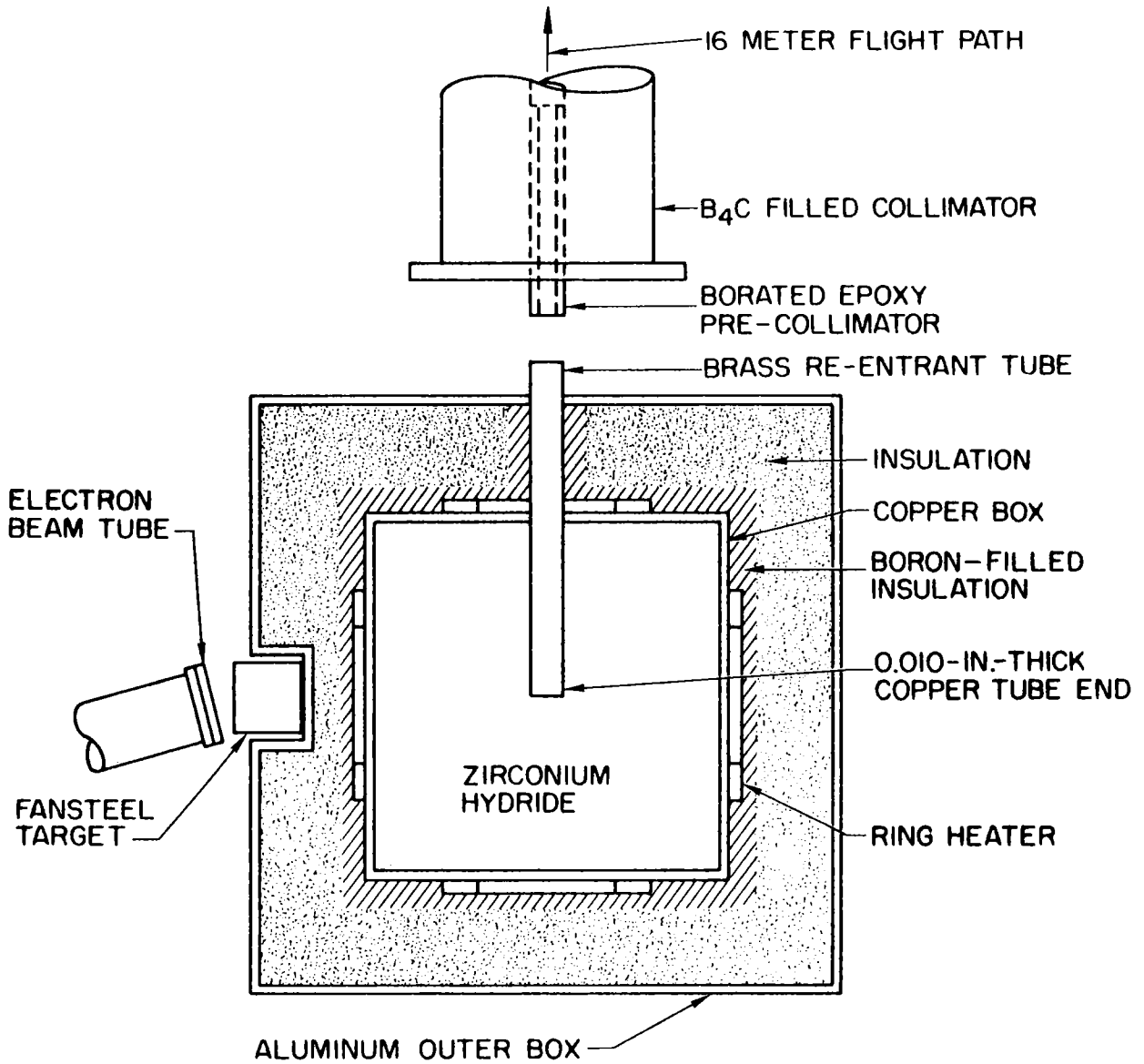


Fig. 6.1--Geometrical arrangement for infinite-medium experiments in zirconium hydride

not sensitive to atom-density variations. One need only guarantee through proper mixing that the ratio of absorber to moderator atoms is constant.

A question of concern at the initiation of the experimental work was that those crystalline properties of zirconium hydride of importance in the thermalization problem might not be the same in the powder as in the metal. A nonstoichiometric mixture was also obtained from the powder manufacturer, so that some hydrogen sites remained unfilled. The hydrided powder material obtained for this work was, however, of a reasonable particle size, so that for all practical purposes we were studying polycrystalline zirconium hydride. Excitation of optical transitions in the lattice should not depend on these macroscopic particle size and neither should the acoustic interactions, which involve a particular hydrogen and at most a few neighboring zirconium atoms. The nonstoichiometric mixture was not of concern either, because effects on the harmonic potential due to neighboring vacant or filled hydrogen sites were thought to be small. The fact that the width of the optical level is invariant as a function of hydrogen-to-zirconium ratio substantiates this observation.

The experiments were performed at two different poison concentrations, 3.4 and 8.0 barns/hydrogen atom, for several temperatures. The results are shown in Figs. 6.2 and 6.3. Predictions of the latest Einstein oscillator model (Section 6.2) with a mass of 360 associated with the acoustic vibrational modes are also shown in Figs. 6.2 and 6.3 for comparison with the measurements. It is clear that this model predicts the thermal-neutron spectrum with good accuracy.

From the standpoint of reactor calculations, it might be of interest to ask whether the refinements in the Rosenbluth-Nelkin Doppler-broadened Einstein oscillator model have really been worthwhile. The spectral-shift temperature coefficients of a hypothetical solid homogeneous $U^{235}\text{-ZrH}_{1.75}$ reactor therefore have been calculated. The temperature coefficient here is due exclusively to changes in ηf . The new and old Einstein oscillator models give temperature coefficients which differ by about 25%, which is a significant change for reactor analysis.

The conclusions from this experiment and analysis are by now evident. The spectra in poisoned zirconium hydride shift markedly with temperature and in about the manner predicted using an Einstein oscillator model. This observation is, however, inconsistent with the model of Miller, *et al.* (34) For particular applications, present knowledge of this kernel is adequate; however, an even more accurate treatment of this moderator would appear to be necessary to remove any residual disagreements between theoretical and experimental spectra.

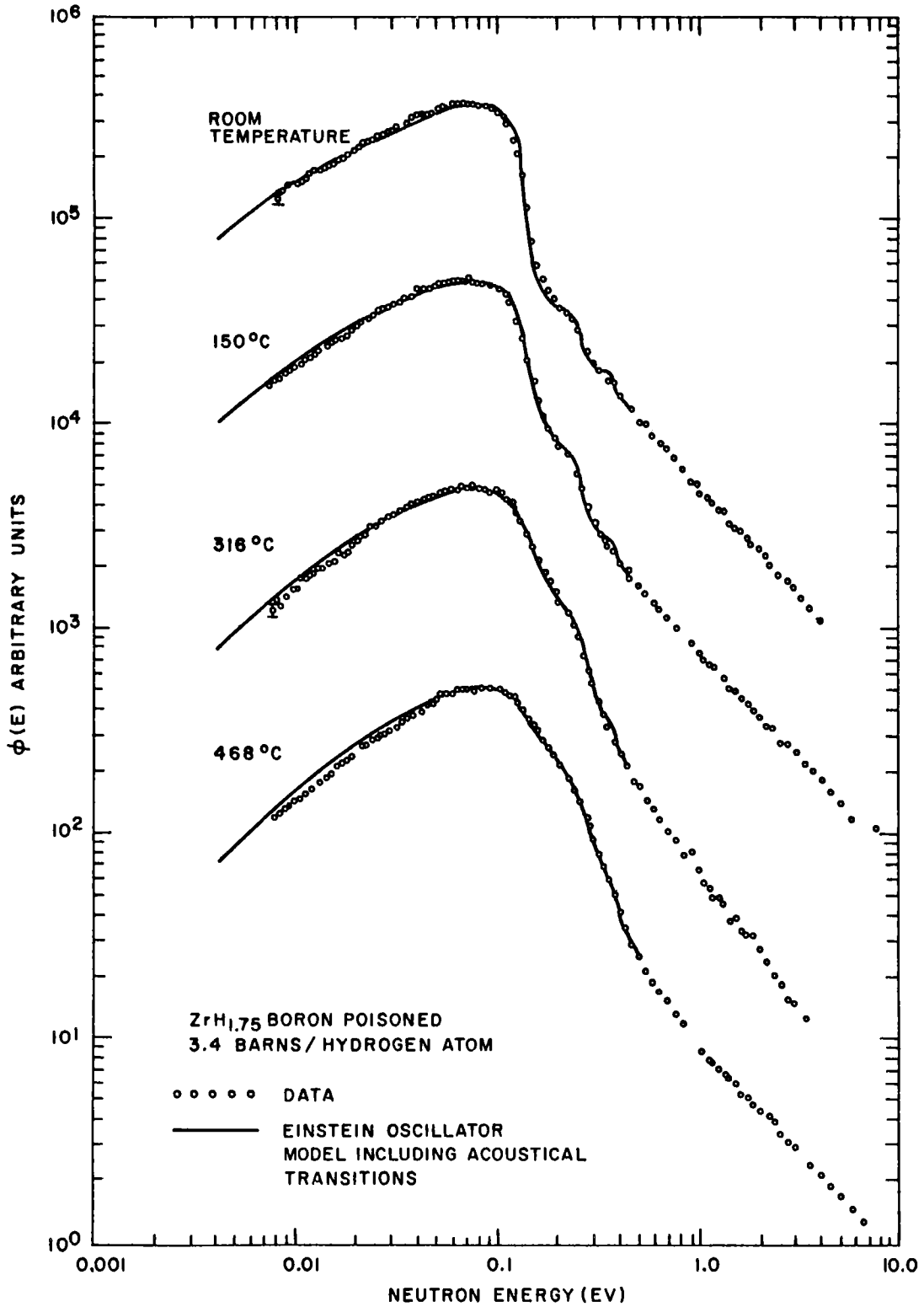


Fig. 6.2--Infinite-medium spectra at various temperatures in zirconium hydride poisoned to 3.4 b/H atom

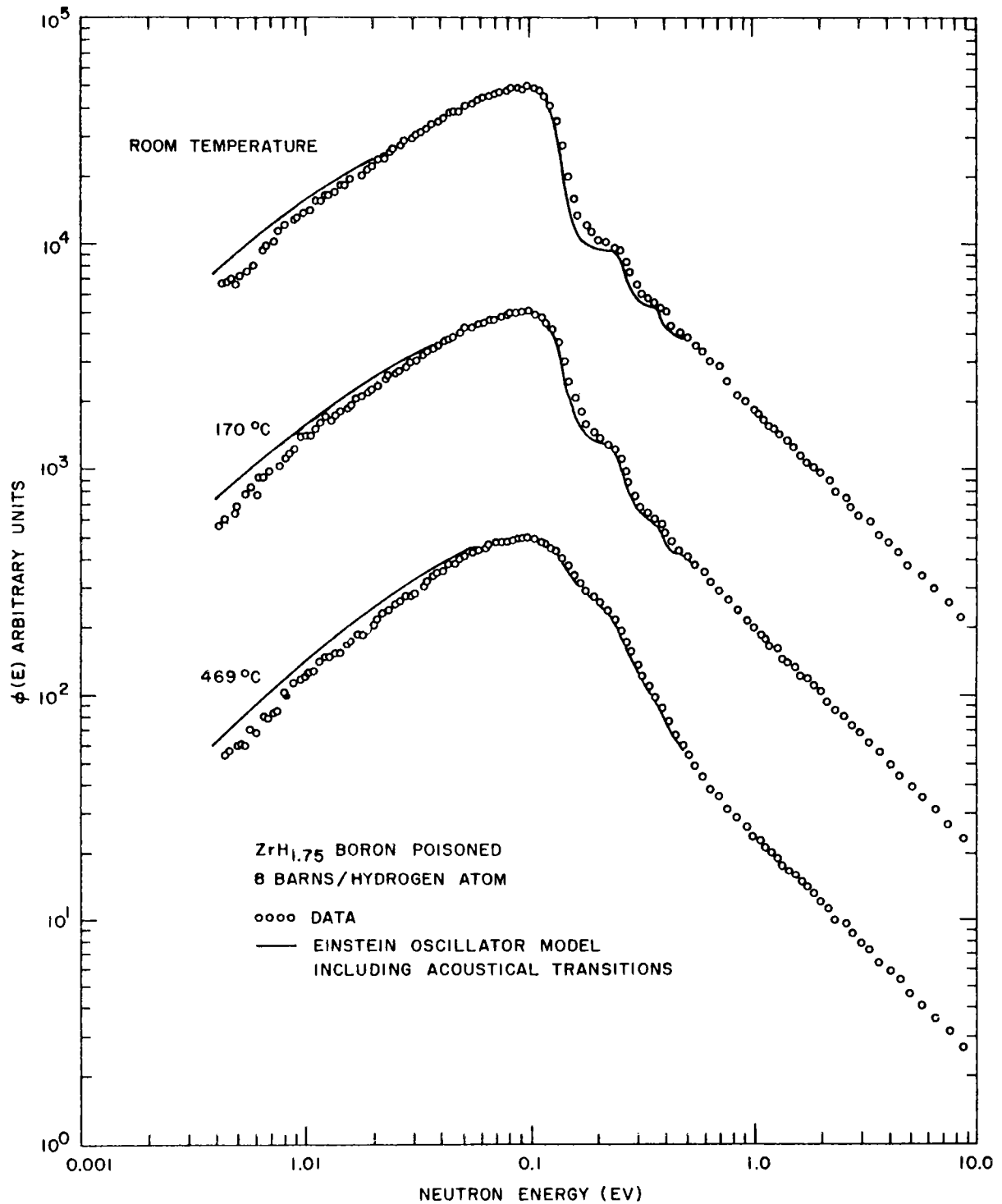


Fig. 6.3--Infinite-medium spectrum at various temperatures in zirconium hydride poisoned to 8 b/H atom

6.2. SCATTERING MODELS FOR ZIRCONIUM HYDRIDE

The crystal structure of gamma-phase zirconium hydride consists of a face-centered-cubic lattice of zirconium atoms with interstitial hydrogen atoms forming a second cube one-half the size of the zirconium cube and centered inside that lattice. Each hydrogen atom has four equidistant nearest zirconium neighbors spaced at 0.433 times the lattice spacing. The hydrogen can thus vibrate more or less isotropically at the center of a tetrahedron of approximately stationary zirconium atoms.

Early experimental work⁽³⁵⁾ indicated that the hydrogen atoms bound in the zirconium lattice do not vibrate with a Debye spectrum of normal-mode frequencies. Instead, equally spaced characteristic frequencies appeared to be excited in the lattice by neutron interactions, more in keeping with the behavior of an Einstein solid. This is the result to be expected on the basis of a simple model in which the proton vibrates isotropically in the harmonic potential well formed by nearest zirconium neighbors. Such an oscillator has energy states $[n + (3/2)] h\nu$, h being Planck's constant, ν the oscillator frequency, and n a positive integer. Neutrons would thus lose or gain energy in discrete amounts, $nh\nu$, by collisions with protons bound in this harmonic potential. In addition to these optical lattice transitions, neutrons may excite acoustic Debye-type vibrations in the zirconium hydride lattice. In the long-wavelength acoustical modes, the hydrogen atoms move in phase with one another. These modes therefore correspond to the motion of a group of atoms whose mass is much greater than that of hydrogen, and indeed even greater than the mass of zirconium. Because of the large effective mass, these modes are very inefficient for thermalizing neutrons, but for neutron energies below $h\nu = 0.137$ eV they provide the only mechanism for the slowing down of neutrons.

The simplest model proposed for considering the problem of neutron slowing-down in zirconium hydride was that of Cohen and Vaughan,⁽³⁶⁾ in which acoustic modes were entirely neglected and only the discrete energy transfers $nh\nu$ between the neutron and the harmonically bound proton were allowed. The population of protons in the various excited states was given by the Boltzmann factor $e^{-h\nu/KT}$. The resulting scattering cross sections showed pronounced dips, as expected, at the energies $nh\nu$. Calculated neutron spectra had pronounced breaks at these same energies, as shown in Fig. 6.4.

At about the same time, another theory was proposed by Rosenbluth and Nelkin,⁽³⁵⁾ based on the oscillator model and on much earlier work by Rosenbluth. The neutron scattering cross section was calculated including, in an approximate manner, acoustical and other molecular effects. The acoustical modes and possible anharmonicities were considered in the simplified model only insofar as they broadened the peaks of the energy

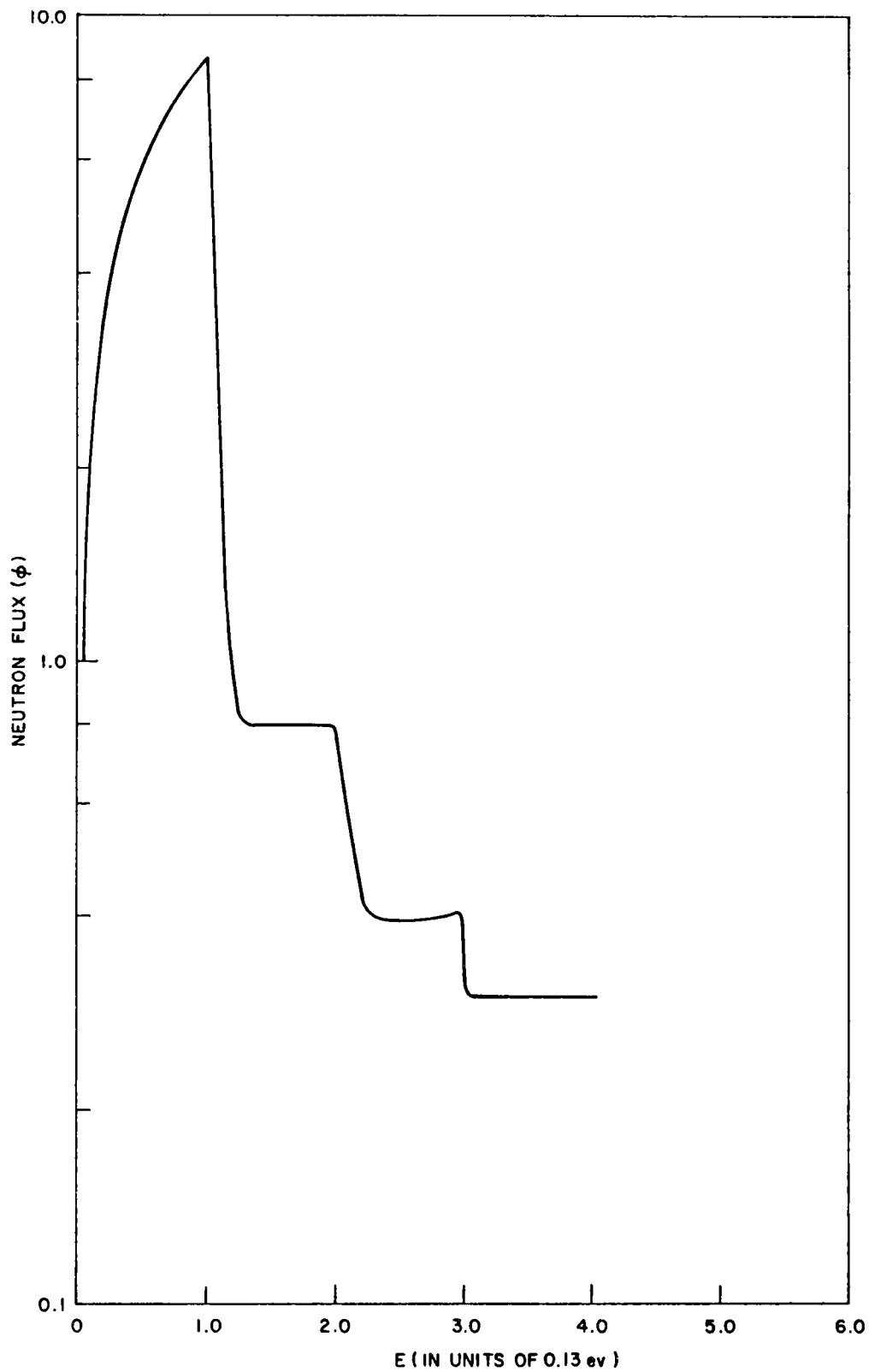


Fig. 6.4--Neutron flux in an infinite, homogeneous mixture of ZrH_2 and U^{235} having 140 hydrogen atoms per U^{235} atom (calculated from model of Cohen and Vaughan)

distribution of neutrons which transferred energy with the discrete optical modes. In effect, what was done was to include a translational degree of freedom as well as the vibrational degree of freedom, and to assign to it a mass sufficient to Doppler-broaden the oscillator levels to conform with experimental total-cross-section work. The average occupation number for the levels was given, as expected, by Bose-Einstein statistics characteristic of the harmonic potential. A disconcerting fact about this model was that, owing to numerical requirement, it was necessary to assign an unrealistically small mass (20) to the translational degrees of freedom to Doppler-broaden the levels.

Recently, a third model describing the properties of the molecular states of zirconium hydride was proposed by Miller, Brehm, and Roberts.⁽³⁴⁾ The model, which is phenomenological in nature, was postulated to explain the small prompt spectral temperature coefficients of reactivity observed for the SER series of reactors. There are three characteristic differences between this model and the former two. Specifically, these are:

1. The zirconium and hydrogen are treated separately, and for zirconium a crystal phonon scattering cross-section formulation is used. A Debye cutoff of 0.02 eV is assumed.
2. The data of Woods, et al.,⁽³⁷⁾ were used directly to obtain a frequency distribution function for the hydrogen in zirconium hydride.
3. The Bose-Einstein statistics for the average occupation numbers of the harmonic oscillator states were replaced by Fermi-Dirac statistics. The justification for this step was that the protons might communicate in the manner of electrons in a semiconductor and would not act like perfectly bound particles. (In other words, the protons would diffuse from one well to another, which indeed does happen.)

The objections to this model are based mainly on consistency arguments. If one assumes protons in a harmonic oscillator potential then one is, by the arguments set forth by Glauber,⁽³⁸⁾ relegated to Bose-Einstein statistics which describe the vector displacements of the protons. In other words, the Bose-Einstein statistics refer to the phonons, not to the protons. There is really no choice in this matter. The use of Fermi-Dirac statistics is appropriate in situations where there are many particles in a large box or well, no two of which can occupy the same state. Here, we have but one particle in any well. Since the protons do diffuse from one well to another, then in an exact treatment this should be taken into account, perhaps by considering the protons to be in some kind of a periodic potential--but this is a difficult problem and would not merely involve a change of

statistics. Furthermore, the use of the one-phonon cross-section formulation, together with a frequency distribution function, is not likely to be as rigorous a treatment of the problem as calculating the cross section directly and exactly on the basis of some realistic physical model.

We have attempted to refine the basic Rosenbluth-Nelkin model for zirconium hydride in a realistic manner to see if the experimental observations could be better explained. The slow-neutron scattering cross section for a system of chemically bound nuclei can be written in the form

$$\frac{d^2\sigma}{dE d\Omega} = \frac{k}{k_0} \frac{a^2}{2\pi} \int_{-\infty}^{\infty} dt e^{i\epsilon t} X(\vec{\kappa}, t), \quad (1)$$

where a is the bound-atom scattering length, $\epsilon = (k^2 - k_0^2)/2$ is the energy transfer, and $\vec{\kappa} = \vec{k} - \vec{k}_0$ is the momentum transfer, with k_0 being the initial momentum and \vec{k} the final momentum of the neutron. The units used are those in which $m = \text{neutron mass} = 1$. The quantity $X(\vec{\kappa}, t)$ contains the molecular dynamics of the scattering system, and is given by the thermal average

$$X(\vec{\kappa}, t) = \left\langle \sum_{j=1}^N \exp[-i \vec{\kappa} \cdot \vec{r}_j(0)] \exp[+i \vec{\kappa} \cdot \vec{r}_j(t)] \right\rangle_T,$$

and $\vec{r}_j(t)$ is the position vector of the j^{th} nucleus at time t . By assuming crystal symmetry and harmonic lattice vibrations, one arrives at the following approximate result:

$$X(\vec{\kappa}, t) = \exp\left\{ \frac{\kappa^2}{2M} [\gamma(t) - \gamma(0)] \right\},$$

with

$$\gamma(t) = \int_{-\infty}^{\infty} d\omega \frac{\rho(\omega)}{2\omega \sinh(\omega/2T)} \exp\left(\frac{\omega}{2T} + i\omega t\right). \quad (2)$$

The quantity $\rho(\omega)$ is the frequency spectrum of the crystal.

For zirconium hydride we have split $\rho(\omega)$ into two parts: $\rho_1(\omega)$ for the optical modes and $\rho_2(\omega)$ for the acoustic modes. For the oscillator levels of the optical modes, $\rho_1(\omega)$ is taken as a Gaussian distribution centered at 0.13 eV, with a width of 0.02 eV chosen to fit the cross-section data of Woods, et al. The frequency distribution $\rho_2(\omega)$ for the acoustical

modes is taken as a Debye spectrum with a cutoff at 0.02 ev. Two trial weights were associated with these modes, 91 and 360. These are the lower and upper limits, respectively, that could be taken as the weight, since the proton is bound to four zirconium atoms, but not in a completely rigid way.

The computer program SUMMIT⁽¹⁷⁾ can be used to solve Eq. (2) by an exact multiphonon expansion, and thus to generate a scattering kernel for computing the thermal-neutron spectrum.

VII. NEUTRON THERMALIZATION IN BeO

7.1. STATUS OF THE PROBLEM

During 1961, neutron spectra were studied in several assemblies of beryllium oxide. These spectra and thermal and epithermal flux distributions throughout the assemblies are given in Ref. 1. The assemblies were poisoned somewhat heterogeneously with borated stainless steel foil, and the spectra were measured at two locations in the assembly. The pulsed neutron source was placed outside of the assembly. As a result of this, the flux distribution in one dimension in the assembly had the characteristic age shape and in the other two dimensions a normal mode or cosine shape. The initial attempts to understand and calculate these spectra, however, did not meet with success. The spectra were spatially dependent and noninfinite-medium in character. The modal expansion method was used to take into consideration the spatial effects, but this procedure did not converge. In other words, we had to consider contributions from the very high-order spatial modes. We have therefore endeavored to approach the study of thermalization in BeO in two ways. First, experimentally we have been studying the feasibility of producing a normal-mode flux distribution in all three dimensions of a BeO assembly. Gamma-ray excitation of the assembly is utilized in this approach. Second, we have been investigating alternative methods of analysis to use in studying the space-dependent spectrum problem in BeO. The progress achieved in these two investigations is discussed in Sections 7.2 and 7.3.

7.2. NORMAL-MODE PRODUCTION

These experimental studies were performed to determine the feasibility of obtaining a three-dimensional, normal-mode flux distribution in a BeO assembly. This accomplishment would obviate any possible need for multiplying-assembly studies of neutron spectra for this moderator if the space-dependent spectral problem remained unsolvable. An X-ray source and the (γ, n) reaction in the beryllium itself were utilized to shape the spatial distribution of the fast flux in the BeO assembly.

The test assembly investigated was constructed from BeO blocks to form a 60-cm cube. The blocks were about 1 cm thick. Between each layer of BeO, borated stainless steel foils (0.010 in. thick) were placed in order to poison the assembly to about 1.3 barns per beryllium atom. The

thin absorbing foils did not necessitate a large self-absorption correction. The neutron spectrum was quite epithermal, owing to the relatively high absorption, but was still expected to be quite sensitive to the scattering model used for BeO. The X-ray source was constructed from a 0.020-in. thickness of tungsten alloy. Approximately 50% of the Linac electron-beam energy was converted to bremsstrahlung by the thick target. The source was water-cooled and backed by 2 in. of aluminum to stop the remaining electrons. The neutron-flux distributions in the BeO were mapped using the cadmium-covered indium foils (indium-resonance neutrons of 1.4 ev). The first geometrical arrangement used is shown in Fig. 7.1. It was hoped that the desired normal-mode flux distributions could be obtained (empirically) by moving the source or changing the distribution of thickness of the BeO filler blocks shown in Fig. 7.1. The neutron distribution measured in this assembly indicated that a fast-neutron flux emanating from the source was falling on the face of the BeO assembly and distorting the total flux shape. A fast-neutron shield was designed to eliminate these neutrons and to collimate the photon beam. The resulting geometrical arrangement is shown in Fig. 7.2. The distribution measured axially from the source in the BeO assembly with and without the shield is shown in Fig. 7.3. The distribution desired with the shield was achieved, but the loss in neutron intensity incurred by placing the source at the distance required for the shielding was too great to make a good spectrum measurement possible.

Further studies are required to determine whether a three-dimensional normal-mode distribution can be achieved in a BeO assembly with sufficient intensity to permit measurements of neutron spectra to be made.

7.3. CALCULATIONS

As mentioned above, previous attempts to analyze the spectral measurements in BeO have not been particularly successful. We have therefore adopted a new procedure for solving the space-dependent spectrum problem. The whole problem is solved utilizing a P_0 source with scattering by means of the discrete transport-theory code GAPLSN. We have concentrated our efforts here on reanalysis of the 1961 data, taken under infinite-medium conditions with a basic geometry similar to that of Fig. 7.1. First, the cell problem had to be solved because of the lumped absorption used in the previous work. A DSN cell problem gave the disadvantage factors associated with the neutron flux in the absorber and moderator. Utilizing these disadvantage factors to weight the absorption cross section, the spectra were calculated by GAPLSN throughout the entire assembly. The spatial source was specified by the flux plots originally taken by foil activation in BeO. The scattering kernel for the analysis is based on a Debye frequency spectrum with a Debye cutoff frequency adjusted to satisfy

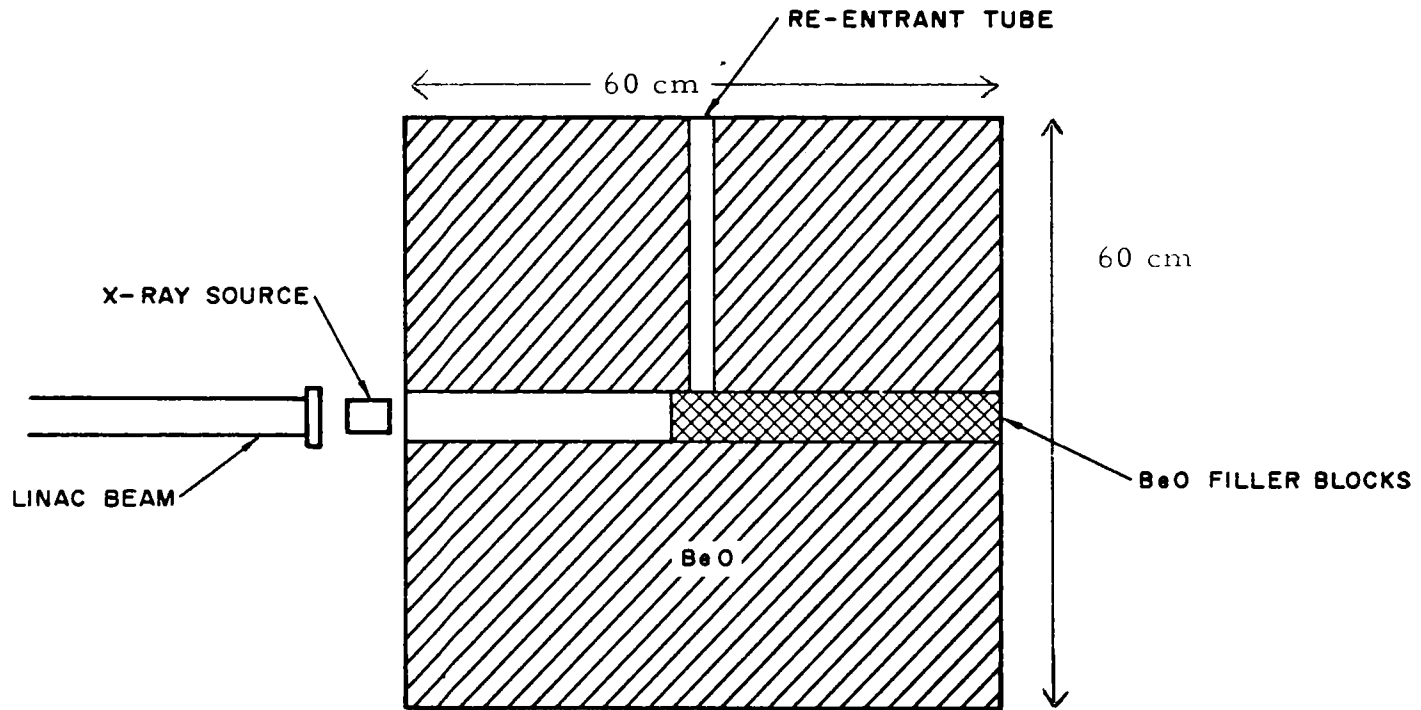


Fig. 7. 1--Initial geometry for normal-mode excitation of poisoned BeO assembly

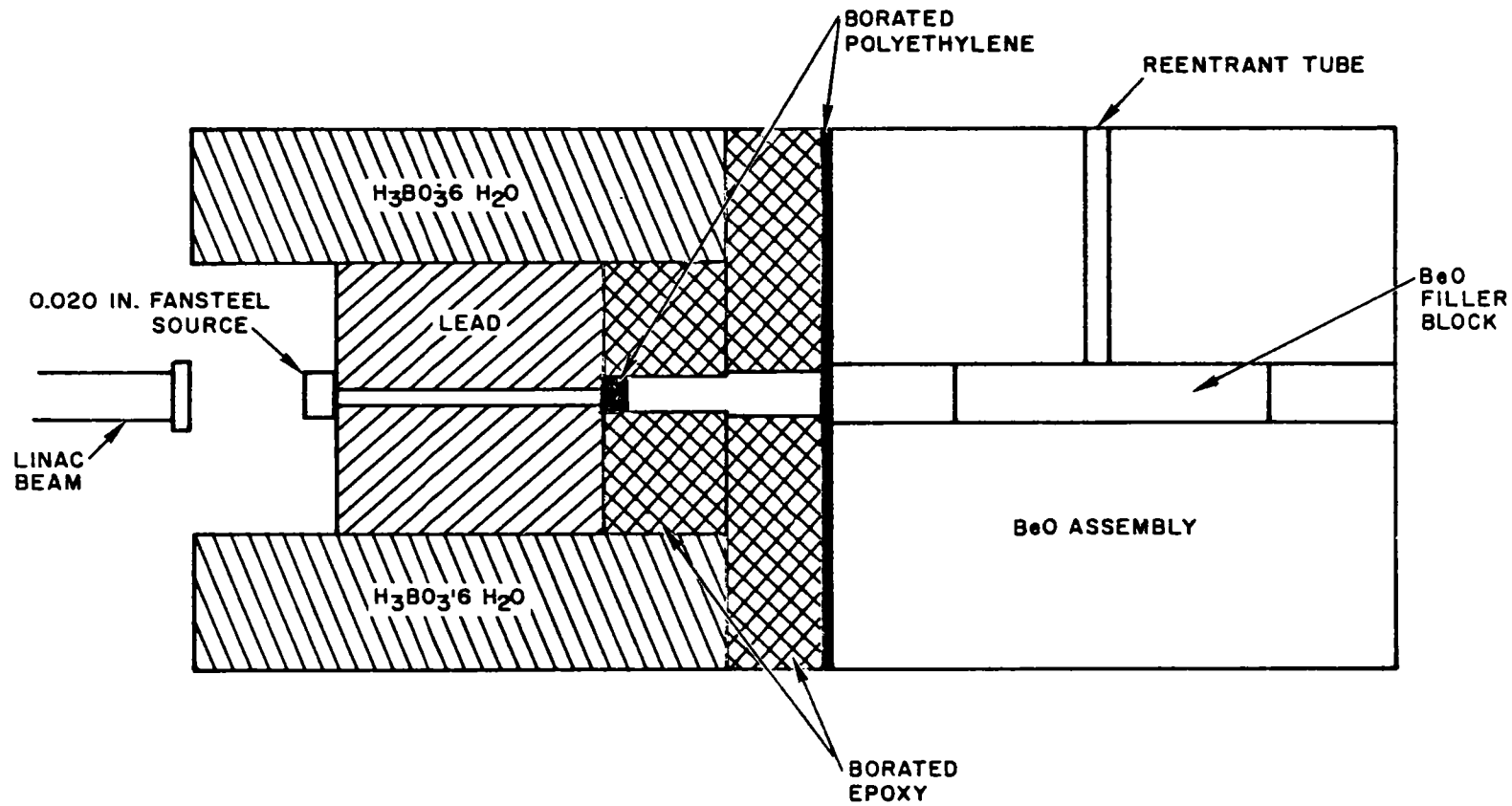


Fig. 7.2--Final geometry for normal-mode excitation of poisoned BeO assembly

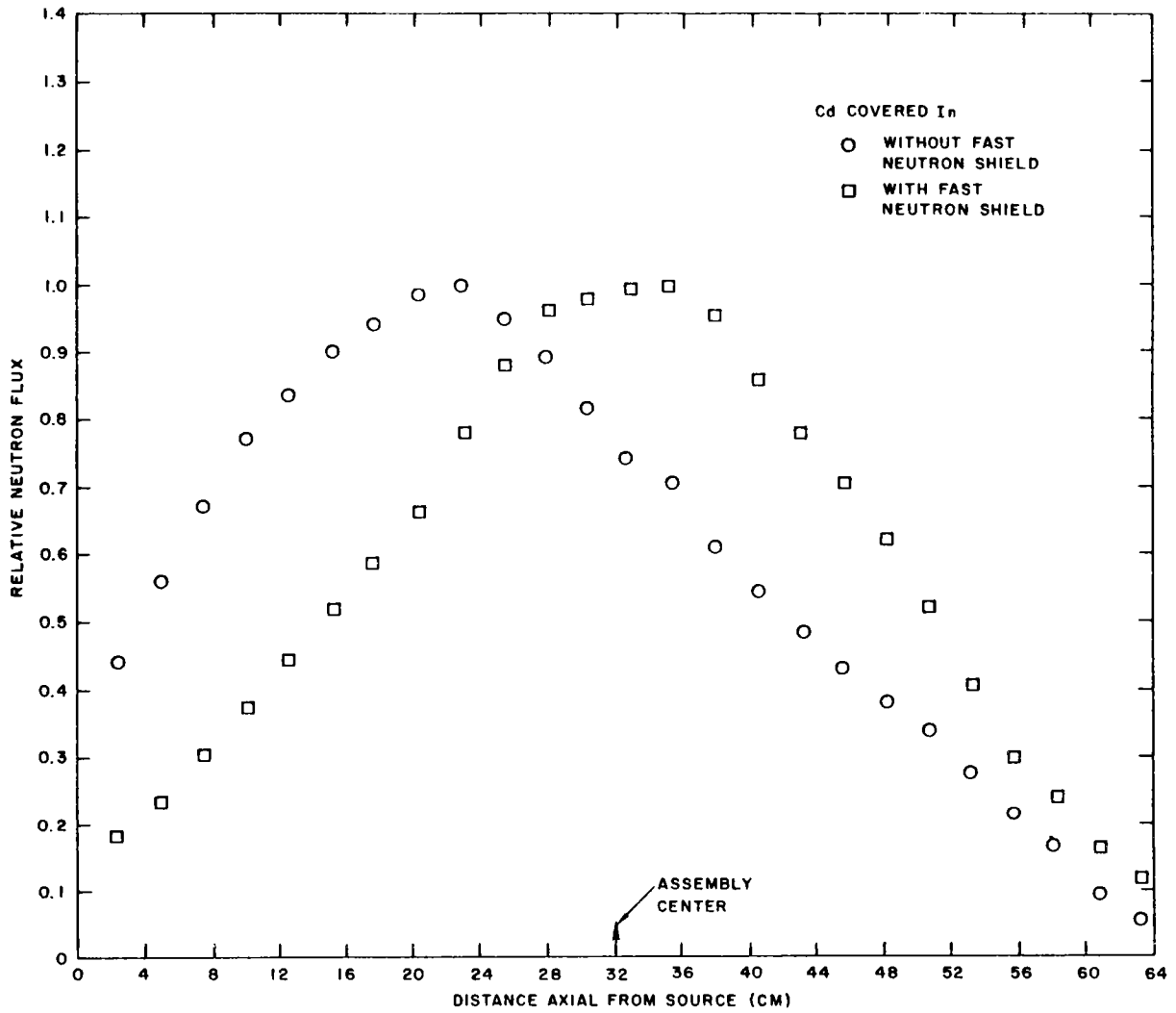


Fig. 7.3--Axial, epithermal flux distributions for two geometrical arrangements of BeO

the specific-heat measurements for BeO. The molar specific heat, C_v , is calculated for the proposed frequency spectrum $\rho(\omega)$, using

$$\frac{C_v}{3R} = \int_0^\theta \left(\frac{\omega}{T}\right)^2 \frac{e^{\omega/T}}{(e^{\omega/T} - 1)^2} \rho(\omega) d\omega \quad , \quad (1)$$

where R is the gas constant, T is the Kelvin temperature measured in electron volts, and θ is the Debye cutoff frequency. The calculated spatially dependent spectra are compared with the measured spectra in Fig. 7.4. The agreement has been improved considerably (especially for the 6-in. measurement) and it appears that a simple molecular model has permitted reasonably accurate spectra to be calculated. However, a discrepancy of 10% between theory and experiment is present at KT for the spectrum at the 12-in. position. The new method of handling the spatial flux problem also seems to give better results.

The above comparisons, although somewhat encouraging, are really preliminary in nature. More spectral data with smaller flux depression corrections, with samarium resonance absorption, and measured over the practical temperature range of interest will be forthcoming during the next year. In addition, the molecular model for BeO will be put on a firmer theoretical foundation, so that all classes of spectral problems associated with this moderator can be handled with confidence by reactor design engineers and physicists.

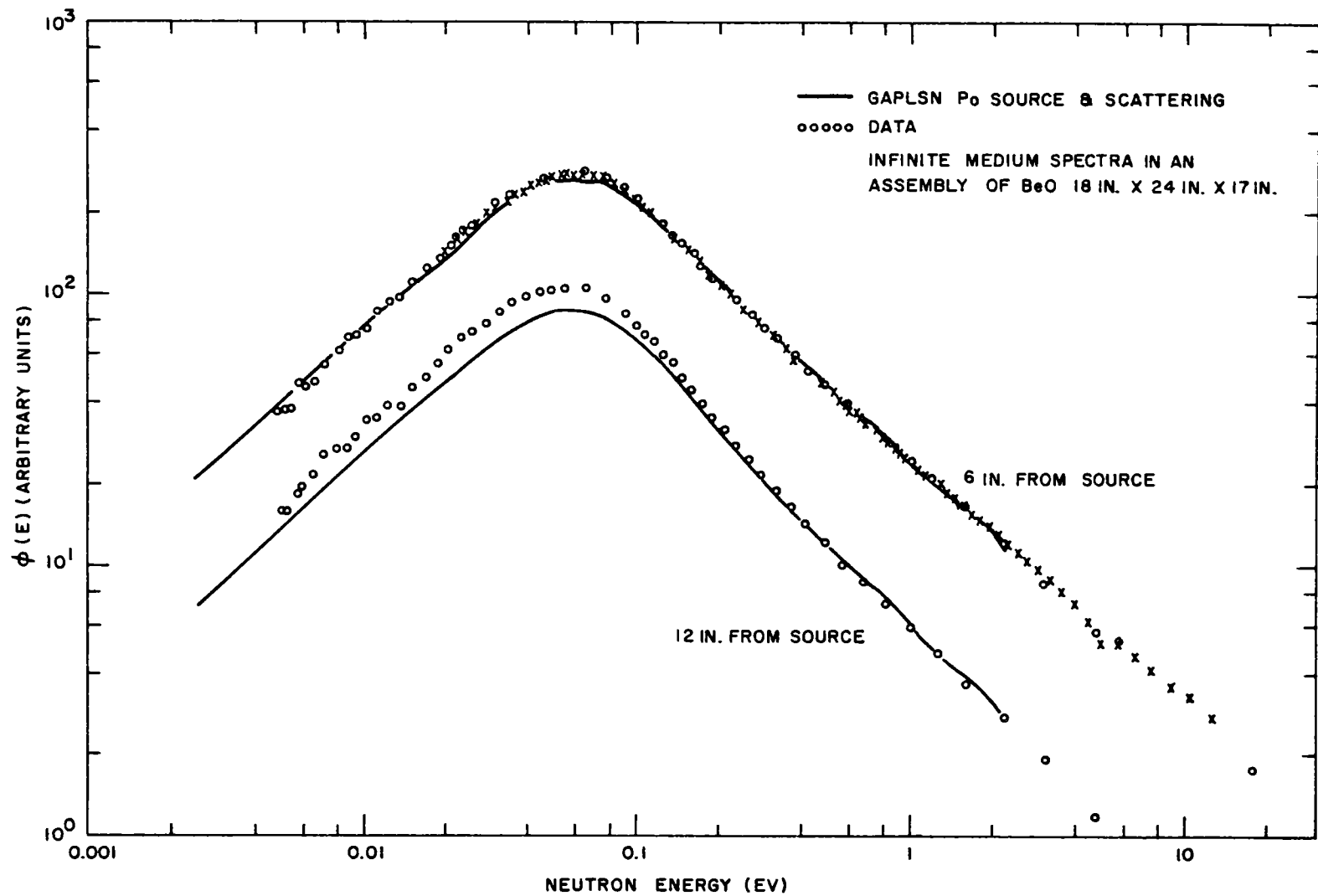


Fig. 7. 4--Comparison of experimental and theoretical neutron spectra in a poisoned BeO assembly

VIII. SCATTERING MODEL FOR BERYLLIUM

Beryllium metal is potentially important both as a moderator and as a reflector for thermal neutrons. In order to be able to calculate thermal-neutron spectra in beryllium, it is necessary to obtain first a scattering kernel. The computer code SUMMIT can be used to generate scattering kernels in the incoherent approximation for an isotropic material at any desired temperature if the frequency spectrum of the lattice vibrations is known. To this end, the dispersion relations in the symmetry directions of a single beryllium crystal have been measured by R. E. Schmunk, *et al.* (39) These authors also showed that a central force model, including up to fifth-nearest-neighbor interactions, gave a reasonably good fit to the experimental data. Using this force model, the frequency spectrum for beryllium has been found. This frequency spectrum is compared with that obtained experimentally by Sinclair, (40) using the extrapolation technique on the scattering law. Also, we have computed the scattering law using SUMMIT in order to make comparisons with the measurements of Sinclair.

As a further test of the theoretical frequency spectrum, the specific heat of beryllium has been computed over a wide temperature range.

8.1. LATTICE DYNAMICS OF BERYLLIUM

For completeness, and ease of understanding, a review will be given here of the crystal structure of beryllium. For more detail the reader is referred to the article of Slutsky and Garland. (41)

Beryllium has a hexagonal close-packed lattice structure with two particles per unit cell. We choose the origin of coordinates at one of the particles. Let j be the cell index and ℓ the lattice index. Thus,

$$\begin{aligned}\vec{x}(\ell, j) &= \vec{x}(\ell) + \vec{x}(j) , \\ \vec{x}(j=1) &= 0, \vec{x}(\ell=0) = 0.\end{aligned}$$

For the second particle in the unit cell, $j=2$, we have

$$\vec{x}(j=2) = \frac{\vec{a}_1}{3} + \frac{2\vec{a}_2}{3} + \frac{\vec{a}_3}{2} ,$$

where $\vec{a}_1, \vec{a}_2, \vec{a}_3$ are the basic vectors for the lattice. Owing to the

hexagonal symmetry, \vec{a}_3 is perpendicular to \vec{a}_1 and \vec{a}_2 , and \vec{a}_1 and \vec{a}_2 make an angle of 120° with each other. Also, $|\vec{a}_1| = |\vec{a}_2| = a$, $|\vec{a}_3| = c$. For beryllium, $a = 2.2856 \text{ \AA}$ and $c = 3.5832 \text{ \AA}$. The volume of a unit cell is $\vec{a}_1 \cdot (\vec{a}_2 \times \vec{a}_3) = \sqrt{3} a^2 c / 2$. Table 8.1 gives the positions of the atoms out to fifth nearest neighbors of the atoms in the zero cell ($\ell=0$). Atom 0 is the atom at the origin ($j=1, \ell=0$) and atom 0' is the atom $j=2, \ell=0$. Atoms 1 to 6 are at a distance a from 0, atoms 7 to 12 at a distance $(c^2/4 + a^2/3)^{1/2}$, atoms 13 to 18 at a distance $(c^2/4 + 4a^2/3)^{1/2}$, atoms 19 and 20 at a distance c , and atoms 21 to 32 at a distance $(c^2/4 + 7a^2/3)^{1/2}$.

For beryllium we make the assumption that the interatomic forces are central. The total potential, ϕ_T , of the lattice is given by the sum of all the two-body central potentials:

$$\phi_T = \frac{1}{2} \sum_{\ell j, \ell' j'} \psi(|\vec{x}(\ell, j) - \vec{x}(\ell', j') + \vec{u}(\ell, j) - \vec{u}(\ell', j')|), \quad (1)$$

where $\vec{x}(\ell, j)$ is the equilibrium position of a particle, and $\vec{u}(\ell, j)$ is the small displacement of that particle from its equilibrium position. By expanding the right-hand side of Eq. (1) in a Taylor series and keeping terms up to second order only, we obtain what is called the harmonic approximation:

$$\begin{aligned} \phi_T = \phi_T(\text{equilibrium}) &+ \frac{1}{2} \sum_{\ell j, \ell' j'} \sum_{\alpha} \left(\frac{\partial \psi}{\partial s} \right)_{s=s_0(\ell \ell', j j')} \\ &\times \frac{[\mathbf{x}_{\alpha}(\ell, j) - \mathbf{x}_{\alpha}(\ell', j')][u_{\alpha}(\ell, j) - u_{\alpha}(\ell', j')]}{s_0(\ell \ell', j j')} + \frac{1}{4} \sum_{\ell j, \ell' j'} \left(\frac{\partial^2 \psi}{\partial s^2} \right)_{s=s_0(\ell \ell', j j')} \\ &\times \frac{1}{s_0^2(\ell \ell', j j')} \left\{ \sum_{\alpha} [\mathbf{x}_{\alpha}(\ell, j) - \mathbf{x}_{\alpha}(\ell', j')][u_{\alpha}(\ell, j) - u_{\alpha}(\ell', j')] \right\}^2, \end{aligned}$$

where $s = |\vec{x}(\ell, j) - \vec{x}(\ell', j') + \vec{u}(\ell, j) - \vec{u}(\ell', j')|$, $s_0 = |\vec{x}(\ell, j) - \vec{x}(\ell', j')|$. Now we readily find to this approximation

$$\begin{aligned} - \left(\frac{\partial \phi_T}{\partial u_{\alpha}} \right)_{(\ell, j)} &= - \sum_{\ell', j'} \left(\frac{\partial \psi}{\partial s} \right)_{s=s_0(\ell \ell', j j')} \frac{\mathbf{x}_{\alpha}(\ell, j) - \mathbf{x}_{\alpha}(\ell', j')}{s_0(\ell \ell', j j')} \\ &- \sum_{\ell', j'} \sum_{\beta} \left(\frac{\partial^2 \psi}{\partial s^2} \right)_{s=s_0} \frac{[\mathbf{x}_{\beta}(\ell, j) - \mathbf{x}_{\beta}(\ell', j')][u_{\beta}(\ell, j) - u_{\beta}(\ell', j')]}{s_0^2(\ell \ell', j j')} [\mathbf{x}_{\alpha}(\ell, j) - \mathbf{x}_{\alpha}(\ell', j')], \end{aligned}$$

Table 8.1
POSITIONS OUT TO FIFTH NEAREST NEIGHBORS IN HEXAGONAL CP LATTICE

Atom Label		j	ℓ_1	ℓ_2	ℓ_3	nth Nearest Neighbor		Atom Label		j	ℓ_1	ℓ_2	ℓ_3	nth Nearest Neighbor	
Referred to 0	Referred to 0'					To Atom 0	To Atom 0'	Referred to 0	Referred to 0'					To Atom 0	To Atom 0'
0	7	1	0	0	0		2	7	20	2	0	0	-1	2	4
1	15	1	1	0	0	1	3	8	0	2	0	0	0	2	
2	17	1	-1	0	0	1	3	9		2	0	-1	-1	2	
3	9	1	1	1	0	1	2	10	5	2	0	-1	0	2	1
4	27	1	-1	-1	0	1	5	11		2	-1	-1	-1	2	
5	28	1	0	-1	0	1	5	12	4	2	-1	-1	0	2	1
6	11	1	0	1	0	1	2	13		2	-1	-2	-1	3	
19	8	1	0	0	1	4	2	14		2	-1	-2	0	3	
	10	1	1	1	1		2	15		2	1	0	-1	3	
	12	1	0	1	1		2	16	1	2	1	0	0	3	1
	13	1	1	2	0		3	17		2	-1	0	-1	3	
	14	1	1	2	1		3	18	2	2	-1	0	0	3	1
	16	1	1	0	1		3	21	3	2	1	1	0	5	1
	18	1	-1	0	1		3	22	6	2	0	1	0	5	1
20		1	0	0	-1	4		23		2	-2	-1	0	5	
	21	1	-1	-1	1		5	24		2	-2	-2	0	5	
	22	1	0	-1	1		5	25		2	0	-2	0	5	
	23	1	2	1	1		5	26		2	+1	-1	0	5	
	24	1	2	2	1		5	27		2	1	1	-1	5	
	25	1	0	2	1		5	28		2	0	1	-1	5	
	26	1	-1	1	1		5	29		2	-2	-1	-1	5	
								30		2	-2	-2	-1	5	
								31		2	0	-2	-1	5	
	29	1	2	1	0		5	32		2	1	-1	-1	5	
	30	1	2	2	0		5	19		2	0	0	1		4
	31	1	0	2	0		5								
	32	1	-1	1	0		5								

NOTE: The force constants for first neighbors are α .
The force constants for second neighbors are β .
The force constants for third neighbors are γ .
The force constants for fourth neighbors are δ .
The force constants for fifth neighbors are ϵ .

which is the force acting on the particle at $\vec{x}(l, j)$ in the α -direction. In equilibrium this force must vanish; thus,

$$-\left(\frac{\partial \phi_T}{\partial u_\alpha}\right)_{(l, j)} \Big|_{\text{equil.}} = 0 = - \sum_{l', j'} \left(\frac{\partial \psi}{\partial s}\right)_{s=s_0(ll', jj')} \frac{x_\alpha(l, j) - x_\alpha(l', j')}{s_0(ll', jj')} .$$

Consequently, in the harmonic approximation we can write for the equation of motion of a particle in the lattice under the influence of central forces:

$$M \ddot{u}_\alpha(l, j) = \sum_{l', j'} \sum_{\beta} K(ll', jj') \frac{s_{0\alpha}(ll', jj') s_{0\beta}(ll', jj')}{s_0^2(ll', jj')} u_\beta(l', j') - \sum_{\beta} u_\beta(l, j) \sum_{l', j'} K(ll', jj') \frac{s_{0\alpha}(ll', jj') s_{0\beta}(ll', jj')}{s_0^2(ll', jj')} , \quad (2)$$

where $K(ll', jj') \equiv (\partial^2 \psi / \partial s^2)_{s=s_0(ll', jj')}$ are the atomic force constants and M is atomic mass. For Eq. (2) we assume the solutions are plane waves:

$$u_\alpha(l, j) = C_\alpha^j(\vec{k}) e^{2\pi i[\vec{k} \cdot \vec{x}(l) - \nu t]} , \quad (3)$$

where \vec{k} is the wave vector, ν the frequency of the wave, and $\vec{C}^j(\vec{k})$ the polarization vectors. After substitution of Eq. (3) into Eq. (2), we find the condition for solubility

$$|D_{\alpha\beta}(\vec{k})_{jj'} - (2\pi\nu)^2 M \delta_{\alpha\beta} \delta_{jj'}| = 0 , \quad (4)$$

where

$$D_{\alpha\beta}(\vec{k})_{jj'} = - \sum_{l'} K(ll', jj') \frac{s_{0\alpha}(ll', jj') s_{0\beta}(ll', jj')}{s_0^2(ll', jj')} e^{2\pi i \vec{k} \cdot [\vec{x}(l') - \vec{x}(l)]} + \delta_{jj'} \sum_{l'', j''} K(ll'', jj'') \frac{s_{0\alpha}(ll'', jj'') s_{0\beta}(ll'', jj'')}{s_0^2(ll'', jj'')} \quad (5)$$

in the literature is called the dynamical matrix. Since $D_{\alpha\beta}(\vec{k})_{jj'}$ is independent of l as indicated, l is set equal to zero in order to conform with Table 8.1.

$D_{\alpha\beta}(\vec{k}_{jj})$ is a 6×6 matrix, and consequently there will be both optical and acoustical branches to the dispersion relations $\omega(\vec{k})$ versus \vec{k} . Schmunk, et al., (39) have measured the dispersion relations from observations of the one-phonon neutron scattering in the symmetry directions of a single beryllium crystal, and thus have determined the force constants which give a best fit of the above model to the experimental data. These force constants for the first five neighbors are $\alpha = 1.60$, $\beta = 2.66$, $\gamma = 0.188$, $\delta = 0.668$, and $\epsilon = 0.454$ in units of 10^4 dynes/cm.

8.2. FREQUENCY SPECTRUM OF BERYLLIUM

All the possible values of the wave vector \vec{k} are obtained by restricting \vec{k} to lie in the first Brillouin zone of the crystal. The first Brillouin zone for a hexagonal close-packed lattice is a hexagonal cylinder.

The reciprocal lattice vectors are defined by

$$\vec{b}_1 = \frac{\vec{a}_2 \times \vec{a}_3}{v_c}, \quad \vec{b}_2 = \frac{\vec{a}_3 \times \vec{a}_1}{v_c}, \quad \vec{b}_3 = \frac{\vec{a}_1 \times \vec{a}_2}{v_c},$$

where $v_c = \sqrt{3} a^2 c / 2$ is the volume of a unit cell. Since

$$\vec{k} = k_1 \vec{b}_1 + k_2 \vec{b}_2 + k_3 \vec{b}_3,$$

if we restrict \vec{k} to lie in the zone defined by the planes normal to the vectors

$$\pm \frac{\vec{b}_1}{2}, \quad \pm \frac{\vec{b}_2}{2}, \quad \pm \frac{\vec{b}_1 - \vec{b}_2}{2}, \quad \pm \frac{\vec{b}_3}{2},$$

the whole frequency range will be covered.

The frequency spectrum $f(\omega)$ is defined such that $f(\omega) d\omega$ gives the number of frequencies between ω and $\omega + d\omega$. If a large computer is available, the best means of finding $f(\omega)$ seems to be to solve Eq. (4) for a large number of values of \vec{k} in the first Brillouin zone of the crystal, and hence to construct a histogram for $f(\omega)$. Owing to symmetry, however, it is possible to reduce the size of the region in which Eq. (4) must be solved. In Fig. 8.1, the central plane ($b_3 = 0$) of the Brillouin zone is shown. It is clear that we can restrict the solutions to the small section shown, which is $1/12$ of the zone, and in the full zone we can make the further restriction of $0 \leq k_3 \leq 1/2$. Thus, it is necessary to solve Eq. (4) only in a region which is $1/24$ of the first Brillouin zone. However, since

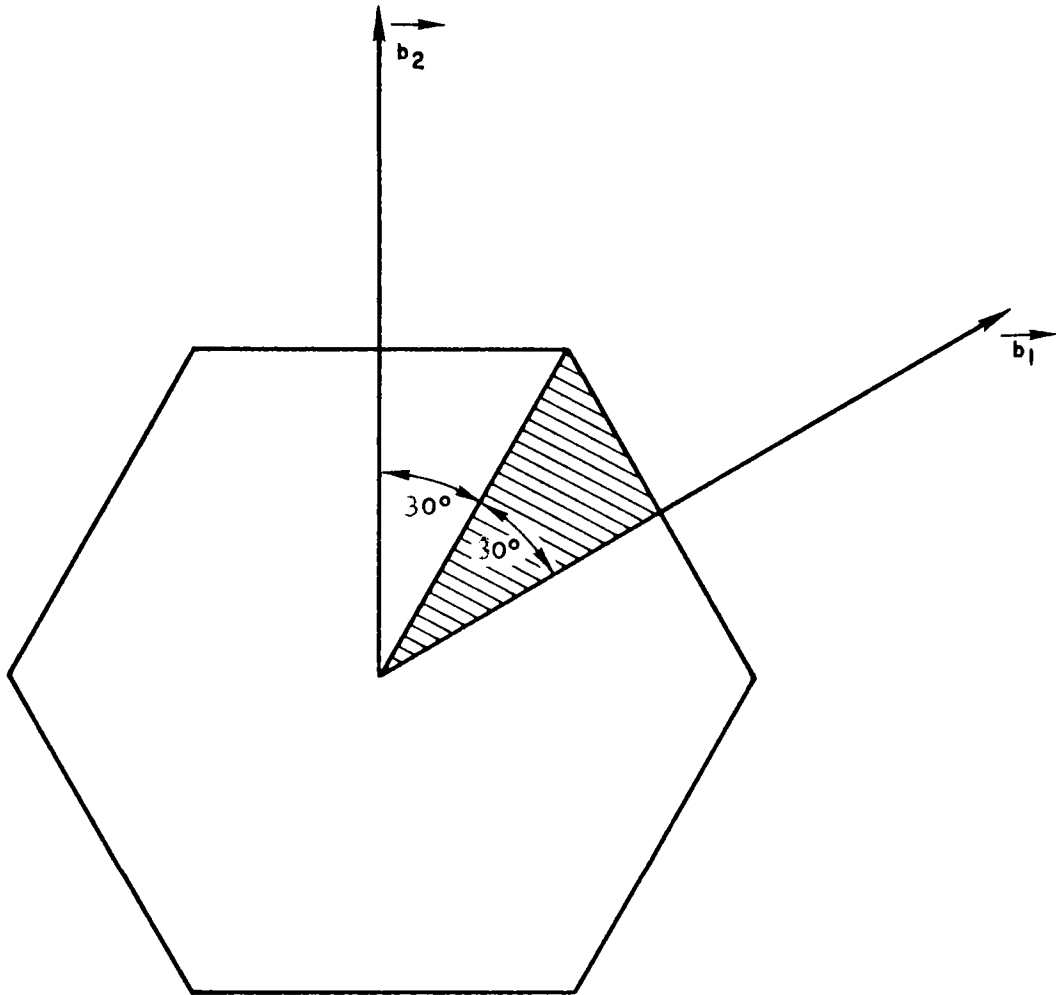


Fig. 8. 1--The plane $\vec{b}_3 = 0$ of the first Brillouin zone of beryllium

we are in effect sampling the roots in the whole zone, we must be careful to weight the points in a manner depending on whether they occur on the faces, corners, or edges of the reduced region. Table 8.2 gives the weights associated with each point of the reduced zone. The weights correspond to the total number of equivalent points in the whole Brillouin zone. The reduced zone is given by $0 \leq k_1 \leq 1/3$, $0 \leq k_2 \leq k_1$, $0 \leq k_3 \leq 1/2$; $1/3 \leq k_1 \leq 1/2$, $0 \leq k_2 \leq 1 - 2k_1$, $0 \leq k_3 \leq 1/2$.

Table 8.2

WEIGHTING OF POINTS IN THE REDUCED BRILLOUIN ZONE
OF THE BERYLLIUM CRYSTAL

Points	Weight
$k_1 = k_2 = k_3 = 0$	1
$k_1 = k_2 = 0, k_3 \neq 0$	2
$k_1 \neq k_2 \neq 0, k_3 = 0$	12
$k_3 \neq 0, k_1 \neq k_2 \neq 0$	24
$k_3 = 0, k_2 = 0, k_1 \neq 0$	6
$k_3 \neq 0, k_2 = 0, k_1 \neq 0$	12
$k_3 = 0, k_1 = k_2 \neq 0$	6
$k_3 \neq 0, k_1 = k_2 \neq 0$	12

Equation (4) was solved on the IBM-7090 for 2413 points in the reduced zone. The frequency spectrum obtained is given in Fig. 8.2.

Sinclair⁽⁴⁰⁾ has measured the differential neutron scattering cross section of beryllium at 293°K. The cross section is given by

$$\frac{d^2\sigma}{dE d\Omega} = \frac{\sigma_b}{4\pi} \frac{k}{k_0} e^{-\beta/2} \frac{S(\alpha, \beta)}{T}, \quad (6)$$

where σ_b is the bound-atom cross section, \vec{k}_0 is the initial neutron momentum, \vec{k} is the final momentum, $\alpha = (\vec{k} - \vec{k}_0)^2 / (2MT)$, $\beta = (k^2 - k_0^2) / (2mT)$, M is the mass of the scatterer, m is the neutron mass, T is the temperature in electron-volts, and $S(\alpha, \beta)$ is the scattering law which depends on the dynamics of the scatterer. The data are presented by plotting $S(\alpha, \beta) / \alpha$ versus α for given β . It has been pointed out that the frequency spectrum can be obtained from the measurements by extrapolating $S_s(\alpha, \beta) / \alpha$ versus

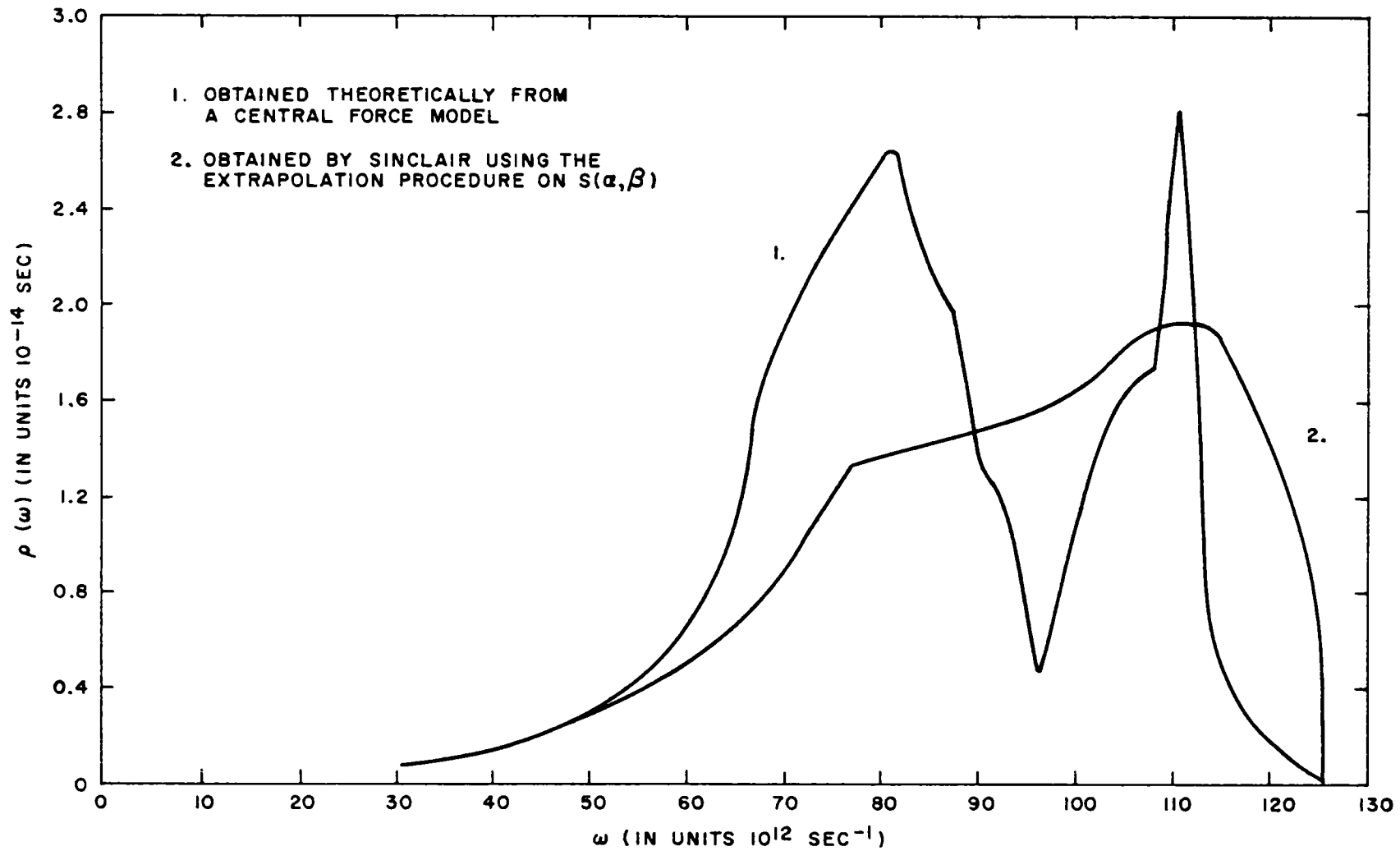


Fig. 8.2--Frequency spectra of beryllium

α to $\alpha = 0$ by using the relation

$$\frac{T}{2\beta \sinh \beta/2} f(\omega) = \lim_{\alpha \rightarrow 0} \frac{S_s(\alpha, \beta)}{\alpha},$$

where $\omega = \beta T$ is the frequency and $S_s(\alpha, \beta)$ is the "self-part" of the scattering law, i. e., in the absence of interference effects. The difficulty with this method is that for small α (small momentum transfer), interference effects are hard to separate, and thus the method is not expected to be sensitive to all the details of the frequency spectrum. In Fig. 8.2, the frequency spectrum of beryllium obtained experimentally by the above method is compared with that obtained from the central force model.

8.3. SCATTERING KERNEL FOR BERYLLIUM

In the absence of interference effects, incoherent approximation, the scattering cross section can be calculated from the expression

$$\frac{d^2\sigma}{dE d\Omega} = \frac{\sigma_b}{4\pi} \frac{k}{k_0} \frac{1}{2\pi} \int_{-\infty}^{\infty} dt e^{i\epsilon t} X(\kappa^2, t), \quad (7)$$

where ϵ is the energy transfer to the neutron, κ^2 is the square of the momentum transfer, and

$$X(\kappa^2, t) = \exp\left[\frac{\kappa^2}{2M} \int_{-\infty}^{\infty} \frac{f(\omega) e^{-\omega/2T}}{2\omega \sinh(\omega/2T)} (e^{i\omega t} - 1) d\omega\right]. \quad (8)$$

Equation (8) is strictly true only for an isotropic substance, which does not strictly apply for beryllium, but should be a more than adequate approximation for reactor applications. To be more precise, it would be necessary to calculate the polarization vectors $\vec{C}^j(\vec{k})$. The IBM-7090 code SUMMIT⁽¹⁷⁾ can be used to evaluate $S_s(\alpha, \beta)$ from Eqs. (6) and (7) once $f(\omega)$ is given. $S_s(\alpha, \beta)/\alpha$, compared with the measurements of Sinclair,⁽⁴⁰⁾ using the theoretical $f(\omega)$ for several values of β at 293° K, is shown in Figs. 8.3 and 8.4. The discrepancy at low values of α is clearly due to the influence of coherent scattering, i. e., interference effects. For neutron slowing-down, however, it is the large values of α which are important, and thus the calculated scattering law using the incoherent approximation and the isotropic approximations can be expected to yield good results, as the comparisons in Figs. 8.3 and 8.4 show.

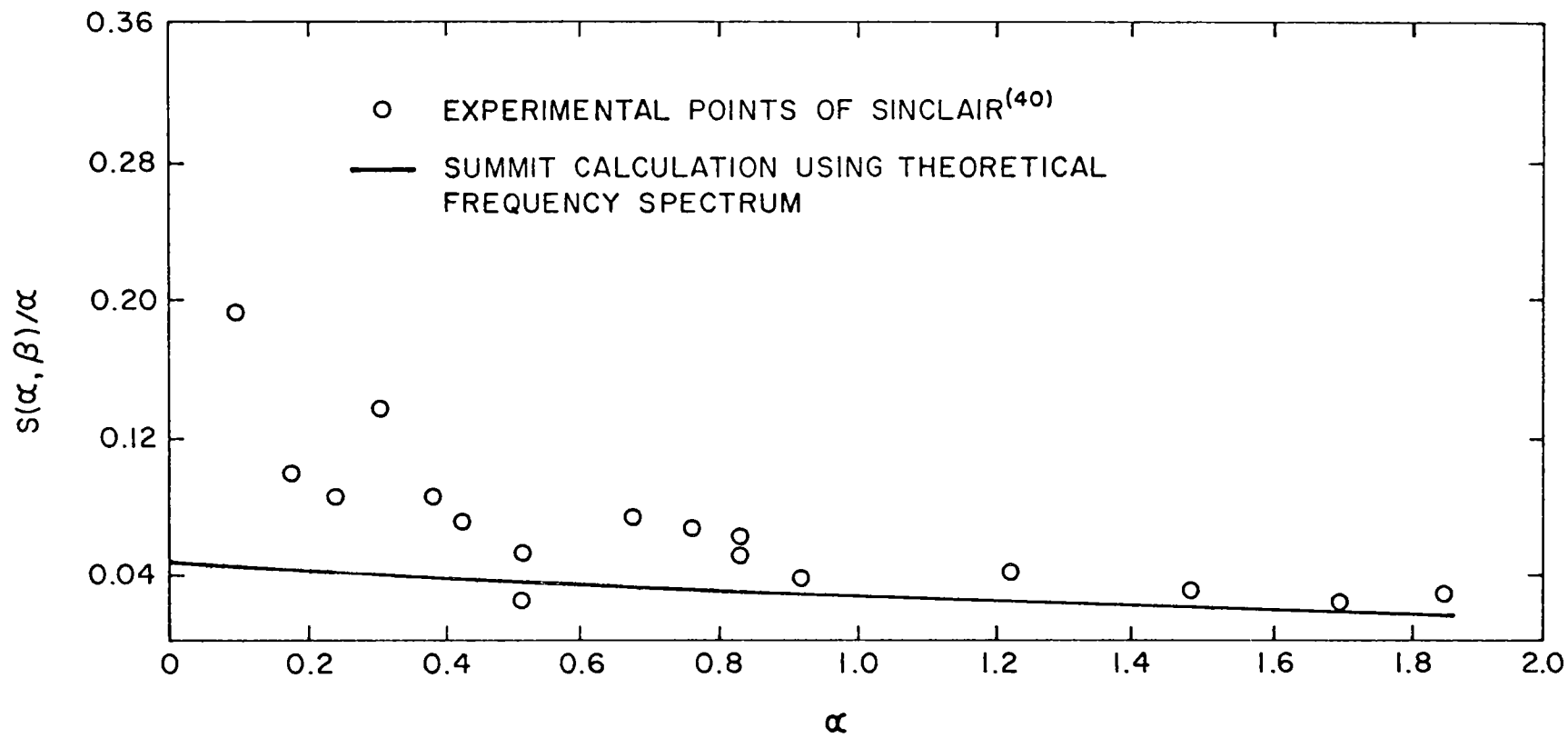


Fig. 8.3--Scattering law for beryllium ($\beta = 1.00$)

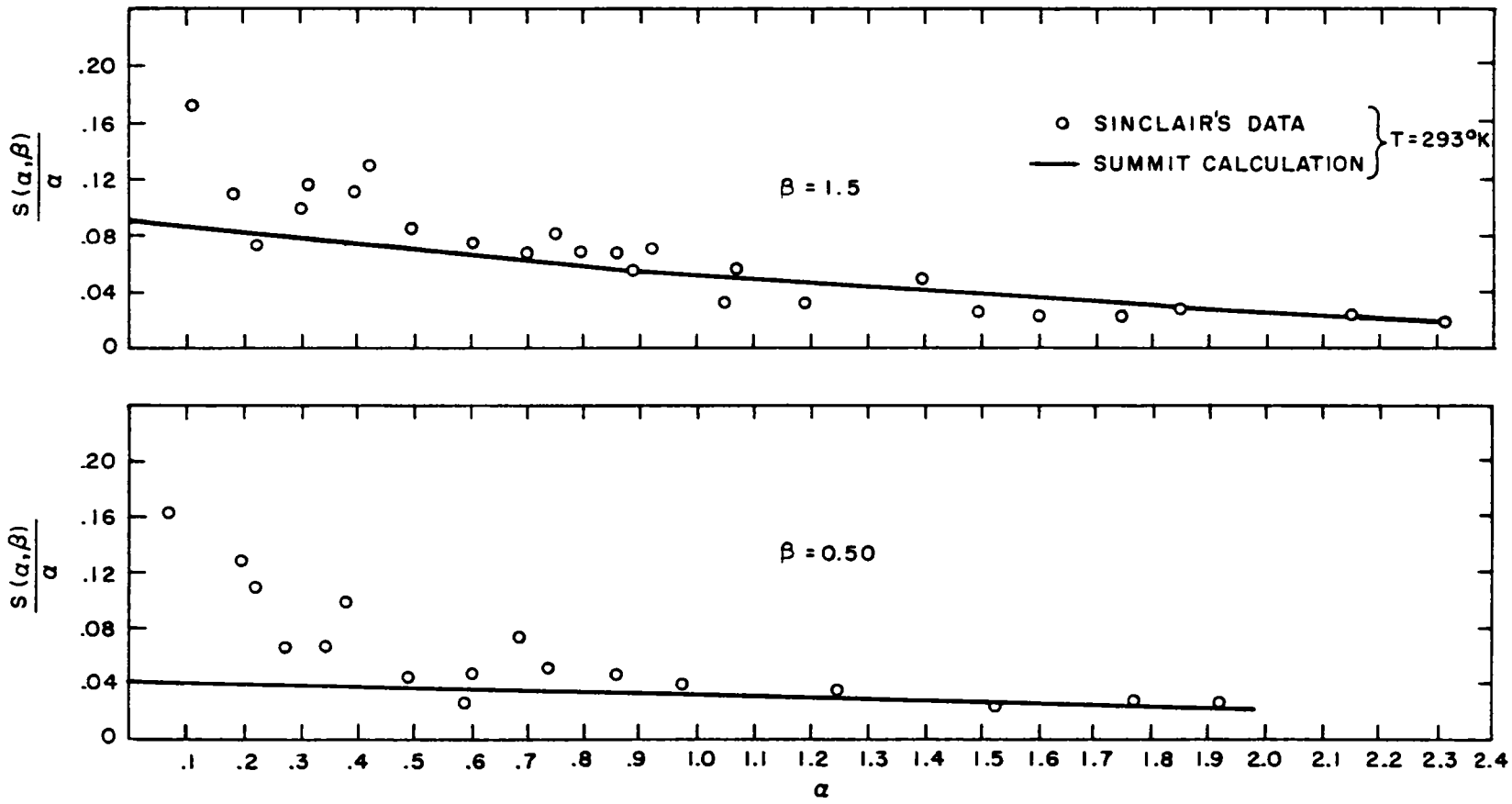


Fig. 8. 4--Scattering law of beryllium for two different values of β

8.4. SPECIFIC HEAT

The frequency spectrum of beryllium can be used to calculate the specific heat at constant volume, C_v , through the fundamental relation given by Eq. (1) in Section VII. The maximum frequency, ω_{\max} , corresponds to a phonon energy $\omega_{\max} = 0.0826$ ev. A curve of $C_v(T)$ versus T obtained from Fig. 8.4 and Eq. (1) is given in Fig. 8.5. At room temperature we find $C_v = 4.10$ cal-mole⁻¹-deg.⁻¹ as compared with a measured value of 4.2 cal-mole⁻¹-deg.⁻¹. The reason for not quoting a greater accuracy for the latter value is that experimentally one measures (for obvious reasons) C_p , but the compressibility of beryllium is not well-enough known to obtain accurately C_v from C_p . At low temperatures this correction is negligible.

8.5. ELASTIC SCATTERING

As stated earlier, the computer code SUMMIT⁽¹⁷⁾ calculates the scattering cross section in the incoherent approximation for inelastic scattering. For transport problems it is also necessary to have the elastic cross section. Elastic scattering is defined as the zero phonon term in a multiphonon expansion. SUMMIT cannot be used to calculate the incoherent elastic scattering. Therefore, in the following we present expressions for the coherent and incoherent elastic scattering.

The multiphonon expansion for the scattering of thermal neutrons from crystalline solids is given by several authors⁽⁴²⁾⁽⁴³⁾ and will not be repeated here. The elastic incoherent scattering per atom is given by

$$\frac{d\sigma_{\text{el, incoh}}}{d\Omega} = \frac{\sigma_{\text{incoh}}}{4\pi} \exp\left[-\kappa^2 h^2 / 2M\right] \int_0^{\omega_{\max}} \frac{f(\omega)}{\omega} \coth \frac{\omega}{2\kappa T} d\omega,$$

where M is the mass of a beryllium atom, $\vec{\kappa}$ is the neutron momentum transfer, and σ_{incoh} is the zero-energy bound-atom cross section. The exponential is just the familiar Debye-Waller factor. The elastic coherent scattering from a single beryllium crystal is given by

$$\frac{d\sigma'_{\text{el, coh}}}{d\Omega} = \frac{N_c}{V_c} \frac{\sigma_{\text{coh}}}{4\pi} (2\pi)^3 \sum_{\vec{\tau}} e^{-\kappa^2 W} \left| F_{\vec{\tau}} \right|^2 \delta^3(\vec{\kappa} - \vec{\tau}),$$

where N_c is the number of unit cells in the crystal, V_c is the volume of a unit cell, σ_{coh} is the zero-energy bound-atom coherent cross section, and $\vec{\tau}$ is a reciprocal lattice vector. $F_{\vec{\tau}}$ is the structure factor for the scattering

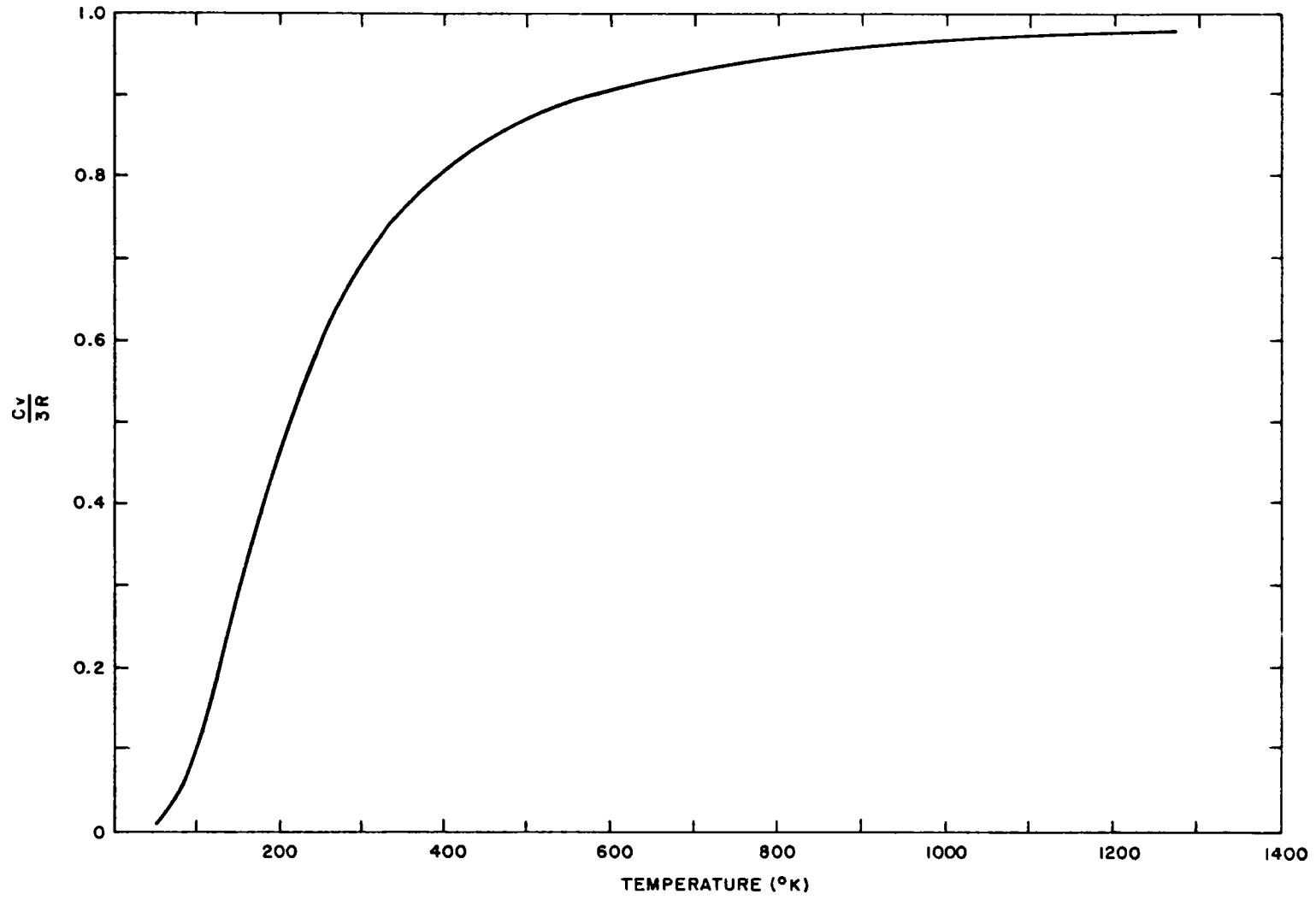


Fig. 8.5--Theoretical variation of specific heat of beryllium with absolute temperature

from a unit cell:

$$F_{\vec{\tau}} = \sum_j e^{i\vec{\tau} \cdot \vec{r}(j)},$$

and

$$W = \frac{\hbar}{2M} \int_0^{\omega_{\max}} \frac{f(\omega)}{\omega} \coth \frac{\omega}{2KT} d\omega.$$

For most applications one will be dealing with a polycrystalline sample of beryllium, so an orientation average is necessary. The orientation average is obtained by integrating over the directions of $\vec{\tau}$, and since

$$\delta^3(\vec{\kappa} - \vec{\tau}) = \frac{\delta^2(\hat{\kappa} - \hat{\tau}) \delta(\kappa - \tau)}{\tau^2},$$

where $\hat{\kappa}$ and $\hat{\tau}$ are unit vectors in the directions of $\vec{\kappa}$ and $\vec{\tau}$, respectively, we find

$$\frac{d\sigma_{\text{el, coh}}}{d\Omega} = \frac{1}{4\pi} \int d\hat{\tau} \frac{d\sigma'_{\text{el, coh}}}{d\Omega},$$

or

$$\left(\frac{d\sigma_{\text{el, coh}}}{d\Omega} \right)_{\text{atom}} = \frac{\pi}{2\sqrt{3} a^2 c} \sigma_{\text{coh}} \sum_{\vec{\tau}} \frac{e^{-\tau^2 W}}{\tau^2} \left| F_{\vec{\tau}} \right|^2 \delta\left(\frac{\tau - 2k_0 \sin \theta/2}{2} \right),$$

since $V_c = \sqrt{3} a^2 c/2$, $\kappa = |\vec{\kappa}| = 2k_0 \sin \theta/2$, and there are two atoms per unit cell. This last equation shows that the angular distribution of coherent, elastically scattered neutrons consists of a series of peaks, each peak occurring whenever the magnitude of the momentum transfer is equal to that of a reciprocal lattice vector.

Since

$$\begin{aligned} \vec{\tau} &= 2\pi (l_1 \vec{b}_1 + l_2 \vec{b}_2 + l_3 \vec{b}_3) \\ &= 2\pi \left(\frac{l_1}{a} \hat{i} + \frac{l_1 + 2l_2}{\sqrt{3} a} \hat{j} + \frac{l_3}{c} \hat{k} \right), \end{aligned}$$

where l_1, l_2, l_3 are integers, and

$$\vec{r}(j=2) = \frac{a}{\sqrt{3}} \hat{j} + \frac{c}{2} \hat{k},$$

then

$$\vec{\tau} \cdot \vec{r} (j=2) = 2\pi \left(\frac{l_1 + 2l_2}{3} + \frac{l_3}{2} \right)$$

and

$$\begin{aligned} \left| \mathbf{F}_{\vec{\tau}} \right|^2 &= \left| 1 + e^{-2\pi i (l_1 + 2l_2/3) + (l_3/2)} \right|^2, \\ &= 2 \left[1 + \cos \pi \left(\frac{2l_1 + 4l_2 + 3l_3}{3} \right) \right]. \end{aligned}$$

We shall be interested primarily in the total and P_1 components of the elastic coherent scattering cross sections per atom:

$$\sigma_{\text{el, coh}} = \sigma_{\text{coh}} \frac{\lambda^2}{2\sqrt{3} a^2 c} \sum_{\tau}^{\tau/2\pi < 2/\lambda} \frac{1}{\tau} e^{-\tau^2 W} \left[1 + \cos \pi \left(\frac{2l_1 + 4l_2 + 3l_3}{3} \right) \right],$$

where λ is the incident neutron wavelength, and

$$\begin{aligned} (\sigma_{\text{el, coh}})_{P_1} &= \sigma_{\text{coh}} \frac{\lambda^2}{2\sqrt{3} a^2 c} \sum_{\tau}^{\tau/2\pi < 2/\lambda} \frac{1}{\tau} e^{-\tau^2 W} \left(1 - \frac{\tau^2 \lambda^2}{8\pi^2} \right) \\ &\quad \left[1 + \cos \pi \left(\frac{2l_1 + 4l_2 + 2l_3}{3} \right) \right]. \end{aligned}$$

Both of the above expressions have been programmed for computation on the IBM-7090. Figure 8.6 shows plots of these expressions for various values of λ at $T = 293^\circ\text{K}$. The value of σ_{coh} is 7.53 barns.

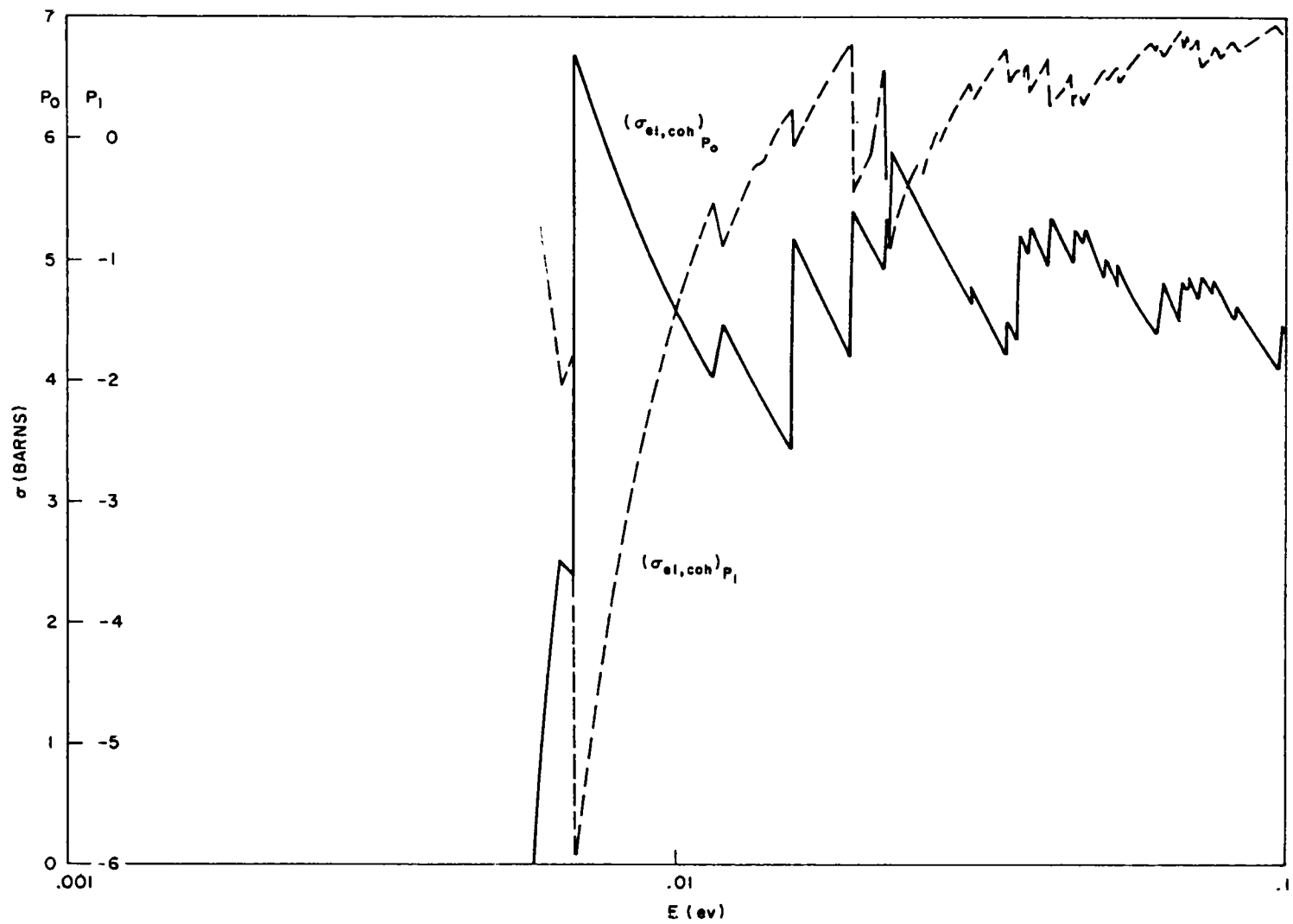


Fig. 8.6--Elastic coherent scattering components of beryllium

IX. PULSED CRITICAL ASSEMBLY

9. 1. INTRODUCTION

The series of pulsed neutron measurements on the Linac multiplying assembly⁽⁴⁴⁾ has been completed. The assembly was designed to be a bare homogeneous slab of enriched uranium-aluminum plates in water. Measurements of the steady-state source multiplication and the neutron counting rate as a function of time after a neutron burst have been made for several subcritical fuel loadings, together with a pulsed neutron measurement at the critical loading. A top view of the arrangement of the assembly and sources is shown in Fig. 9. 1. Two views of the actual assembly are shown in Figs. 9. 2 and 9. 3. The assembly was set up in a large room far from the walls and ceilings in order to reduce time-dependent effects from room return. The nearest wall was 8 ft away, and all assembly support structure was kept to a minimum so that the geometry was clean and calculable.

The Linac electron beam was piped to a small heavy-metal target just outside one face of the slab. The neutron-versus-time behavior was obtained from a small fission counter remotely positioned in a cylindrical tube or "glory hole" which passed through the assembly in the thin dimension. Repetition rates of from 30 to 120 pps were used, and the time distribution of counts was obtained from 4 μ sec after the burst to a time just before the next burst, using multichannel time analyzers.

From these data, the die-away of the fundamental mode was obtained, and by the method of Garelis and Russell,⁽⁴⁵⁾ the number of dollars subcritical and the value of $k \beta / \ell$ was obtained at each subcritical loading. From a knowledge of the critical size, the subcritical size, and the subcritical multiplication measurements, a value of subcritical k was inferred.

9. 2. PULSED NEUTRON MEASUREMENTS

9. 2. 1. General

For many of the subcritical loadings made in the approach to critical, pulsed neutron measurements were made. These consisted in measuring the neutron count rate at some position in the core as a function of time after a short pulse of neutrons generated just external to the core. This

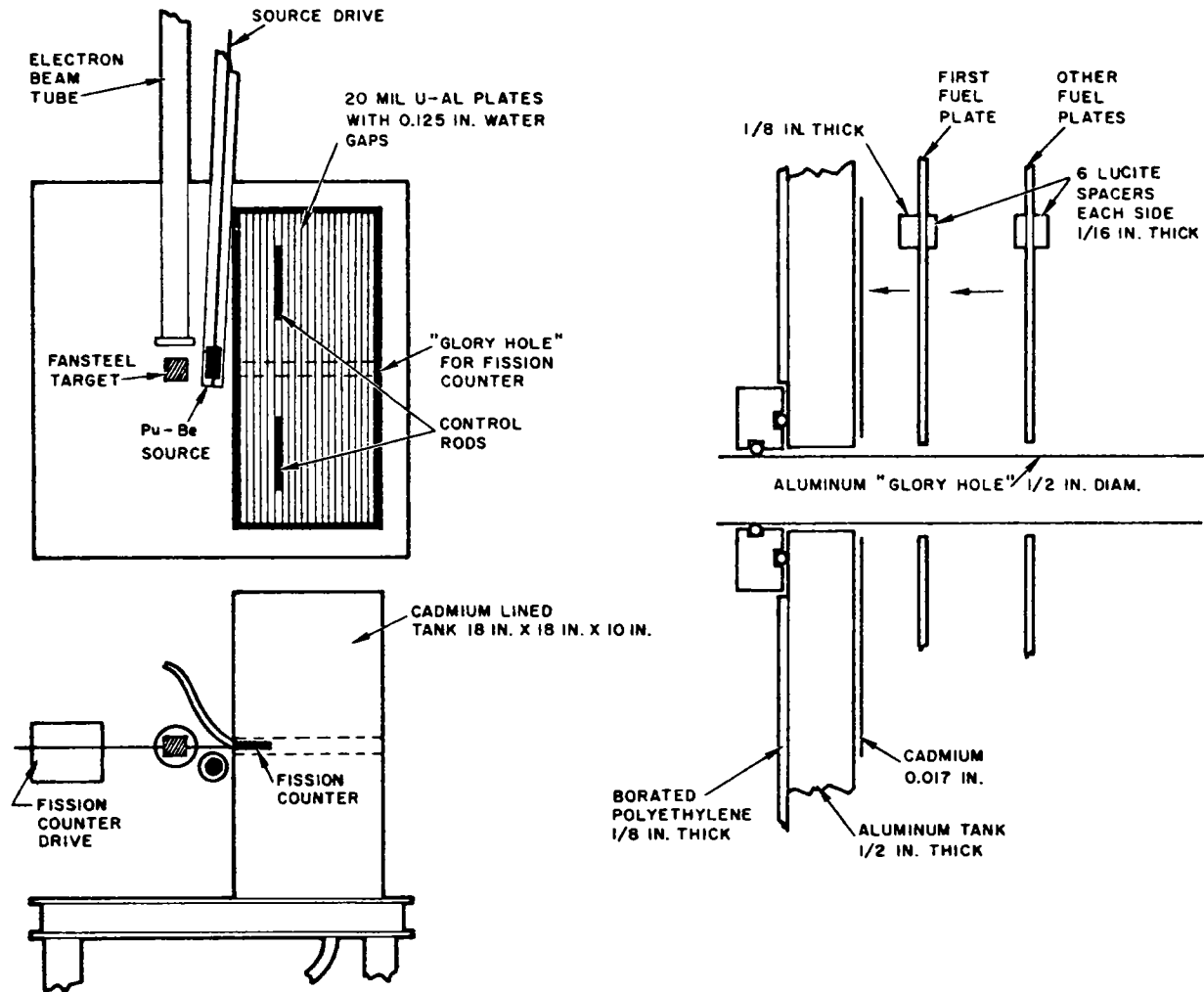


Fig. 9. 1--Geometrical arrangement for pulsed neutron measurements on the multiplying assembly

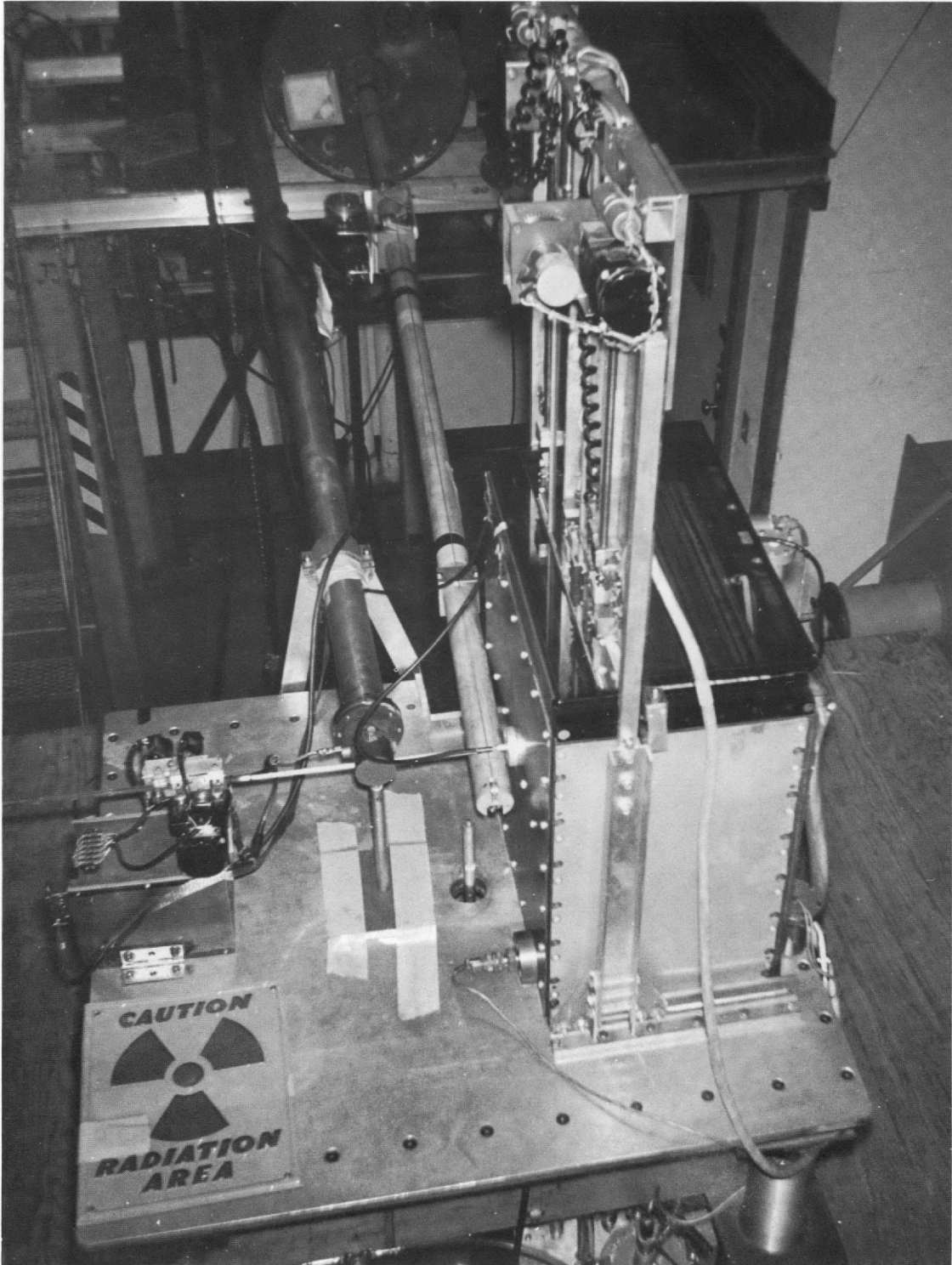


Fig. 9.2--End-on view of the multiplying assembly

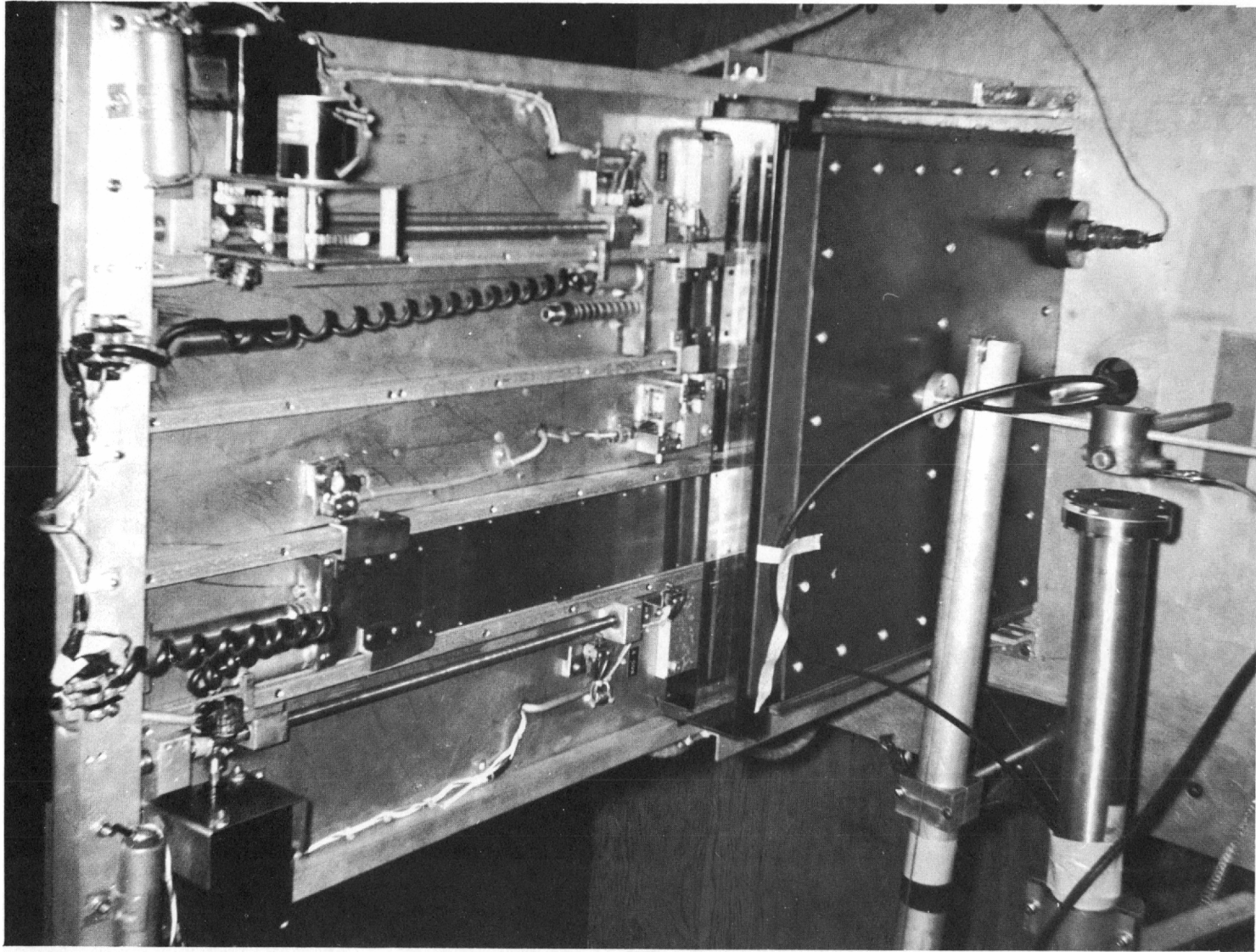


Fig. 9.3--Side view of multiplying assembly

neutron pulse was generated by an electron-beam pulse striking a heavy-metal (Fansteel) target. The target, which was about 2 in. in diameter and 2 in. long, was placed about 3 in. from the center of one face of the slab. The neutron pulse was typically generated by a Linac pulse of about 30 Mev with a width of 0.1 μ sec and a current of 1 ma during this time.

The neutron counting rate was measured using a miniature fission counter (1/4 in. in diameter by 1 in. long) positioned in a tube running through the center of the core perpendicular to the faces of the slab. This counter could be remotely positioned from one edge of the core to the other, and in three cases, measurements were made on the same loading with the counter at from 8 to 12 positions across the core thickness to determine how large any modal effects might be. The modal analysis was discussed in a previous report. (46)

The counts from this fission counter were time-analyzed using two time analyzers simultaneously, a 1024-channel analyzer (TMC) and a 256-channel analyzer (RCL). The 1024-channel analyzer was set on short channel widths (as small as 2 μ sec) to obtain the detailed shape of the early time behavior and exponential decay, while the 256-channel analyzer was set on long channel widths (16, 32, or 64 μ sec) to obtain more statistics on the delayed neutron tail. The analyzers were gated on at a definite time after the accelerator pulse, using a digital delay. This delay time was in most cases 4 μ sec, being limited to the time at which the effects of the gamma flash (from the electrons hitting the target) on the fission counter had recovered.

A typical time behavior of the neutrons following a repetitive pulse is shown in Fig. 9.4. After a few minutes of pulsing, the delayed neutron tail reached equilibrium and data were accumulated on the analyzers for many pulses until the statistics on the counts were at the desired level.

9.2.2. Determination of α

The data from the two time analyzers are corrected for any count loss by a code for the IBM-7090 and then are least-squares-fitted to an exponential over an appropriate region of time by another code (CORC). The fit is weighted by the inverse square of the relative standard deviation of the counts. The delayed neutron background is subtracted prior to the fitting. The appropriate region over which to fit the exponential is that which contains only the decay of the fundamental mode. The spatial modal analysis reported previously⁽⁴⁶⁾ has shown that the fundamental mode alone exists (for this particular assembly) after about 200 μ sec. A plot of the spatial distribution of neutrons at various times after the pulse is shown in Fig. 9.5 for loading 8.

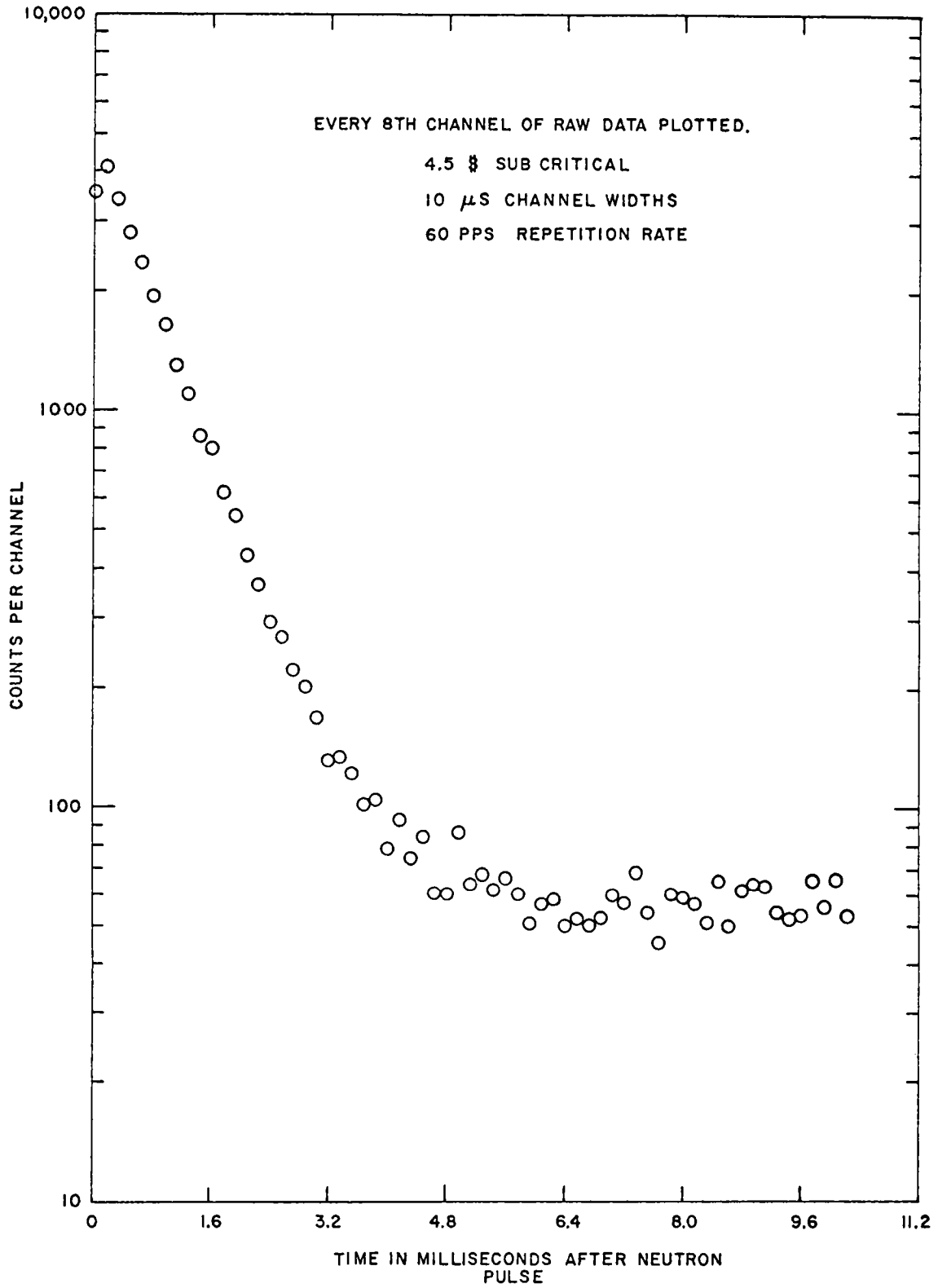


Fig. 9.4--Typical time behavior after pulsing of the multiplying assembly

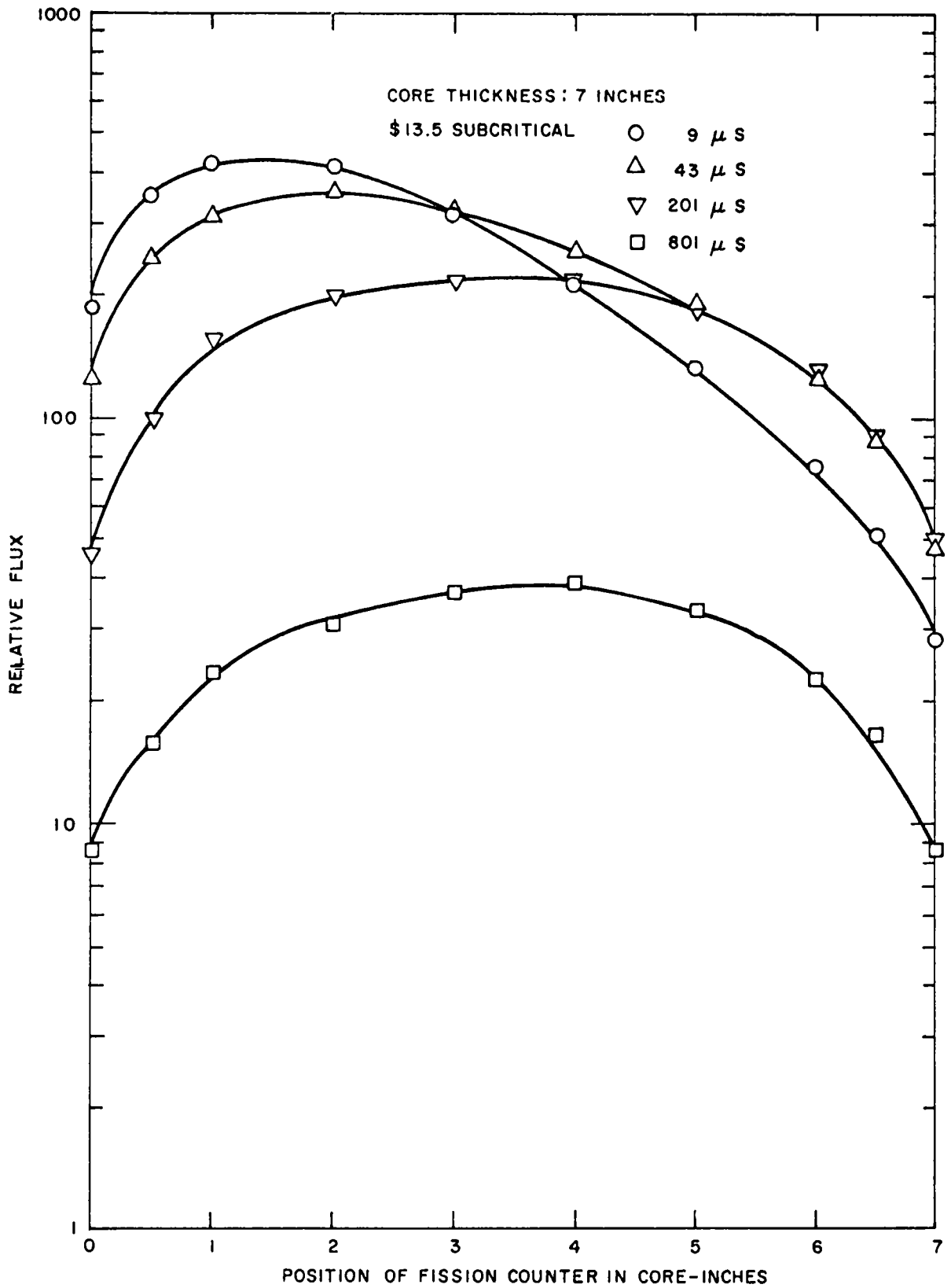


Fig. 9.5--Time variation of the spatial distribution of thermal neutrons in the multiplying assembly

In this way, a value for the reciprocal of the die-away time, namely, α (sec^{-1}), is obtained from each measurement. This α , combined with the α at critical (α_c), provides one common method of determining the number of dollars subcritical from

$$\$ = \frac{\alpha}{\alpha_c} - 1 .$$

To determine α_c , several measurements of α below critical were made and extrapolated to critical in addition to pulsing the assembly at critical and measuring the α . At critical, the delayed neutron background is a large part of the count rate, so a large number of counts must be accumulated to obtain good statistics on the difference between the measured count and the delayed neutron background.

9. 2. 3. Application of Method of Garelis and Russell

The method of Garelis and Russell⁽⁴⁵⁾ has been applied to the analysis of the data to determine the number of dollars subcritical and the value of $k \beta/\ell$. A brief description of the method is given in Section 9. 4. The method makes use of the entire shape of the neutron time behavior, including the delayed neutron tail. From the experimentally determined values of (1) α , (2) the delayed neutron level, and (3) a weighted integral over the prompt (measured minus delayed neutron background) part of the curve, a determination of dollars and $k \beta/\ell$ is made. An iteration is required to find the correct weighting factor, which is a function of $k \beta/\ell$; this iteration has been performed by hand but could also be done by machine code.

9. 2. 4. Results

A summary of results is given in Table 9. 1. The value of α listed is the average of data from both analyzers. The buckling is calculated from the dimensions using an extrapolation length of 2. 23 cm in the thin dimension and an extrapolation length of 4 cm in the transverse dimensions (18 in. by 18 in.).

Table 9. 2 gives the results of measurements of control-rod worths at several of the loadings. The rod worth is obtained from the difference in the number of dollars subcritical with and without the rod present. The No. 1 rod, which is referred to as the control rod (No. 2 is the safety rod), was reduced in total worth between loadings 11 and 12 so that the change in reactivity per inch of travel would be less than 5 cents/sec at its maximum worth when the k was greater than about 0. 9.

Table 9.1
SUMMARY OF PULSED NEUTRON MEASUREMENTS WITH NO RODS IN CORE

Loading Number	U ²³⁵ (g)	Core Thickness (in.)	Buckling (cm ⁻²)	Repetition Rate (pulses/sec)	Counter Distance from Source Side (in.)	α (sec ⁻¹)	Method of Russell and Garelis			Reactivity $\rho = \frac{\alpha}{\alpha_c} - 1$	k_{eff} from Buckling Change	Relative Inverse Counting Rate	By Source Multiplication	
							\$ Sub-critical	$k\beta/l$	k for β/l Constant				Δk_{eff}	k_{eff}
19 (critical)	2921.51	8.64	0.0209	30	0	231.7	0	231.7	1.00	0	1.00			
18	2904.47	8.50	0.0213	30	0	285.11	0.239	230.1	0.99	0.0230	0.992	1.00	0.00184	0.998
15	2852.95	8.38	0.0217	30	Center	560.01	1.411	232.2	----	1.417	0.983	6.99	0.013	0.987
12	2801.66	8.14	0.0224	60	Center	759.13	2.374	225.0	0.97	2.276	0.969	11.20	0.021	0.979
11	2750.17	8.04	0.0227	60	0	1221.72	4.496	222.3	0.96	4.273	0.964	20.79	0.038	0.962
					4	1235.30	4.507	224.4		4.331				
					8	1250.83	4.558	225.1		4.398				
10	2647.45	7.72	0.0238	60	Center	1759.25	6.941	221.5	0.96	6.593	0.943	30.44	0.056	0.944
9	2544.55	7.43	0.0249	60	Center	2206.0	9.112	218.1	0.94	8.521	0.923	37.54	0.069	0.931
8	2390.55	6.99	0.0268	60	0.5	3104	13.362	216.1	0.93	12.397	0.890	50.47	0.093	0.907
					3.0	3082	13.676	210.0	0.91	12.302				
					6.5	3102	13.539	213.3	0.92	12.388				
7	2236.40	6.53	0.0291	60	3.25	4232.43	20.81	194.1	0.84	17.267	0.853	66.25	0.122	0.878
6	2082.26	6.10	0.0316	60	3.25	5234.50	26.26	192.0	0.83	21.592	0.817	78.90	0.145	0.855
5	1928.05	5.63	0.0348	120	2	6616.68	33.08	194.1	0.84	27.557	0.774	94.70	0.174	0.826
					3.25	6527.81	34.61	183.3	0.79	27.173				

Table 9. 2

PULSED NEUTRON MEASUREMENTS OF ROD WORTH

Loading Number	Rod Position	α	Garelis and Russell			Using Critical α	
			$k \beta / \ell$	\$	Rod Worth (\$)	\$	Rod Worth (\$)
18	Out	285. 11	230. 1	0. 239	1. 11	0. 224	1. 08
	No. 1 in	537. 48	228. 7	1. 350		1. 308	
15	Out	560. 1	232. 2	1. 411	1. 15	1. 404	1. 08
	No. 1 in	811. 33	228. 0	2. 559		2. 483	
12	Out	759. 13	225. 0	2. 374	1. 11	2. 259	1. 12
	No. 1 in	1020. 79	227. 8	3. 481		3. 383	
No. 1 Rod Worth Changed							
11	Out	1235. 30	224. 3	4. 507		4. 304	1. 83
	No. 1 in	1661. 5	224. 1	6. 412	1. 90	6. 134	
	No. 2 in	1696. 5	222. 5	6. 625	2. 12	6. 284	
	Both in	2185. 5	224. 5	8. 733	4. 23	8. 384	
10	Out	1759. 25	221. 5	6. 941	2. 05	6. 554	1. 95
	No. 1 in	2213. 5	221. 5	8. 991		8. 504	
9	Out	2206. 0	218. 1	9. 112	2. 26	8. 472	1. 91
	No. 1 in	2651. 5	214. 2	11. 376		10. 384	
8	Out	3082	210. 0	13. 676		12. 233	2. 35
	No. 1 in	3629	209. 5	16. 322	2. 65	14. 582	
	No. 2 in	3689	211. 5	16. 441	2. 76	14. 839	
	Both in	4334	207. 3	19. 906	6. 23	17. 609	

A measurement made at loading 18 with the fission counter at the center of the core and at the edge of the core (effectively out of the core) resulted in a worth of -5 cents for the counter at the center of the core.

Figure 9. 6 shows a plot of α versus dollars subcritical for the dollars determined both from the method of Garelis and Russell and from the use of the critical α_c .

The reactivities obtained from these two methods of analysis of the data differ because of assumptions in the derivation of the expression

$$\$ = \frac{\alpha}{\alpha_c} - 1$$

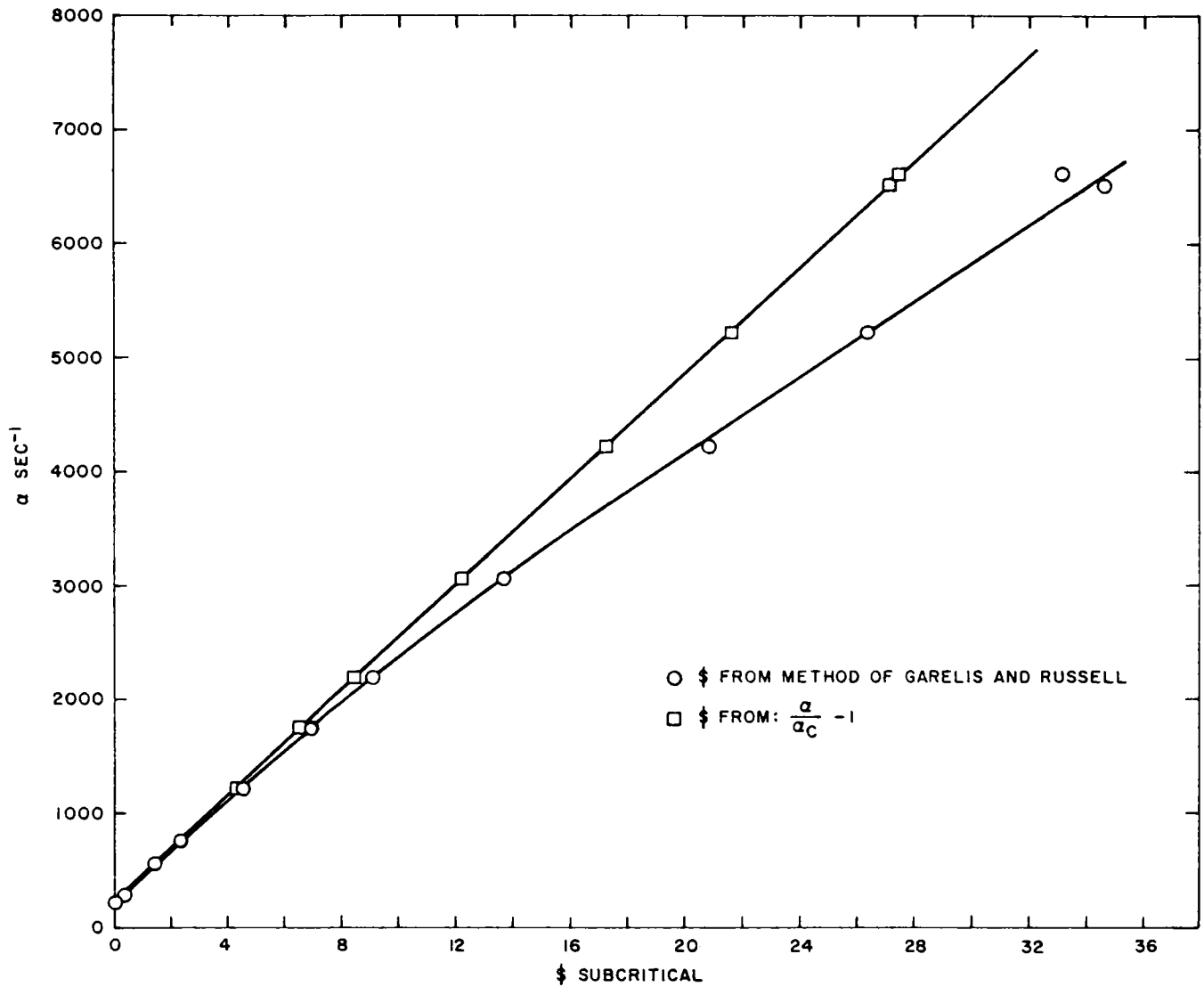


Fig. 9.6--Variation of α with dollars subcritical

This may be seen as follows:

$$\begin{aligned}\alpha &= \frac{1 - k}{l} p = \frac{1 - k(1 - \beta)}{l} , \\ &= \frac{k\beta}{l} \left(\frac{1 - k}{k\beta} + 1 \right)\end{aligned}$$

The reactivity in \$ is defined as

$$\$ = \frac{1 - k}{k\beta} ,$$

so

$$\alpha = \frac{k\beta}{l} (\$ + 1) .$$

The assumption is made that $k \cong 1$ and thus $\alpha = (\beta/l) (\$ + 1)$. Then assuming that the β/l measured at critical ($\alpha_c = \beta/l$) does not change with sub-criticality, we have

$$\$ = \frac{\alpha}{\alpha_c} - 1$$

In the Garelis and Russell method we have

$$\$ = \frac{\alpha}{k\beta/l} - 1 .$$

The ratio between $(\$ + 1)$ obtained in this way and $(\$ + 1)$ obtained from the Garelis and Russell method is just \underline{k} if β/l is constant, since a \underline{k} has been dropped in the use of the α_c method. More generally, the ratio between the two is x/α_c , where $x = k\beta/l$ and $\alpha_c = \beta_c/l_c$.

Figure 9.7 shows a plot of the results for $k\beta/l$ obtained using the method of Garelis and Russell. The value of $k\beta/l$ is plotted versus the dollars subcritical. In attempting to infer any change in β/l from these data, it is found that there is not enough information available without making assumptions about changes in β or l .

Certain inferences can be made on the basis of consistency. The straight line in Fig. 9.7 is consistent with a constant β/l (to within 10%). Table 9.3 shows some values of k determined from Fig. 9.7 assuming a constant β/l and a β consistent with this k and the reactivity in \$.

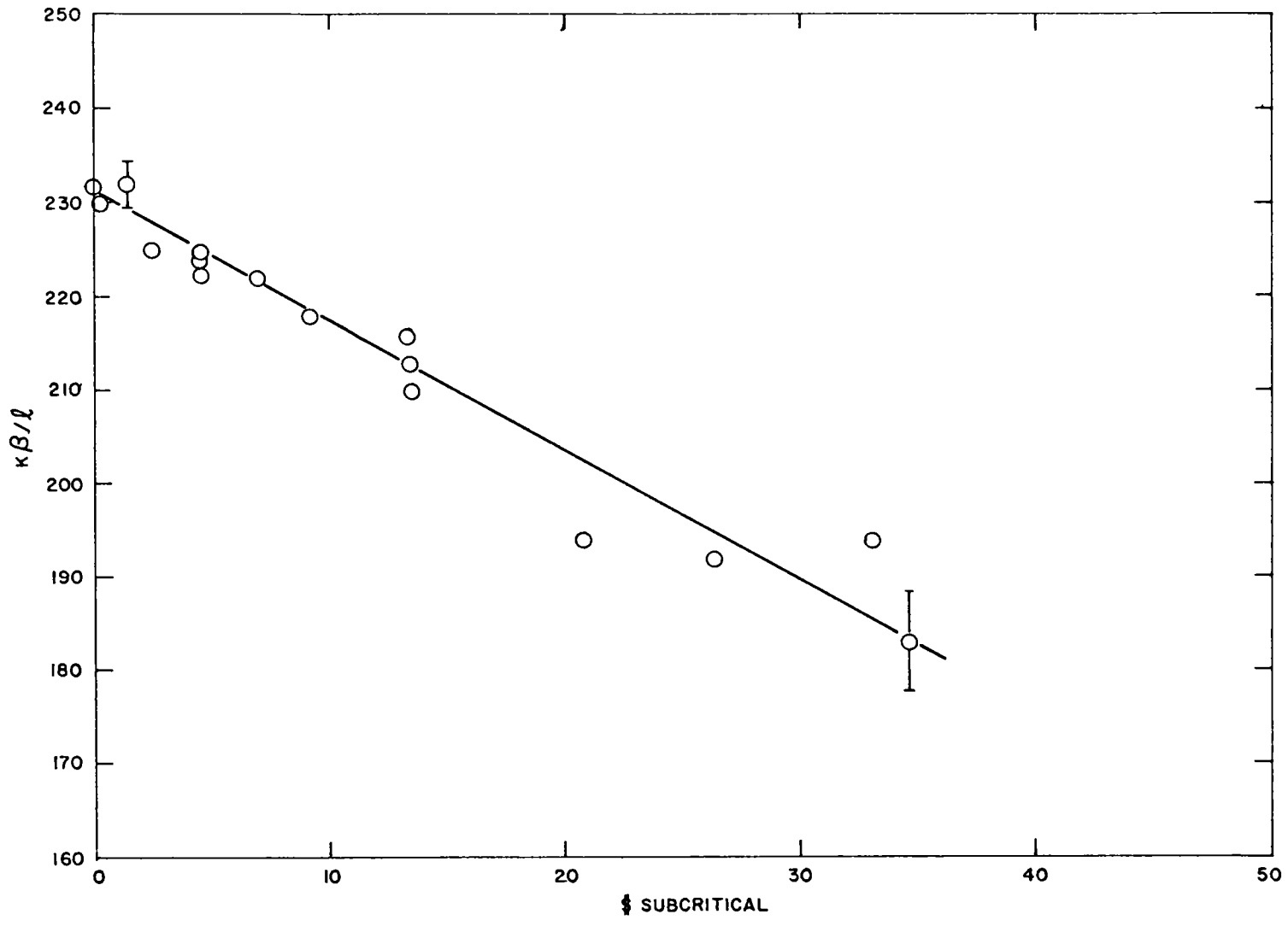


Fig. 9.7--Variation of $\kappa\beta/l$ with dollars subcritical by the method of Garelis and Russell

Table 9. 3

MULTIPLICATION CONSTANTS DETERMINED BY THE
METHOD OF GARELIS AND RUSSELL

$\$_{GR}$	α	$k\beta/\ell$	k $\beta/\ell = 232$	$\beta = \frac{1 - k}{k\$}$
5	1320	224	0.966	0.0070
10	2400	217	0.935	0.0070
15	3330	210	0.905	0.0070
20	4180	203	0.875	0.0071
25	5020	196	0.895	0.0073
30	5850	189	0.815	0.0076
35	6700	182	0.784	0.0079

As a test of the Garelis and Russell⁽⁴⁵⁾ method in treating the effects of modes at early times, data were taken at two loadings with the counter at three positions in the core. In Table 9. 1 the results for loadings 11 and 8 are shown with the counter at the core edge nearest the source, at the center, and at the edge furthest from the source. The results for the dollars subcritical are within about $\pm 1\%$. The shape of the initial time behavior for loading 11 is shown in Fig. 9. 8. The α 's for all three cases are the same, and the fact that the reactivities (β) agree indicates that the Garelis and Russell method is correctly handling the shape of the prompt part and the magnitude of the delayed neutron tail, which are different in each of these three cases. It can be seen in Fig. 9. 8 that there is a counter position between 0 and 4 in. where the modal effects are minimized.

As shown in Table 9. 1, the determination of k from the subcritical buckling after normalizing to a migration area at critical is not entirely satisfactory. Another way of arriving at the subcritical reactivity is to assume that the reactivity is known at one subcritical loading and then use the change in multiplication from that point to other points to determine the reactivity. Applying this technique here leads to a more satisfactory agreement than the use of the buckling change.

The use of α_c and α at a given subcriticality to determine the reactivity makes the assumption that β/ℓ does not change. In Table 9. 1 it can be seen that this method leads to the same result as that obtained from Garelis and Russell if account is taken of the difference in definitions. For example, the 20% decrease in k at loading 5 is enough to bring the $[(\alpha/\alpha_c) - 1]$ method into agreement with Garelis and Russell.

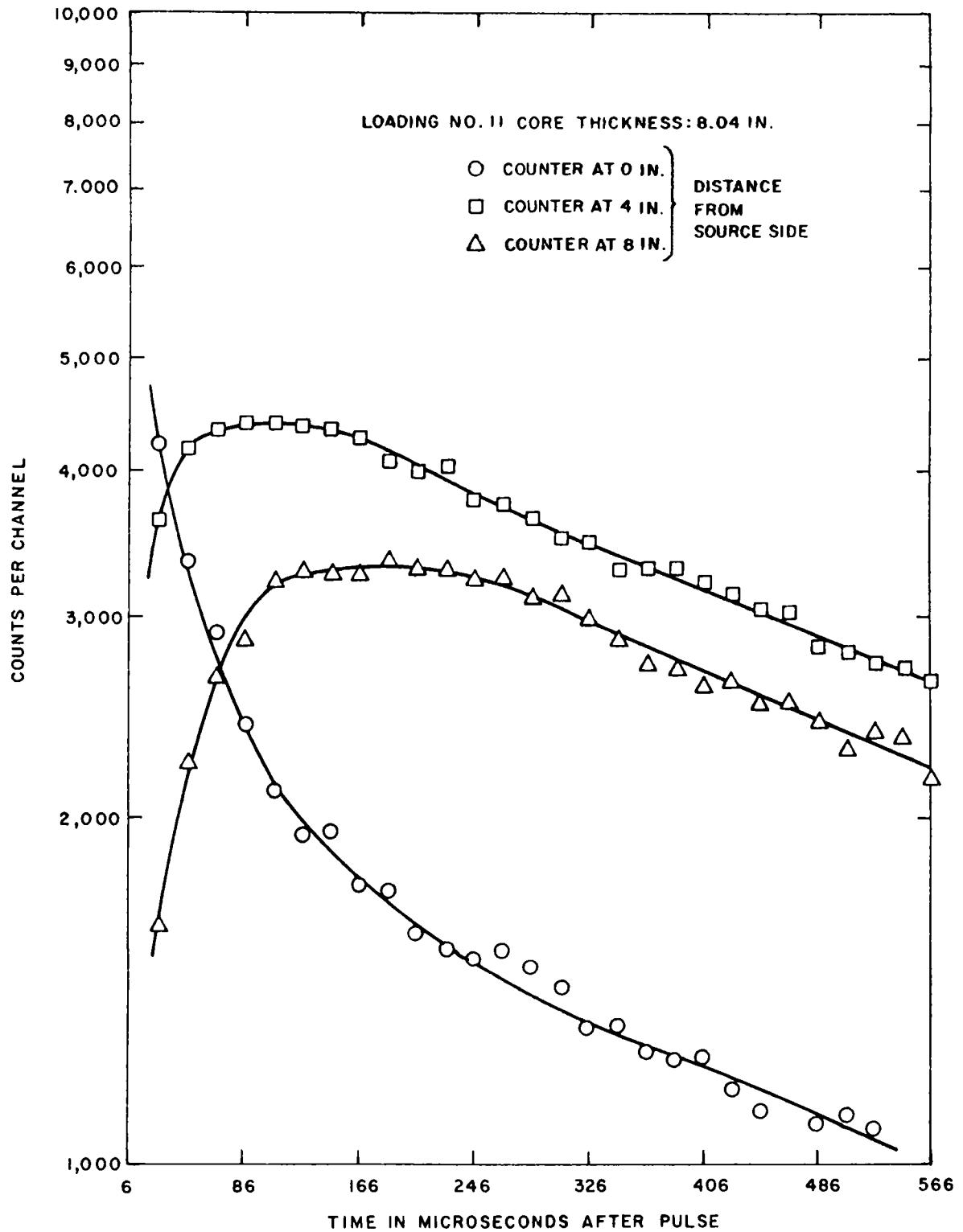


Fig. 9.8--Early time behavior of multiplying assembly measured after pulse at different counter positions

9.2.5. Error Assignments

In the determination of α , the least-squares weighted fit leads to a value with a statistical uncertainty of a few tenths of 1%. The values of α obtained from the two time analyzers agree to better than 1/2 of 1%. The value of α_c is less accurately known, since the delayed neutron background is so large and subtracting it from the observed counts to get the exponential leaves counts with poor statistics. As a result, a conservative estimate of the uncertainty on the subcritical α 's is $\pm 1\%$ for the data presented in Tables 9.1 and 9.2.

With the analysis method of Garelis and Russell, ⁽⁴⁵⁾ the value of α is used and the ratio (detailed in Section 9.4) of neutrons at time zero to neutrons in the delayed neutron tail. In the data used here, the neutrons at time zero are known to better than 1%, and in most of the cases, enough channels could be added together to determine the delayed neutron background to about 1% for small subcritical reactivities (to about \$10) and increasing to about 3% at the largest negative reactivities. This results in uncertainties in the reactivity (\$) varying from about 1% near critical to about 3% at \$30 subcritical. The value of $k\beta/\ell$ determined has essentially the same uncertainty as dollars. In specific cases, these uncertainties could all be reduced by longer counting intervals to improve statistics.

Using $(\alpha/\alpha_c) - 1$ to determine reactivity, the uncertainty, with the data presented here, is about 1%, since the value of α_c has an uncertainty of 1%, which is larger than the uncertainty in the subcritical α 's.

All the errors and uncertainties discussed above are those arising from statistical considerations. Systematic errors are difficult to assess. A repeat measurement on loading 5 during unloading from critical gave values for α within a few tenths of 1% and values of dollars within 3% of the earlier measurement. This is within the statistical uncertainty and indicates that systematic errors are probably low. Of course, the use of different calculational models to infer the number of dollars subcritical leads to different results, since different assumptions are inherent in the definition of reactivity in each.

The errors in the determination of the k from either the buckling change or the multiplication change are more difficult to estimate and may be large (10% to 50%). In the case of the buckling change, the value of extrapolation length to use for the subcritical loadings is uncertain and can lead to large systematic errors. In the case of the multiplication change, the inverse counting rate used as a quantity proportional to multiplication is not linear with subcriticality and thus leads to systematic errors. The use of the multiplication change technique gives reasonably good ($\pm 10\%$) values for reactivity near the reactivity that is assumed known.

That is, using a known reactivity (measured at critical or by some other means) to calibrate the subcritical multiplication works reasonably well for determining other reactivities near the known reactivity.

9.2.6. Conclusions

In general, the use of pulsed neutron techniques in subcritical assemblies can lead to useful data for reactor analysis. In particular, the use of the analysis method of Garelis and Russell can provide information about subcritical reactivity without the need for taking the assembly critical. The experimentally determined values of α , β , and $k\beta/\ell$ can be compared with the results of nuclear-analysis code calculations as a check on the parameters in the code. The determination of α , in particular, can provide a good check on the ability of the code to correctly calculate the particular core design.

9.3. SUBCRITICAL MULTIPLICATION AND CRITICAL BUCKLING

A steady-state neutron source, consisting of a 5-curie plutonium-beryllium capsule, was remotely driven to a fixed position just outside the center of one face of the slab, and neutron levels were obtained on each of two ion chambers and one fission counter located under the assembly. The ion-chamber data gave satisfactory plots of reciprocal neutron level versus loading, but the fission chamber did not, apparently owing to geometrical effects. These plots were shown in a previous report. (46)

The critical conditions were determined to be 2921.5 g of U²³⁵ and a core thickness of 8.64 in. (21.95 cm). A flux plot obtained at critical using uranium foils is shown in Fig. 9.9. These data are fitted satisfactorily by a cosine giving an extrapolation length of 0.88 in. (2.245 cm) on each side of the slab. In the transverse dimensions (18 in. by 18 in.), an extrapolation length of 4.2 cm was measured previously. (44) In that measurement, there was lead shielding just outside the assembly, which apparently increases the extrapolation length since in the thin dimension, with lead shielding present, the extrapolation length at $k = 0.9$ was 2.65 cm instead of 2.23 cm. The flux in the transverse dimension was not measured at critical; but using an extrapolation length of 4 cm based on previous measurements, the buckling at critical is

$$B_c^2 = \frac{\pi^2}{(21.95 \times 4.46)^2} + \frac{2\pi^2}{(45.72 + 8.0)^2} = 0.0141 + 0.0068 ,$$

$$B_c^2 = 0.0209 \text{ cm}^{-2}$$

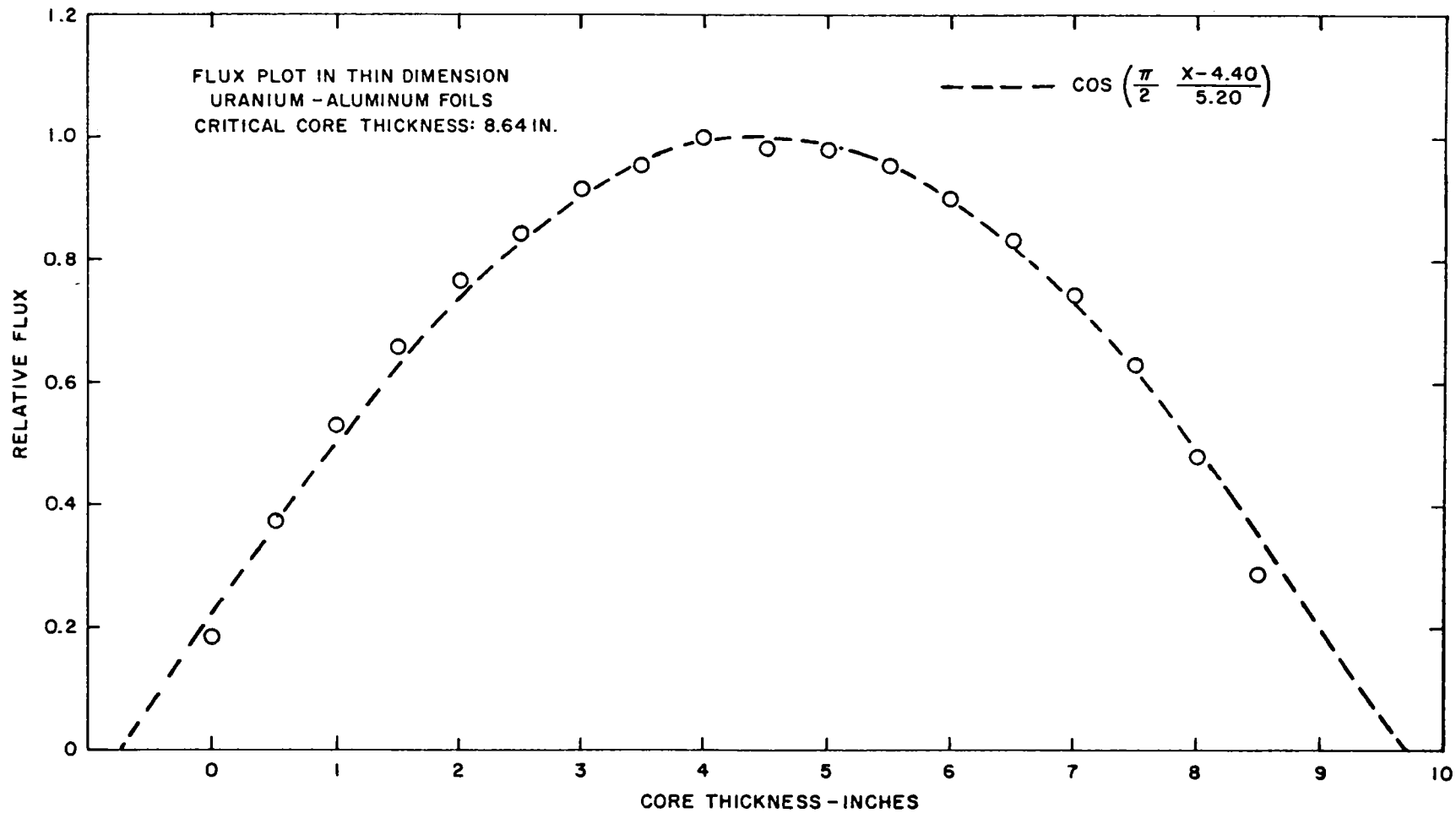


Fig. 9.9--Flux plot at critical of the multiplying assembly

Using the following modified one-group criticality equation,

$$k_{\text{eff}} = \frac{k_{\infty}}{1 + M^2 B_c^2} ,$$

where $k_{\infty} = 1.78$ and M^2 is the migration area, we can find a value of M^2 at critical to fit the equation:

$$M^2 = \frac{k_{\infty} - 1}{B_c^2} = 37.32 \text{ cm}^2 .$$

At any other subcritical loading, the value of k_{eff} is calculated from

$$k_{\text{eff}} = \frac{1 + M^2 B_c^2}{1 + M^2 B_x^2} ,$$

where B_c^2 is again the buckling at critical and B_x^2 is the buckling at the loading in question. In determining B_x^2 from the core thickness, the value of extrapolation length determined at critical has been used.

The k 's obtained in this manner are listed in Table 9.1 for the subcritical loadings measured.

If the reactivity at one subcritical loading is known, the reactivity at other loadings can in principle be determined from the change in multiplication. To investigate this approach in the present assembly, the reactivity at loading 18 is assumed to be known, the value used being that from the Garelis and Russell analysis with $\beta = 0.0077$. The results of this reactivity determination are shown in Table 9.1 together with the measured inverse counting rates which are proportional to inverse multiplication.

9.4. SUMMARY OF EQUATIONS USED IN ANALYSIS METHOD OF GARELIS AND RUSSELL

The analysis method of Garelis and Russell is described in detail in Ref. 45. Essentially, the method determines the parameter $(k\beta/\ell)$ using the complete time-response curve of a repetitively pulsed assembly after quasi-equilibrium has been attained. This value of $(k\beta/\ell)$ coupled with the measured value of α yields the reactivity directly. The analytical model is based on a bare one-group diffusion-theory system with m -delayed precursors, but the applicability is apparently much broader.

The relationship used in the analysis of the experimental data is as follows for a repetitive pulse:

$$\frac{N_D}{R} = \int_0^{1/R} N_p e^{k\beta t/\ell} dt - \int_0^{1/R} N_p dt, \quad (1)$$

where R is the repetition rate in pulses per second, N_D is the delayed neutron count rate, $N_p(t)$ is the prompt neutron count rate obtained by subtracting the constant N_D from the measured neutron count rate, and $k\beta/\ell$ is to be determined.

In Eq. (1) all the quantities are experimentally determined except $k\beta/\ell$, which must be determined by iteration. Essentially, the N_p at each time point is multiplied by a weighting factor $(e^{k\beta t/\ell} - 1)$ and all the values are added together.

This sum is then compared with the measured value of N_D/R , and if they are the same, the correct value of $k\beta/\ell$ has been used. The reactivity in dollars is obtained as follows:

$$\alpha = \frac{1 - k(1 - \beta)}{\ell} = \frac{k\beta}{\ell} \left(\frac{1 - k}{k\beta} + 1 \right),$$

since

$$\$ = \frac{1 - k}{k\beta}$$

Then

$$\$ = \frac{\alpha}{k\beta/\ell} - 1$$

If the pulse shape has no modal effects, i. e., if the fundamental-mode decay exists from time zero, then N_p varies as $e^{-\alpha t}$ from time zero and Eq. (1), above, can be integrated, resulting in an expression for the reactivity in dollars.

$$\$ = \frac{RQ}{\alpha N_D},$$

where Q is N_p at $t = 0$.

If only the first few time channels are disturbed by modal effects, i. e., if they deviate from the fundamental-mode exponential decay, then up to the point in time where the fundamental mode exists, the integration is done point by point and beyond that time the exponential decay rate is substituted, giving an analytical expression for the rest of the time. This

can be represented as follows:

$$\frac{N_D}{R} = \left[\sum_{n=1}^E (e^{x t_n} - 1) N_p t_n \Delta t + \frac{N_p t_E}{\alpha} \left(\frac{e^{x t_E}}{1 - x/\alpha} - 1 \right) \right] ,$$

where $x = k\beta/\ell$ and t_E is the time at which the exponential decay of N_p starts. When finite-length time channels are used, the t_n are the times at the midpoint of the channel but t_E is the time at the end (beginning of next channel) of the channel or the time midway between two channels.

X. FAST-NEUTRON SHIELDING STUDIES

Measurements of fast-neutron spectra have in the past been extremely difficult to obtain directly. The only reliable technique has been that with nuclear plate emulsions, which has been extremely limited in its applicability. The spectral index procedure has produced some information, but none of the more integral techniques yield the type of data necessary to reveal the processes going on in a shield. The kind of data that is really needed is that of the calibre taken at thermal energies, namely, good differential spectra. In this approach, one knows precisely the spectra going into a shield and the spectra and intensity coming out of the shield, and thus the shield analyst can determine quantitatively whether the analytical problem is being solved correctly. One must contend with the same general questions at thermal energies: (1) Are the cross-section data correct? (2) Is the method of experimental analysis appropriate and exact? We have therefore been tempted to try to apply the general techniques for spectral study developed during the thermalization program to the fast shielding problem, where little or no definitive experimental data exist for the purpose of checking analytical methods.

The first breakthrough in this process was the experimental study made at General Atomic of fast leakage spectra for lithium hydride shields⁽⁴⁷⁾ by V. V. Verbinski of Oak Ridge. The second program of measurements was also conducted with Verbinski for one-dimensional water shields. The experiments were exploratory in nature, and some of the data shown here, while illustrative, are not particularly amenable to comparisons with theory.

The experiments were performed as follows: After a particular shield configuration had been selected and set up in the Linac low-back-ground cave, the penetration neutron spectrum was measured, initially with Verbinski's detection equipment and afterwards under identical conditions with the General Atomic fast-neutron spectrometer. This produced two independent sets of spectral data. The General Atomic equipment and techniques are discussed below.

For neutrons with energies in excess of 100 kev, the most efficient detector is the organic scintillator, from which recoil-proton scintillations can be analyzed. Since Verbinski had previously selected the Forté method of pulse-shape discrimination for rejection of gamma scintillations, we adopted the Owen-Batchelor method.⁽⁴⁸⁾⁽⁴⁹⁾ This involved the special design of discriminator and coincidence circuits. In the pilot experiments

it became clear that in the time interval 1.0 to 10 μ sec after the Linac burst, there were very few gamma rays relative to neutrons. Placing a 2-in. gamma-ray lead filter across the beam at the 16-meter position removed virtually all gamma rays, while 30% to 40% of the neutrons were transmitted. At the 32-meter position, a thick wall of wax and lead was constructed with an 8 by 8 in. aperture for the beam. Finally, at 50 meters the 2 by 2-1/2 in. scintillator was placed in the center of the 12 by 12 in. beam. Initially, many pilot runs were made at low Linac intensities in order to examine the neutron-to-gamma ratios. Later, high-intensity runs were made in which pulse-shape discrimination was omitted and replaced by transmission tests. Two transmission samples which were used are listed in Table 10.1.

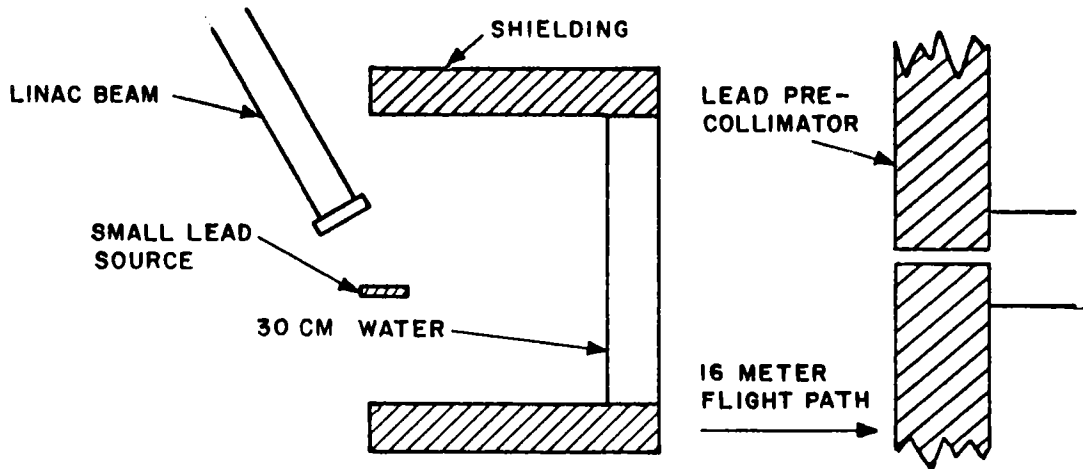
Table 10.1
SAMPLE TRANSMISSIONS

Sample	Thickness (g/cm ²)	Transmitted Gamma Rays (%)	Transmitted Fast Neutrons (%)
Pb	60	<9	30 to 40
CH ₂	7	>70	40 at 10 Mev 4 at 1 Mev

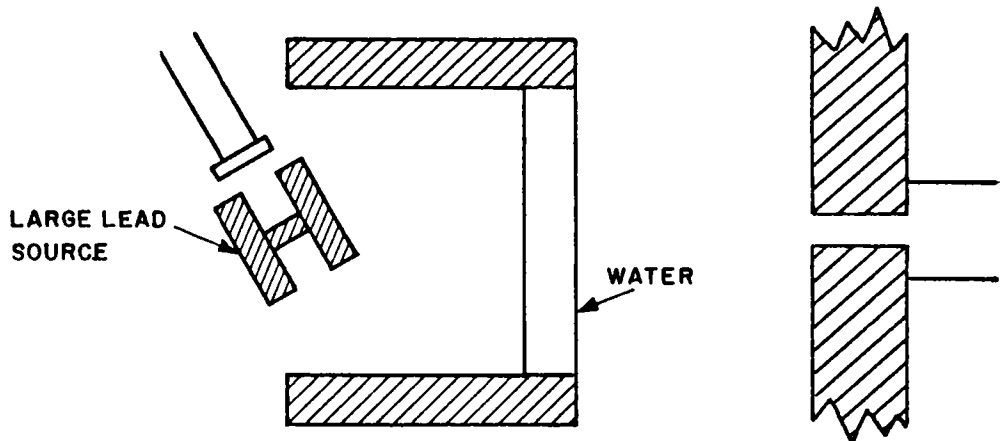
The neutron transmissions of these samples from 0.5 to 15 Mev agreed with the calculated transmissions to within statistics ($\pm 6\%$). The presence of gammas in the scintillation spectra would have caused a low value for lead and a high value for the polyethylene transmission. The results to date indicate that there is less than 5% gamma contamination in the fast-neutron flux for all experimental shielding configurations. This transmission test was repeated with a 20-cm water shield in the beam at the cave, and similar results were obtained. Since the gamma contamination was lower than 5%, it was decided to omit pulse-shape discrimination; this permitted the Linac intensity to be increased by a factor of more than 10, giving much shorter run times.

The water-shield experiments performed are listed in Table 10.2. The shields were extended by boxes of wax to form an approximate half sphere around the large target. The three geometrical setups are shown in Fig. 10.1.

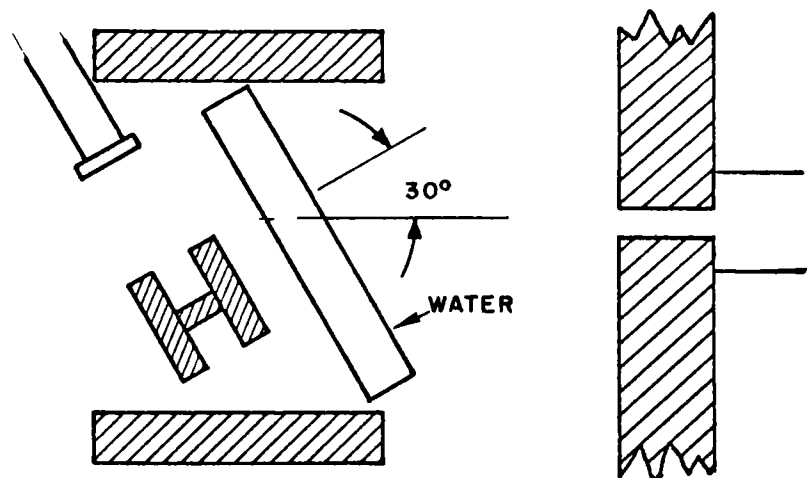
The measured neutron spectra are shown in Figs. 10.2, 10.3, and 10.4. The time-of-flight spectra were converted to energy flux by dividing out of the measurements a calculated detector energy sensitivity and the



10.1A



10.1B



10.1C

Fig. 10.1--Geometrical arrangements for the fast-neutron shielding experiments

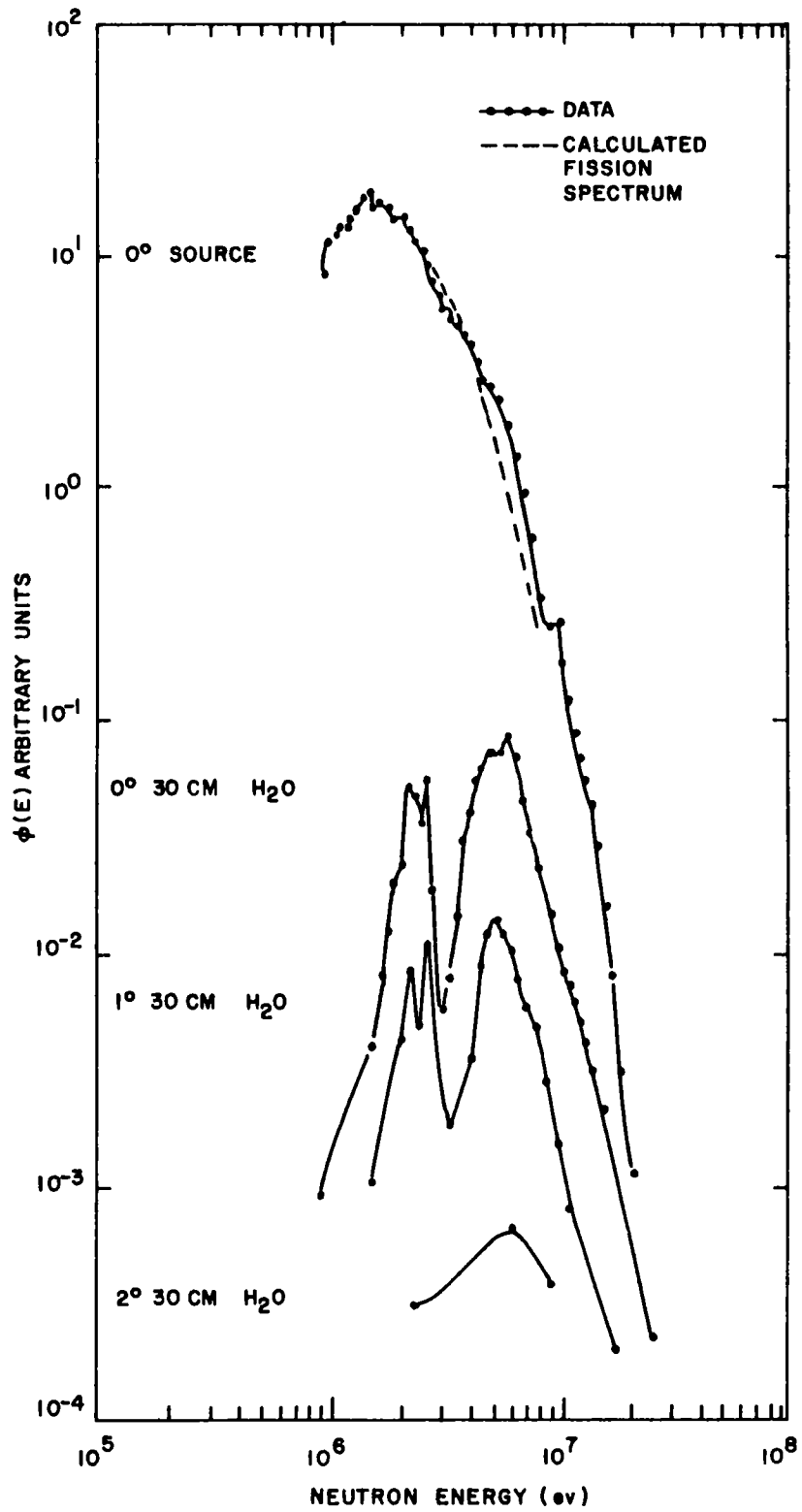


Fig. 10.2--Neutron spectra measured in the geometry of Fig. 10.1.A

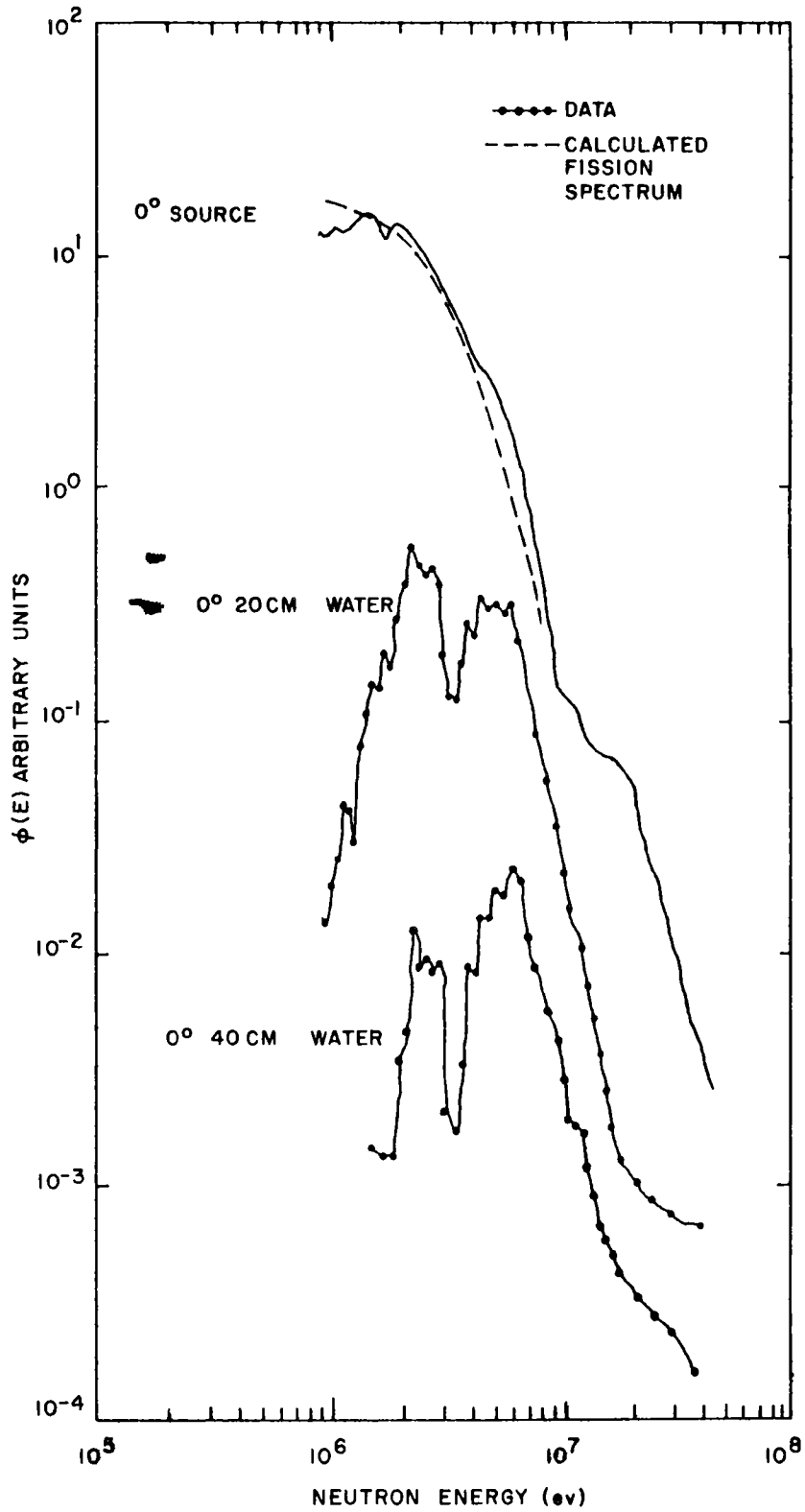


Fig. 10.3--Neutron spectra measured in the geometry of Fig. 10.1.B

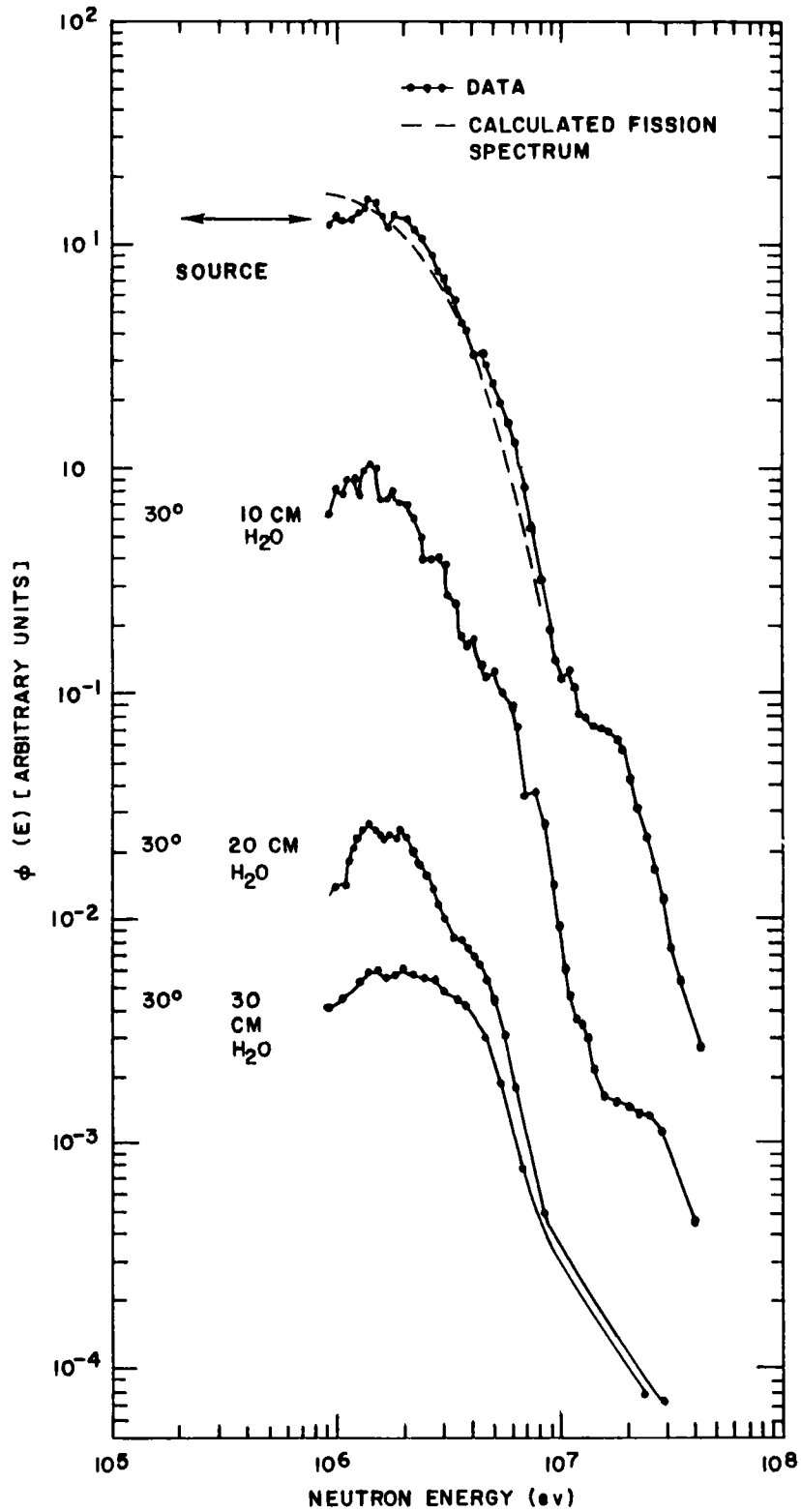


Fig. 10.4--Neutron spectra measured in the geometry of Fig. 10.1. C

flight-path neutron transmission. The flight-path transmission is well known and can be removed from the measured result with little uncertainty. The detector energy sensitivity is based completely on the calibration at Batchelor for an identical liquid scintillator and is subject to some uncertainty at present. Methods of measuring the detector sensitivity are being developed, but this problem is not solved as yet. However, the results are considered sufficiently accurate to discuss at this time.

Table 10.2
WATER-SHIELD EXPERIMENTS

Water Thickness (cm)	Angle of Emergence (degrees)	
	Large Target, 8 × 8 × 8 in.	Small Target, 3/4 × 2-in. Diam.
0	0	
10	30	
20	0, 30	
30	30	0, 1, 2
40	0	

In Fig. 10.2 the small-source plane-shield results are given. A narrow collimator viewed the shield surface, and the spectra emanating from the shield at several small angles were studied. The source was sufficiently far removed from the shield that a quasi-plane-wave solution to this problem might successfully approximate the geometry. In this method of analysis we would attempt to replace the source by a surface source on the shield with the average angular properties produced at the shield by the displaced source. The unobstructed source spectrum is shown at the top of Fig. 10.2, and then in descending order are shown the 0° , 1° , and 2° spectra emanating from a 30-cm slab of water. The dotted curve is the shape of the conventional fission neutron spectrum. Pronounced resonance structure is observed in the measured spectra, all of it being due to the resonances in oxygen. Furthermore, large variations of neutron flux intensity with angle of emission from the shield were also observed at small angles. This effect cannot be explained by simple transmission of the uncollided flux. A definite build-up effect in the forward direction is apparent. This effect has, by the way, been observed for much greater shield thicknesses and for other shielding materials. Thus, most of the neutron leakage through a shield in a given direction can be attributed to source points roughly in the direct line of sight extrapolated through the shield. The importance of performing shielding analysis in such a way that the angular mesh properly weights the forward direction of emission

for a shield is clearly indicated. It is, of course, desirable to try to analyze this shielding experiment, if possible with a transport-theory code. DSN and GAPLSN have given excellent results in the past for spatially dependent problems, and we will endeavor to use these codes in the future. The angular mesh of GAPLSN will, however, have to be changed to permit the spectra to be calculated correctly in the forward direction. This task is now being performed.

The spectra shown in Figs. 10.3 and 10.4 are included for completeness, but these data are not considered analyzable. In this experiment, an attempt was made to use a large source so that the code NIOBE could handle the problem in spherical geometry. The source was made by surrounding a conventional small source with 8 in. of lead. It was discovered after completion of the experimental program, however, that the source spectrum was not the same at all points in the large source. The figures indicate the fine structure, which can be easily studied by these experimental techniques, and show the degree of precision obtainable in the experiments.

In summary, the above series of measurements has revealed the feasibility and desirability of studying deep-penetration, fast-neutron spectra with a pulsed neutron source. The small-source series of data was taken on relatively clean geometry and is probably amenable to analysis. Further work in one-dimensional configurations is contemplated starting with graphite.

XI. EXPERIMENTAL TECHNIQUES

11.1. SENSITIVITY FUNCTION OF THE 16-M DETECTOR BANK

The relative sensitivity of the detector bank of 32 stacked B¹⁰F₃ counters for the 16-m flight path has been checked twice during the last year. Periodic checks are required since this sensitivity function is one of the most important corrections made to obtain the neutron spectra from the time-of-flight data.

The first check was carried out by comparing the response from the main detector bank with that from a set of low-pressure BF₃ counters, which were taken as 1/v detectors. The sensitivity function, S(E), of the main detector bank can then be expressed as

$$S(E) = \frac{k}{\sqrt{E}} T_0(E) T(E) \frac{C_{16}(E)}{C_0(E)},$$

where k is a constant, T(E) is the transmission through the flight path, and T₀(E) is the transmission through the copper walls of the set of 1/v detectors. C₁₆(E) and C₀(E) are the counts in each channel of the main detector bank and the 1/v detector, respectively. A small discrepancy between the new S(E) function and the one used previously was observed above 100 ev. Since the new function provided a better 1/E spectrum when the spectrum was expected to be 1/E, the new function has been accepted as the standard S(E), and is detailed in Table 11.1.

A second check of the response of the main detector bank has been carried out by comparison with a Li⁶ glass detector, whose sensitivity was calculated over the energy range of interest. The S(E) of the main detector bank obtained in this way differed from that obtained previously below 0.05 ev by up to 10%, but there was good agreement above this energy. The alpha alumina reflector supplied with the Li⁶ glass detector was removed and the test was repeated, but the result was the same. No explanation for this later discrepancy has been found, but a further check of the sensitivity is planned with both the Li⁶ glass detector and a new end-on window B¹⁰F₃ counter with calculable geometry.

Because of the 10% discrepancy referred to above, the question of whether or not the 1-in. -diameter bank of BF₃ detectors really has a 1/v

153
Table 11.1

16-M S(E) VERSUS NEUTRON ENERGY

E (ev)	S(E)	E (ev)	S(E)
0.0005	0.01	7.0	0.0014
0.001	0.0125	8.0	0.0013
0.0015	0.0135	9.0	0.00124
0.002	0.014	10	0.00118
0.0025	0.014	15	0.00098
0.003	0.0138	20	0.00086
0.0035	0.0135	30	0.00072
0.004	0.0132	50	0.00057
0.005	0.0127	70	0.00049
0.006	0.012	100	0.00042
0.007	0.0117	150	0.00035
0.008	0.0114	200	0.00031
0.009	0.0113	220	0.0003
0.0095	0.0113	230	0.00026
0.01	0.0114	245	0.00028
0.011	0.0115	300	0.00026
0.013	0.0116	400	0.000225
0.015	0.0116	500	0.000205
0.018	0.0114	550	0.000195
0.01	0.0111	560	0.000185
0.025	0.0107	570	0.000175
0.03	0.0102	580	0.00014
0.04	0.0094	590	0.00015
0.05	0.0088	600	0.000164
0.06	0.0084	620	0.000174
0.08	0.0078	640	0.000176
0.09	0.0075	660	0.000176
0.1	0.00725	700	0.000176
0.15	0.0064	800	0.000167
0.2	0.00585	900	0.000158
0.3	0.0051	1000	0.00015
0.4	0.0046	1500	0.000125
0.5	0.00425	2100	0.000108
0.6	0.00395	3000	0.000091
0.7	0.00371	5000	0.000073
0.8	0.00354	5500	0.000070
0.9	0.00337	5700	0.000068
1.0	0.00325	6100	0.000066
1.5	0.00275	6300	0.0000655
2.0	0.0024	7300	0.000062
3.0	0.002	8000	0.000059
4.0	0.00178	9100	0.0000555
5.0	0.0016	10000	0.000053
6.0	0.00149		

response has arisen. The response of the detector should follow rigorously an expression

$$S(E) = T_w(E) (1 - e^{-N_0 \sigma_{TB} \bar{x}_B}) \frac{\sigma_{B\alpha}}{\sigma_{TB}}, \quad (1)$$

where $T_w(E)$ is the effective transmission of the copper wall between the counting volume and the neutron source, σ_{TB} is the boron total cross section, $\sigma_{B\alpha}$ is the boron (n, α) cross section, and \bar{x}_B is the effective length of the counting volume. We have in the past approximated this true sensitivity function by using

$$S'(E) = T_{Cu}(E) N_0 \sigma_{B\alpha} \bar{x}_B, \quad (2)$$

where $T_{Cu}(E)$ is given by $e^{-N_0 \sigma_T \bar{x}_{Cu}}$. σ_T was the total cross section of copper, $N_0 \bar{x}_B$ were constants which it was not necessary to specify exactly in Eq. (2), and σ_B was assumed to follow $1/\sqrt{E}$. Expanding the exponential in Eq. (1), we can get some idea of the error we are making in our procedures:

$$S(E) = T_w(E) N_0 \sigma_{\alpha B} \bar{x}_B \left(1 - \frac{N_0 \sigma_{TB} \bar{x}_B}{2} + \dots \right). \quad (3)$$

The detector sensitivity, $S(E)$, and the good-geometry detector transmission are related quantities. The detector transmission is given by

$$T(E) = e^{-N_0 \sigma_B \bar{x}_B} T_w^*(E), \quad (4)$$

where $T_w^*(E)$ is the total transmission of the entire copper wall (both sides of the cylinder) rather than of one side. In order to determine whether the copper and BF_3 were present in the quantity and purity we expected, we have measured the detector transmission three times in good geometry and compared these results (Fig. 11.1) with $T(E)$ calculated with Eq. (4). The calculated and measured transmission are in excellent agreement for one set of data, but the calculated transmission lies 1% or 2% below the measured transmission for the other two sets of data. This variation is negligible from the standpoint of pointing to any discrepancies in the energy sensitivity function. The percentage discrepancy in the worst case does not vary with neutron energy, which is an effect (probably due to only being able to monitor the beam to $\sim 1\%$) that would not even influence the energy-dependent detector sensitivity. Further, the small discrepancy that does exist between theory and experiment is in the wrong direction, i. e., the detector transmission is higher, not lower, than we had been considering it to be.

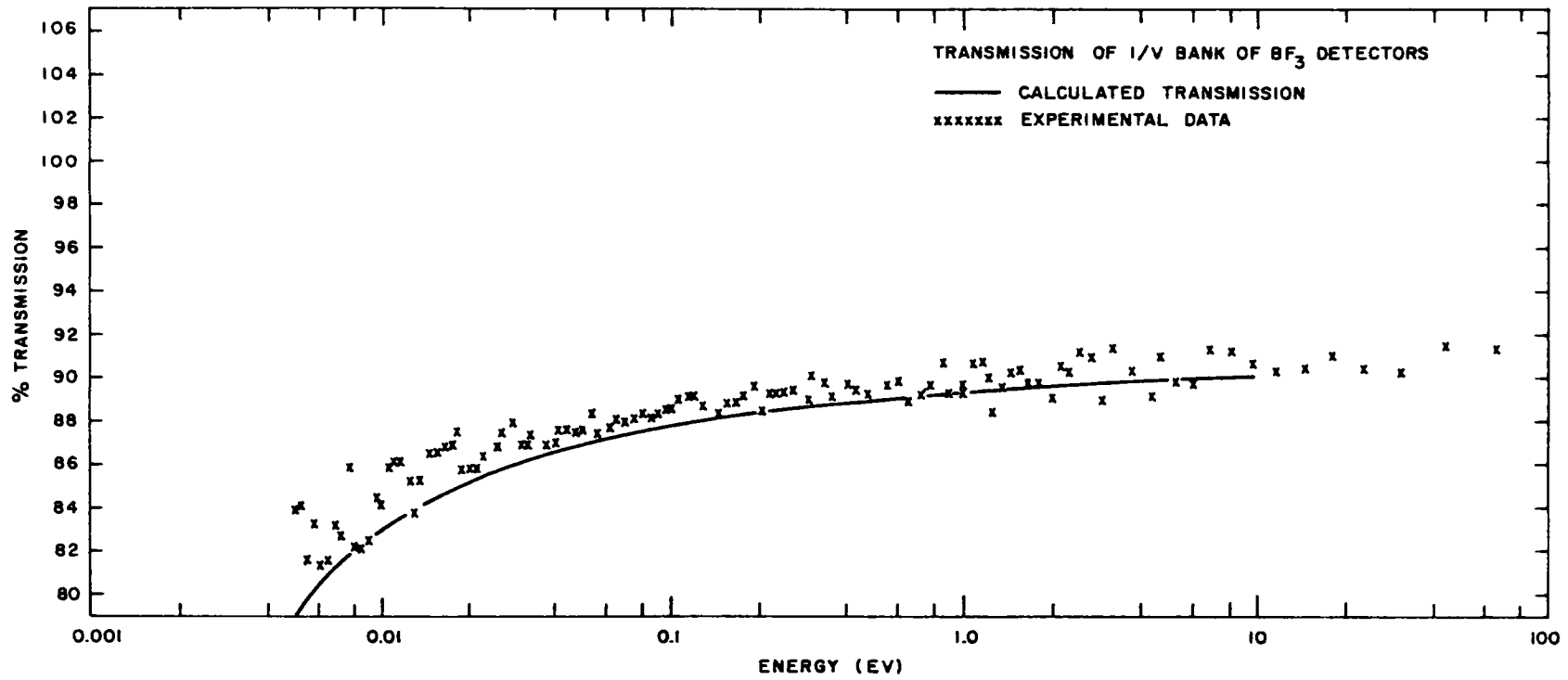


Fig. 11.1--Transmission function of the 1/v detector bank

If we still desire to postulate a mechanism for obtaining a detector sensitivity at low energies less than that given by Eq. (2), one obvious approach is to conjecture that the detector has more B^{10} in it than we assume. Thus, the negative term $(N_0\sigma_{B^{10}}\bar{x}_B/2)$ in Eq. (3) would have to be larger than expected. From manufacturers' specifications and our calculations, $N_0\sigma_{B^{10}}\bar{x}_B$ should attain a maximum value of 0.017 at 0.01 ev. To make a 10% error in the shape of $S(E)$ by this mechanism alone, $N_0\sigma_{B^{10}}\bar{x}_B$ must be 0.2 at least. Quantitatively, for this mechanism to be present the measured transmission would have to be about 0.75 at 0.01 ev, not the value of 0.85 given in Fig. 11.1. A second physical mechanism, which could make possible an error using Eq. (2), is that $T_w(E)$ (the true detector-wall transmission) might be lower and more energy-dependent (owing to the presence of a mystery absorber) than $T_{Cu}(E)$ alone. We say, since we know the wall is copper, that at least

$$T_w(E) = T_{Cu}(E) T_m(E), \quad (5)$$

where $T_m(E)$ is the transmission through the mystery absorber whose function is to depress the detector sensitivity by 10% at 0.01 ev, i. e., $T_m(0.01 \text{ ev}) = 0.90$. Obviously, when one measures the good-geometry transmission of the detector, the result (because of both walls) is

$$T_w^*(E) = [T_{Cu}(E)]^2 \times [T_m(E)]^2. \quad (6)$$

In our calculated detector-transmission curve in Fig. 11.1, we have included $[T_{Cu}(E)]^2$. At 0.01 ev, if our second mechanism is valid, we would expect to measure a total detector transmission of $0.67 = T$. This is even further off than our first mechanism.

A third mechanism investigated is that there is some ambiguity as to what cross sections to use in calculating $T_w(E)$ for the $S(E)$ only. We approximate T_w with $T_{Cu}(E)$ calculated using the total cross section. If wall scattering does not prevent neutrons from getting into the sensitive gas volume of the detectors, then σ_α only should be used. This is in a sense the other extreme from the use of σ_T only. One can say then that

$$T_w(E) = T_{Cu}(E) e^{-N_0\sigma_s(E)x}$$

Unfortunately, for this argument the scattering cross section, $\sigma_s(E)$, of copper is relatively flat at energy above 0.01 ev, so removing all wall scattering when calculating $T_w(E)$ makes very little difference in the relative energy response of the detector. One could possibly think of some mechanism whereby all the scattering is neglected in calculating

$T_w(E)$ at high energies and is included in calculating $T_w(E)$ at, say, 0.01 ev. This mechanism must include some reason why the scattering angular distribution from copper is far more forward peaked at 1 ev than at 0.01 to 0.02 ev. In fact, since there is copper on the other side of the detector to scatter neutrons back into the sensitive detector volume, the scattering in the wall cancels out completely to a first approximation.

As of now, there is no reason to believe the $1/v$ counter is not a $1/v$ counter. The detector-transmission study was a sensitivity check and the detector acted as expected. The question exists of how far from $1/v$ response the detector could be and still satisfy our total cross section. It appears that one can see by the transmission technique a variation of 3% from $1/v$ response for this detector.

11.2. COLLIMATION STUDIES

During the last year, the collimation system of the 16-m flight path has been carefully studied to determine

1. That the collimators were properly aligned (found to be adequate).
2. The effect of the postcollimator on the measured spectra (no detectable difference).
3. The effects of varying sizes and materials of the precollimators.
4. The effects of varying distances between the precollimator and neutron-emitting surface.

Five commonly used sizes of precollimators, made of brass or epoxy resin, were selected, and interchanging these precollimators made no observable difference in the shape of the neutron spectrum. However, different counting rates were encountered, and it was decided that for maximum counting efficiency, a large, fairly short precollimator should be used provided that it is compatible with the geometry of the experiment.

Varying the position of the precollimator did not significantly change the count rate, and it was concluded that the position was not too critical. However, the precollimator position must ensure that the detector cannot see more area than the neutron-emitting surface, and that the precollimator does not become a strong source of reflected neutrons.

The following principles have been developed for selecting the precollimator and re-entrant tube sizes:

1. The re-entrant tube should be as large as possible without perturbing the flux spectrum in the assembly.

2. The precollimator diameter should be as large as possible without seeing more than the neutron-emitting surface at the base of the re-entrant tube.

In this way, the greatest allowable count rate will be achieved for given machine operating conditions. That part of the background dependent on machine conditions and independent of precollimator size will then be minimized.

Since the alignment of the collimators was found to be satisfactory and since only a fraction of the neutron-emitting surface was viewed, no elaborate calculations of the source-detector view factor were found necessary. However, alignment may be more difficult to obtain on the 50-m flight path, and off-center collimation may be required in surveying the neutron-emitting surfaces of a heterogeneous assembly. A code has therefore been written by H. Honeck⁽⁵⁰⁾ to calculate the relative view factor over the flight path exactly for any arrangement of cylindrical or rectangular collimators. This code is called CAP, Collimator Analysis Program, and computes the relative efficiency, ρ , for each source point P in Fig. 11.2, where ρ is the ratio of the detector response with all collimators in position to the response when only the last collimator is in place:

$$\begin{aligned} \rho &= \frac{L^2}{A} \int_{\phi \text{ min}}^{\phi \text{ max}} d\phi \int_{\theta \text{ min}(\phi)}^{\theta \text{ max}(\phi)} d\theta, \\ &= \frac{L^2}{A} \int_{\phi \text{ min}}^{\phi \text{ max}} [\theta \text{ max}(\phi) - \theta \text{ min}(\phi)] d\phi. \end{aligned}$$

An arbitrary number of rectangular or circular collimators of finite thickness (the front and back edges are treated as separate collimators) can be used. The alignment is not critical provided that the coordinates of the center and the dimensions of each collimator can be well specified. The source points, P, can be arbitrarily chosen so as to obtain more detail in regions of interest. The output of the code includes information about which collimator limits the beam for each source point.

The code has been assembled and tested with a sample case, but has not been put to specific use, since ρ is 1.0 for the experiments done to date. Future modifications to the code could include scattering from collimator edges.

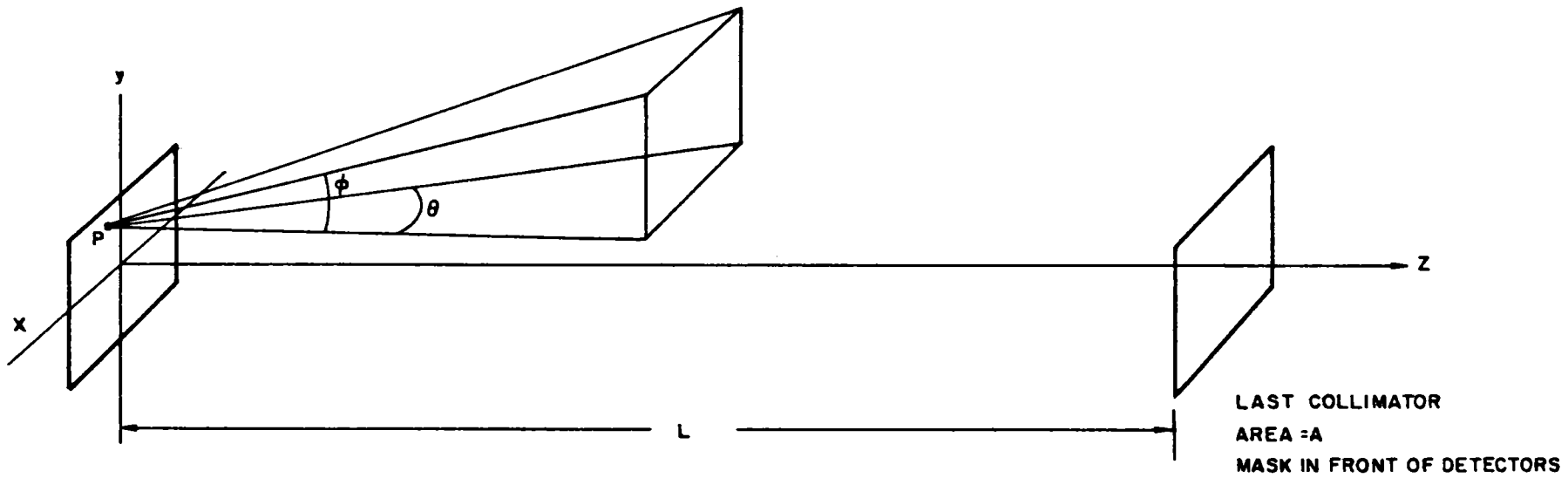


Fig. 11.2--Elemental collimator geometry

XII. UNIVERSAL SCATTERING-KERNEL CODE

The purpose in this section is to outline the general procedures and formulae which will serve as a basis for the calculation of the scattering kernel in a form suitable for application to all of the important moderating materials. At this time, we restrict ourselves to the problem of calculating the scattering law. In a future report we will consider the problem of calculating the P_r -components of the differential energy transfer cross sections.

The problem of calculating slow-neutron scattering is most conveniently formulated in terms of the so-called intermediate scattering function $\chi(\kappa, t)$.⁽⁴³⁾ In terms of this function, the noninterfering part of the scattering can be expressed as

$$\sigma(E_0, E, \theta) = \frac{\sigma_b}{4\pi} \sqrt{\frac{E}{E_0}} S(\kappa, \epsilon) , \quad (1)$$

where

$$S(\kappa, \epsilon) = (1/2\pi) \int_{-\infty}^{\infty} dt e^{i\epsilon t} \chi(\kappa, t) , \quad (2)$$

$$\sigma_b = \sigma_0 [1 + (1/M)]^2 , \quad (3)$$

E_0 = initial neutron energy ,

E = final neutron energy ,

M = atomic mass of the scatterer (in units of the neutron mass) ,

θ = angle of scattering,

$$\frac{\kappa^2}{2} = E + E_0 - 2(EE_0)^{1/2} \cos \theta , \quad (4)$$

ϵ = energy transfer .

We are adopting units where the neutron mass and Planck's constant, $h/2\pi$, are one. We also assume for future purposes that Boltzmann's constant is one.

The obvious advantage of the formulation of Eq. (1) is that the calculation of $\sigma(E_0, E, \theta)$ requires knowledge only of $S(\kappa, \epsilon)$, which is a function of just two variables. This is a factor of extreme importance from the viewpoint of computer economics as well as from a physical viewpoint.

An important property of $S(\kappa, \epsilon)$ is that it satisfies the detailed balance condition

$$S(\kappa, -\epsilon) e^{-\epsilon/T} = S(\kappa, \epsilon) . \quad (5)$$

Through this, we can define the symmetric function,

$$S_0(\kappa, \epsilon) = e^{\epsilon/2T} S(\kappa, \epsilon) = S_0(\kappa, -\epsilon) . \quad (6)$$

To take advantage of the symmetry implied by Eq. (6), a great deal of the formulation will be expressed in terms of $S_0(\kappa, \epsilon)$.

The basic simplifying assumption that we shall make is that the χ -function in Eq. (2) has the Gaussian form

$$\chi(\kappa, t) = e^{-(\kappa^2/2) w^2(t)} , \quad (7)$$

where $w^2(t)$ is a complex function of t which contains all the information about the dynamics of the scatterer. Next, we shall assume that the motion of any particle in the scatterer can be expressed as a sum of motions of independent dynamical degrees of freedom, all of which commute with one another. This implies that

$$w^2(t) = \sum_{i=1}^N w_n^2(t) \quad (8)$$

and

$$\chi(\kappa, t) = \prod_{i=1}^N \chi_n(\kappa, t) , \quad (9)$$

where

$$\chi_n(\kappa, t) = e^{-(\kappa^2/2) w_n^2(t)} \quad (10)$$

As a consequence of this, the scattering law can be described in terms of a convolution of the different modal functions

$$S_n(\kappa, \epsilon) = \frac{1}{2\pi} \int_{-\infty}^{\infty} e^{i\epsilon t} \chi_n(\kappa, t) dt \quad (11)$$

and its symmetrical equivalent

$$S_{0n}(\kappa, \epsilon) = e^{\epsilon/2T} S_n(\kappa, \epsilon) . \quad (12)$$

Noting that

$$S_0(\kappa, \epsilon) = \frac{1}{2\pi} \int_{-\infty}^{\infty} dt e^{i\epsilon t} \prod_{n=1}^N \chi_n(\kappa, t) , \quad (13)$$

the convolution theorem for Fourier transforms gives

$$S_0(\kappa, \epsilon) = \int_{-\infty}^{\infty} S_{0N}(\kappa, \epsilon') S_0^{(N-1)}(\kappa, \epsilon - \epsilon') d\epsilon' . \quad (14)$$

In general, any m-fold convolution can be calculated from

$$S_0^{(m)}(\kappa, \epsilon) = \int_{-\infty}^{\infty} S_{0m}(\kappa, \epsilon - \epsilon') S_0^{(m-1)}(\kappa, \epsilon') d\epsilon' \quad (15)$$

m = 1, 2, . . . N .

This sequence of equations, together with an initially given $S_0^0(\kappa, \epsilon) = S_{01}(\kappa, \epsilon)$, forms a convenient basis for an iterative calculation of $S(\kappa, \epsilon)$. Equation (15) will be one of the most basic in a program for calculating the scattering law. Now let us turn to the calculation of $S_{0m}(\kappa, \epsilon)$, which contains the influence of the various degrees of freedom on the scattering.

12.1. CALCULATION OF $S_{0m}(\kappa, \epsilon)$

The calculation of each of the $S_{0m}(\kappa, \epsilon)$ will be one of the initial calculations to be performed. After the quantities are determined, Eq. (15) can be applied to calculate the entire scattering law. In order to obtain $S_0^{(m)}$ we must give a description of the dynamics in the modes of motion described by the index m. In general, we shall consider three basic types of motion. These are (1) free translations, (2) diffusive motions, and (3) vibrations. We denote the scattering function corresponding to free translations by S_{0G} . It is given by

$$S_{0G}(\kappa, \epsilon) = \frac{\exp \{ -M_G [\epsilon + (\kappa^2 / 2M_G)^2 / 2\kappa^2 T] \}}{(2\pi\kappa^2 T / M_G)^{1/2}} e^{\epsilon / 2T}, \quad (16)$$

where M_G is the mass corresponding to the free translations and T is the temperature (in this expression energy and temperature are in the same units).

The scattering function corresponding to diffusive motions is⁽⁵¹⁾

$$S_{0D}(\kappa, \epsilon) = \frac{1}{\pi} \left[\exp -dc \frac{\kappa^2}{M_G T} \right] \frac{d(c^2 + 1/4)^{1/2}}{[\epsilon^2 + (d\kappa^2 / M_G)^2]^{1/2}} \left(\frac{\kappa^2}{M_G} \right) \\ \times K_1 \left\{ \left(c^2 + \frac{1}{4} \right)^{1/2} \left[\left(\frac{\epsilon}{T} \right)^2 + \left(\frac{d\kappa^2}{M_G T} \right)^2 \right] \right\}^{1/2}, \quad (17)$$

where $K_1(x)$ is the modified Bessel function of the second kind.⁽⁵²⁾ The parameter d is a diffusion coefficient, and c is a measure of the time during which atoms oscillate around their initial positions before diffusing away. Both c and d will be input parameters.

Now let us consider the calculation of effects due to vibrations. We shall assume that there exist $N - 2$ independent modes of vibration and that the properties of these modes which are relevant for neutron scattering are contained in the frequency distribution functions $\rho_i(\omega)$ ($i = 1 \dots N - 2$) for ($0 \leq \omega \leq \theta_i$). The $\rho_i(\omega)$ will be part of the input to the code. In addition, we will require as input a set of quantities M_i , which are the effective masses associated with the $\rho_i(\omega)$. We also note that $\rho_i(\omega)$ will be a non-zero function only in the interval $\theta_i^L \leq \omega \leq \theta_i$.

The $S_{0i}(\kappa, \omega)$ for vibrations will be computed by one of two methods. Which of these methods is used depends on the magnitudes of ϵ and κ .

(I) for sufficiently small values of κ^2 , $(\kappa / 2M_i)^2 \alpha_i < \bar{n}_i$ (see below),

$$S_{0i}(\kappa, \omega) = \exp \left(-\frac{\kappa^2}{2M_i} \alpha_i \right) [\delta(\omega) + \Delta S_{0i}], \quad (18)$$

$$\Delta S_{0i}(\kappa, \omega) = \left[\exp \left(-\frac{\kappa^2}{2M_i} \alpha_i \right) \right] \sum_{n=1}^{\infty} \frac{1}{n!} \left(\frac{\kappa^2}{2M_i} \alpha_i \right)^n g_i^{(n)}(\omega), \quad (18a)$$

where

$$g_i^{(1)}(\omega) = \frac{\rho_i(\omega)}{2\omega\alpha_i \sinh(\omega/2T)} \quad (19)$$

$$g_i^{(n+1)}(\omega) = \int_{-\infty}^{\infty} g_i^{(1)}(\omega' - \omega) g_i^{(n)}(\omega') d\omega' \quad (20)$$

and $g_i^{(n)}(-\omega)$ is defined by

$$g_i^{(n)}(-\omega) = g_i^{(n)}(\omega) . \quad (21)$$

The α_i are defined by

$$\alpha_i = \int_{-\infty}^{\infty} \frac{\rho_i(\omega) \exp(\omega/2T)}{2\omega \sinh(\omega/2T)} d\omega . \quad (22)$$

The expansion given in Eq. (20) will be used when

$$\frac{\kappa^2}{2M_i} \alpha_i \leq \bar{n}_i , \quad (23)$$

where \bar{n}_i is an input number.

For large values of n , the calculation of $g_i^{(n+1)}(\omega)$ by the iterative procedure defined by Eq. (20) becomes quite time-consuming. For large n , however, it is a good approximation to set

$$g_i^{(n)}(\omega) = (2\pi n\sigma_i^2)^{-1/2} \exp \left[\frac{-(\omega + n\bar{\omega}_i)^2}{2n\sigma_i^2} + \frac{\omega}{2T} \right] \quad \text{for } \omega < 0 \quad (24)$$

and

$$g_i^{(n)}(+|\omega|) = g_i^{(n)}(-|\omega|) .$$

This form for $g_i^{(n)}(\omega)$ will be used whenever $n > n_0^{(i)}$, where $n_0^{(i)}$ is an input number. The quantities $\bar{\omega}_i$ and $\bar{\sigma}_i^2$ are defined by

$$\bar{\omega}_i = \int_{-\infty}^{\infty} \omega g_i^{(1)}(\omega) \exp\left(\frac{\omega}{2T}\right) d\omega , \quad (25)$$

$$\sigma_i^2 = \int_{-\infty}^{\infty} \omega^2 g_i^{(1)}(\omega) \exp \frac{\omega}{2T} d\omega - (\bar{\omega}_i)^2 \tag{26}$$

In carrying out the calculation of $g_i^{(n)}(\omega)$, the programmer should take advantage of the property given in Eq. (21).

(II) For $(\kappa^2/2M_i) \alpha_i > \bar{n}_i^{(1)}$, the preceding formulae will continue to apply if the conditions

$$\left[\left(\omega + \frac{\kappa^2}{2M_i} \right)^2 / \frac{2\kappa^2}{M_i} \bar{T}_i \right] > (\bar{n}_i^{(2)})^2, \tag{27}$$

$\omega < 0$ are also satisfied. Here, $\bar{n}_i^{(2)}$ is an input number and \bar{T}_i is defined by

$$\bar{T}_i = \frac{\sigma_i^2 + \bar{\omega}_i^2}{2}. \tag{28}$$

If $(\kappa^2/2M_i) \alpha_i > \bar{n}_i^{(1)}$, but Eq. (27) is not satisfied, then

$$S_{0i}(\kappa, \omega) = \exp \left[\frac{\omega}{2T} \right] \left(2\pi \frac{\kappa^2}{M_i} \bar{T}_i \right)^{-(1/2)} \exp \left[- \left(\omega + \frac{\kappa^2}{2M_i} \right)^2 / 2 \frac{\kappa^2}{M_i} \bar{T}_i \right] \text{ for } \omega < 0 \tag{29}$$

$$S_{0i}(\kappa, |\omega|) = S_{0i}(\kappa, -|\omega|) \text{ for } \omega > 0.$$

Figure 12.1 shows, in a rough schematic way, the regions in the $\omega - \kappa^2/2M_i$ plane in which Eqs. (18) and (29) apply.

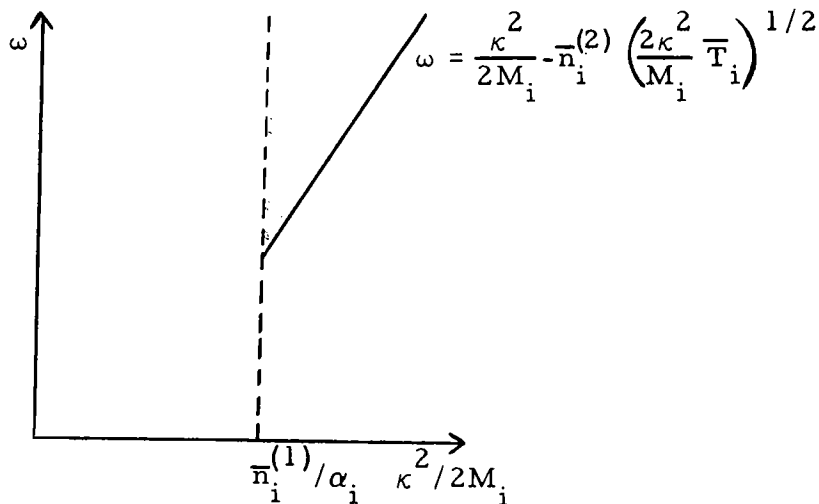


Fig. 12.1--Area of $\omega - \kappa^2/2M_i$ plane for calculation of $S_{0i}(\kappa, \epsilon)$

At this point, everything necessary for the calculation of $S_{0i}(\kappa, \epsilon)$ has been written down. Let us now consider in a little more detail the calculation of $S_{0i}(\kappa, \epsilon)$ by means of a digital computer.

12.2. INFORMATION FOR THE PROGRAMMER

Basic Input I

1. $M = \text{mass.}$
2. $T = \text{temperature.}$
3. Either the sets of non-negative numbers $[\epsilon] = [\epsilon_1, \epsilon_2, \dots, \epsilon_{N1}]$

$$\left[\frac{\kappa^2}{2} \right] = \left[\left(\frac{\kappa^2}{2} \right)_1, \left(\frac{\kappa^2}{2} \right)_2, \dots, \left(\frac{\kappa^2}{2} \right)_{N2} \right]$$

or the sets of non-negative numbers

$$[\beta] = [\beta_1, \beta_2, \dots, \beta_{N1}]$$

$$[\alpha] = [\alpha_1, \alpha_2, \dots, \alpha_{N1}] ;$$

$$0 \leq N_1 \leq 125, 0 \leq N_2 \leq 125 .$$

If β 's and α 's are read in, we will want to convert to ϵ 's and κ 's by means of

$$\beta T = \epsilon ,$$

$$\alpha M T = \frac{\kappa^2}{2}$$

before we can apply the formulae given in the previous sections. In the output, however, we will want to tabulate α , β , and the function which the program is intended to calculate.

Required Operations

Before further specifying the details of input, it will be convenient to discuss briefly some of the mathematical operations which the computer will be required to perform. Basically, given the sets ϵ and $\kappa^2/2$, the machine will be required to compute any or all of the quantities

$$S_{0G} \text{ (Eq. 16) ,}$$

$$S_{0D} \text{ (Eq. 17) ,}$$

$$S_{0i} \text{ (Eqs. 18 through 29) } i = 1, 2, \dots, K .$$

Having computed these, it will then be required to do convolution as indicated in Eq. (15). This will be discussed in more detail later.

Input II

Each of the S_{0G} , S_{0D} , S_{0i} will be computed when, and only when, the input relating to them is specified.

In addition to the input parameters listed under "Input I," there is the input relating to the various S's:

Input for S_{0G} M_G

Input for S_{0D} c, d

Input for S_{0i} $i = 1, 2, \dots, N - 2 \leq 4$

(a). $\rho_i^{(u)}(\omega) =$ unnormalized frequency distribution at a number of evenly spaced points $\omega_k = k\Delta(k^2 - K_i)$,

$$\rho_i(\omega) = \frac{\rho_i^{(u)}(\omega)}{\int_0^\infty \rho_i^{(u)}(\omega) d\omega} . \quad (30)$$

Note: $\rho_i(\omega)$ is non-zero only for $0 < \omega \leq \theta_i$.

Since K_i , θ_i are specified in the input, determine Δ and the following parameters:

$$\alpha_i \text{ (Eq. 22) ,}$$

$$\bar{\omega}_i \text{ (Eq. 25) ,}$$

$$\sigma_i^2 \text{ (Eq. 26) ,}$$

$$\bar{T}_i \text{ (Eq. 28) .}$$

(b). Input control parameters and their function:

1. $\bar{n}_i^{(1)}$. If $\frac{\kappa^2}{2M_i} \alpha_i \leq \bar{n}_i^{(1)}$, Eq. (18) will be used to calculate

S_{0i} for all ω . (The way in which the δ -function in Eq. (18) is treated is discussed later.)

2. $\bar{n}_i^{(2)}$. If $\frac{\kappa^2}{2M_i} \alpha_i > \bar{n}_i^{(1)}$,

$$(i) \text{ and } |\omega| \leq \frac{\kappa^2}{2M_i} - \bar{n}_i^{(2)} \sqrt{\frac{2\kappa^2 T_i}{M_i}},$$

Eq. (18) will be used;

$$(ii) \text{ and } |\omega| > \frac{\kappa^2}{2M_i} - \bar{n}_i^{(2)} \sqrt{\frac{2\kappa^2 T_i}{M_i}}$$

Eq. (29) will be used.

3. $n_i^{(0)}$. If $\frac{\kappa^2}{2M_i} \alpha_i \leq \bar{n}_i^{(1)}$,

(i) and $n \leq n_i^{(0)}$, the term $g_i^{(n)}(\omega)$ in Eq. (18) will be calculated from $g_i^{(n-1)}(\omega)$ by means of Eq. (20);

(ii) and $N > n_i^{(0)}$, the term $g_i^{(n)}(\omega)$ in Eq. (18) will be calculated by means of Eq. (24).

12.3. EXAMPLE SHOWING A POSSIBLE FLOW OF THE PROGRAM

First:

1. $[\beta]$, $[\alpha]$ are read in.
2. $[\beta]$, $[\alpha]$ are converted to $[\epsilon]$, $[\kappa^2/2]$

Second:

3. $\rho_i^{(u)}(\omega)$ and M_1 are read in.
4. Calculate and store $\rho_1(\omega)$ (Eq. (30)).

5. Calculate and store α_1 (Eq. (22)).
6. Calculate and store $g_1^{(1)}(\omega)$ (Eq. (19)).
7. Calculate and store $\bar{\omega}_1$ and σ_1^2 (Eqs. (25) and (26)).

Third: The quantities $\bar{n}_1^{(1)}$, $\bar{n}_1^{(2)}$, and $n_1^{(0)}$ are read in.

Fourth: Calculate and store

$$g_1^{(2)}(\omega) = \int_{-\infty}^{\infty} g_1^{(1)}(\omega' - \omega) g_1^{(1)}(\omega') d\omega' ,$$

$$g_1^{(3)}(\omega) = \int_{-\infty}^{\infty} g_1^{(1)}(\omega' - \omega) g_1^{(2)}(\omega') d\omega' ,$$

$$g_1^{(n_0)}(\omega) = \int_{-\infty}^{\infty} g_1^{(1)}(\omega' - \omega) g_1^{(n_0-1)}(\omega') d\omega' .$$

Note: If $g_1^{(1)}(\omega)$ is nonvanishing only in $-\theta_1 \leq \omega \leq \theta_1$, $g_1^{(n)}(\omega)$ is nonvanishing only in $-n \theta_1 \leq \omega \leq n \theta_1$.

Fifth:

(A) Pick lowest values of $(\kappa^2/2M_1) \alpha_1 < \bar{n}_1^{(1)}$; go to Eq. (18a); and calculate $\Delta S_{01}(\kappa, \epsilon)$ at all points ϵ in the set $[\epsilon]$ of input numbers,

commencing with the lowest value of ϵ . This will require

- (1) The set of functions $g_1^{(n)}(\omega)$ $1 \leq n \leq n_0$ generated in step 4 above.
- (2) For $n > n_0$, the quantities defined by Eq. (24).
- (3) Interpolation: The points ω at which $g_1^{(n)}(\omega)$ are calculated will not in general contain or be contained in the set $[\epsilon]$.
- (4) A convergence criterion for terminating the series in Eq. (18a).

(B) If $(\kappa^2/2M_1) \alpha_1 > \bar{n}_1^{(1)}$, test the quantity

$$n = \epsilon - \frac{\kappa^2}{2M_1} + \bar{n}_1^{(2)} \sqrt{\frac{2\kappa^2 \bar{T}_1}{M_1}} ,$$

commencing with the lowest value of ϵ .

If $\eta \leq 0$, use Eq. (18a) to calculate $\Delta S_{01}(\kappa, \epsilon)$.

If $\eta > 0$, use Eq. (29) to calculate $S_{01}(\kappa, \epsilon)$. Go to next-lowest value of ϵ , get new n , and repeat the procedure.

Sixth:

Having gone through all values of ϵ , pick a new value of $\kappa^2/2$ and repeat the procedures outlined in the fifth step. In this way, $S_{01}(\kappa, \epsilon)$ will be calculated for all points in the sets $[\epsilon]$, $[\kappa^2/2]$. These $S_{01}(\kappa, \epsilon)$ are stored, probably on tape.

Seventh:

To obtain $S_{02}(\kappa, \epsilon)$, one reads in the appropriate input numbers and repeats the procedure used for calculating $S_{01}(\kappa, \epsilon)$.

Eighth:

Apply Eq. (15). Calculate and store

$$S_0^{(2)}(\kappa, \epsilon) = \int_{-\infty}^{\infty} S_{02}(\kappa, \epsilon' - \epsilon) S_{01}(\kappa, \epsilon') d\epsilon'$$

at the points $\epsilon = \kappa^2/2$.

Ninth:

Read in M_G .

Use Eq. (16). Calculate and store $S_{0G}(\kappa, \epsilon)$.

Tenth:

Apply Eq. (15). Calculate and store

$$S_0^{(3)}(\kappa, \epsilon) = \int_{-\infty}^{\infty} S_{0G}(\kappa, \epsilon' - \epsilon) S_0^{(2)}(\kappa, \epsilon') d\epsilon' .$$

Eleventh:

Print out $\bar{S}_0(\alpha, \beta)$ α, β , where $\bar{S}_0(\alpha, \beta) = T S_0(\kappa^2, \epsilon)$.

The code must also include coherent elastic scattering, the $\delta(\epsilon)$ in incoherent elastic scattering, $\sigma(\theta, \epsilon)$, $\sigma(\theta)$, σ_T , $S(\alpha, \beta)$, Debye-Waller factor, infinite-medium spectrum, and P_r components.

XIII. CADMIUM-CURTAIN EXPERIMENT

It is known that because of the very large mean free path of high-energy neutrons in H_2O , it is not possible to set up a truly thermal spectrum in this moderator using a fast-neutron source. As mentioned in a previous report, (2) this difficulty can be circumvented by interposing a cadmium curtain between the fast source and the probe. The neutrons absorbed in the curtain constitute a negative source with no high-energy tail. The spectrum produced by this source is obtained from a difference measurement and is expected to go over into a Maxwellian-like asymptotic spectrum, far enough from the curtain. The experiment was performed using the 50-m flight path because the mean-emission-time correction applying to this measurement is very hard to estimate and should be reduced to a minimum.

The result of the measurement was found to be in good agreement with a Maxwellian at $302^\circ K$ between 0.01 and 0.2 ev. This is seen in Fig. 13.1, where the flux divided by the energy is plotted as a function of energy. Also shown for comparison are two other Maxwellians, at 300° and $303^\circ K$. The discrepancies at very low energy (less than 0.01 ev) are probably due to inaccuracy of the sensitivity function used for reducing the experimental data. At high energy, beyond 0.2 ev, the two fluxes to be subtracted come so close together that the method breaks down.

It also was attempted to measure a leakage flux due to the negative source, far enough from the latter, and to compare it with the theoretical results corresponding to the multivelocity Milne problem. This was abandoned because of lack of intensity.

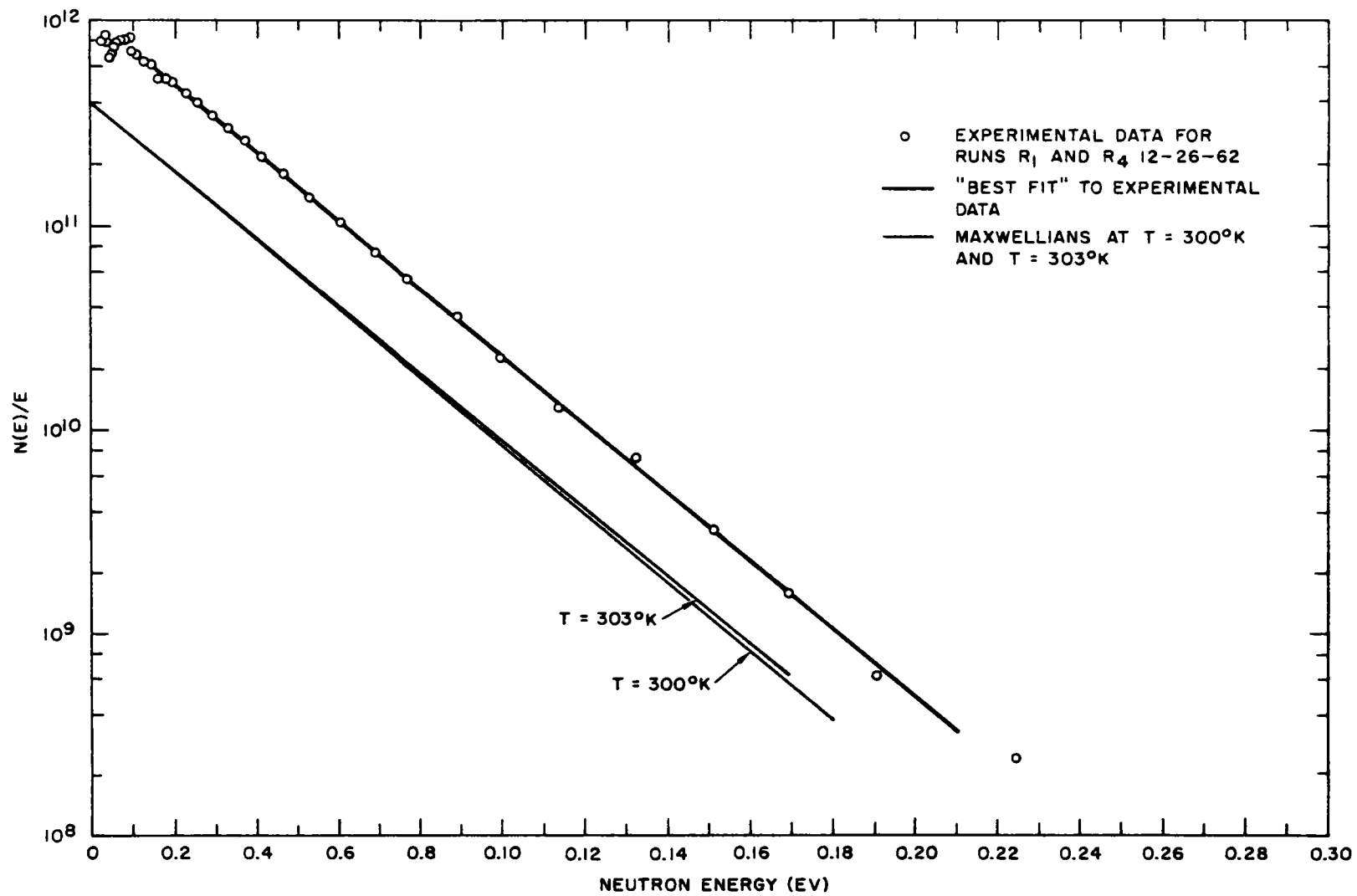


Fig. 13. 1--Neutron spectrum from cadmium-curtain experiment

XIV. ASYMPTOTIC (DIFFUSION-COOLED) NEUTRON SPECTRA

When a burst of fast neutrons is produced in a finite moderating assembly, once the time required to approach equilibrium has elapsed, the energy distribution of the neutrons will not change any further and the whole neutron population will die away with some decay constant depending on the size of the assembly. This asymptotic spectrum deviates from a Maxwellian because of the energy dependence of the leakage and absorption probabilities. The absorption probability usually is constant ($1/v$ absorber), whereas the leakage probability is strongly energy-dependent. In the diffusion approximation, it is

$$P_{\text{leak}} = B^2 D v \ ,$$

and even for constant D it is seen to increase linearly with the neutron velocity. This preferential leakage of fast neutrons is the reason for the so-called diffusion cooling of the asymptotic spectrum. But the diffusion constant, D , also depends on energy; actually, it vanishes for $E = 0$ because

$$D = \frac{1}{3\Sigma(1 - \bar{\mu})} \quad \text{and} \quad \lim_{v \rightarrow 0} \Sigma v > 0 \ .$$

For a crystalline moderator like graphite or beryllium, Σ fluctuates sharply for a neutron wavelength of the order of the separation of the reflecting planes. At the Bragg cutoff energy, Σ elastic drops suddenly to zero and only the much smaller inelastic cross section is left over. Owing to these strongly distorting factors, the asymptotic neutron spectrum will deviate from a Maxwellian. The deviations of the asymptotic neutron spectrum from a Maxwellian due to the energy-dependent leakage will be strongly influenced by the energy exchange properties of the scattering kernel of the moderator. As an example, calculations were carried out for graphite. Figures 14.1 and 14.2 compare the results obtained for a mass-12 gas model and a Parks crystalline model. It is seen that the spectra calculated with the gas kernel are smooth and close to a room-temperature Maxwellian. However, the spectra calculated with the crystalline kernel are strongly distorted and show maxima in correspondence with the Bragg peaks of σ_s . This is in agreement with the trapping effect predicted by de Saussure⁽⁵³⁾ and shows explicitly the much poorer energy-transfer properties of the crystalline solid compared with those of the gas.

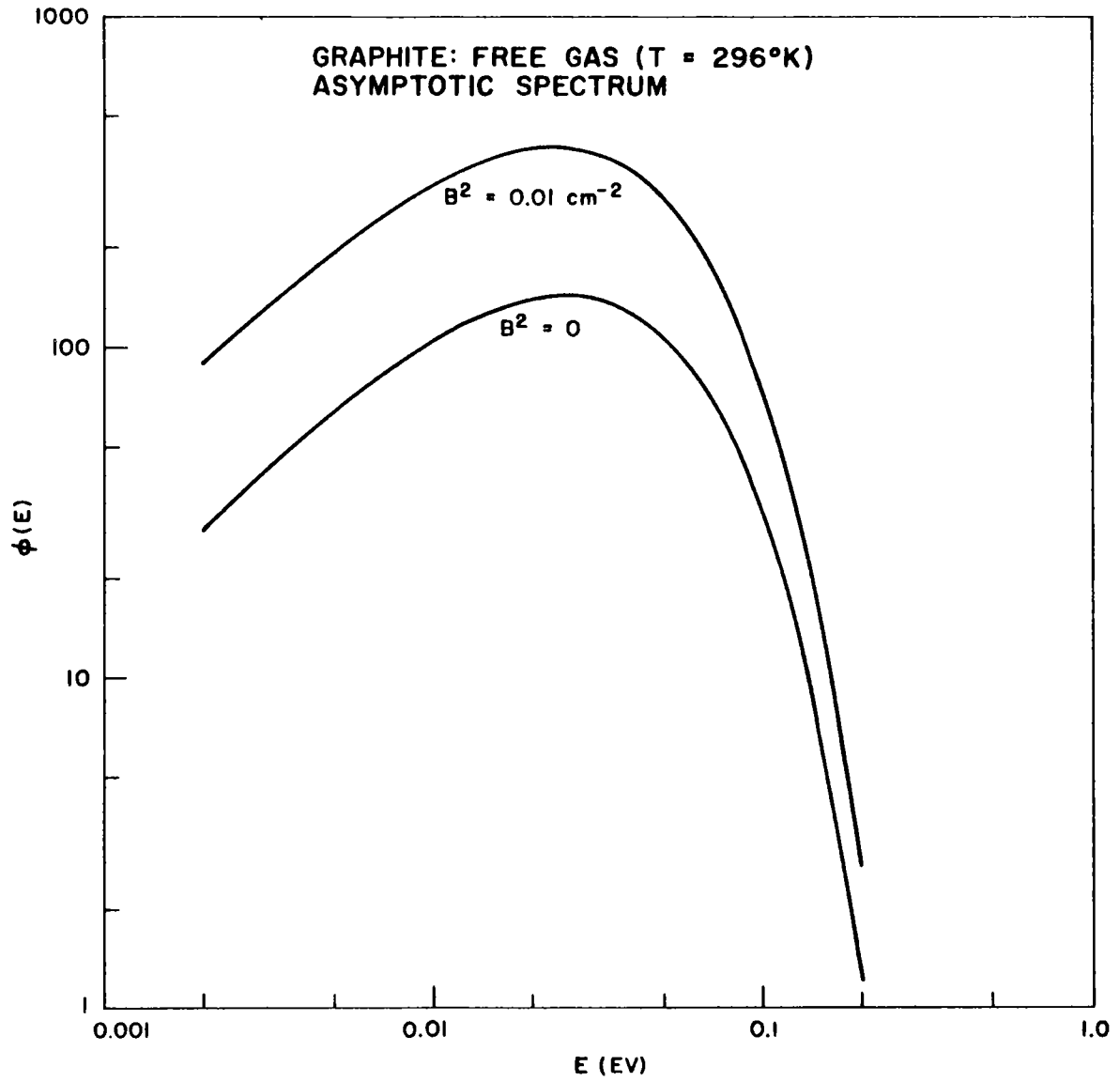


Fig. 14.1--Neutron spectrum calculated from a free-gas model

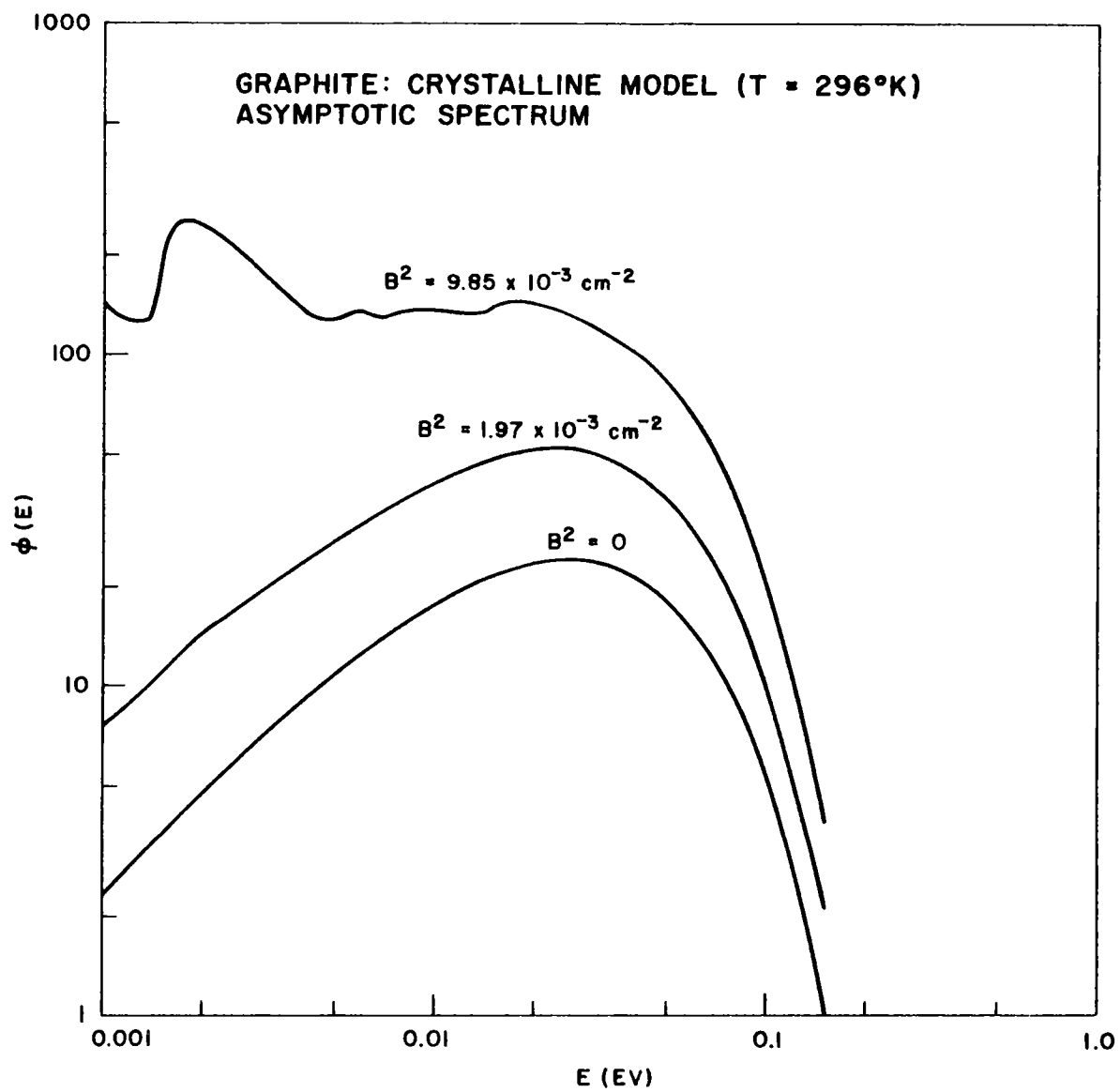


Fig. 14.2--Neutron spectrum calculated from a crystalline model

XV. RESEARCH EQUIPMENT

15. 1. LINAC FACILITY

During this last contract year, many significant improvements have been made in the General Atomic Linac Facility. These consist of additions to the physical plant as well as major machine changes and improvements.

A new office and Linac expansion building has been added behind the existing Linac cell. This provides space for one extra Linac section and all four necessary klystron power supplies. The klystrons will all be located out of the irradiation cell so that they may be operated at the higher power levels available today without incurring radiation breakup of the pulse. The building has been completed, and permanent shield-wall construction is under way. The entire construction project has been carried out without incurring any shutdown of the Linac or any loss of Linac operating time. The movement of modulators from the present radiation cell will begin toward the end of 1963 and will continue for an extended period of time. As the modulators are moved, they will be upgraded to handle the new 20-Mw klystrons now available from both Litton Industries and Sperry Rand Corporation.

The next stage planned for the Linac installation will consist of four sections of L-band Linac, each powered by a 20-Mw klystron and fed by a vastly improved current injection system. The section to be added will serve as a test stand for the projected improvements, so the existing three-section installation can stay in operation.

Specifications for a new Linac injector have been prepared and sent out on bid. A 20-amp electron gun is desired for the newer higher r-f power Linac. Gun delivery from one of the many interested suppliers is expected early in 1964. Short pulse current capability will be greatly enhanced by this step.

In addition to the major improvements initiated this contract year, a significant number of improvements have been made in the basic three-section machine. The tube-type triggering circuitry has been replaced by a completely transistorized trigger and trigger delay system using the latest tunnel-diode techniques. Defective channels can be easily isolated when they occur (which is rare) and the necessary plug-in card can be easily replaced. This step minimized costly trouble-shooting and downtime, replaced marginal circuitry, and freed large sections of badly needed

space in the accelerator console. The elimination of jitter between pulses, which was extremely troublesome for fast spectral studies, was also accomplished.

The injector system for the Linac was also improved considerably by the installation of an isolation valve and ferrite current monitor. During gun installation, the r-f accelerator system can be isolated. In addition, the injector current output performance can be readily studied for optimum machine tuning, rather than having to rely on the output beam from the accelerator.

Further improvements in the Linac vacuum system are well under way. Vac-ion pumps are being installed in the positions occupied by the old trapped-oil diffusion-pumping systems as these systems require replacement. The entire vacuum system on the Linac is over 6 yr old, and during this time high-vacuum technology has advanced so markedly that it would be foolhardy to replace defective existing high-vacuum systems with identical high-maintenance oil systems.

Another area where considerable re-engineering and rebuilding have been carried out is in the klystron modulators. Several nearly disastrous fires revealed basic flaws in the engineering design of the standard modulators. These problems have been solved by design and construction of ultra-flat pulse lines and installation of new ceramic thyratrons. Greatly improved machine performance has thus been attained.

As a result of the extensive maintenance and defect correction efforts made during the last year, an extremely high operating level was attained on the Linac -- more than 4000 hr of contract operation, with some 1500 hr of usage devoted to AEC work.

15.2. PRESSURE VESSEL

A versatile research tool which has been used to measure infinite-medium neutron spectra for poisoned solutions at elevated temperatures is the pressure vessel shown in Fig. 15.1. This vessel has been used to measure infinite-medium neutron spectra for borated water at moderator temperatures ranging from ambient temperature to 600^oF, and for pressures up to 1550 psi.

The pressure vessel is constructed entirely of Type 316 stainless steel, because this type of stainless steel has the best anti-corrosion properties and can therefore be used to contain a variety of salt solutions at high temperatures. The pressure vessel has cylindrical walls, the axis of the cylinder being vertical. The bottom of the vessel is hemispherical.

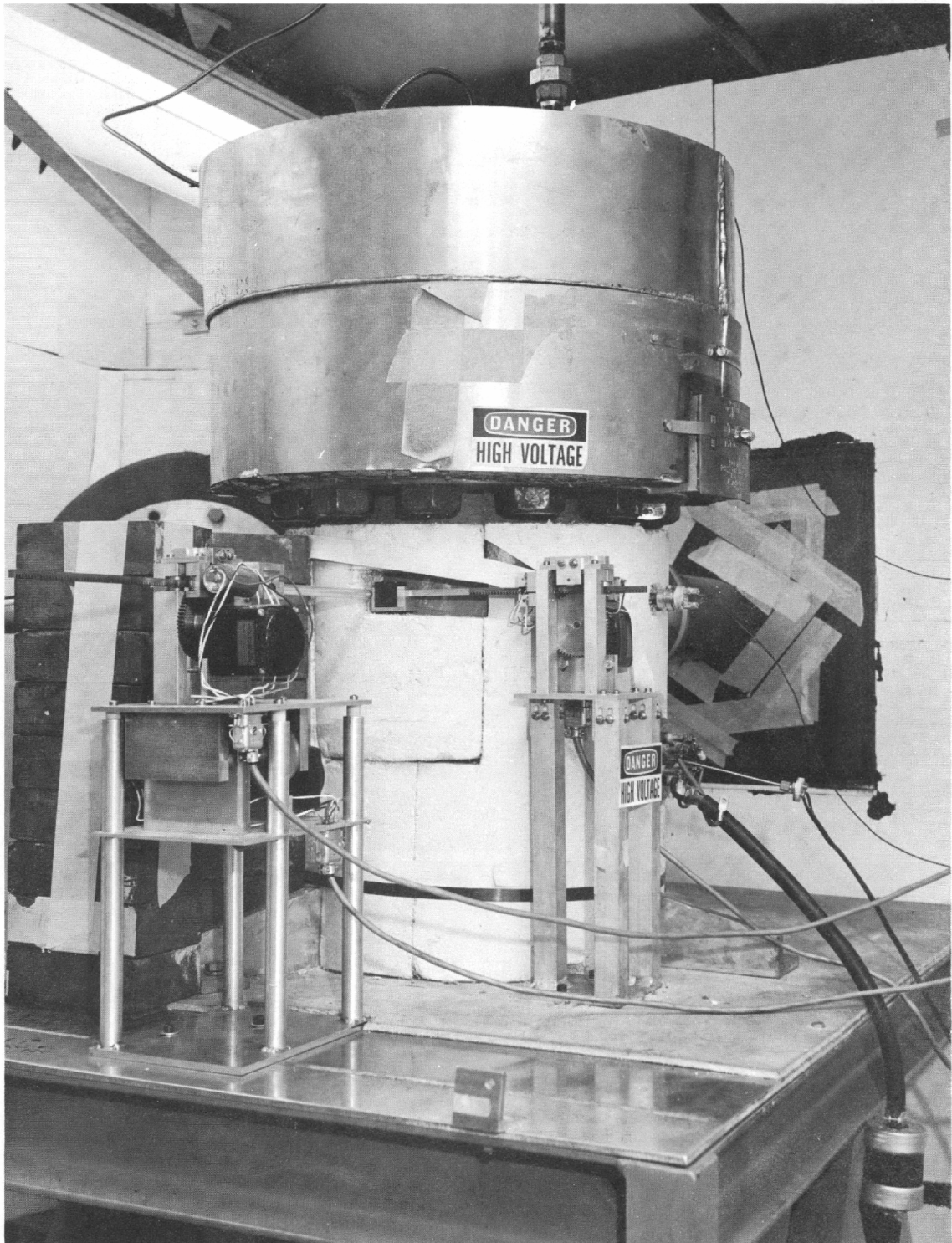


Fig. 15.1--View of pressure vessel showing the zirconium scatterer and background-plug drive mechanisms

The top of the vessel is a 3-5/8-in. -thick blind-flange head which is attached to the cylindrical body of the vessel by twelve 1-5/8-in. -diameter bolts and sealed with a stainless-steel-covered abestos gasket, using a torque load of 1200 ft-lb. The vessel is supported by a welded tripod arrangement. The vessel is heat-insulated and shielded from thermal-neutron room return by a 3/4-in. thickness of Johns-Manville cement, heavily loaded with amorphous boron, which was packed around the vessel and baked dry. Outside this layer of cement is a 2-in. thickness of heat-insulating material (Kaylo 20). The vessel has an internal diameter of 10 in. and an over-all internal height of 23 in.

The pressure vessel is self-pressurized by means of a 5-kw immersion-type electrical heater located near the bottom of the vessel. The temperature of the solution within the vessel is monitored with Chromel-Alumel thermocouples sheathed in Type 316 stainless steel. The pressure is monitored with a stand-off standard pressure gauge in order to eliminate the need for expensive temperature-compensated instrumentation. The safety head, rated at 2000 psi and 620^oF, is vented outside of the room for safety reasons, as can be seen in Fig. 15.1. The "glory hole," a cylindrical tube 0.43-in. in inside diameter with a wall thickness of 0.035 in., extends through the center perpendicular to the cylindrical axis of the vessel. The wall of the glory hole is purposely made thin in order to minimize neutron absorption and thus is considered a secondary rupture disk. The pressure vessel was constructed according to standard ASME-code practices. All welds were carefully radiographed, and the pressure vessel, including the glory hole, was checked hydrostatically at 3300 psi. The vessel has been certified for operation at 2200 psi and 620^oF.

Neutron spectra are measured by placing a zirconium scatterer at the center of the glory hole, and the neutron beam emerging from the glory hole is analyzed using standard pulsed-beam time-of-flight techniques.

Because of the glory hole, safety of operation is paramount, so positioning of the zirconium scatterer (see Fig. 15.1) for signal runs, positioning of the B₄¹⁰C plug for background runs, and changing of heater power are performed completely by remote control.

15.3. PULSED CRITICAL ASSEMBLY

The pulsed critical assembly was originally built to facilitate neutron-spectrum measurements. It was designed to approximate as closely as possible a homogeneous, one-dimensional, bare multiplying assembly. Over-all views of the assembly are shown in Figs. 9.2 and 9.3. The fuel plates for the assembly are of uranium-aluminum alloy, 17 wt-% uranium 93% enriched in U²³⁵. The plates are 18 in. long by 6 in. wide by 0.020 in. thick.

This assembly has recently been taken critical (Section IX) and measurements have been made of the decay constant associated with various loadings. Previously, ⁽³³⁾ measurements were made of the scalar and angular neutron spectra when the assembly (loading to a multiplication of about 10) was operated as a bare homogeneous multiplying assembly. The design of the assembly permits loading of the core in such a way that lattice problems may also be studied.

15.4. NEW FLIGHT PATH AND LOW-ROOM-RETURN NEUTRON CAVE

The design of a new 70-m flight path and a new, enlarged, low-room-return neutron cave has been completed. Most of the materials necessary for construction have been ordered, and this facility should be completed in the near future. A plan view of the Linac experimental area is shown in Fig. 15.2, including the existing cave, the old flight paths, the new flight path, and the enlarged cave. The enlarged cave will permit much larger assemblies to be studied. The new cave walls will be thin but heavily absorbing, and are to be constructed of removable panels. Albedo experiments were performed to determine the most suitable wall material (H_3BO_3) and thickness for the enlarged low-room-return neutron cave. Essentially, the experiment consisted in measuring the surface leakage of reflected neutrons from various materials which might be used in the new cave. The new, evacuated, 70-m flight path may be used to measure neutron spectra in various moderators and shields from 0.001-ev up to about 20-Mev neutron energy.

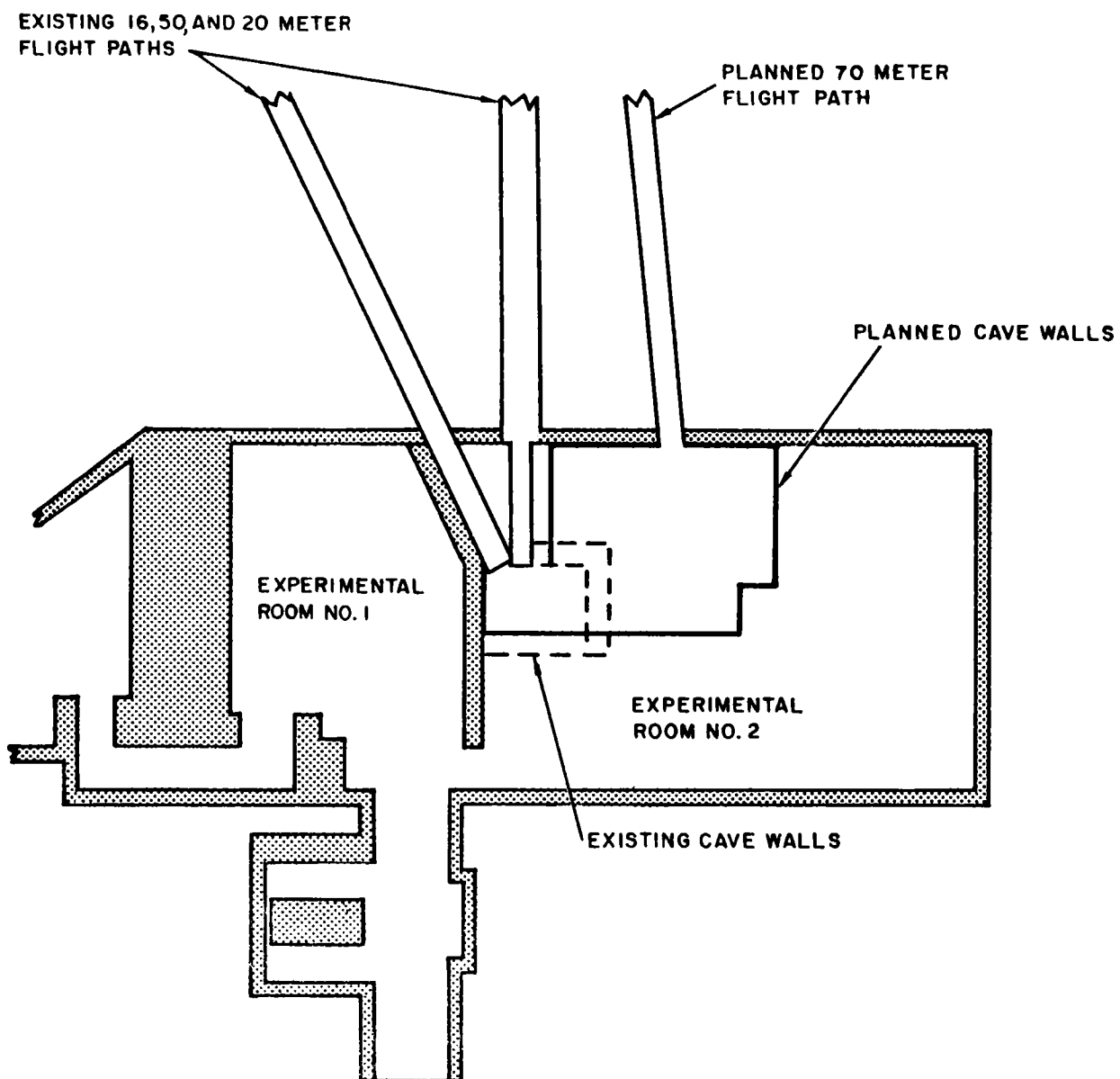


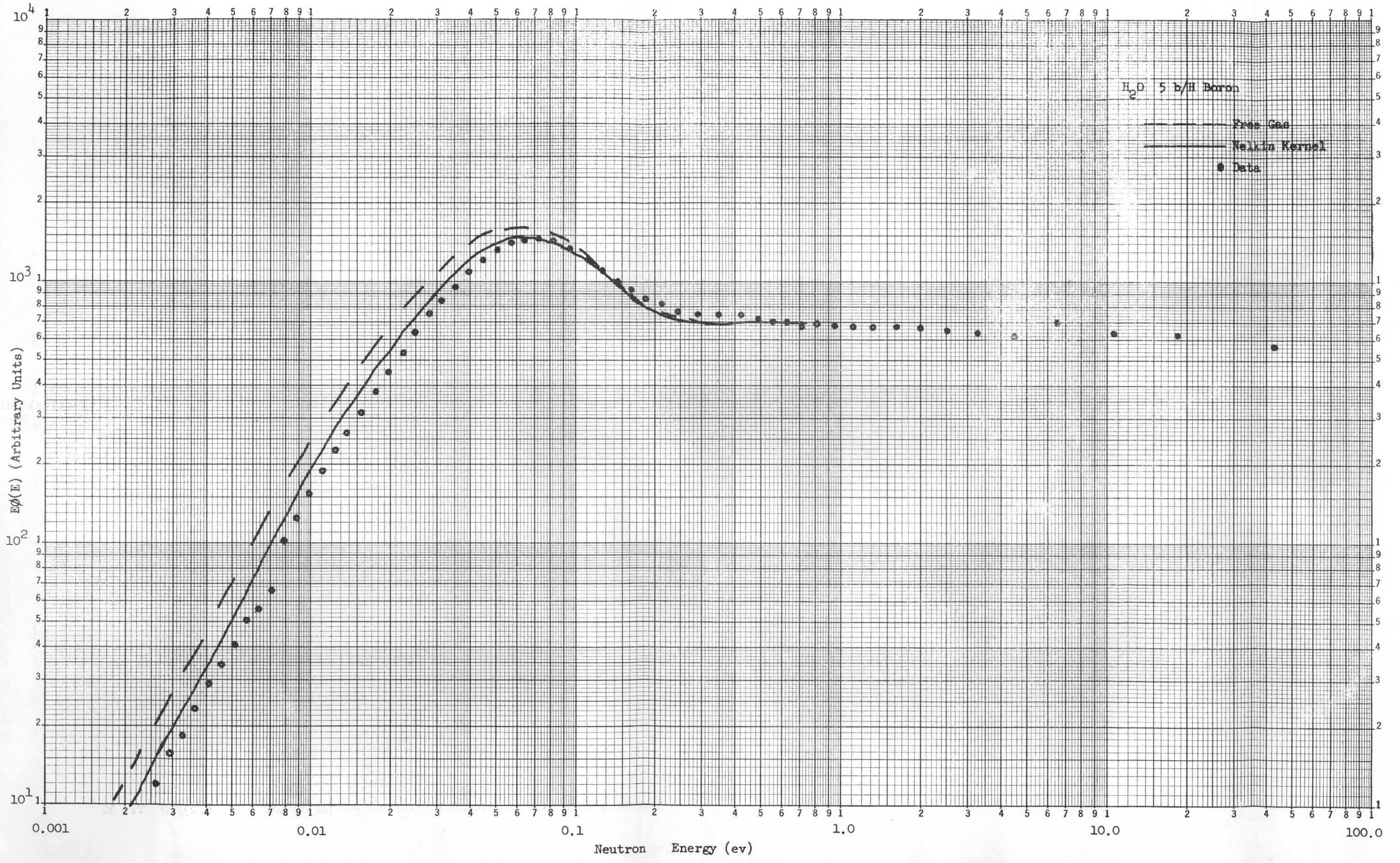
Fig. 15. 2--Plan view of the Linac experimental room

Appendix I

FORMAT FOR NEUTRON-SPECTRA DATA BOOK

The presentation of experimental and theoretical data concerning neutron spectra has previously been troublesome and cumbersome. It is hoped that the format set forth in this Appendix will initiate a procedure for displaying data in a standard form so that sufficient information is given for comparisons of data and calculations obtained at this and other laboratories. It should be pointed out that while this format is of a typical experiment previously performed at General Atomic, it could be expanded to include all "best data" available. A compilation of this sort should be a highly valuable and useful tool for all reactor physicists. It is tentatively planned to make this spectrum compilation jointly with the thermalization group of UKAEA at Harwell, England.

In the following two pages, the geometrical arrangement and information necessary to calculate the spectrum using the most recent theoretical model are shown, together with the experimental results for comparison.



INFINITE MEDIUM NEUTRON
SPECTRUM IN BORATED H₂O

CALCULATION PARAMETERS

Kernel: Nelkin Water (ID 43700) and Free Gas (ID 40205)

Code: SPECTRUM

Temperature: 0.0255 ev

Source: erf $\sqrt{E/KT_{eff}}$ (KT_{eff} 0.117 ev)

ATOM DENSITIES x 10⁻²⁴

$$N_H = 0.0666$$

$$N_B = 0.000427$$

LOCAL BUCKLING

$$B_{transverse}^2 = 0.02 \text{ cm}^{-2}$$

$$B_{axial}^2 = 0$$

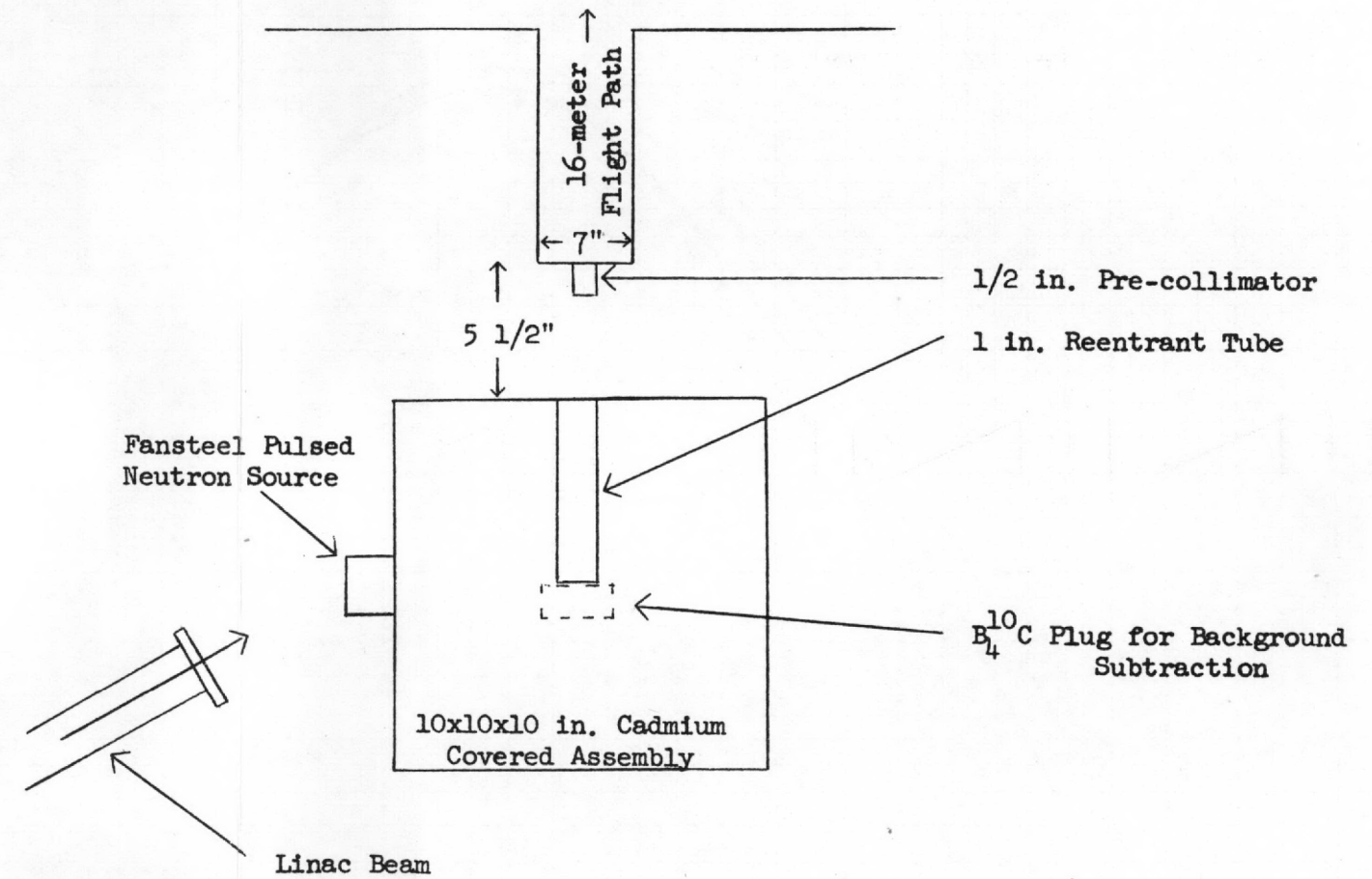
$$\left(\frac{\text{total absorptions}}{\text{slowing down density}} \right) = 1.002$$

COMMENTS:

Spatial Effects Negligible

EXPERIMENTAL ARRANGEMENT

PLAN VIEW



Appendix II

MEAN-EMISSION-TIME CORRECTION FOR THE MEASUREMENT OF STATIONARY SPECTRA BY THE PULSED-NEUTRON-SOURCE TECHNIQUE

In the measurement of stationary neutron spectra by the pulsed source method, it is generally assumed that after each pulse the neutron density in the assembly decays in a time which is short compared with the time of flight. Only in this case, one gets the exact integral over the time-dependent spectrum which is equivalent to the stationary spectrum to be measured:

$$\phi(v) = \int_0^{\infty} \phi(v, t) dt \quad , \quad (1)$$

where $\phi(v, t)$ stands for the flux produced by a source of the form $Q(v)\delta(t)$.

Of course, this ideal situation is never met in practice. The magnitude actually measured in the experiment is the number of counts ΔC accumulated in each time channel, and for sufficiently small channel width Δt_0 it is

$$\frac{\Delta C(t_0)}{\Delta t_0} \cong \frac{dC(t_0)}{dt_0} = \int_0^{\infty} \phi\left(v, t_0 - \frac{L}{v}\right) \eta(v) dv \quad , \quad (2)$$

where $C(t_0)$ is the total number of counts in the time interval $0 < t < t_0$, and the origin of the time scale is supposed to be in coincidence with the source burst. $\phi(v, t)$ stands for the transient neutron flux at some point of the assembly; $\eta(v)$ is a coefficient related to solid angle and over-all detector sensitivity; and L is the flight-path length.

In the ideal case of a very large flight path and very fast die-away of the neutron pulse in the assembly, one may write, with $\Psi(v, t) = \eta(v)\phi(v, t)$:

$$\Psi(v, t) = \Psi(v)\delta\left(t_0 - \frac{L}{v}\right) \quad . \quad (3)$$

Thus,

$$\frac{dC(t_0)}{dt_0} = \int_{v_0}^{\infty} \Psi(v)\delta\left(t_0 - \frac{L}{v}\right) dv = \frac{1}{L} v_0^2 \Psi(v_0) \quad , \quad (4)$$

where

$$v_0 = \frac{L}{t_0} \quad (5)$$

The meaning of the factor $(1/L) v_0^2$ appearing in Eq. (4) becomes more evident by writing Eq. (4) in the form

$$-dC(t_0) = \Psi(v_0)dv_0 \quad (6)$$

In a real case, the relation between $\Psi(v_0)$ and $C(t_0)$ is not that simple, and we shall have to find a procedure to correct Eq. (4) for finite times of flight. In the past, it was assumed that in general the equation still holds if t_0 is replaced by a corrected time $t_0 - \tau(v)$, where $\tau(v)$ is the average time at which neutrons of velocity v are emitted by the assembly being measured:

$$\tau(v) = \frac{\int \phi(v, t)t dt}{\int \phi(v, t) dt} \quad (7)$$

It turns out that this correction neglects terms of order $(\tau/t_0)^2$ and $d\tau/dt_0$ and might thus lead to relatively large errors in the spectrum at those energies at which τ rises quite fast from the nearly zero slowing-down time to the mean lifetime of thermal neutrons in the assembly. The effect, which is rather small for H_2O , obviously increases with decreasing values of the moderating ratio, $\xi\sigma_s/\sigma_a$, and probably becomes quite important for D_2O or graphite. In order to find a relation valid for large values of t_0 , between the counts per unit time

$$c(t_0) = \frac{dC(t_0)}{dt_0} \quad (8)$$

and the stationary spectrum $\phi(v)$ as given by Eq. (1), we start from the Laplace transform of Eq. (2) (with respect to t_0),

$$\bar{c}(p) = \int_{v_0}^{\infty} e^{-p(L/v)} \bar{\Psi}(v, p) dv \quad (9)$$

and expand $\bar{\Psi}(v, p)$ in a series of powers of p ,

$$\bar{c}(p) = \int_{v_0}^{\infty} dv e^{-p(L/v)} \left[\Psi_0(v) - p\Psi_1(v) + \frac{p^2}{2!} \Psi_2(v) - \dots \right] \quad (10)$$

From a well-known theorem it is seen that the coefficients of this expansion are simply the time moments of $\Psi(v, t)$, i. e. ;

$$\Psi_n(v) = \int \Psi(v, t) t^n dt . \quad (11)$$

Anti-transforming Eq. (10) term by term, we find

$$c(t_0) = \sum_{n=0}^{\infty} \frac{(-1)^n}{n!} \int_{v_0}^{\infty} \delta^{(n)}\left(t_0 - \frac{L}{v}\right) \Psi_n(v) dv , \quad (12)$$

or

$$c(t_0) = \frac{1}{L} \sum_{n=0}^{\infty} \frac{(-1)^n}{n!} \int_0^{t_0} \delta^{(n)}(t_0 - t) \Psi_n(v) v^2 dt , \quad (13)$$

where t now stands for L/v and $\tau^{(n)}$ means the n^{th} derivative of the τ -function. Using the known properties of these derivatives and performing some algebra, it is found that

$$c(t_0) = F(t_0) - \frac{d}{dt_0} [F\bar{\tau}] + \frac{1}{2!} \frac{d^2}{dt_0^2} [F\bar{\tau}^2] - \dots , \quad (14)$$

where

$$F(t_0) = \Psi(v_0) v_0^2 \frac{1}{L} \quad (15)$$

and

$$\bar{\tau}^n(v) = \frac{\int \Psi(v, t) t^n dt}{\int \Psi(v, t) dt} . \quad (16)$$

It is interesting to check Eq. (14) for a case which can be solved exactly, namely, when

$$\begin{aligned} \Psi(v, t) &= e^{-\lambda t} \Psi(v) && \text{for } t \geq 0 , \\ &= 0 && \text{for } t < 0 \end{aligned} \quad (17)$$

Here we have the simple velocity-independent relation,

$$\bar{\tau}^n = \frac{n!}{\lambda^n} , \quad (18)$$

which, when substituted into Eq. (14), yields

$$c(t_0) = F(t_0) - \frac{1}{\lambda} \frac{dF}{dt_0} + \frac{1}{\lambda^2} \frac{d^2 F}{dt_0^2} - \dots \quad (19)$$

Multiplying Eq. (19) by $1/\lambda$, differentiating, and adding the result to Eq. (19), we find the exact result:

$$F(t_0) = c(t_0) + \frac{1}{\lambda} \frac{dc}{dt_0} \quad (20)$$

Of course, this formula could have been obtained directly from Eq. (9) by using the convolution theorem of the Laplace transform. Equation (14) can be solved by successive approximation if, as usual, the expressions

$$\frac{1}{F(t_0)} \frac{d^{(n)}}{dt_0^n} [F(t_0) \bar{\tau}^n]$$

are small.

Denoting the n^{th} approximation by $F^{(n)} = \Psi^{(n)}(v_0) v_0^2 (1/L)$, it is found up to second order

$$F^{(0)} = c(t_0) \quad (21)$$

$$F^{(1)} = c(t_0) \left[1 + \frac{d\bar{\tau}}{dt_0} \right] + \bar{\tau} \frac{dc}{dt_0} \quad (22)$$

$$F^{(2)} = c(t_0) \left\{ 1 + \frac{d\bar{\tau}}{dt_0} + \frac{1}{2} \frac{d^2}{dt_0^2} \left[(\bar{\tau})^2 - \bar{\tau}^2 \right] \right\} \\ + \frac{dc}{dt_0} \left\{ \bar{\tau} + \frac{d}{dt_0} \left[\frac{3}{2} (\bar{\tau})^2 - \bar{\tau}^2 \right] \right\} + \frac{d^2 c}{dt_0^2} \left[(\bar{\tau})^2 - \frac{1}{2} \bar{\tau}^2 \right] \quad (23)$$

Formula (22) shows clearly that even to first order, the usual mean-emission-time correction is not sufficient.

A formula correct to first order can also be obtained directly from the continuous slowing-down model, where

$$\Psi(v, t) = \Psi(v)\delta[t - \tau(v)] \quad . \quad (24)$$

Here, the mean emission time is simply $\tau(v)$, and by introducing Eq. (24) into Eq. (1) it is found that

$$c(t_1) = \frac{1}{L} v_0^2 \Psi(v_0) \left(1 - \frac{d\tau}{dt_1}\right) , \quad (25)$$

where now, however, the relation between velocity and time is given implicitly by

$$v_0 = \frac{L}{t_1 - \tau(v_0)} \quad . \quad (26)$$

It is worthwhile to point out that for the case of spectra measurement in multiplying media, where the mean emission time becomes quite large, the pure exponential decay corresponding to Eq. (17) is quite a good approximation for systems not too far away from criticality. This is most easily seen when the capture and fission ($1/v$ cross sections) probabilities do not depend on energy and the leakage can be neglected. The transient neutron flux corresponding to this simplified case is

$$N^*(v, t) = N(v, t) + \frac{ke - (\delta kt/\ell)}{\ell} \int_0^t N(v, t') e^{\delta kt/\ell} dt' \quad , \quad (27)$$

where ℓ is the lifetime, k is the prompt multiplication constant, and $\delta k = 1 - k$. $N(v, t)$ stands for the transient flux produced in the same assembly, by the same source, but assuming that $\nu = 0$ (ν being the number of neutrons produced per fission). It is easily seen from Eq. (27) that after times of the order of ℓ , the pulse decays exponentially with a mean life $1/\lambda = \ell/\delta k \gg \ell$, thus justifying the use of Eqs. (17) and (20) for computing the mean-emission-time correction for neutron-spectra measurements in these conditions. Another convenient feature in the case of multiplying assemblies is that the die-away time $1/\lambda = \bar{\tau}$ can be obtained directly from the experiment. In nonmultiplying media, however, the correction terms $\bar{\tau}$ and $\bar{\tau}^2$ and their derivatives have to be computed from theoretical scattering models by the conventional source iteration method of calculating spectrum time moments.

REFERENCES

1. Beyster, J. R., et al., "Integral Neutron Thermalization, Annual Summary Report, October 1, 1960, through September 30, 1961," USAEC Report GA-2544, General Atomic Division, General Dynamics Corporation, 1961. 218p.
2. Beyster, J. R., et al., "Integral Neutron Thermalization, Annual Summary Report, October 1, 1961, through September 30, 1962," USAEC Report GA-3542, General Atomic Division, General Dynamics Corporation, 1962. 205p.
3. Nelkin, M. S., "Scattering of Slow Neutrons by Water," Phys. Rev. 119, 741 (1960).
4. Radkowski, A., "Temperature Dependence of Thermal Transport Mean Free Path," Argonne National Laboratory Report ANL-4476, July, 1950, p.89.
5. Campbell, C. G., R. G. Freemantle, and M. J. Poole, "Measurements of Reactor Spectra by Time-of-Flight and Integral Methods," Second Geneva Conference Proceedings, United Nations, Geneva, 1958, v. 16, p. 233 (P/1384).
6. Mostovoi, V., et al., "Neutron Spectrum Measurements in Uranium-Water Lattices," Second Geneva Conference Proceedings, United Nations, Geneva, 1958, v. 16, p. 254 (P/2152).
7. Melkonian, E., "A Precise Determination of the Slow Neutron Cross Section of the Free Proton," Phys. Rev. 76, 1744-1749 (1949).
8. Egelstaff, P. A., private communication.
9. Hinman, G. W., private communication.
10. Young, J. C. et al., "Measurement of Neutron Spectra and Decay Constants in a Water Moderated Multiplying Assembly," Trans. Am. Nucl. Soc. 2, No. 4, 269 (1961).
11. Placzek, G., "The Scattering of Neutrons by Systems of Heavy Nuclei," Phys. Rev. 86, 377-388 (1952).
12. Honeck, H. C., "THERMOS. A Thermalization Transport Theory Code for Reactor Lattice Calculations," Brookhaven National Laboratory Report BNL-5826, 1961.
13. Egelstaff, P. A., in Proceedings of Symposium on Inelastic Scattering of Neutrons in Solids and Liquids, Vienna, 1960, International Atomic Energy Agency, 1961, p. 25.

14. Whittemore, W. L., and A. W. McReynolds, in Proceedings of Symposium on Inelastic Scattering of Neutrons in Solids and Liquids, Vienna, 1960, International Atomic Energy Agency, 1961, p. 511.
15. Reinsch, O., "Messung des differentiellen Wirkungsquerschnittes und des mittleren logarithmischen Energieverlustes bei der Streuung langsamer Neutronen an Wasser und Eis" Z. Physik, 163, 424-434 (1961).
16. Vinyard, G. H., "Multiple Scattering of Neutrons," Phys. Rev. 96, 93 (1954).
17. Bell, J., "SUMMIT. An IBM-7090 Program of the Computation of Crystalline Scattering Kernels," USAEC Report GA-2492, General Atomic Division, General Dynamics Corporation, February 1, 1962. 111p.
18. Hughes, D. J., and R. B. Schwartz, "Neutron Cross Sections," Brookhaven National Laboratory Report BNL-325 (2nd ed.), 1958.
19. Starr, E., and J. U. Koppel, "Determination of Diffusion Hardening in Water," Nucl. Sci. Eng. 14, 224-229 (1962).
20. Honeck, H. C., "An Incoherent Thermal Scattering Model for Heavy Water," Brookhaven National Laboratory, internal report.
21. Brown, H. D., and D. S. St. John, "Neutron Energy Spectrum in D₂O," Du Pont de Nemours and Company, Inc., Report DP-33, February, 1954.
22. Parks, D. E., J. R. Beyster, and N. F. Wikner, "Thermal Neutron Spectra in Graphite," Nucl. Sci. Eng. 13, 306-324 (1962).
23. Goldman, D. T., and F. D. Federighi, "The Calculation of Neutron Spectra for Perfect Gas, Water and Polyethylene-Moderated Systems," Knolls Atomic Power Laboratory Report KAPL-2000-16, January, 1962.
24. Nielsen, J. R., and A. H. Woollett, "Vibrational Spectra of Polyethylenes and Related Substances," J. Chem. Phys. 26, 1391 (1957).
25. Goldman, D., private communication.
26. Esch, L. J., "Temperature Dependence of the Neutron Transport Cross Section in Paraffin and Polyethylene," Knolls Atomic Power Laboratory Report KAPL-2204, 1962.
27. Wunderlich, B. W., "Motion in Polyethylene I and II," J. Chem. Phys. 37, 1203-1207 (1962).
28. Glaser, W., in Proceedings of Symposium on Inelastic Scattering of Neutrons in Solids and Liquids, Chalk River, Canada, 1962, International Atomic Energy Agency, 1963, p. 53.
29. Brugger, R. M., "Complication of Reduced Slow Neutron Partial Differential Scattering Cross Sections," presented at the Brookhaven National Laboratory Conference on Neutron Thermalization, 1962.

30. Boffi, V. C., V. G. Molinari, and D. E. Parks, in Proceedings of Symposium on Inelastic Scattering of Neutrons in Solids and Liquids Chalk River, Canada, 1962, 1963, Paper SM-30/11.
31. Crawford, B. L., and F. A. Miller, "The Planar Vibrations of Benzene" J. Chem. Phys. 17, 249-255 (1949).
32. Boffi, V. C., V. G. Molinari, and D. E. Parks, "Slow-neutron Scattering by Benzene," General Atomic Report GA-3471, September 5, 1962. 17p.
33. Young, J. C., et al., "Neutron Spectrum Measurements in H₂O, CH₂ and C₆H₆" Nucl. Sci. Eng. (in print).
34. Miller, J., R. L. Brehm, and W. J. Roberts, "Temperature Coefficients and Spectra in the Hydride Moderated SNAP Reactors," Atomics International Report NAA-SR-7140, December 30, 1962.
35. General Atomic Staff, "Technical Foundations of Triga," General Atomic Report GA-471, August 27, 1958. 119p.
36. Cohen, E. R., and E. U. Vaughan, "Thermal Neutron Spectrum in Harmonically Bound Hydrogen Moderators," Atomics International Report NAA-SR-3377, January 15, 1959.
37. Woods, A. B., et al., "Energy Distributions of Neutrons Scattered from Graphite, Light and Heavy Water, Ice, Zirconium Hydride, Lithium Hydride, Sodium Hydride, and Ammonium Chloride by the Beryllium Detector Method," in Proceedings of Symposium on Inelastic Scattering of Neutrons in Solids and Liquids, Vienna, 1960, International Atomic Energy Agency, 1961. p. 487.
38. Glauber, R. J., "Time-dependent Displacement Correlations and Inelastic Scattering by Crystals," Phys. Rev. 98, 1692 (1955).
39. Schmunk, R. E., et al., "Lattice Dynamics of Beryllium," Phys. Rev. 128, 562-573 (1962).
40. Sinclair, R. N., in Proceedings of Symposium on Inelastic Scattering of Neutrons in Solids and Liquids, Chalk River, Canada, 1962, International Atomic Energy Agency, 1963, Paper SM-30/36.
41. Slutsky, L. J., and C. W. Garland, "Lattice Dynamics of Hexagonal Close-packed Metals" J. Chem. Phys. 26, 787-793 (1957).
42. Sjolander, A., Arkiv Physik, 11, 315 (1958).
43. Parks, D., "Relation of Crystal Symmetry in Graphite to Lattice Vibrations and Their Interaction With Slow Neutrons," USAEC Report GA-2125, General Atomic Division, General Dynamics Corporation, March 15, 1961. 20p.
44. Young, J. C., et al., "Development of Multiplying Assembly. Final Report," USAEC Report GA-2471, General Atomic Division, General Dynamics Corporation, 1961. 70p.

45. Garelis, E., and J. L. Russell, Jr., Nucl. Sci. Eng. 16 263-270 (1963).
46. Young, J. C., et al., "Integral Neutron Thermalization. Quarterly Progress Report for period ending June 30, 1963," General Atomic Report GA-4426, July 25, 1963. 36p.
47. Verbinski, V. V., "Fast Neutron Transport in LiH," Trans. Am. Nucl. Soc. 6, No. 1, 190 (1963).
48. Batchelor, R., et al., Nucl. Inst. Methods 8, 146 (1960).
49. Batchelor, R., et al., Nucl. Inst. Methods 13, 70 (1961).
50. Honeck, H. C., private communication.
51. Egelstaff, P. A., and P. Schofield, "On the Evaluation of the Thermal Neutron Scattering Law," Nucl. Sci. Eng. 12, 260 (1962).
52. Erdelyi, A., et al., Higher Transcendental Functions, Vol. 2, McGraw-Hill Book Company, New York, 1953, p. 5.
53. de Saussure, G., "The Neutron Asymptotic Decay Constant in a Small Crystalline Moderator Assembly," Proceedings of the Brookhaven National Laboratory Conference on Neutron Thermalization, April, 1962.

